

Measuring the neutrino mass hierarchy with the future KM3NeT/ORCA detector

Messung der Neutrinomassenhierarchie
mit dem zukünftigen KM3NeT/ORCA-Detektor

Der Naturwissenschaftlichen Fakultät
der Friedrich-Alexander-Universität Erlangen-Nürnberg
zur Erlangung des Doktorgrades Dr. rer. nat.

vorgelegt von
Jannik Hofestädt
aus München

Als Dissertation genehmigt von der Naturwissenschaftlichen Fakultät
der Friedrich-Alexander-Universität Erlangen-Nürnberg

Tag der mündlichen Prüfung: 22.02.2017

Vorsitzender des Promotionsorgans: Prof. Dr. Georg Kreimer

Gutachter: Prof. Dr. Gisela Anton
Prof. Dr. Ulrich Katz
Prof. Dr. Dorothea Samtleben

Abstract

The neutrino mass hierarchy can be determined by measuring the energy- and zenith-angle-dependent oscillation pattern of few-GeV atmospheric neutrinos that have traversed the Earth. This measurement is the main science goal of KM3NeT/ORCA ('Oscillation Research with Cosmics in the Abyss'), a planned multi-megaton underwater Cherenkov detector in the Mediterranean Sea. A key task is the reconstruction of shower-like events induced by electron neutrinos in charged-current interactions, which substantially affect the neutrino mass hierarchy sensitivity.

In this thesis, numerous aspects of the expected neutrino detection performance of the planned ORCA detector are investigated. A new reconstruction algorithm for neutrino-induced shower-like events is developed. Excellent reconstruction accuracies are achieved, with a neutrino energy resolution better than 26%/24%, and a median neutrino direction resolution better than $11^\circ/9^\circ$ for electron neutrinos/antineutrinos in charged-current interactions with energies above 7 GeV. It is shown that these resolutions are close to the reconstruction accuracy limits imposed by intrinsic fluctuations in the Cherenkov light signatures. These intrinsic resolution limits are based on generic assumptions about event reconstruction in Cherenkov detectors and are derived as part of this thesis. Differences in event reconstruction capabilities between water- and ice-based Cherenkov detectors are discussed. The configuration of existing trigger algorithms is optimised for the ORCA detector. Based on the developed shower reconstruction, a detector optimisation study of the photosensor density is performed. In addition, it is shown that optical background noise in the deep Mediterranean Sea is not expected to compromise the feasibility of the neutrino mass hierarchy measurement with ORCA.

Together, these investigations contribute significantly to the estimated neutrino mass hierarchy sensitivity of ORCA published in the 'Letter of Intent' for KM3NeT, illustrate why a new optimised detector geometry is proposed, and give pointers as to how to improve the neutrino detection performance and consequently the neutrino mass hierarchy sensitivity of ORCA.

Contents

1	Introduction	10
	I Scientific context	13
2	Neutrinos	15
2.1	Neutrino interactions with matter	15
2.1.1	Scattering kinematics	15
2.1.2	Weak interactions between neutrinos and fermions	16
2.1.3	Deep inelastic scattering	19
2.1.4	Neutrino-nucleon scattering at the GeV-scale	20
2.1.5	Effects from the nucleus	21
2.1.6	Precision of neutrino interaction predictions	22
2.2	Neutrino oscillation	23
2.2.1	Mixing of neutrino eigenstates	23
2.2.2	Neutrino oscillation in vacuum	23
2.2.3	Neutrino oscillation in matter	25
2.2.3.1	Effective matter potential	25
2.2.3.2	Neutrino propagation in matter	26
2.2.3.3	Resonance enhancement and MSW effect	26
2.2.3.4	Parametric enhancement	27
2.2.4	Current experimental status	28
3	Measuring neutrino mass hierarchy	31
3.1	Neutrino mass hierarchy	31
3.2	Neutrino mass hierarchy signature in atmospheric neutrino experiments	32
3.2.1	Atmospheric neutrinos	32
3.2.2	Oscillation probabilities in the Earth	34
3.2.3	Neutrino mass hierarchy signature	36
3.2.4	Classes of detector signatures for neutrino-induced events	38
3.2.5	Possible neutrino-antineutrino separation techniques	38
3.3	Neutrino mass hierarchy sensitivity calculation for ORCA	40
3.3.1	Event rate calculation	40
3.3.2	Sensitivity calculation	41
3.3.3	Expected sensitivity	41
3.3.4	Detector layout optimisation	42
3.4	Neutrino oscillation experiments for neutrino mass hierarchy determination	42
4	Cherenkov detectors for neutrinos	47
4.1	Cherenkov radiation	47
4.2	Muon propagation	48
4.3	Electromagnetic showers	49
4.4	Hadronic showers	50
4.5	Light propagation	52
4.6	Light detection	54
4.7	Event reconstruction	55
4.8	Background	55
4.8.1	Optical noise	56
4.8.2	Atmospheric muons	56
4.9	Triggering	57

5	The KM3NeT/ORCA detector	59
5.1	Digital optical module	60
5.2	Detector layout	61
5.3	Data acquisition	62
5.4	Prototypes and first KM3NeT detection strings	63
5.5	Timeline for ORCA detector construction	63
5.6	Additional scientific goals	63
6	Simulations	65
6.1	Simulation tools	65
6.2	Comparison of different simulation tools	66
6.3	Benchmark detector	67
6.4	Implementation of different detector configurations	67
6.5	Event generation for full detector simulation	68
6.6	Detector-geometry-independent simulations	69
II Fundamental investigations for ORCA-like detectors		71
7	Phenomenology of few-GeV electron neutrino events	73
7.1	Neutrino interaction characterisation	73
7.1.1	Interaction mode	73
7.1.2	Interaction kinematics	74
7.2	Characterisation of electromagnetic and hadronic showers	75
7.2.1	Hadronic shower composition	76
7.2.2	Cherenkov light production	76
7.2.3	Muons from hadronic showers	81
7.2.4	Detected light characteristics	84
7.3	Considerations for event reconstruction	87
7.3.1	Sensitivity to interaction inelasticity	87
7.3.2	Leading particle direction	89
7.3.3	Possible reconstruction strategies	89
7.3.4	Important detection distances	90
8	Comparison of seawater and ice as detector media	93
8.1	Comparison of optical properties	93
8.2	Comparison of event reconstruction capabilities	95
8.3	Validation of ice simulation	98
8.4	Conclusions	99
9	Intrinsic limits on resolution of few-GeV neutrinos	101
9.1	Methods	101
9.1.1	Sources of intrinsic fluctuations	102
9.1.2	Simulations	102
9.1.3	Characterising fluctuations	102
9.1.4	Breaking the limits	103
9.2	Muons	103
9.2.1	Energy resolution	103
9.2.2	Direction resolution	107
9.3	Electrons	107
9.3.1	Energy resolution	108
9.3.2	Direction resolution	109

9.4	Hadronic showers	109
9.4.1	Energy resolution	110
9.4.2	Direction resolution	110
9.5	Resolutions of electron and muon neutrino charged-current events	111
9.5.1	Selecting hadronic showers	111
9.5.2	Using naive energy and momentum conservation	113
9.5.3	Using expected neutrino-lepton scattering angle	118
9.5.4	Treating electron neutrino events as one single shower	118
9.5.5	Interaction inelasticity resolution	121
9.6	Conclusions, implications and discussion	122
III Developments and investigations towards ORCA		127
10	Bioluminescence studies	129
10.1	Bioluminescence	129
10.2	ANTARES detector and its data acquisition	130
10.3	Characteristics of hit rates and bioluminescence in ANTARES	131
10.4	Investigation of the dominant class of bioluminescence bursts	132
10.4.1	Data selection	132
10.4.2	Inspection of an example bioluminescence burst	134
10.4.3	Duration	135
10.4.4	Intensity	139
10.4.5	Frequency of occurrence	144
10.4.6	Contribution from non-local bursts to the mean hit rate	146
10.4.7	Biological interpretations	147
10.4.8	Extrapolations for ORCA detector	148
10.5	Short-scale variability	149
10.6	Coincident hits from bioluminescent burst	150
10.7	Conclusions and implications for ORCA	151
11	Trigger studies	153
11.1	Trigger algorithms	153
11.1.1	Basic idea	153
11.1.2	Hit definitions	154
11.1.3	Shower trigger	154
11.1.4	Muon trigger	154
11.2	Trigger configuration studies	155
11.2.1	Optimisation strategy	155
11.2.2	Complementarity of shower and muon trigger	157
11.3	Trigger performance	158
11.3.1	Trigger rate and event purity	158
11.3.2	Effective volume	159
11.4	Conclusions and suggestions for improvements	161
12	Shower reconstruction	163
12.1	Shower reconstruction algorithm	163
12.1.1	Vertex reconstruction	164
12.1.2	Reconstruction of energy, direction and inelasticity	167
12.1.3	Decisions in reconstruction flow	170
12.2	Event selection	171

12.3	Reconstruction performance	171
12.3.1	Performance for charged-current electron neutrino events	171
12.3.2	Performance for other shower-like neutrino events	178
12.3.3	Correlations between energy and direction resolutions	180
12.3.4	Performance for different vertical spacings between DOMs	181
12.3.5	Effect of variation in seawater/PMT properties and noise level	183
12.3.6	Performance for track-like events	185
12.3.7	Suppression of pure-noise events	188
12.4	Advantages due to reconstructing interaction inelasticity	191
12.4.1	Separation between different shower-like neutrino event classes	191
12.4.2	Improvement of energy resolution	193
12.5	Comparisons of reconstruction performance	193
12.5.1	Comparison of effective volume with respect to trigger level	194
12.5.2	Comparison of resolutions with intrinsic limitations	194
12.5.3	Comparison with PINGU	197
12.6	Conclusions	199
13	Neutrino mass hierarchy sensitivity in shower channel	201
13.1	Simplified sensitivity calculation	201
13.2	Sensitivity studies	202
13.2.1	Effect of finite Monte Carlo statistics	204
13.2.2	Improvement due to interaction inelasticity	204
13.2.3	Detector layout optimisation	206
13.2.4	Comparison of uncorrelated and correlated resolutions	207
13.3	Conclusions	207
14	Summary and outlook	209
	Zusammenfassung und Ausblick	213
A	Further simulation details	217
A.1	KM3NeT PMT and DOM characteristics	217
A.2	GEANT settings for GENSHWR simulations	219
B	Further material for bioluminescence studies	220
B.1	Trident bursts	220
B.2	Additional plots	223
C	Hit scoring	227
D	Further shower reconstruction details	229
D.1	Energy correction procedure	229
D.2	Additional plots	230
	Bibliography	231

1 Introduction

The Nobel Prize in Physics of the year 2015 was awarded to T. Kajita and A. B. McDonald “for the discovery of neutrino oscillations, which shows that neutrinos have mass” [1]. This reward recognises their key contributions to the experiments that demonstrated unambiguously that neutrinos change from one flavour to another when propagating over macroscopic distances. This phenomenon of neutrino flavour change is known as ‘neutrino oscillation’. Its discovery led to the far-reaching conclusion that neutrinos, which for a long time were generally considered massless in the Standard Model of elementary particle physics, must have some mass, and that the masses of the three neutrino states are different.

During the past two decades, most parameters governing neutrino oscillation have been measured by many dedicated experiments. One open question is the so-called ‘neutrino mass hierarchy’. It refers to the sign of one of the two independent neutrino mass differences, the absolute value of which has already been known for about 20 years. Although it is only a sign, this fundamental parameter is crucial for interpreting the information obtained from other neutrino experiments and for model building in various fields of particle physics and astroparticle physics.

The neutrino mass hierarchy can be determined by measuring the differences in oscillation probabilities of neutrinos and antineutrinos in matter. A promising pathway to this measurement are neutrino experiments probing the oscillation of (anti)neutrinos that are created by cosmic-ray air showers in the atmosphere and propagated through the Earth [2]. This experimental approach is pursued by the KM3NeT collaboration, which plans to build a multi-megaton underwater Cherenkov detector, named ORCA (‘Oscillation Research with Cosmics in the Abyss’), in the Mediterranean Sea [3].

The idea of installing a large array of photosensitive devices deep underwater and reconstructing the properties of neutrino interactions from the produced charged particles with the help of Cherenkov radiation is not new, having been proposed by M. Markov already in 1960 [4]. This detector design allows large detector volumes to be instrumented in natural environments, such the sea. Large-scale detectors are needed in order to detect a significant number of neutrinos, as neutrinos interact only weakly with matter. Most existing detectors of this kind are optimised for neutrino energies in the TeV regime. The more-densely instrumented ORCA detector will lower the energy threshold down to a few GeV, where signatures of the neutrino mass hierarchy appear.

The degree to which ORCA can contribute to the neutrino mass hierarchy determination depends significantly on the attainable reconstruction accuracy and detection efficiency of neutrinos in the few-GeV energy regime. In this thesis, these key performance indicators of the future ORCA detector are evaluated, and used to optimise the detector layout. For this, a new reconstruction method is developed for shower-like neutrino events, in particular electron neutrinos in charged-current interactions. Shower-like neutrino events consist only of electromagnetic and hadronic showers. This event class plays an important role in the determination of the neutrino mass hierarchy. The reconstruction of neutrino-induced events is complicated by event-by-event fluctuations in the observed Cherenkov signatures. As shown in this thesis, these intrinsic fluctuations dominate the achievable neutrino reconstruction accuracy.

This thesis is organised into three parts. Part I, ‘Scientific context’, briefly summarises neutrino interactions with matter as well as neutrino oscillation in vacuum and matter in Section 2. Specific issues related to the determination of the neutrino mass hierarchy, in particular with ORCA-like detectors, are discussed in Section 3. General detection principles of Cherenkov detectors are outlined in Section 4. The planned ORCA detector is

introduced in Section 5, and its simulation is described in Section 6. Part II, ‘Fundamental investigations for ORCA-like detectors’, describes in detail the phenomenology of few-GeV neutrinos interacting in seawater and the detected Cherenkov light signatures in Section 7. Differences with signatures observed in ice-based Cherenkov detectors are discussed in Section 8. Neutrino reconstruction accuracy limits imposed by intrinsic fluctuations in Cherenkov light signatures are derived in Section 9. Part III, ‘Developments and investigations towards ORCA’, investigates the influence of optical background from bioluminescence on ORCA in Section 10. Existing trigger algorithms and their optimisation for ORCA are described in Section 11. Section 12 presents a new shower reconstruction method developed for the needs of ORCA, and evaluates the reconstruction performance. In Section 13, ORCA’s sensitivity to the neutrino mass hierarchy is studied with regard to the performance of the developed shower reconstruction, including a detector layout optimisation. Finally, Section 14 summarises how this work has contributed to the neutrino mass hierarchy sensitivity of ORCA, and points the way towards future improvements.

Part I

Scientific context

This part introduces the scientific context and relevant phenomenology of neutrino physics. It also introduces the basic concepts of underwater Cherenkov detectors that are needed to understand the principle of measurement of the neutrino mass hierarchy using few-GeV atmospheric neutrinos detected with the future KM3NeT/ORCA detector. In addition, the simulation tools used in this thesis are described.

2 Neutrinos

Neutrinos are elementary particles with no electric charge and half-integer spin, i.e. they are fermions. The (electron) neutrino was first postulated by Pauli [5] in 1930 and its existence was proven by Reines and Cowan [6] in 1956. Since then, two further neutrino flavours have been discovered, namely muon neutrino [7] and tau neutrino [8]. Each neutrino flavour is associated with its charged partner, called electron e , muon μ and tau τ . These particles are grouped within the Standard Model of elementary particle physics¹ into three lepton generations, corresponding to the three quark generations. For each of these fermions, there exists an antiparticle partner.

As electrically-neutral and color-neutral particles, neutrinos only interact via the weak force. Neutrino interactions with matter, in particular neutrino-nucleon scattering processes, are discussed in Sec. 2.1.

In the Standard Model, neutrinos are assumed to be massless. However, the observation of neutrino oscillations [12] implies that neutrinos have non-zero masses. The term ‘neutrino oscillation’ describes the phenomenon that neutrinos propagating over macroscopic distances can change their flavour on their way between production and detection. This phenomenon can only occur if the neutrino mass eigenstates are different. Neutrino oscillation in vacuum and matter are discussed in Sec. 2.2.

Differences between neutrinos and antineutrinos are important for many parts of this thesis, therefore they are labelled as ν and $\bar{\nu}$ for exclusively neutrinos or antineutrinos, while the notation $\vec{\nu}$ refers to ‘either ν or $\bar{\nu}$ ’. Furthermore, throughout the entire thesis natural units ($\hbar = c = 1$) are used.

2.1 Neutrino interactions with matter

Weak interactions between point-like elementary particles are well-described within the Standard Model. However, the complexity of possible targets can make the description of neutrino interactions quite complicated.

In the following, neutrino interactions with normal matter at neutrino energies of $\mathcal{O}(\text{GeV})$ are briefly discussed. A recent review work on neutrino interactions and their cross sections can be found in [13]. A more pedagogical introduction can be found in [14]. The overall structure and the content of this section are inspired by other PhD theses [15, 16].

For the scope of this thesis, interactions in the neutrino energy range of 1–50 GeV are of interest. Most interactions of GeV-scale neutrinos with normal matter are neutrino-nucleon scatterings. Nucleons, i.e. protons and neutrons, are compound objects consisting of quarks and gluons. Most neutrinos detectable with the planned KM3NeT/ORCA detector (see Sec. 5) will interact directly with a quark constituent in a nucleon and break up the nucleon. This process is called ‘deep inelastic scattering’ and is discussed in more detail than other interaction modes.

2.1.1 Scattering kinematics

It is useful to introduce the conventional notation used to describe neutrino scattering kinematics. A generic neutrino interaction is shown in Fig. 2.1. The incoming neutrino interacts with a target, generating a final-state lepton l (which could be either a neutral

¹ The Standard Model of elementary particle physics is a set of quantum field theories that describe elementary particles and their interactions by the electromagnetic, strong and weak force. Detailed overviews can e.g. be found in [9, 10, 11].

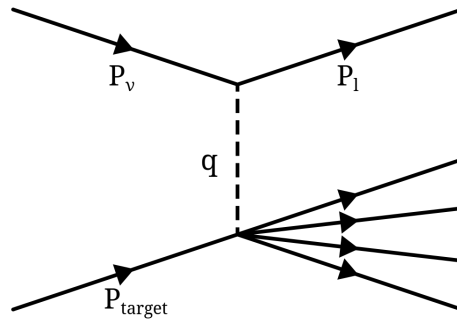


Figure 2.1: A generic neutrino interaction with a target, generating a (charged or neutral) lepton and an unspecified system of other outgoing particles. Taken from [16].

or charged lepton depending on the weak interaction current involved) and an unspecified system of other outgoing particles.

Lorentz invariant quantities can be constructed from the four-momenta of the neutrino p_ν , the lepton p_l and the target p_{target} :

$$s = (p_\nu + p_{\text{target}})^2 \quad (\text{centre-of-mass energy}), \quad (2.1)$$

$$Q^2 = -q^2 = -(p_\nu - p_l)^2 \quad (\text{four-momentum transfer}), \quad (2.2)$$

$$y = \frac{q \cdot p_{\text{target}}}{p_\nu \cdot p_{\text{target}}} \quad (\text{inelasticity}), \quad (2.3)$$

$$x = \frac{Q^2}{2 \cdot p_{\text{target}} \cdot q} \quad (\text{Bjorken scaling variable}), \quad (2.4)$$

$$W^2 = (q + p_{\text{target}})^2 \quad (\text{invariant hadronic mass}). \quad (2.5)$$

In the laboratory frame, in which the target is at rest, the inelasticity – often also referred to as Bjorken y – is the fraction of neutrino energy transferred to the target system:

$$y = \frac{E_\nu - E_l}{E_\nu}. \quad (2.6)$$

The Bjorken scaling variable x is most commonly used to describe deep inelastic neutrino-nucleon scattering (see Sec. 2.1.3), where it can be thought of as the fraction of the target nucleon’s four-momentum carried by the struck quark.

2.1.2 Weak interactions between neutrinos and fermions

For the understanding of neutrino cross section phenomenology, it is useful to discuss first the scattering of neutrinos from effectively massless fermions, such as neutrino-electron scattering. For sufficiently high energies, this is also a good approximation to deep inelastic scattering (see Sec. 2.1.3), where the neutrino scatters off a free quark constituent in a nucleon.

The weak force has two contributions: charged current (CC) and neutral current (NC) interactions mediated by massive W^\pm and Z^0 bosons, respectively. For both currents, a tree-level diagram for neutrino-fermion scattering are shown in Fig. 2.2. The neutrino remains a neutrino (of the same flavour) in NC interactions, and the neutrino turns into a charged lepton in CC interactions. The flavour of the neutrino is associated with the flavour of the charged lepton produced in CC interactions.

The form of the cross section for neutrino-fermion scattering depends on the spin configuration of the initial states. The CC interaction is maximally parity-violating [17], selecting only left-handed fermions and right-handed antifermions. As neutrinos and antineutrinos have distinct helicities² in the Standard Model [18], their CC interactions can be separated into two types of processes: neutrino-fermion (equivalent to antineutrino-antifermion) and neutrino-antifermion (equivalent to antineutrino-fermion). In the case of the NC interaction, a left-handed neutrino can scatter off a right-handed fermion and the coupling is given in terms of the electromagnetic and weak couplings by the electroweak unification theory.

In the following, it is always assumed that the four-momentum transfer Q^2 is small compared to the W^\pm mass ($Q^2 \ll m_W^2$) and the centre-of-mass energy s is large compared to the mass m_l of the lepton ($s \gg m_l^2$), so that propagator effects and production threshold effects can be neglected.

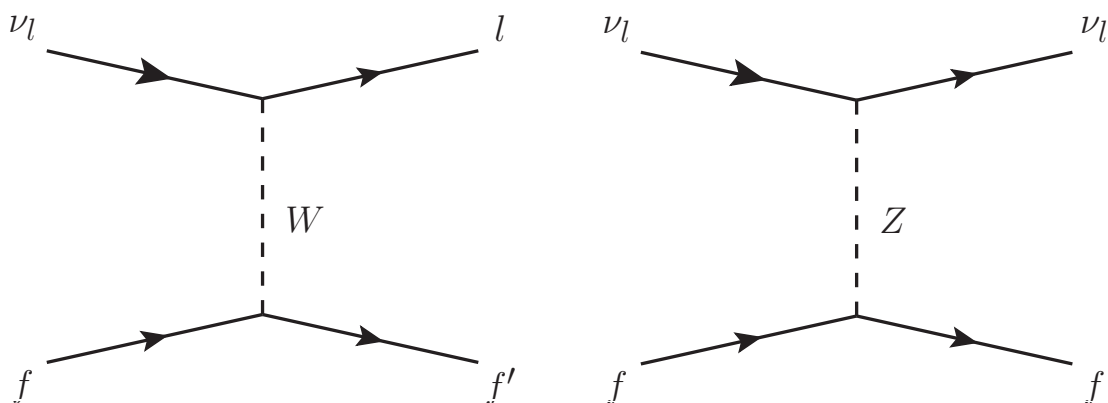


Figure 2.2: Feynman diagrams for neutrino-fermion scattering via the charged current (left) and neutral current (right).

Neutrino-fermion CC interaction

In the following process of a pure charged current interaction:

$$\nu_l + f \rightarrow l + f' \quad (l \neq f), \quad (2.7)$$

a neutrino ν_l scatters off a free fermion f (which is different from the produced charged lepton)³ and produces a charged lepton l and a different fermion f' . The differential and total cross section are given by:

$$\frac{d\sigma_{CC}(\nu f)}{d\Omega} = \frac{G_F^2 s}{4\pi^2}, \quad \sigma_{CC}(\nu f) = \frac{G_F^2 s}{\pi}, \quad (2.8)$$

where the Fermi constant $G_F \approx 1.166 \times 10^{-5} \text{ GeV}^{-2}$ describes the coupling strength.

From this, three observations can be made. First, the cross section depends linearly on s . For a target fermion with mass m_f at rest holds $s = 2m_f(m_f + E_\nu)$, so that the cross sections increases linearly with neutrino energy for $E_\nu \gg m_f$. Second, the cross section grows linearly with m_f . As a consequence, the cross section for neutrino-electron scattering

²Helicity is the projection of spin along the direction of a particle. For massless particles, such as neutrinos in the Standard Model, helicity and chirality/handedness are equivalent. A non-zero neutrino mass m_ν implies a small frame-dependent positive helicity component, which is proportional to m_ν/E_ν . However, for the relevant neutrino energy range, this positive helicity component can be entirely neglected.

³For $l = f$, there is a NC interaction with identical initial and final state leading to an interference of both processes.

is approximately three orders of magnitude smaller than for neutrino-nucleon scattering⁴. Third, the cross section does not depend on the neutrino-lepton scattering angle θ^* in the centre-of-mass frame, as there is no net spin along the interaction axis.

Neutrino-antifermion CC interaction

A similar process to that of Eq. 2.7, but with antifermion \bar{f} in the initial state is:

$$\nu_l + \bar{f} \rightarrow l + \bar{f}' \quad (l \neq f). \quad (2.9)$$

In this case, the total spin along the interaction axis is $J = 1$, leading to a preference for forward scattering ($\theta^* = 0$) as opposed to backward scattering ($\theta^* = \pi$) due to angular momentum conservation along the interaction axis. This results in an extra factor of $[1 + \cos(\theta^*)]^2$ in the cross section. In the centre-of-mass frame, the inelasticity y is connected to θ^* via $y = [1 - \cos(\theta^*)]/2$.

The differential cross section and total cross section are given by:

$$\frac{d\sigma_{CC}(\nu\bar{f})}{d\Omega} = \frac{G_F^2 s}{16\pi^2} [1 - \cos(\theta^*)]^2, \quad \frac{d\sigma_{CC}(\nu\bar{f})}{dy} = \frac{G_F^2 s}{\pi} (1 - y)^2, \quad \sigma_{CC}(\nu\bar{f}) = \frac{G_F^2 s}{3\pi}. \quad (2.10)$$

Compared to the total cross section of neutrino-fermion CC interactions (Eq. 2.8), this gives $\sigma_{CC}(\nu\bar{f})/\sigma_{CC}(\nu f) = 3$. The suppression comes entirely from helicity considerations.

Neutrino-fermion NC interaction

For a pure neutral current interaction, like

$$\bar{\nu}_l + f \rightarrow \bar{\nu}_l + f \quad (l \neq f), \quad (2.11)$$

the interaction couples to both the left-handed and right-handed component of the fermion f . Hence, there is a contribution from spin $J = 0$ and $J = 1$ along the interaction axis.

In general, the differential cross sections for (anti)neutrino-fermion NC interactions can be written as:

$$\frac{d\sigma_{NC}(\nu f)}{dy} = \frac{G_F^2 s}{\pi} [g_L^2 + (1 - y)^2 g_R^2], \quad \frac{d\sigma_{NC}(\bar{\nu} f)}{dy} = \frac{G_F^2 s}{\pi} [g_L^2 (1 - y)^2 + g_R^2], \quad (2.12)$$

where g_L and g_R are the left- and right-handed couplings of the fermion the neutrino is interacting with and their values for each fermion species are given in Tab. 2.1.

Z^0 coupling	g_L	g_R
ν_e, ν_μ, ν_τ	1/2	0
e, μ, τ	$-1/2 + \sin^2(\theta_W)$	$\sin^2(\theta_W)$
u, c, t	$1/2 - (2/3) \sin^2(\theta_W)$	$-(2/3) \sin^2(\theta_W)$
d', s', b'	$-1/2 + (1/3) \sin^2(\theta_W)$	$(1/3) \sin^2(\theta_W)$

Table 2.1: Weak neutral current couplings g_L and g_R (Eq. 2.12). Quark states d' , s' and b' are the weak interaction eigenstates, which are given by the mass eigenstates rotated by the CKM matrix [11], similarly to the mixing of neutrino mass eigenstates (see Sec. 2.2.1). The value of the weak mixing angle θ_W is about 29° .

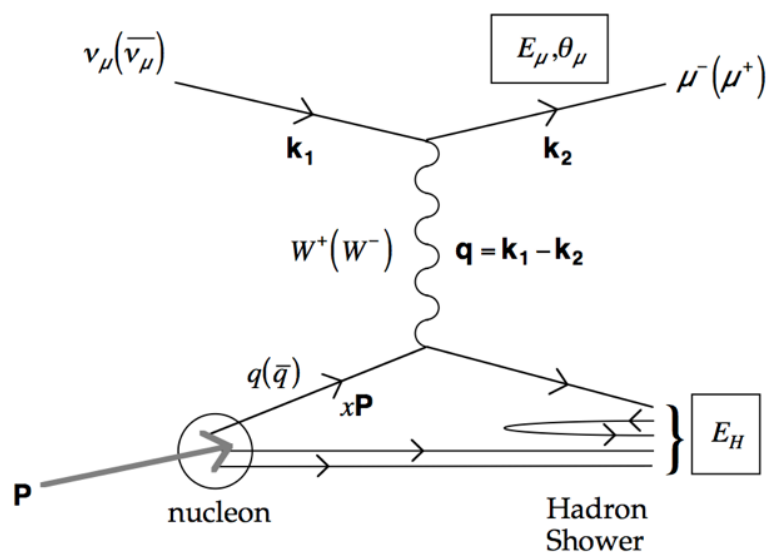


Figure 2.3: Generic diagram for a charged current (anti)neutrino-nucleon DIS interaction with a nucleon. Here, four-momenta are denoted by k . Taken from [19].

2.1.3 Deep inelastic scattering

A generic deep inelastic scattering (DIS) diagram for a (anti)neutrino-nucleon CC interaction is shown in Fig. 2.3, and is written as:

$$\bar{\nu}_l + N \rightarrow l^\pm + X, \quad (2.13)$$

where N denotes the target nucleon and X an unspecified set of outgoing hadrons. In this interaction the neutrino scatters off a (anti)quark inside the nucleon. The nucleon is effectively broken up, and the recoil quark together with the nucleon remnant produce a spray of hadrons. The process of hadron formation is called *hadronisation*⁵.

In the parton model, a nucleon consists of three valence quarks as well as a sea of short-lived quark-antiquark pairs and gluons. In the DIS regime, the neutrino interacts with essentially free quarks in the same way as discussed in Sec. 2.1.2. For the cross section, each elementary scattering process contributes according to the probability density $f_{q_i}^N(x, Q^2)$ of finding a quark q_i with momentum fraction x at resolution scale Q^2 . This information is encoded in the so-called parton distribution functions⁶. Then, the cross sections for neutrino-nucleon scattering are given by an incoherent sum of the cross sections for all possible neutrino-quark interactions, weighted by their probability $f_{q_i}^N(x)$:

$$\frac{d^2\sigma(\bar{\nu}N)}{dxdy} = \sum_q f_q^N(x) \frac{d\sigma(\bar{\nu}q)}{dy} + \sum_{\bar{q}} f_{\bar{q}}^N(x) \frac{d\sigma(\bar{\nu}\bar{q})}{dy}. \quad (2.14)$$

The individual neutrino-quark cross sections are those given in Sec. 2.1.2.

As the sea quark content at GeV-scale is low, it is mostly the valence quarks that provide targets for scattering of (anti)neutrinos. According to Eq. 2.8 and Eq. 2.10, the neutrino-nucleon CC cross section is approximately independent of y , while the antineutrino-nucleon

⁴ For deep inelastic scattering (see Sec. 2.1.3), the effective mass of a quark in a nucleon can be considered as $m_q = xm_N$ with the Bjorken scaling variable x and the nucleon mass m_N .

⁵The hadronisation process is a research topic on its own. For further details, see e.g. [11].

⁶Parton distribution functions have been extracted from DIS data. For further details, see [11, 20].

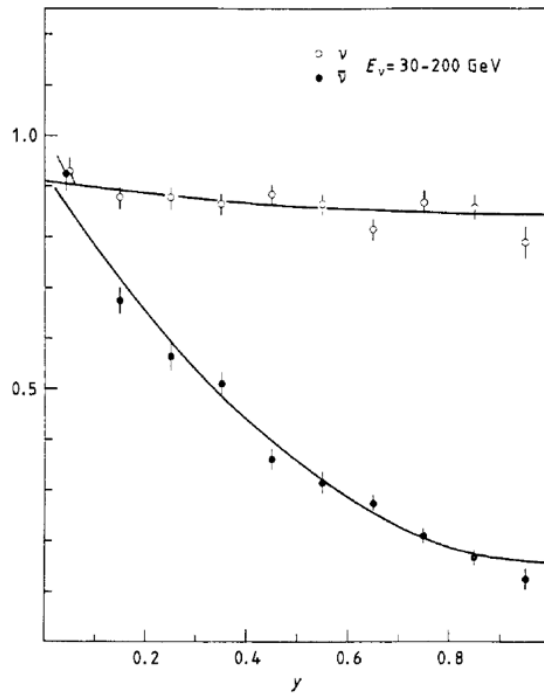


Figure 2.4: Differential charged current cross sections for deep inelastic scattering of neutrinos ν (hollow circle) and antineutrinos $\bar{\nu}$ (filled circle) on an isoscalar target (equal number of neutrons and protons) as a function of inelasticity y . Taken from [22].

CC cross section shows a $(1-y)^2$ dependence. Due to the antiquark component in the sea, these strict dependences are attenuated. The differential CC cross sections as a function of y are shown in Fig. 2.4 for neutrinos and antineutrinos separately. The ratio of total CC cross sections for neutrinos and antineutrinos interacting with an isoscalar target is roughly $\sigma_{CC}(\nu N)/\sigma_{CC}(\bar{\nu} N) \approx 2$ and NC interaction cross sections are about a factor ~ 3 smaller than those of CC interactions [21].

2.1.4 Neutrino-nucleon scattering at the GeV-scale

Neutrino-nucleon scattering provides much larger cross sections than neutrino-electron scattering⁷. Therefore, nucleons are the dominant interaction targets for the detection of neutrinos. However, the structure of the nucleons is more complicated than the simple assumption about three asymptotically free valence quarks made above.

Although the total cross section for neutrino-nucleon interactions is a function of the neutrino energy, it is the four-momentum transfer Q that determines what features of the target nucleon can be resolved. However, the maximal available Q^2 is limited by the centre-of-mass energy s , which depends on the neutrino energy.

For neutrino energies of $\mathcal{O}(\text{GeV})$, several distinct neutrino interaction modes play a role:

- **Elastic and quasi-elastic scattering (QE):** At low Q^2 , the neutrino scatters off an entire nucleon, liberating it (possibly together with other nucleons) from the target nucleus. Many interaction models parametrise the nucleon in terms of form factors in the so-called ‘dipole approximation’ [24]. In case of charged (neutral) current

⁷ Besides for neutrino energies of $\sim 6 \text{ PeV}$, where the $\bar{\nu}_e e^-$ CC cross section shows a resonant enhancement, which is often called ‘Glashow resonance’ [23].

interaction, this process is referred to as quasi-elastic scattering (elastic scattering). This interaction mode dominates at neutrino energies of ~ 1 GeV and below.

- **Resonance production (RES):** For higher energies, the scattering process becomes increasingly inelastic as the available Q^2 increases and it becomes unlikely that the nucleon remains intact. The energy regime of 1–5 GeV is dominated by the production of discrete baryon resonances with the most important being the $\Delta(1232)$. For this process, there has to be a baryonic state available at the mass of the hadronic system W . The produced resonances then decay to nucleons accompanied by a variety of possible mesonic final states including single or multiple pions, kaons or radiative photons.
- **Deep inelastic scattering (DIS):** At even higher energies the momentum transfer by the boson can be sufficient to resolve the internal structure of the nucleon and the neutrino scatters directly off the quark constituents. This process manifests in the break up of the nucleon containing the struck quark leading to a spray of hadrons. This interaction mode is discussed in more detail in Sec. 2.1.3.

All of these processes have both CC and NC contributions. As mentioned before, NC interactions with isoscalar targets show roughly 3 times smaller cross sections than CC interactions. Existing measurements for the total neutrino and antineutrino CC cross sections in the relevant energy range are shown in Fig. 2.5. Additionally, the cross sections for the various contributing processes are shown individually. The cross sections for QE and RES reach a plateau for higher neutrino energies and their relative contributions decrease, as the total cross section increases linearly with E_ν (see Sec. 2.1.2).

In the considered neutrino energy range, the masses of the final state charged leptons can be neglected in neutrino-nucleon CC interactions for $\bar{\nu}_e$ and $\bar{\nu}_\mu$, but not for $\bar{\nu}_\tau$. The severely reduced CC interaction cross sections for $\bar{\nu}_\tau$ are discussed in [25].

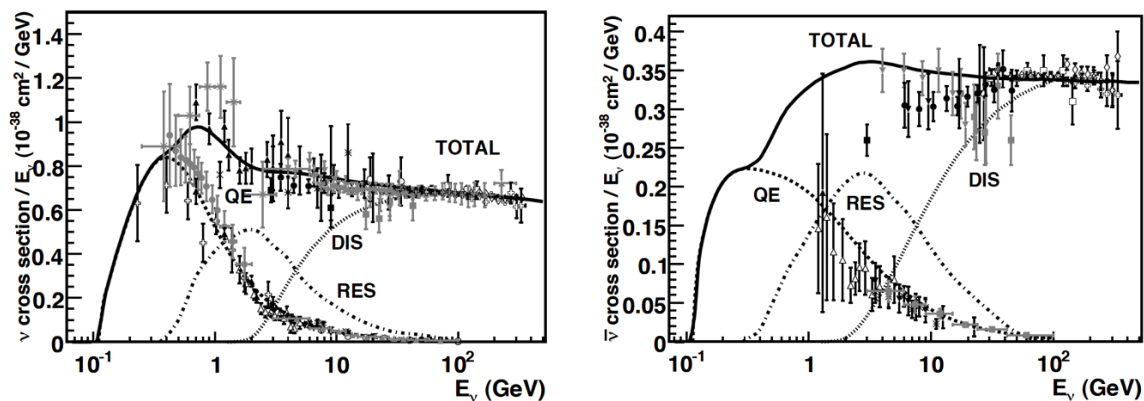


Figure 2.5: Total CC cross section per nucleon for neutrinos (left) and antineutrinos (right) on an isoscalar target divided by neutrino energy E_ν . Shown are measurements from various experiments and predictions from the NUANCE generator [26] for quasi-elastic (QE), resonant production (RES) and deep inelastic scattering (DIS) contributions. Taken from [13].

2.1.5 Effects from the nucleus

The set of interactions described in the previous section provide a fairly complete overview of the interactions between neutrinos and (free) nucleons as a whole or their constituents, whereas in a real experiment the nucleons are often contained within nuclei. In the case of the ORCA detector, the target is seawater, where most nucleons are part of oxygen nuclei.

The effects from the nucleus modify the interaction cross section as well as the resulting event signatures observed in the detector, especially at low neutrino energies.

One effect is the motion of the target nucleon inside the nucleus. This effect is usually referred to as ‘Fermi smearing’, as often relativistic Fermi Gas models [27] are employed. More sophisticated treatments, such as ‘spectral functions’ [28], are also investigated. The target nucleon momenta can reach up to a few hundred MeV.

Once created in the initial neutrino interaction, the final-state particles have to escape the nucleus. Along their journey, the particles can re-interact in the nucleus. These ‘final-state interactions’ can alter the number, identity and kinematics of outgoing particles [29].

Both effects are present at all energy regimes, but are less important for higher neutrino energies for two reasons. First, for higher neutrino energies the relative contribution from the Fermi motion becomes less important. Second, in the DIS regime the number, type and kinematics of the outgoing particles are less relevant, especially for experiments that are not capable of reconstructing individual low energetic particles.

On the other hand, the fact that the target is a nucleus opens an additional interaction mode, which is known as ‘coherent scattering’. In this case, the neutrino coherently scatters off the entire nucleus and produces a distinctly forward-scattered single pion final state. This interaction mode is characterised by a small four-momentum transfer to the nucleus, so that the nucleus remains intact. Cross sections are small ($\sim 1\%$) compared to the other interaction processes mentioned in the previous section.

2.1.6 Precision of neutrino interaction predictions

Historically, adequate theoretical models for each of the interaction modes (QE, RES, and DIS) have been formulated, however, there is no uniform model that is capable of globally describing the transition between these processes. Current models interpolate between disjointed regimes. Consequently, the transition regions are not well-understood. The level of understanding of each individual interaction process and the ability to make predictions is currently limited by the available experimental data, which is often sparse and scattered.

The total cross section shown in Fig. 2.5 is reasonably well described by predictions, with some freedom in absolute normalisation ($\sim 10\%$ at energies of a few GeV) and shape. The uncertainties are smaller for higher energies, where DIS becomes dominant. In order to constrain the theoretical models for the different interaction modes and their relative contributions, more specific measurements are required. However, measurements at these energies are notoriously challenging, complicating progress in the modeling. See [13] for further discussions. It is also essential to disentangle the effects from the initial nuclear state, hadronisation and final-state interactions.

Uncertainties in neutrino-nucleus interaction cross sections and kinematics are dominant systematics in future precision neutrino oscillation experiments. Therefore, a considerable effort is currently being made on the theoretical side as well as on the experimental side. For example, the MINER ν A [30] experiment in the 1 – 10 GeV NuMI beam at Fermilab seeks to reduce the uncertainties on neutrino cross sections in the relevant energy regime in the near future, and will also perform studies of nuclear effects using a suite of nuclear target including oxygen, the main component of water.

In this thesis, the neutrino event generator GENIE [31] (version 2.8.4) is employed for simulating neutrino interactions in seawater.

2.2 Neutrino oscillation

Neutrinos have the peculiar feature that the flavour eigenstates are different from the mass eigenstates. The three flavour eigenstates are a mixture of the three mass eigenstates with unequal masses. This leads to a phenomenon called *neutrino oscillation*, which refers to the periodic change of the probability of a neutrino produced in an eigenstate α to be detected in another eigenstate β , where $\alpha \neq \beta$, when travelling over macroscopic distance⁸.

The relevant theory behind this phenomenon is discussed in the following. More detailed information can be found in many textbooks, e.g. [33, 34]. The content of this section is inspired by other PhD theses [15, 35].

2.2.1 Mixing of neutrino eigenstates

The three⁹ flavour eigenstates, denoted as $|\nu_\alpha\rangle$ with $\alpha = e, \mu, \tau$, are the eigenstates of the weak interaction. Hence, neutrinos are always created as a pure flavour eigenstate and have to be projected onto these eigenstates whenever they interact.

The three mass eigenstates, denoted as $|\nu_k\rangle$ with $k = 1, 2, 3$, describe the free particle evolution and are the eigenstates of the corresponding Hamiltonian. These eigenstates have to be considered when describing the propagation of neutrinos in vacuum. In matter, the Hamiltonian and mass eigenstates are modified due to the matter potential, see Sec. 2.2.3.

Transformations between neutrino flavour and mass eigenstates can be expressed as:

$$|\nu_k\rangle = \sum_{\alpha=1,2,3} U_{\alpha k} |\nu_\alpha\rangle, \quad (2.15)$$

$$|\nu_\alpha\rangle = \sum_{k=1,2,3} U_{\alpha k}^* |\nu_k\rangle, \quad (2.16)$$

where $U_{\alpha k}$ are the elements of the unitary neutrino mixing matrix U . This neutrino mixing matrix is often called PMNS matrix¹⁰.

The matrix U can be parameterised [11] by three mixing angles θ_{ij} , and one complex phase δ that is related to possible CP violation:

$$U = \begin{pmatrix} 1 & 0 & 0 \\ 0 & c_{23} & s_{23} \\ 0 & -s_{23} & c_{23} \end{pmatrix} \begin{pmatrix} c_{13} & 0 & e^{i\delta} s_{13} \\ 0 & 1 & 0 \\ -e^{i\delta} s_{13} & 0 & c_{13} \end{pmatrix} \begin{pmatrix} c_{12} & s_{12} & 0 \\ -s_{12} & c_{12} & 0 \\ 0 & 0 & 1 \end{pmatrix}. \quad (2.17)$$

In this notation, c_{ij} and s_{ij} stand for cosine and sine of the mixing angle θ_{ij} . If neutrinos are Majorana particles, two additional complex phases enter. Here, these have been neglected, since they have no effect on oscillation experiments [39].

2.2.2 Neutrino oscillation in vacuum

Consider the case that a neutrino with energy E_ν is propagating over a distance L in vacuum. The time evolution in the mass basis is given by the Schrödinger equation:

$$i \frac{d}{dt} |\nu_k(t)\rangle = H |\nu_k\rangle, \quad \text{with } |\nu_k\rangle = |\nu_k(0)\rangle \quad (2.18)$$

⁸ Oscillations are only observable if the neutrino production as well as detection are coherent and the coherence is not lost during neutrino propagation. Coherent production and detection is usually satisfied due to the tininess of neutrino masses (see Sec. 2.2.4). Coherence during propagation is preserved for GeV-scale atmospheric neutrinos (see Sec. 3.2.1), while is often lost for astrophysical neutrinos, such as solar neutrinos. Detailed discussions can be found in [32]. Hence, for atmospheric neutrinos detectable with detectors such as ORCA (see Sec. 5), coherence is always granted and neutrino oscillations are present.

⁹ The existence of exactly three Standard Model-like neutrino generations (with mass below half of the Z^0 mass) is known from precision measurements of the Z^0 decay at the LEP collider [36].

¹⁰ Named after the pioneers of the idea of neutrino oscillation: Pontecorvo, Maki, Nakagawa, and Sakata [37, 38].

For freely propagating particles, the Hamiltonian H is independent of time, and the solutions of the Schrödinger equation can be described as plane waves¹¹:

$$|\nu_k(t)\rangle = \exp(-i(E_k t - \vec{p}_k \cdot \vec{x})|\nu_k(0)\rangle, \quad (2.19)$$

where E_k and \vec{p}_k are the energy and momentum of the corresponding mass state, and \vec{x} is the neutrino's position. In the ultrarelativistic limit ($m_k \ll E_k \Rightarrow t \approx L$ in natural units), the phase in the equation above can be approximated as:

$$E_k t - \vec{p}_k \cdot \vec{x} \approx \left(p_k + \frac{m_k^2}{2p_k}\right)L - p_k L \approx \frac{m_k^2}{2E_\nu} L. \quad (2.20)$$

The probability for detecting a neutrino produced in flavour state ν_α with flavour ν_β after propagating over a distance L is given by the square of the transition amplitude:

$$P_{\nu_\alpha \rightarrow \nu_\beta}(L) = |\langle \nu_\beta | \nu_\alpha(t) \rangle|^2 = \sum_{k,j} U_{\alpha k}^* U_{\beta k} U_{\alpha j} U_{\beta j}^* \exp\left(-i \frac{\Delta m_{kj}^2 L}{2E_\nu}\right), \quad (2.21)$$

with the mass-squared difference $\Delta m_{kj}^2 = m_k^2 - m_j^2$. This expression can be rewritten to separate the real and imaginary part of the mixing matrix explicitly, as:

$$\begin{aligned} P_{\nu_\alpha \rightarrow \nu_\beta}(L) = \delta_{\alpha\beta} & - 4 \sum_{k>j} \Re[U_{\alpha k}^* U_{\beta k} U_{\alpha j} U_{\beta j}^*] \sin^2\left(\frac{\Delta m_{kj}^2 L}{4E_\nu}\right) \\ & \pm 2 \sum_{k>j} \Im[U_{\alpha k}^* U_{\beta k} U_{\alpha j} U_{\beta j}^*] \sin\left(\frac{\Delta m_{kj}^2 L}{2E_\nu}\right). \end{aligned} \quad (2.22)$$

The sign of the imaginary part is different for neutrinos (+) and antineutrinos (-).

The real part is insensitive to the signs of the mass differences, as they enter as arguments of even functions. On the other hand, the imaginary part can add a contribution sensitive to the signs of the mass difference. However, only if CP is violated in the neutrino sector (which has not yet been observed), the imaginary part is present in Eq. 2.22.

Obviously, the oscillation probability reduces to $P_{\nu_\alpha \rightarrow \nu_\beta} = \delta_{\alpha\beta}$ if all masses were equal. Therefore, the observation of transitions between all three neutrino flavours implies that all three masses are different from each other, and in particular different from 0 (at least two of them).

In general, the neutrino flavour transition probability depends on the mixing matrix (determining the oscillation amplitude), the mass-squared differences, the traveled distance and the neutrino energy (latter three together determine the oscillation frequency).

Two flavour case

As one of the mass-squared differences usually gives the dominant effect for a given neutrino travel distance L , it is often sufficient to consider only the two-neutrino scheme for oscillation. In this, only one mass splitting $\Delta m_{2\nu}^2 = \Delta m_{21}^2 = m_2^2 - m_1^2$ exists and the mixing matrix U turns into a 2×2 matrix with only a single mixing angle $\theta_{2\nu}$:

$$U_{2\nu} = \begin{pmatrix} \cos(\theta_{2\nu}) & \sin(\theta_{2\nu}) \\ -\sin(\theta_{2\nu}) & \cos(\theta_{2\nu}) \end{pmatrix}. \quad (2.23)$$

¹¹ Assuming plane waves gives the same results as a more complete treatments for all practical purposes [40]. A description that provides the full phenomenology of neutrino oscillation requires that the production and detection processes are taken into account, and that the particles are described as wave packets. For details, see [41].

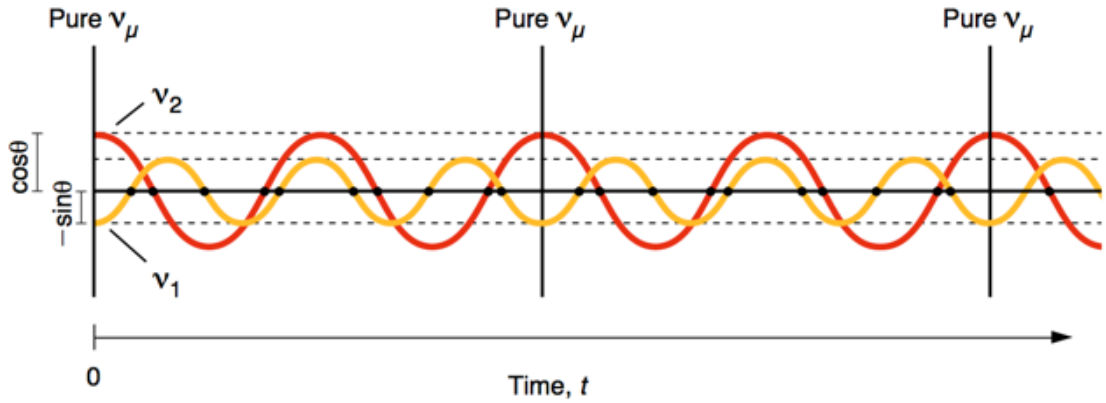


Figure 2.6: Time evolution of a muon neutrino in two-neutrino scheme. A pure ν_μ is produced at time $t = 0$ as a specific linear combination of mass eigenstates: $\nu_\mu = -\sin(\theta_{2\nu})\nu_1 + \cos(\theta_{2\nu})\nu_2$. Different masses $m_1 \neq m_2$ result in a phase difference for $t > 0$. Taken from [42].

Substituting $U_{2\nu}$ and $\Delta m_{2\nu}^2$ in Eq. 2.21 simplifies the probability for a flavour transition to:

$$P_{\nu_\alpha \rightarrow \nu_\beta}^{2\nu}(L) = \sin^2(2\theta_{2\nu}) \sin^2\left(\frac{\Delta m_{2\nu}^2 L}{4E_\nu}\right) \quad (\alpha \neq \beta). \quad (2.24)$$

The length for one oscillation cycle is often approximated in more convenient units as:

$$L^{\text{osc}} = \frac{4\pi E_\nu}{\Delta m_{2\nu}^2} \approx 2.47 \frac{E_\nu}{\text{GeV}} \frac{\text{eV}^2}{\Delta m_{2\nu}^2} \text{ km}. \quad (2.25)$$

From Eq. 2.24, the influence of the mixing angles becomes obvious. They define the amplitude of oscillation, with $\theta_{2\nu} = \pi/4 = 45^\circ$ giving rise to so-called ‘maximal mixing’, where a full transition between neutrino flavours is possible.

The time evolution of a neutrino produced as pure ν_μ is depicted in the two-neutrino scheme in Fig. 2.6. As each mass state oscillated with a different frequency, the phases differ for $t > 0$ and the mass states get out of phase with one another. The resulting interference means that the neutrino contains components from all flavour states and the flavour composition oscillates as the neutrino evolves in time.

2.2.3 Neutrino oscillation in matter

Neutrinos transversing normal matter can scatter off electrons and nucleons. These possible interactions give rise to an effective potential which neutrinos are experiencing. This effect is known as coherent forward scattering and the implications were first discussed by Wolfenstein [43]. The result is that neutrinos in matter have different effective masses than neutrinos in vacuum analogous to photons passing through a transparent medium with a reduced velocity compared to that in vacuum.

2.2.3.1 Effective matter potential

All possible elastic interactions between (anti)neutrinos and normal matter are shown in Fig. 2.7. Elastic NC interactions (see Fig. 2.7a) have the same coupling strength for all neutrino flavours. The sign of the contribution of each interaction channel is determined by the electric charge of the target. As normal matter is macroscopically neutral with equal number of electrons and protons, their contribution cancel each other. The scattering off

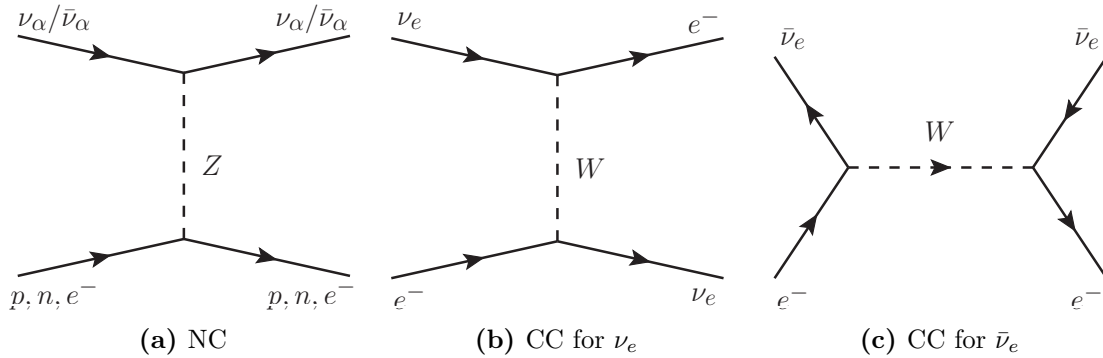


Figure 2.7: Elastic interactions between (anti)neutrinos and normal matter.

neutrons is independent of the neutrino flavour, hence all neutrino mass eigenstates are affected in the same way, leaving the mass-squared differences unchanged and adding only an overall phase, which is unobservable [44]. Consequently, there is no effect for neutrino oscillations from NC processes.

The only elastic CC interactions that neutrinos can undergo while traveling through normal matter are those of ν_e and $\bar{\nu}_e$ with electrons, as shown in Fig. 2.7b and 2.7c. The presence of electrons can be interpreted as an effective potential V_{CC} which only affects $\vec{\nu}_e$, and is given by [34]:

$$V_{CC} = \pm\sqrt{2}G_F N_e, \quad (2.26)$$

where G_F is the Fermi coupling constant (see Sec. 2.1.2) and N_e the electron number density. The positive (negative) sign applies to ν_e ($\bar{\nu}_e$).

2.2.3.2 Neutrino propagation in matter

The additional matter potential for $\vec{\nu}_e$ leads to an effective Hamiltonian, which is not diagonal in the mass basis, unlike in the case of vacuum. However, the effective Hamiltonian can be diagonalised resulting in effective mass-squared differences and effective mixing angles. These are indicated by a superscript M in the following.

For simplicity, the resulting effects on neutrino propagation in matter are discussed in the two-neutrino scheme (see Sec. 2.2.2). In this case, the effective mass-squared difference is given by:

$$\Delta^M m_{2\nu}^2 = \sqrt{(\Delta m_{2\nu}^2 \cos(2\theta_{2\nu}) - A)^2 + (\Delta m_{2\nu}^2 \sin(2\theta_{2\nu}))^2}, \quad (2.27)$$

where $A = 2E_\nu V_{CC}$, and for the effective mixing angle holds:

$$\tan(2\theta_{2\nu}^M) = \frac{\tan(2\theta_{2\nu})}{1 - \frac{A}{\Delta m_{2\nu}^2 \cos(2\theta_{2\nu})}}. \quad (2.28)$$

The flavour transition probability has the same form as in Eq. 2.24 but with the corresponding matter mixing parameters, $\theta_{2\nu} \rightarrow \theta_{2\nu}^M$ and $\Delta m_{2\nu}^2 \rightarrow \Delta^M m_{2\nu}^2$. Note that in the limit of small electron number densities $N_e \rightarrow 0$ the vacuum values for $\theta_{2\nu}$ and $\Delta m_{2\nu}^2$ are recovered.

The formulation of neutrino propagation in the presence of matter within the framework of three neutrino flavours can be found in the literature, e.g. [45].

2.2.3.3 Resonance enhancement and MSW effect

From Eq. 2.28, it can be seen that for

$$A^{\text{res}} = \Delta m_{2\nu}^2 \cos(2\theta_{2\nu}) \iff N_e^{\text{res}} = \frac{\Delta m_{2\nu}^2 \cos(2\theta_{2\nu})}{\pm 2\sqrt{2}E_\nu G_F} \iff E_\nu^{\text{res}} = \frac{\Delta m_{2\nu}^2 \cos(2\theta_{2\nu})}{\pm 2\sqrt{2}N_e G_F} \quad (2.29)$$

a resonance occurs, where the effective mixing angle approaches $\pi/4$, so that the mixing amplitude in Eq. 2.24 approaches unity and a full transition between neutrino flavours is possible. Oscillation in matter can become maximal, regardless of how small the mixing might be in vacuum. The enhancement of the oscillation probabilities due to this resonance in neutrino energy or matter density is known as *resonance enhancement*. In a medium with slowly changing density, a similar effect occurs, which is known as *MSW effect*¹² [46, 47].

On the other hand, for $A \gg \Delta m_{2\nu}^2 \cos(2\theta_{2\nu})$ a saturation effect occurs, where the effective mixing angle approaches $\pi/2$. In this saturation regime, the flavour transition is suppressed by a factor $\sin^2(2\theta_{2\nu}^M)$.

It is very important to note that the resonance condition can only be fulfilled if $\Delta m_{2\nu}^2 \cos(2\theta_{2\nu})$ and A have the same sign, where the sign of A is different for neutrinos (+) and antineutrinos (-). Thus, from observing the resonance for either neutrinos or antineutrinos, the sign of $\Delta m_{2\nu}^2$ can be inferred. As the oscillation probabilities are the same for neutrinos in the case of $\Delta m_{2\nu}^2 > 0$ and antineutrinos in the case of $\Delta m_{2\nu}^2 < 0$, the experiment (detector or source) has to distinguish between neutrinos and antineutrinos in order to determine the sign of $\Delta m_{2\nu}^2$.

The sign of Δm_{21}^2 has been determined by observing this resonance for solar neutrinos. The SNO experiment [48] measured both the flux of solar ν_e and the all-flavour flux of solar neutrinos independently, which allowed to test the oscillation hypothesis independent of the solar model¹³. As the MSW resonance was observed for solar ν_e propagating from the dense core of the Sun to the outside and no $\bar{\nu}_e$ are produced in the Sun, it was concluded that Δm_{21} is positive. Further experimental evidence was provided the Borexino experiment [50].

2.2.3.4 Parametric enhancement

Given abrupt periodical changes in matter density along the neutrino's trajectory, the flavour transition probability can be strongly enhanced although the matter densities are not at their resonance values. This phenomenon is known as 'parametric enhancement'. More detailed explanations than the qualitative discussions below are given in [51, 52, 53].

For neutrinos travelling through the Earth and crossing its core, the matter potential can be approximated by a so-called 'castle wall' profile [54]. The neutrinos traverse the Earth's mantle, core and then again mantle, where the layer thicknesses are given by R^{mantle} and R^{core} , respectively. The principal enhancement occurs if both R^{mantle} and R^{core} are close to half an oscillation length (see Eq. 2.25) in the respective region, i.e.

$$R = L_{\text{osc}}/2. \quad (2.30)$$

This can be fulfilled by choosing an appropriate neutrino energy and zenith angle, which defines the neutrino trajectory through the Earth.

Qualitatively, the process can be described as follows: the transition probability reaches its maximum when the neutrinos reach the first border between different density regions (mantle \rightarrow core). Entering the core, the matter potential changes quasi instantaneously to another value, leading to a different mixing angle and effective mass-squared difference (see Eq. 2.27 and Eq. 2.28). The latter changes also the oscillation phase. In turn, the transition probability can continue increasing instead of starting to decrease. Similar happens at the second border between different density regions (core \rightarrow mantle). Each half-wave

¹²Named after Mikheyev, Smirnov and Wolfenstein.

¹³This measurement also solved the so-called 'solar neutrino problem' [49], which refers to the observation that the ν_e flux from the Sun measured on Earth appears too low compared to theoretical predictions from the solar model.

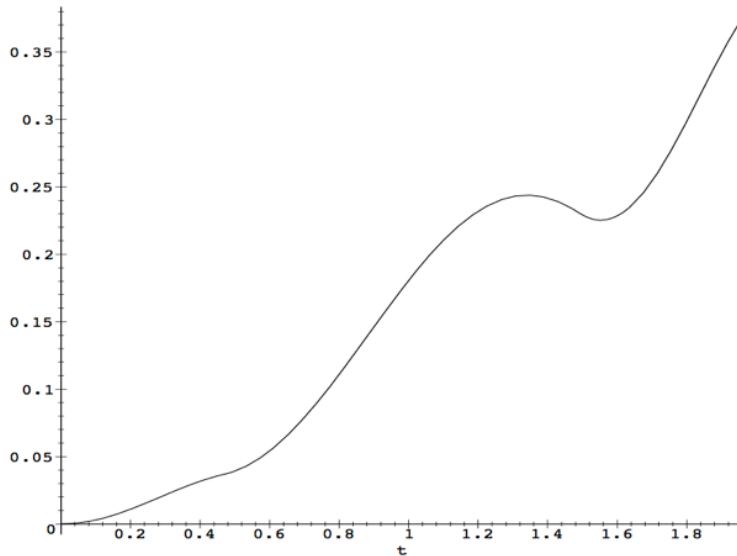


Figure 2.8: Illustration of ν_e disappearance probability in the Earth as a function of distance t (measured in units of the Earth’s radius) along the neutrino trajectory with zenith angle $\theta_\nu = 168.5^\circ$. Taken from [55].

The assumed values for neutrino mixing parameters differ from current best-fit values, but the general effect and the qualitative characteristics are the same for more up-to-date values.

oscillation of the transition probability is placed on top of the previous one, i.e. the transition probability builds up [53]. This is shown qualitatively in Fig. 2.8. The parametric enhancement depends on the sign of Δm^2 in the same way the resonance enhancement (see Sec. 2.2.3.3) does.

It is a consequence of a number of remarkable numerical coincidences that the parametric resonance condition (Eq. 2.30) is approximately met for GeV-scale atmospheric neutrinos (see Sec. 3.2.1) transversing the Earth’s core.

2.2.4 Current experimental status

Over the last decades, a variety of experiments have contributed to establish neutrino oscillation as an experimental fact. These experiments have been performed using different neutrino sources as well as detection techniques and covered a wide range of neutrino energies and travel distances (often referred to as baselines). From these experiments, the parameters governing the oscillation of neutrinos have been deduced. The current world knowledge of these parameters has recently be summarised by several groups, e.g. [56, 57, 58, 59, 60], forming a fairly consistent global picture.

In the 3ν scheme, the only unknown parameters of neutrino oscillation are the ‘neutrino mass hierarchy’ (see Sec. 3.1), the CP-violating phase δ_{CP} and two possible further complex phases, if neutrinos are Majorana particles. However, the two Majorana phases have no effect on oscillation experiments [39].

Best-fit values and contributing experiments

The best-fit values reported in [56] are given in Tab. 2.2. Two of the neutrino mixing angles, θ_{12} and θ_{23} , are rather large (θ_{23} could be close to maximal mixing within the current precision), while the third one, θ_{13} , is small but non-zero. One of the three mass-squared differences is significantly smaller than the other two, i.e. $|\Delta m_{32}^2| \approx |\Delta m_{31}^2| \gg |\Delta m_{21}^2|$.

Parameter (hierarchy)	Best fit	3σ range
$\sin^2(\theta_{12})/10^{-1}$ (NH or IH)	3.08	2.59 – 3.59
$\sin^2(\theta_{13})/10^{-2}$ (NH)	2.34	1.76 – 2.95
$\sin^2(\theta_{13})/10^{-2}$ (IH)	2.40	1.78 – 2.98
$\sin^2(\theta_{23})/10^{-1}$ (NH)	4.37	3.74 – 6.26
$\sin^2(\theta_{23})/10^{-1}$ (IH)	4.55	3.80 – 6.41
δ_{CP}/π (NH)	1.39	[0, 2]
δ_{CP}/π (IH)	1.31	[0, 2]
$\Delta m_{21}^2/10^{-5} \text{ eV}^2$ (NH or IH)	7.54	6.99 – 8.18
$\Delta m_{\text{large}}^2/10^{-3} \text{ eV}^2$ (NH)	2.43	2.23 – 2.61
$\Delta m_{\text{large}}^2/10^{-3} \text{ eV}^2$ (IH)	2.38	2.19 – 2.56

Table 2.2: Best-fit values and 3σ -ranges of neutrino mixing parameters from [56], assuming the normal (NH) or inverted (IH) mass hierarchy hypothesis (see Sec. 3.1).

Convention: $\Delta m_{\text{large}}^2 = \Delta m_{31}^2 - \Delta m_{21}^2/2$, with $\Delta m_{\text{large}}^2 > 0$ for NH and $\Delta m_{\text{large}}^2 < 0$ for IH.

Therefore, the subscripts ‘large’ and ‘small’ are sometimes used¹⁴. This pronounced difference often justifies the usage of the two-neutrino scheme discussed in Sec. 2.2.2. Experiments measuring the disappearance of solar ν_e and long baseline (LBL) reactor $\bar{\nu}_e$ are dominated by oscillations with wavelength $\propto E_\nu/\Delta m_{21}^2$ and amplitudes controlled by θ_{12} , while experiments measuring the disappearance of atmospheric and long baseline accelerator $\bar{\nu}_\mu$ are dominated by oscillations with wavelength $\propto E_\nu/|\Delta m_{32}^2| \approx E_\nu/|\Delta m_{31}^2| \ll E_\nu/\Delta m_{21}^2$ and amplitudes controlled by θ_{23} . The mixing angle θ_{13} controls the amplitude of oscillations involving ν_e flavour with wavelengths $E_\nu/|\Delta m_{31}^2|$ and can be measured in medium baseline (MBL) reactor $\bar{\nu}_e$ experiments. The measurements for δ_{CP} are not very stringent, so that the whole range $[0, 2\pi]$ is allowed on the 3σ -level. The ordering of the neutrino mass eigenstates is also not known, as discussed in Sec. 3.1.

Tab. 2.3 summarise which experiments contribute dominantly to the present determination of the different parameters. For further details, see [57, 11] and references therein.

Although very large neutrino telescopes, such as ANTARES¹⁵ [61] and IceCube/DeepCore [62], are rather new players in the neutrino oscillation game, they have proven to be competitive in measuring atmospheric neutrino parameters (θ_{23} , $|\Delta m_{\text{large}}^2|$). A recent review work on these measurements can be found in [63].

Anomalous results beyond the standard paradigm

Although most of the oscillation data is well accommodated in the standard three-flavour neutrino paradigm, it should be noted that a couple of experiments have reported measurements that cannot be described within this paradigm, and suggest new physics beyond it. Possible explanations invoke ‘sterile neutrinos’ and ‘non-standard interactions’. However, this is outside the scope of this thesis. More information on this subject can for instance be found in [64, 65, 66, 67]

¹⁴ Also the subscripts ‘sol’ and ‘atm’ are in use, as these mass-squared differences dominate the solar and atmospheric neutrino oscillations.

¹⁵ Astronomy with a Neutrino Telescope and Abyss environmental RESearch.

Experiment	Dominant	Important
Solar experiments (Homestake, GALLEX/GNO, SAGE, SNO, Borexino, Super-Kamiokande)	θ_{12}	$\Delta m_{21}^2, \theta_{13}$
Reactor LBL (KamLAND)	Δm_{21}^2	θ_{12}, θ_{13}
Reactor MBL (Double Chooz, Daya Bay and RENO)	θ_{13}	$ \Delta m_{\text{large}}^2 $
Atmospheric experiments (Super-Kamiokande)	θ_{23}	$ \Delta m_{\text{large}}^2 , \theta_{13}, \delta_{CP}$
Accelerator LBL ν_μ disapp.	$ \Delta m_{\text{large}}^2 , \theta_{23}$	
Accelerator LBL ν_e app. (Minos, NO ν A, T2K)	δ_{CP}	$\theta_{13}, \theta_{23}, \text{sign}(\Delta m_{\text{large}}^2)$

Table 2.3: Experiments contributing to the present determination of the neutrino oscillation parameters. Adopted from [57].

Absolute neutrino masses

The observation of neutrino oscillations has unambiguously shown that neutrinos have non-zero masses. However, no information on the absolute neutrino mass can be deduced from neutrino oscillation measurement, as only the mass-squared differences determine the oscillation probabilities.

A promising approach to measure the absolute neutrino masses is to investigate the effects of the neutrino mass on the distortion at the upper end of the energy spectrum of the outgoing electron in tritium β decays. The current best limits on the mass of electron (anti)neutrinos¹⁶ come from the Mainz [68] and Troitsk [69] experiments:

$$m_{\bar{\nu}_e} < 2.3 \text{ eV}. \quad (2.31)$$

The KATRIN experiment will perform the same measurement with a higher precision and is expected to reach a sensitivity of 0.20 eV [70].

Further possibilities to determine the neutrino mass are based on time-of-flight measurements of neutrinos from astrophysical events – such as a core-collapse supernova [71] – and observations of cosmological perturbations – such as cosmic microwave background anisotropies [72]. However, these methods are model- and analysis-dependent. Depending on the model complexity and the input data used, upper limits on the sum of the neutrino masses can be obtained: $\sum_i m_i < (0.1 - 1.3) \text{ eV}$ [73, 74, 75, 76].

¹⁶ These experiments measure the superposition of mass eigenstates that correspond to the ν_e and $\bar{\nu}_e$ flavour eigenstate: $m_e^2 = \sum_i |U_{ei}^2| m_i^2$.

3 Measuring neutrino mass hierarchy

Although the absolute values of the mass-squared differences between different mass eigenstates are known from oscillation experiments, it is still unknown how the neutrino masses eigenstates are arranged relative to each other on the mass scale, i.e. the signs of the mass-squared differences. This so-called *neutrino mass hierarchy* (NMH) is discussed in Sec. 3.1.

The determination of the NMH has become a central goal of upcoming neutrino physics experiments. A promising pathway to this measurement are atmospheric neutrino experiments probing neutrino oscillation in the Earth. This experimental approach is pursued by the KM3NeT collaboration, which plans to build a megaton-scale underwater Cherenkov detector named ORCA in the Mediterranean Sea [3]. A similar detector, named PINGU¹⁷ [77, 78], is planned to be built at the South Pole by the IceCube collaboration. The principle of measurement for the NMH with this kind of experiments is explained in Sec. 3.2.

A dedicated study to evaluate the potential of the planned ORCA detector to determine the NMH has been performed within the KM3NeT collaboration, and is presented in their ‘Letter of Intent’ [3]. The results presented in this thesis constitute an essential ingredient of the ORCA sensitivity study and are a substantial contribution to the ‘Letter of Intent’. In order to put the content of this thesis into a wider context, the ORCA sensitivity study is briefly summarised in Sec. 3.3.

Besides atmospheric neutrino experiments, there are many other experimental approaches to determine the NMH. They are briefly discussed and compared among each other in Sec. 3.4.

3.1 Neutrino mass hierarchy

From the three neutrino mass eigenstates, three mass-squared differences can be constructed, but only two of them are independent, as obviously:

$$\Delta m_{32}^2 + \Delta m_{21}^2 = \Delta m_{31}^2. \quad (3.1)$$

Current neutrino oscillation experiments are mainly sensitive to the absolute values of these mass-squared differences, since they enter the oscillation probabilities as arguments of even functions¹⁸ (see Sec. 2.2.2). Due to the pronounced difference between the absolute mass-squared differences $\mathcal{O}(30)$, the relative ordering of the three neutrino mass eigenstates has not been resolved yet, as it is not possible to disentangle $|\Delta m_{32}^2|$ and $|\Delta m_{31}^2|$ with the currently achieved experimental precision (cf. Tab. 2.2). The ordering of the first two mass eigenstates has been determined by observing the MSW resonance for solar ν_e (see Sec. 2.2.3.3). Consequently, there are two possible non-equivalent orderings for the mass eigenvalues.

The convention is to choose m_1 and m_2 as the mass eigenstate that are close to each other, with $m_1 < m_2$. The third mass eigenstate is separated from the other two, either above or below. The ordering $m_1 < m_2 < m_3$ is customary referred to as *normal hierarchy* (NH) and $m_3 < m_1 < m_2$ as *inverted hierarchy* (IH). Both possible neutrino mass hierarchies (NMH) scenarios are illustrated in Fig. 3.1. Additionally, the flavour composition of the three mass eigenstates are shown.

The NMH is frequently also referred to as ‘neutrino mass ordering’.

¹⁷Precision IceCube Next-Generation Upgrade.

¹⁸ If CP is violated in the neutrino sector, which has not been observed yet, the imaginary part in Eq. 2.22 adds a contribution sensitive to the signs of the mass-squared differences.

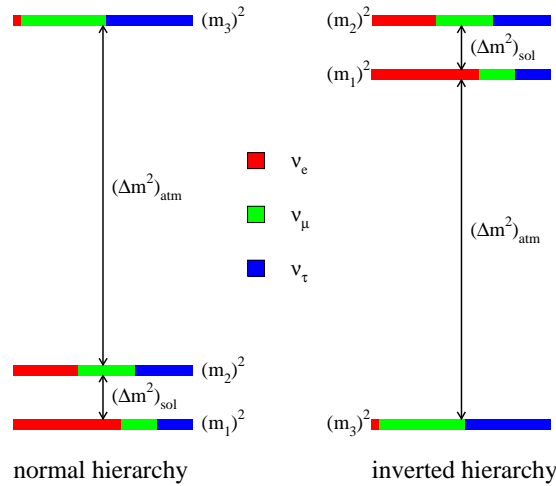


Figure 3.1: Schematic illustration of the two distinct neutrino mass hierarchies. The colour code indicates the flavour composition (ν_e, ν_μ, ν_τ) in each mass eigenstates (ν_1, ν_2, ν_3). Taken from [64].

Importance of determining the neutrino mass hierarchy

Resolving the NMH is of the utmost importance, for both practical and fundamental reasons. First, knowing the NMH will allow to optimise the information obtained from other neutrino experiments, including searches for the leptonic CP violation (i.e. $\delta_{\text{CP}} \neq 0, \pi$), searches for the absolute value of the neutrino masses, and searches for the violation of the lepton number via neutrinoless double-beta decays (which aim to reveal whether neutrinos are Dirac or Majorana particles) [64]. Second, resolving the NMH would rule out some neutrino mass models based on flavour symmetries and/or grand unification schemes [79]. Third, the NMH may have important implications on the cosmological probe of the neutrino mass scale, i.e. $\sum_i m_i$ [80]. Further discussions can be found in [81].

3.2 Neutrino mass hierarchy signature in atmospheric neutrino experiments

This section describes all relevant pieces of information needed to understand the observable NMH signature imprinted in atmospheric neutrinos that have transversed the Earth. Most parts of this section follow closely the line of arguments pursued in [3] and [63].

3.2.1 Atmospheric neutrinos

Cosmic rays (CR) permanently arrive at the Earth from all directions and initiate showers of particles due to interactions with nuclei (N) in the atmosphere. During the development of these air showers, charged mesons are produced, which can decay to muons and muon neutrinos:

$$\begin{aligned}
 \text{CR} + N &\rightarrow X + \pi^\mp, K^\mp, \\
 \pi^-, K^- &\rightarrow \mu^- + \bar{\nu}_\mu, \\
 \pi^+, K^+ &\rightarrow \mu^+ + \nu_\mu.
 \end{aligned}
 \tag{3.2}$$

These muons eventually decay producing additional neutrinos:

$$\begin{aligned}
 \mu^- &\rightarrow e^- + \bar{\nu}_e + \nu_\mu, \\
 \mu^+ &\rightarrow e^+ + \nu_e + \bar{\nu}_\mu.
 \end{aligned}
 \tag{3.3}$$

All resulting neutrinos and antineutrinos are called *atmospheric neutrinos*.

The flux of atmospheric neutrinos follow a power-law energy spectrum with a spectral index close to 3 in the relevant energy range of a few GeV. Fig. 3.2 (left) shows the direction-averaged energy spectra of atmospheric neutrino fluxes per flavour (ν_μ , $\bar{\nu}_\mu$, ν_e , $\bar{\nu}_e$). Atmospheric neutrinos are dominated by $\bar{\nu}_\mu$, which also have a slightly harder energy spectrum than $\bar{\nu}_e$. The latter are mainly produced in muon decays (see Eq. 3.3), which become more and more unlikely for higher muon energies due to time dilation. For muon energies of a few GeV and below, also the muon energy loss in the atmosphere leads to a hardening of the energy spectrum of $\bar{\nu}_e$ compared to $\bar{\nu}_\mu$. In addition, both effects lead to a substantial zenith angle dependence of the $\bar{\nu}_e$ flux, as can be seen in Fig. 3.3. The zenith angle determines the path length of the muon through the atmosphere and therefore its probability to decay. A zenith angle of $\theta_\nu = 0$ ($\cos \theta_\nu = 1$) corresponds to vertical upgoing neutrinos, i.e. they have traveled through the entire Earth on their way to the detector, and $\theta_\nu = \pi/2$ ($\cos \theta_\nu = 0$) corresponds to horizontal neutrinos. The relative contribution of $\bar{\nu}_\mu$ and $\bar{\nu}_e$ to the total atmospheric neutrino flux depends strongly on neutrino energy E_ν and zenith angle θ_ν , as shown in Fig. 3.2 (right). The flux ratio $(\nu_\mu + \bar{\nu}_\mu)/(\nu_e + \bar{\nu}_e)$ grows both with energy and $|\cos(\theta_\nu)|$. In the considered energy range, the direction-averaged flux of $\nu_{e,\mu}$ is between 1.1 and 1.3 times larger than of $\bar{\nu}_{e,\mu}$ (see Fig. 3.2 left).

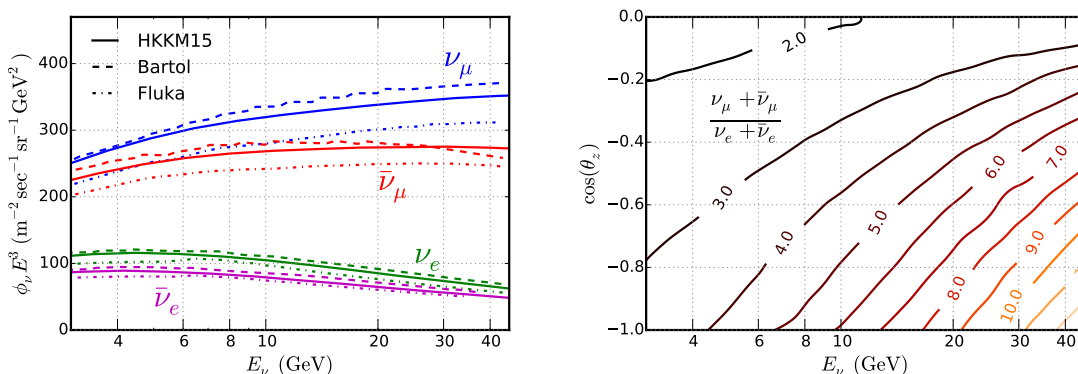
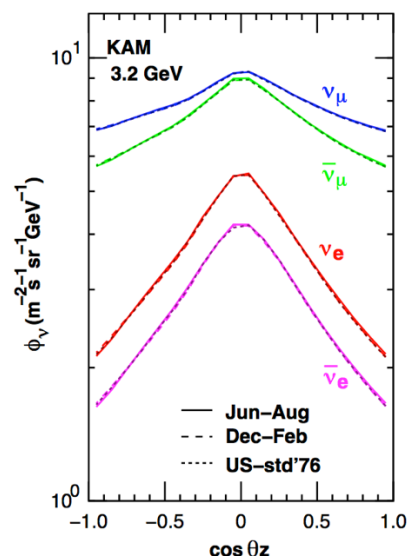


Figure 3.2: Left: direction-averaged energy spectra of atmospheric neutrino fluxes per flavour (ν_μ , $\bar{\nu}_\mu$, ν_e , $\bar{\nu}_e$) as a function of neutrino energy E_ν and arrival direction $\cos(\theta_\nu)$. Right: isocontour lines of flux ratio $(\nu_\mu + \bar{\nu}_\mu)/(\nu_e + \bar{\nu}_e)$. Taken from [63], which used predictions from [82, 83, 84].

Figure 3.3: Arrival zenith-angle-dependent atmospheric neutrino fluxes at $E_\nu = 3.2 \text{ GeV}$. Taken from [82].

This is for the Super-Kamiokande site in Kamioka, Japan. For other sites, e.g. the ORCA site in the Mediterranean Sea, the angular dependence looks slightly different, as the exact angular dependence is influenced by the local atmosphere density and the geomagnetic effects at the interaction point. However, general characteristics are very similar for the ORCA site.



Uncertainties in atmospheric neutrino flux

Atmospheric neutrinos have been measured over a wide energy range by several experiments and their flux is predicted by multiple models, e.g. [82, 83, 84] are shown in Fig. 3.2. While these models agree in flux shapes, the absolute flux normalisations differs by up to $\sim 15\%$. This normalisation uncertainty is essentially a consequence of the uncertainty in the neutrino-nucleon cross section normalisation (see Sec. 2.1.6).

3.2.2 Oscillation probabilities in the Earth

Neutrino oscillation in matter has been discussed in the 2ν scheme in Sec. 2.2.3. In the following, the relevant oscillation probabilities in the 3ν scheme for neutrinos propagating through the Earth are discussed.

The oscillation of atmospheric neutrinos in the few-GeV range are mainly driven by the large mass-squared differences Δm_{31}^2 and the mixing angles θ_{13} and θ_{23} . For illustrative purposes, it is very convenient to give a set of analytical expressions of oscillation probabilities. In the ‘one dominant mass scale’ approximation ($\Delta m_{21}^2 \ll |\Delta m_{31}^2|$), the $\nu_\mu \leftrightarrow \nu_e$ transition probability $P_{\mu e}$, the ν_μ survival probability $P_{\mu\mu}$ and the $\nu_\mu \leftrightarrow \nu_\tau$ transition probability $P_{\mu\tau}$ are given by [85]:

$$P_{\mu e} \approx \sin^2(\theta_{23}) \sin^2(2\theta_{13}^M) \sin^2\left(\frac{\Delta^M m_{31}^2 L}{4E_\nu}\right), \quad (3.4)$$

$$\begin{aligned} P_{\mu\mu} \approx & 1 - \sin^2(2\theta_{23}) \cos^2(\theta_{13}^M) \sin^2\left(\frac{(\Delta m_{31}^2 + \Delta^M m_{31}^2)L}{8E_\nu} + \frac{AL}{4}\right) \\ & - \sin^2(2\theta_{23}) \sin^2(\theta_{13}^M) \sin^2\left(\frac{(\Delta m_{31}^2 - \Delta^M m_{31}^2)L}{8E_\nu} + \frac{AL}{4}\right) \\ & - \sin^4(\theta_{23}) \sin^2(2\theta_{13}^M) \sin^2\left(\frac{\Delta^M m_{31}^2 L}{4E_\nu}\right), \end{aligned} \quad (3.5)$$

$$P_{\mu\tau} \approx 1 - P_{\mu e} - P_{\mu\mu}, \quad (3.6)$$

where the effective neutrino mixing parameters θ_{13}^M and $\Delta^M m_{31}^2$ are defined analogously as in the 2ν framework and A is the matter potential (see Sec. 2.2.3). The oscillation baseline L is the length of the neutrino trajectory through the Earth and is determined by the zenith angle θ_ν .

As already discussed in Sec. 2.2.3.3, the resonance enhancement that leads to maximal mixing can only happen for neutrinos in the case of NH and antineutrinos in the case of IH. For the Earth, the resonance energies for maximal 1-3 mixing are $E_\nu^{\text{res}} \approx 6 \text{ GeV}$ (3 GeV) in the Earth’s mantle (core).

The survival probabilities of ν_e and ν_μ as a function of neutrino energy and arrival direction are shown in Fig. 3.4 for NH – conditions under which the resonance enhancement can appear.

In the ν_e channel, the resonance in the Earth’s mantle is clearly visible at $E_\nu = [5, 8] \text{ GeV}$ and $\cos(\theta_\nu) = [-0.85, -0.5]$, where (nearly) all ν_e disappear. Above $E_\nu \gtrsim 15 \text{ GeV}$, this disappearance is suppressed due to saturation, as discussed in Sec. 2.2.3.3. For zenith angle values below $\cos(\theta_\nu) \lesssim -0.85$, the neutrinos pass through the Earth’s core and parametric enhancement can occur, if the oscillation length coincides with the structural length of the mantle-core-mantle profile of the Earth (see Sec. 2.2.3.4). Another effect is the interference between mantle and core effects, leading to additional ‘valleys’.

In the ν_μ channel, the effects of the resonance in the 1-3 mixing is less obvious than in the ν_e channel, as ν_μ oscillate (to ν_τ) even if the resonance conditions are not fulfilled. Resonant matter effects appear in the ν_μ survival probability as modifications on top of the otherwise smooth and periodic disappearance pattern shown in Fig. 3.4 (right). The

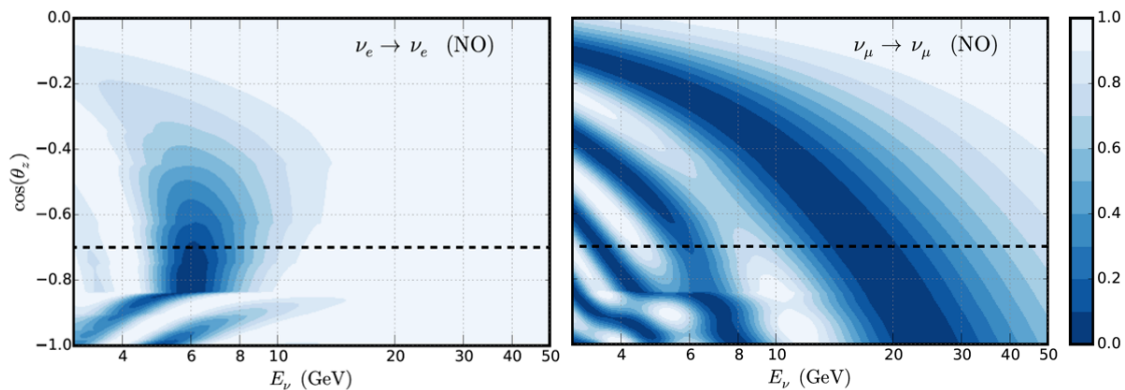


Figure 3.4: Survival probabilities for ν_e (left) and ν_μ (right) as a function of neutrino energy E_ν and arrival direction $\cos(\theta_\nu)$. Normal hierarchy is assumed. Dashed lines indicate the connection with Fig. 3.5. Taken from [63].

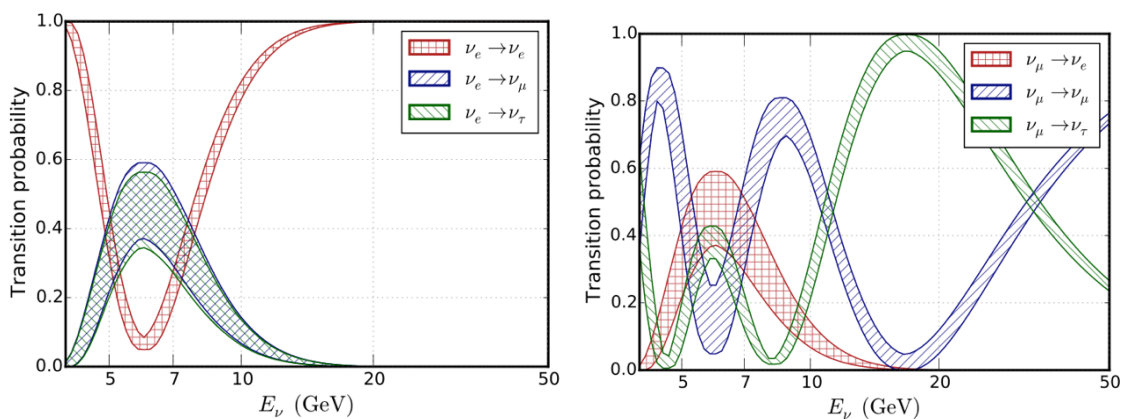


Figure 3.5: Oscillation probabilities for ν_e (left) and ν_μ (right) into different flavours as a function of neutrino energy E_ν for $\cos(\theta_\nu) = -0.7$ (indicated by dashed lines in Fig. 3.4). Normal hierarchy is assumed. Shaded bands represent the uncertainties on expected probabilities due to including uncertainties on oscillation parameters. Taken from [63].

core-mantle border at $\cos(\theta_\nu) \approx -0.85$ is clearly visible as an abrupt change in ν_μ survival probability for $E_\nu \lesssim 15$ GeV.

Fig. 3.5 shows the oscillation probabilities of ν_e and ν_μ into different flavours for a fixed arrival direction with $\cos(\theta_\nu) = -0.7$ and assuming NH. This corresponds to one-dimensional slices of Fig. 3.4 along the dashed lines. The bands indicate the influence on the expected probabilities due to the current uncertainties on the oscillation parameters.

At the resonance energy $E_\nu \sim 6$ GeV, ν_e nearly fully disappear and oscillate equally to ν_μ and ν_τ . If the resonance was absent – i.e. vacuum oscillation, or antineutrinos in NH, or neutrinos in IH – the $\nu_e \rightarrow \nu_e$ survival probability would be larger $\gtrsim 0.9$ in the considered energy range. This can be inferred from Eq. 3.4, where the oscillation amplitude is dictated by $\sin^2(2\theta_{13}^M)$, which gives roughly $\sin^2(2\theta_{13}) \approx 0.1$ in vacuum.

The oscillation probabilities of ν_μ to other flavours look more complicated than that of ν_e , as matter effects open the $\nu_\mu \leftrightarrow \nu_e$ transition and thus modify the ν_μ survival probability. If the resonance was absent, only $\nu_\mu \leftrightarrow \nu_\tau$ oscillations would occur for the length scales given by trajectories of neutrinos through the Earth.

From the oscillation probabilities, it is obvious that the NMH can only be accessed with neutrino energies below $E_\nu \lesssim 15$ GeV, where matter-induced resonances occur either for neutrinos (for NH) or antineutrinos (for IH).

3.2.3 Neutrino mass hierarchy signature

The basic idea to determine the NMH is to identify whether the matter-induced resonance occurs for neutrinos (for NH) or antineutrinos (for IH).

Atmospheric neutrino experiments face the problem that similar amounts of ν and $\bar{\nu}$ are produced in the atmosphere (differences smaller than 1.1–1.3, see Fig. 3.2) and the oscillation probabilities for ν in NH and $\bar{\nu}$ in IH are (nearly) degenerated, as discussed in Sec. 2.2.3.3. However, due to differences in the interaction cross sections between ν and $\bar{\nu}$ (roughly a factor of 2, see Fig. 2.5), a net asymmetry in the combined $\nu + \bar{\nu}$ event rates between NH and IH for a given neutrino flavour can be observed. Therefore, also experiments that are not capable of separating neutrinos from antineutrinos on an event-by-event basis – like water/ice-based Cherenkov detectors such as ORCA and PINGU – are sensitive to the NMH.

A convolution of the oscillation probabilities with the atmospheric neutrino fluxes and the neutrino-nucleon interaction cross sections allows to obtain two-dimensional patterns of event rates ($\nu + \bar{\nu}$) as a function of neutrino energy E_ν and $\cos(\theta_\nu)$ for both NH and IH, with an appreciable difference between NH and IH. In order to identify the phase space region where the NMH effects are large and therefore the discrimination more powerful, it is convenient to define asymmetry variables:

$$\mathcal{A} = \frac{N_{\text{IH}} - N_{\text{NH}}}{\sqrt{N_{\text{NH}}}}, \quad (3.7)$$

$$\mathcal{A}' = \frac{N_{\text{IH}} - N_{\text{NH}}}{N_{\text{NH}}}, \quad (3.8)$$

where N_{NH} and N_{IH} are the number of expected events at a given E_ν and $\cos(\theta_\nu)$ for NH and IH, respectively. \mathcal{A}' has the advantage of being independent of the accumulated event statistics, while \mathcal{A} is useful to provide an estimation of the expected significance of the NMH measurement, as used by [2]. As this approach typically overestimates the sensitivity, more sophisticated statistical treatments, as e.g. discussed in [86, 87, 88], are usually applied in sensitivity calculations.

Fig. 3.6 shows the \mathcal{A}' asymmetry for $\overleftrightarrow{\nu}_e$ CC and $\overleftrightarrow{\nu}_\mu$ CC events assuming the true neutrino energy and arrival direction are known, i.e. no smearing due to detector resolution is applied. If resolution effects are included the asymmetry patterns are blurred and the asymmetry effect is partly washed out reducing the NMH sensitivity. This is illustrated in Fig. 3.7, where a realistic detector resolution is applied. In particular, the delicate pattern at low energies in the $\overleftrightarrow{\nu}_\mu$ channel are washed out.

While the asymmetry effect is much larger for the $\overleftrightarrow{\nu}_\mu$ channel than the $\overleftrightarrow{\nu}_e$ channel if no detector resolutions are applied (see Fig. 3.6), the asymmetry effect is slightly larger in the $\overleftrightarrow{\nu}_e$ channel than the $\overleftrightarrow{\nu}_\mu$ channel for realistic detector resolutions (see Fig. 3.7). The $\overleftrightarrow{\nu}_e$ channel is much more robust against smearing. This comes due to an interesting feature in the oscillation probabilities and atmospheric neutrino fluxes. Instead of fully oscillating into ν_τ (as in vacuum), ν_μ also change to ν_e for $E_\nu \sim 6$ GeV and $\cos(\theta_\nu) \lesssim -0.5$. These transitions are nearly symmetric between both flavours, i.e. $P(\nu_\mu \rightarrow \nu_e) \approx P(\nu_e \rightarrow \nu_\mu)$, as can be seen in Fig. 3.5. Since the flux of $\overleftrightarrow{\nu}_\mu$ is ~ 4 times larger than that of $\overleftrightarrow{\nu}_e$ in the E_ν - θ_ν region of interest (see Fig. 3.2 right), the resulting ν_e ($\bar{\nu}_e$) flux reaching the detector shows a significant excess in NH (IH) compared to the original unoscillated flux. In conjunction with the $\nu_e/\bar{\nu}_e$ cross section differences and the initial $\nu_\mu/\bar{\nu}_\mu$ flux differences, this results in significantly different numbers of $\overleftrightarrow{\nu}_e$ -induced events (up to 30% more events for NH than for IH) in a relatively large phase space region compared to the detector resolutions.

For both the $\overleftrightarrow{\nu}_e$ and $\overleftrightarrow{\nu}_\mu$ channel, the asymmetry is evident for energies above $\gtrsim 4$ GeV. Integrating the event rates above 4 GeV, typically 4650 $\overleftrightarrow{\nu}_\mu$ CC and 2850 $\overleftrightarrow{\nu}_e$ CC events per year in a 1 Mton detector are expected for NH [3], and slightly less for IH.

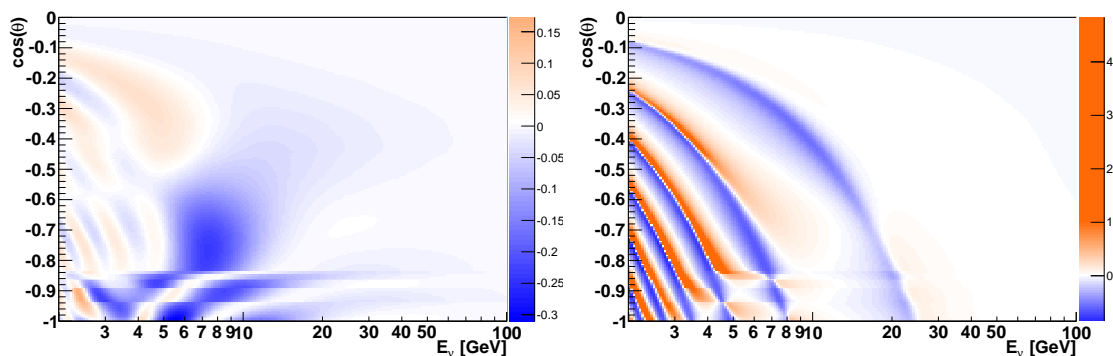


Figure 3.6: Asymmetry \mathcal{A}' (Eq. 3.8) between the number of $\nu + \bar{\nu}$ CC events expected in case of NH and IH, expressed as a function of neutrino energy E_ν and arrival direction $\cos(\theta_\nu)$. Colour code represents \mathcal{A}' per bin (200 bins per axis). The true neutrino properties E_ν and $\cos(\theta_\nu)$ are used, i.e. no smearing is applied. The left (right) plot applies to $\bar{\nu}_e$ (ν_μ). Figure provided by J. Brunner.

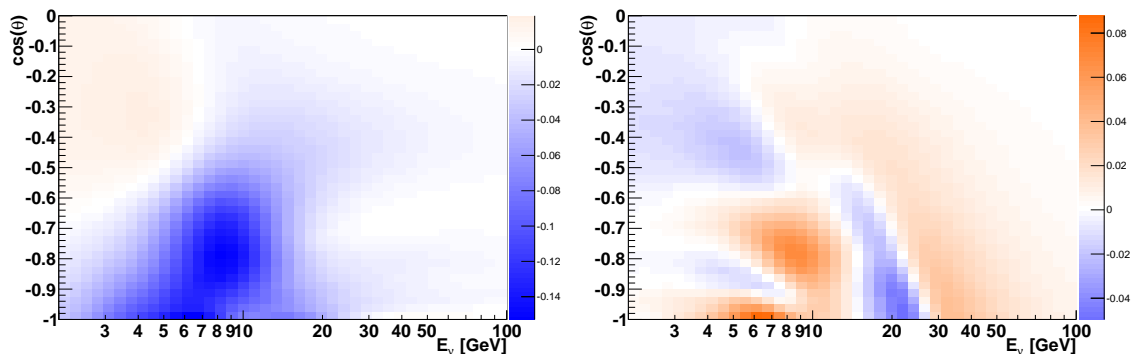


Figure 3.7: Same as Fig. 3.6, but a Gaussian smearing with $\sigma_{E_\nu}/E_\nu = 25\%$ in energy and $\sigma_\theta = \sqrt{\frac{m_p}{E_\nu}}$ in zenith angle is applied. Number of bins reduced by factor 5 in each axis compared to Fig. 3.6. Taken from [3].

The $\bar{\nu}_\tau$ appearance channel is less relevant for the NMH measurement for two reasons. First, the number of $\bar{\nu}_\tau$ CC events is small compared to the event statistics in the $\bar{\nu}_e$ and $\bar{\nu}_\mu$ channel due to reduced CC interaction cross sections in the relevant energy range [25]. Second, the fact that momentum and energy is carried away from outgoing neutrinos in the τ decays leads to intrinsically worse resolution of the initial neutrino properties.

Taking a closer look at Fig. 3.6 and Fig. 3.7 reveals that the typical size of the NMH asymmetry pattern in the $\bar{\nu}_e$ channel is about $\Delta E^{\bar{\nu}_e \text{NMH}}/E \approx 0.3$ for $E_\nu \approx 6$ GeV and about $\Delta\theta^{\bar{\nu}_e \text{NMH}} \approx 60^\circ$ around $\theta = 180^\circ$ (vertical upgoing). A comparison with realistic energy and direction resolutions assumed in Fig. 3.7 ($\Delta E^{\text{reso}}/E = 0.25$ and $\Delta\theta^{\text{reso}} \approx 23^\circ$ for $E_\nu \approx 6$ GeV), shows that $\Delta E^{\text{reso}}/\Delta E^{\bar{\nu}_e \text{NMH}} \approx 0.5 \Delta\theta^{\text{reso}}/\Delta\theta^{\bar{\nu}_e \text{NMH}}$. Therefore, the energy resolution is much more relevant than the direction resolution for the NMH determination in the $\bar{\nu}_e$ channel. For the $\bar{\nu}_\mu$ channel, the importance of energy and direction resolution is more balanced.

From this, it is obvious that the NMH sensitivity for atmospheric neutrino experiments depends dramatically on the attainable neutrino energy and direction resolution in both the $\bar{\nu}_e$ and $\bar{\nu}_\mu$ channel as well as the detection efficiency in the few-GeV range, where most

of the NMH asymmetry effect is evident. These key features of the detector performance are studied in this thesis.

Unfortunately, water/ice-based Cherenkov detectors are not capable of perfectly separating $\vec{\nu}_e$, $\vec{\nu}_\mu$ and $\vec{\nu}_\tau$ CC events from each other and from their NC counterparts. Instead, only two main classes of detector signatures can be distinguished: *track-like* and *point-like*. These classes of neutrino-induced events are briefly discussed below.

3.2.4 Classes of detector signatures for neutrino-induced events

The detection principle of water/ice-based Cherenkov detectors (see Sec. 4) in conjunction with the light detection sensor density limits the ability of the planned megaton-scale detectors to identify the different final state channels of neutrino interactions.

Muons are the only class of particles that can be confidently identified, because they are the only particles that appear as *tracks* in the detector (track length ~ 4 metres per GeV). Electrons and hadrons initiate particle showers that develop over distances of a few metres. Compared to elongated muon tracks, these showers appear as *point-like* in the detector. Particle propagation of muons and shower development in water/ice are further discussed in Sec. 4.2, 4.3 and 4.4.

Tab. 3.1 illustrates the detector signatures for events induced by the different neutrino flavours. All neutrino-induced events producing a muon with sufficient energy are called *track-like*, i.e. $\vec{\nu}_\mu$ CC events and $\vec{\nu}_\tau$ CC events with muonic τ decays. All other neutrino-induced events are called *shower-like*¹⁹, i.e. $\vec{\nu}$ NC events, $\vec{\nu}_e$ CC events and $\vec{\nu}_\tau$ CC events with non-muonic τ decays.

3.2.5 Possible neutrino-antineutrino separation techniques

The NMH determination involving matter-induced effects is always based on the separation of ν and $\bar{\nu}$ events. So far, only the different total interaction cross sections (see Sec. 2.1) have been discussed and are utilised in Sec. 3.2.3. However, there are additional possible $\nu/\bar{\nu}$ separation techniques²⁰, including:

- Magnetic deflection of the outgoing lepton in CC interactions. Usually, this technique is utilised by particle physics detectors at colliders, such as ATLAS [89] and CMS [90] at the LHC²¹. This separation technique is also the motivation for another experiment aiming for the NMH determination using atmospheric neutrinos, the planned magnetised iron calorimeter ICAL [91] at INO²². This detector will be able to differentiate μ^-/μ^+ emerging from $\nu_\mu/\bar{\nu}_\mu$ CC interactions on an event-by-event basis. This technique is hardly realisable for very large water/ice-based Cherenkov detectors.
- Stopping μ^- have the possibility to get captured by a nucleus (in seawater $\sim 10\%$ probability [92]). These captured μ^- have slightly shorter lifetimes ($\sim 1.6 \mu\text{s}$ compared to $\sim 2.2 \mu\text{s}$) and different secondary particles with lower energy deposits ($\sim 6 \text{ MeV}$ compared to $\sim 40 \text{ MeV}$) in the detector compared to decaying μ^\pm [92]. Therefore, by measuring the amount of Cherenkov light and the time when it is emitted at the end of a muon track, it is in principle possible to differentiate between μ^+ and μ^- on a statistical basis. This method is in principle also applicable by

¹⁹ Both terms ‘shower-like’ and ‘point-like’ describe the same class of events. While ‘shower-like’ is deduced from the underlying physics processes, ‘point-like’ characterises the spatial distribution of the Cherenkov light emission.

²⁰ The possibility for $\nu/\bar{\nu}$ separation at the $\vec{\nu}$ source, e.g. in beam experiments, is not discussed.

²¹ Large Hadron Collider at the European Organisation for Nuclear Research (CERN).

²² India-based Neutrino Observatory.

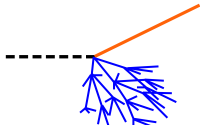
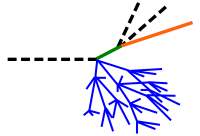
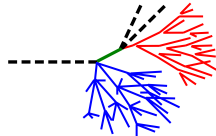
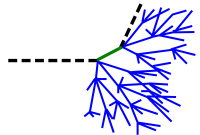
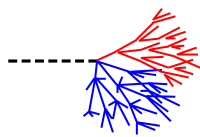
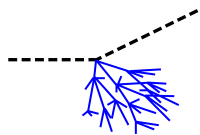
Interaction	Particle signature	Detector signature
$\bar{\nu}_\mu$ CC		hadronic shower and μ track
		track-like
		hadronic shower and μ track ($\tau^\pm \rightarrow \mu^\pm \bar{\nu}_\mu \bar{\nu}_\tau$, $\sim 17\%$ BR)
$\bar{\nu}_\tau$ CC		hadronic and EM shower ($\tau^\pm \rightarrow e^\pm \bar{\nu}_e \bar{\nu}_\tau$, $\sim 18\%$ BR)
		hadronic showers ($\tau^\pm \rightarrow \text{hadrons}$, $\sim 65\%$ BR)
		point-like or shower-like
$\bar{\nu}_e$ CC		hadronic and EM shower
$\bar{\nu}$ NC		hadronic shower

Table 3.1: Possible signatures of neutrino-induced events in water/ice-based Cherenkov detectors. Black dashed lines represent neutrinos, orange lines are muons, blue lines are particles in hadronic showers, red lines are electrons/positrons in electromagnetic (EM) showers and green lines are τ leptons. Depending on the τ decay mode (branching fraction, BR), the signature looks different. Adopted from [15].

water/ice-based Cherenkov detectors, however, the light detection sensor density of the planned ORCA and PINGU detectors is not sufficient to exploit this effect.

- Different numbers of charged pions and therefore muons are produced in hadronic showers from few-GeV ν and $\bar{\nu}$ CC events. This is caused by the positive charge excess in the nuclei (protons). Further details are given in Sec. 7.2.3. This feature is for example exploited in Super-Kamiokande to separate ν and $\bar{\nu}$ events on a statistical basis [93]. However, the light detection sensor density of the planned ORCA detector is not sufficient to identify the delayed Cherenkov light signal from the electromagnetic showers initiated when the muons decay ($\sim 2.2 \mu\text{s}$) due to the ubiquitous noise background in seawater (see Sec. 4.8.1).
- Exploiting the different distributions of interaction inelasticity y (Eq. 2.6). These differences are also observable with water/ice-based Cherenkov detectors for CC interactions if the energy of the outgoing lepton and the hadronic shower can be measured separately. This separation technique works obviously only on a statistical basis and not on an event-by-event basis.

The last mentioned option has the best prospects of success for the planned water/ice-based Cherenkov detectors ORCA and PINGU.

For $\bar{\nu}_\mu$ CC events, determining the inelasticity y is relatively easy, as energetic muons and hadronic showers show very discriminative detector signatures. Muon energy is usually estimated from the track length and shower energy from the Cherenkov light yield, as discussed in detail in Sec. 4.2, 4.3 and 4.4. Depending on the attainable inelasticity resolution, the possible gain in NMH sensitivity in the $\bar{\nu}_\mu$ channel can up to a factor ~ 2 in operation time [94].

For $\bar{\nu}_e$ CC events, it is not obvious how to differentiate the outgoing electron (initiating electromagnetic shower) and hadronic shower with water/ice-based Cherenkov detectors, because both electromagnetic and hadronic showers appear point-like to the detector (see Sec. 3.2.4). However, it could be shown as part of the research for this thesis that this separation is partly possible due to differences in the angular light distributions. This is discussed in Sec. 7. The shower reconstruction method developed in Sec. 12 includes an estimation of the interaction inelasticity y . This allows of course also a separation of $\bar{\nu}_e$ CC events from $\bar{\nu}$ NC and $\bar{\nu}_\tau$ CC events on a statistical basis, which will in turn increase the NMH sensitivity.

3.3 Neutrino mass hierarchy sensitivity calculation for ORCA

In the following, the NMH sensitivity calculation that has been performed for the ORCA experiment in the ‘Letter of Intent’ [3] is briefly summarised. First, the calculation of the expected rate of observed events is explained. Then, the statistical method for the NMH sensitivity calculation is described. Finally, the expected sensitivity is discussed.

Note that ν and $\bar{\nu}$ are assumed to be indistinguishable in the detector, as the potential of the determination of the interaction inelasticity and the subsequent $\nu/\bar{\nu}$ separation had not been available at the time of the writing of the ‘Letter of Intent’ [3]. The possible gain in NMH sensitivity for shower-like events is studied in Sec. 13.

3.3.1 Event rate calculation

In the ORCA experiment, the data will consist of observed number of events as a function of the reconstructed neutrino energy E_{reco} and zenith angle θ_{reco} . In order to determine the NMH, the observed event rates have to be compared to expected event rates.

The calculation of the expected rate of events can be separated into two parts. First, the expected neutrino interaction rate at the detector site is calculated as a function of the true neutrino properties E_{true} and θ_{true} . Second, the expected detector response is applied, leading to rates of reconstructed events as a function of E_{reco} and θ_{reco} . As mentioned above, the reconstructed inelasticity y_{reco} has not been used in the current version of the ORCA sensitivity calculation.

In the first part of the event rate calculation, all detector-independent ingredients are convoluted, namely the atmospheric neutrino fluxes²³, the oscillation probabilities and the interaction cross sections. The procedure yields results as discussed in Sec. 3.2.3. Note that the interaction rate depends on the assumed oscillation parameters.

In the second part of the event rate calculation, all detector-dependent ingredients are taken into account, including:

- **Effective detector mass:** The effective mass of the detector determines how many of the interacting neutrinos can be reconstructed. Often the *effective volume* (defined in Eq. 11.5) is used, which is related to the effective mass via the seawater density.

²³ Atmospheric neutrino fluxes predicted by the HKKM2014 [82] model for the Fréjus site (without mountain) and minimum solar activity are used.

- **Event signature classification:** As discussed in Sec. 3.2.4, the ORCA detector can in principle only distinguish between track-like and shower-like event signatures. Based on the observed detector signature the events are classified according to these two classes.
- **Energy and direction resolutions:** The energy and direction resolutions determine how well the true neutrino properties can be reconstructed from the observed detector signature. The attainable resolutions influence significantly the NMH sensitivity and are therefore the key parameter of the detector performance.
- **Background:** Neutrino-induced events have to be separated from events due to possible background sources, which consist mainly of misreconstructed atmospheric muons. These and other possible background sources are discussed in Sec. 4.8. It has been shown that the contamination with misreconstructed atmospheric muons in the final neutrino sample is of the order of a few percent [3].

All of these ingredients have been parametrised from detector simulations.

The evaluation of the energy and direction resolution as well as the effective detector volume in particular for shower-like events are part of this thesis and these results have been used in the NMH sensitivity calculation presented in the ‘Letter of Intent’ [3].

3.3.2 Sensitivity calculation

The NMH sensitivity is calculated using likelihood ratio distributions from pseudo-experiments. A pseudo-experiment (PE) is a simulated experimental measurement of event distributions in the $E_{\text{reco}}-\theta_{\text{reco}}$ plane.

For each PE, either NH or IH is assumed and a set of true oscillation parameters is selected according to Gaussian distributions given by the current world best-fit values and their uncertainties. In addition, several other systematics are taken into account, including those of the overall event rate normalisation, CC/NC ratio, $\nu/\bar{\nu}$ ratio, $\vec{\nu}_e/\vec{\nu}_\mu$ ratio and energy scale. Then, the expected number of events for a given operation time are calculated (see Sec. 3.3.1) and pseudo-data is generated by randomly drawing a detected number of events based on Poisson statistics. Each PE is analysed by performing for the NH and IH assumption a maximum likelihood fit with the oscillation parameters and systematics as free parameters. The best-fit likelihoods are used to calculate the log-likelihood ratio, which is used to quantify the separability of the two NMH hypotheses.

3.3.3 Expected sensitivity

The expected NMH sensitivity depends on the true NMH as well as the true value of θ_{23} and δ_{CP} . Fig. 3.8 shows the median significance to exclude the wrong hierarchy hypothesis after three years of operation as a function of the true value of θ_{23} and assuming no CP-violation, i.e. δ_{CP} equals 0 or π . The median significance can be interpreted as the minimum significance, commonly given in Gaussian- σ , with which the wrong hierarchy hypothesis can be excluded in at least half of the PEs. For the experimentally not excluded range of θ_{23} and assuming $\delta_{\text{CP}} = 0$, the NMH can be measured with more than 3σ within three years of operation. If $\delta_{\text{CP}} = \pi$ is realised in nature, it is about 0.5σ less significant, i.e. about 2.5σ within three years of operation. The significance increases dramatically in case of NH and θ_{23} in the second octant ($\theta_{23} > \pi/4$). The full-size ORCA detector (array of 115 detection strings, see Sec. 5) could be completed in 2020 [3], so that the NMH could be determined with 3σ in 2023.

Besides the NMH sensitivity, ORCA can also improve the uncertainties on other oscillation parameters: Δm_{31}^2 and θ_{23} . Both parameters are determined unconstrained in

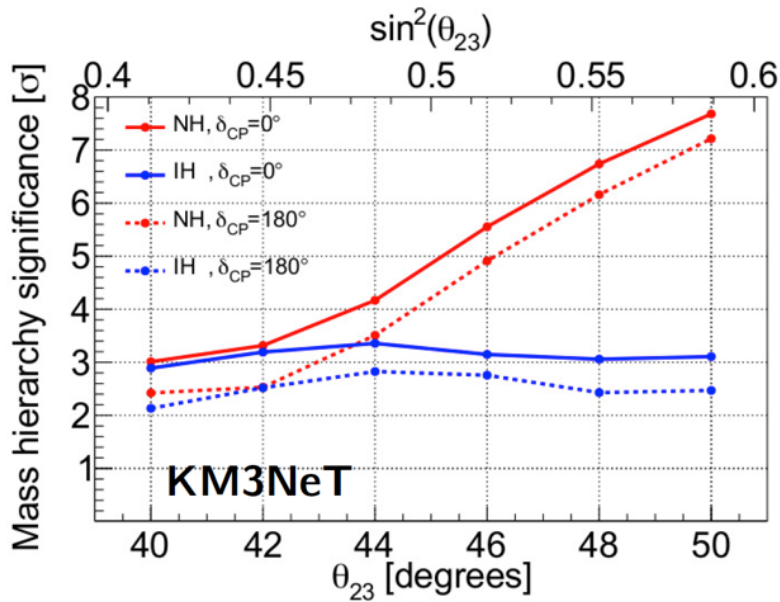


Figure 3.8: Median NMH significance to exclude the other hierarchy hypothesis assuming true NH (red) or IH (blue) as a function of true θ_{23} and assuming $\delta_{CP} = 0$ (solid) or $\delta_{CP} = \pi$ (dashed). Three years of operation time of the ORCA detector with 9 m vertical spacing between DOMs (see Sec. 5) is assumed. Taken from [3].

conjunction with the NMH. The expected measurement uncertainties on both parameters after three years are better than the current results of MINOS [95] and T2K [96], and competitive with the predicted performances of NO ν A [97] and T2K [96] in 2020.

3.3.4 Detector layout optimisation

A main part of the ‘Letter of Intent’ [3] is the optimisation of the ORCA detector layout under technical and financial constrains. The expected NMH significance in Fig. 3.8 is for the detector layout which turned out to give the best NMH significance This is the ORCA detector with vertical spacing between DOMs of 9 m (see Sec. 5). The detector layout obviously influences detector performance and consequently the expected NMH sensitivity. Therefore, the ORCA detector performance studied in the scope of this thesis is often presented for different detector layouts.

3.4 Neutrino oscillation experiments for neutrino mass hierarchy determination

The relatively large²⁴ value of θ_{13} has provided good opportunities to determine the NMH in different neutrino oscillation configurations²⁵, which include:

- Atmospheric neutrino $\vec{\nu}_{\mu,e} \rightarrow \vec{\nu}_{\mu,e}$ oscillation experiments, such as the planned water/ice Cherenkov detectors ORCA[3], PINGU [77], Hyper-Kamiokande [100] and ICAL [91], and the existing Super-Kamiokande detector.

²⁴ Here, ‘relatively large’ means significantly larger than zero and at the edge of the limits set by CHOOZ in 2003 [98]. Of course, θ_{13} is small compared to the other two mixing angles.

²⁵ Neither the possibility to determine the NMH from the energy spectra of supernova burst neutrinos (see e.g. [99]) nor the NMH determination from upper bounds on the sum of all three neutrino masses from cosmological observations (see e.g. [72]) are discussed here.

- Long-baseline accelerator (anti)neutrino $\bar{\nu}_\mu \rightarrow \bar{\nu}_e$ oscillation experiments, such as the planned LBNF²⁶ facility together with the DUNE [101] experiment and the existing NO ν A [102] experiment.
- Medium-baseline (~ 50 km) reactor antineutrino $\bar{\nu}_e \rightarrow \bar{\nu}_e$ oscillation experiments, such as the setup of JUNO [103], for which construction has started, and the planned setup of RENO-50 [104].

While the first two approaches depend on matter effects (discussed in Sec. 2.2.3) in neutrino oscillation driven by the large mass-squared difference, the last approach relies on oscillation interference between Δm_{31}^2 and Δm_{32}^2 .

The principle of atmospheric neutrino oscillation experiments (first approach), is elaborately discussed in Sec. 3.2. In the following, the other two approaches are briefly introduced and all three approaches are compared among each other.

Long-baseline accelerator experiments

These experimental setups are designed to measure the energy-dependent $\bar{\nu}_e$ appearance probability using $\bar{\nu}_\mu$ beams. They are sensitive to NMH and δ_{CP} , since both matter effects and CP-violation introduce a neutrino-antineutrino asymmetry (see Eq. 2.22 and Eq. 2.26). Therefore, the accelerators have to be able to produce beams with mainly either ν_μ or $\bar{\nu}_\mu$.

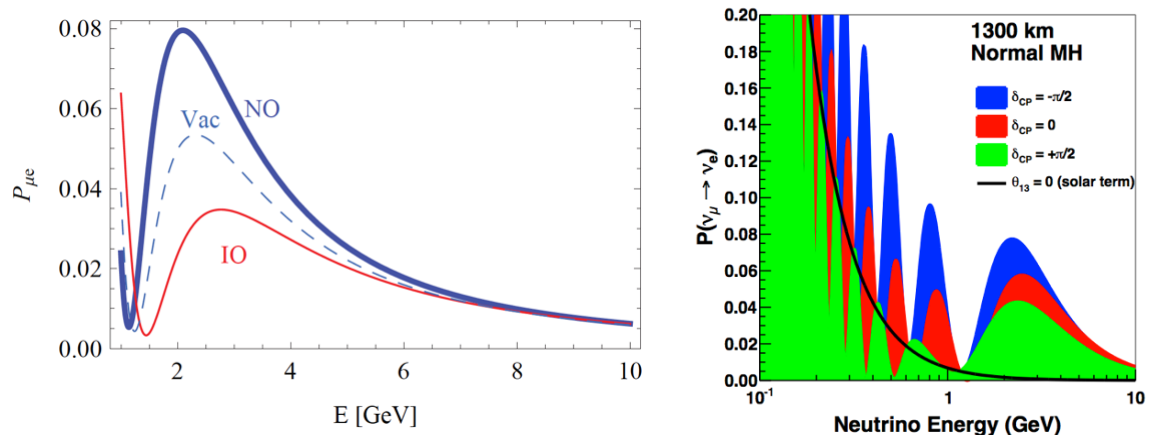


Figure 3.9: Electron neutrino appearance probability $P(\nu_\mu \rightarrow \nu_e)$ for a baseline of 1300 km. Probabilities for vacuum, NH and IH assuming the oscillation parameters as given in Tab. 2.2, i.e. $\delta_{\text{CP}} \approx -1/2\pi$, (left) and for different values of δ_{CP} assuming NH (right) are shown. Taken from [81] (left) and [101] (right).

Fig. 3.9 shows the ν_e appearance probability at a baseline of 1300 km as a function of neutrino energy for NH and IH as well as different values of δ_{CP} . At the oscillation maximum with the highest neutrino energy, which is usually called ‘first oscillation maximum’ and appears at $\sim E_\nu \approx 3$ GeV for the baseline depicted in Fig. 3.9, the transition probability is pulled apart from the vacuum case and the modification is different for NH and IH due to the resonance enhancement (see Sec. 2.2.3.3). However, similar transition probabilities can be achieved by changing the value of δ_{CP} (see Fig. 3.9 right). This illustrates the possible degeneracy between matter effects and CP-violation effects.

In the few-GeV energy range, the asymmetry at the first oscillation maximum due to matter effect increases with the length of the baseline, hence experiments with longer baselines are more sensitive to the NMH, while experiments with shorter baselines are more

²⁶Long-Baseline Neutrino Facility.

sensitive to δ_{CP} if the NMH is known²⁷. It has been shown [105] that this degeneracy can be resolved for baselines longer than ~ 1200 km. Hence, the DUNE experiment is planned with a baseline of ~ 1300 km, so that the NMH can be determined with a simultaneous measurement of δ_{CP} [101].

For the existing NO ν A and T2K experiments, with baselines of 810 km and 295 km, respectively, the NMH sensitivity depends on the value of δ_{CP} due to the afore mentioned degeneracies.

Medium-baseline reactor experiments

These experiments are designed to study very precisely the energy spectrum of $\bar{\nu}_e$ from nuclear reactors. For medium-baseline (~ 50 km) reactor experiments, the interplay of all three oscillation frequencies (from Δm_{21}^2 , Δm_{31}^2 and Δm_{32}^2) is visible. The interference between Δm_{31}^2 and Δm_{32}^2 leads to a distortion in the observed energy spectrum depending on the NMH.

The relative shape of the $\bar{\nu}_e$ flux for both NH and IH is shown as a function of L/E in Fig. 3.10. The energy spectrum of the $\bar{\nu}_e$ flux produced by the reactor covers multiple oscillation periods, which allows to distinguish between NH and IH. However, in order to extract the NMH information from the spectral distortion, an excellent energy resolution (about $3\%/\sqrt{E_\nu}$), absolute energy calibration and very large statistics are required [103]. In order to increase the statistics, the experimental setups are often planned to have two or more reactors at nearly identical baselines.

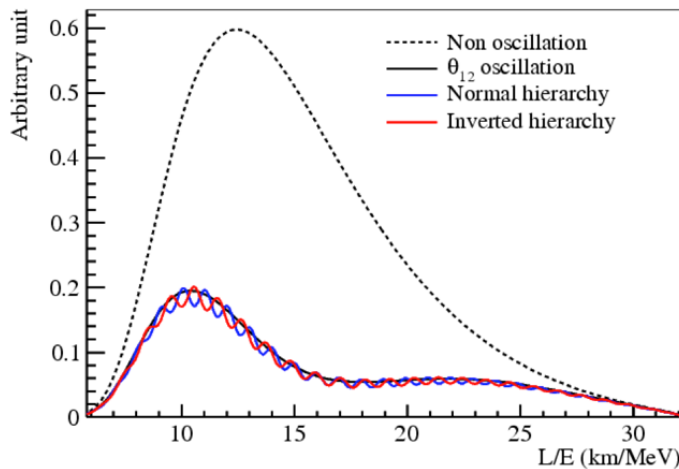


Figure 3.10: Relative shape of reactor $\bar{\nu}_e$ flux assuming NH (blue) and IH (red) as a function of L/E . Unoscillated flux is shown as black dashed line. Fast oscillation is driven by Δm_{31}^2 and slow oscillation is driven by Δm_{21}^2 (see Sec. 2.2.4). Taken from [103].

Sensitivity comparison

The expected NMH sensitivity of the experiments discussed above, their main risks and possible timescales have been compared by many authors, e.g. [81, 86, 106]. Fig. 3.11 shows a similar comparison plot as in [86], but including the sensitivity from ORCA as well as Hyper-Kamiokande. As the sensitivity of different experiments is often based on different assumptions about true oscillation parameters, these kind of plots should be taken with a

²⁷ This shows the importance of determining the NMH first in order to be able to measure δ_{CP} afterwards.

grain of salt. Nevertheless, they give a rough overview of the expected NMH sensitivities and planned timescales of the experiments.

From this, it is conceivable that ORCA/PINGU may be the first experiments giving a 3σ indication for the NMH, whereas the full-size DUNE experiment will have the best final sensitivity, which is expected to be greater than 5σ .

The main risks of the experiments are different:

- **LBNF-DUNE**: NMH sensitivity strongly depends on the true value of δ_{CP} and is also affected by true value of θ_{23} , whereas most robust against systematical errors compared to the other experiments [81, 107].
- **ORCA** and **PINGU**: NMH sensitivity is affected by true NMH, θ_{23} and δ_{CP} (see Fig. 3.8), but the energy and direction resolution are among the crucial performance indicators, as has been discussed by many authors [2, 86, 107].
- **JUNO**: NMH sensitivity depends very strongly on the achieved energy resolution [86], as can be inferred from Fig. 3.10.

As many authors suggest, it is important to pursue the NMH determination with different experimental strategies [107], because the systematics are very different and information from different approaches can be combined yielding increased sensitivity [107, 108].

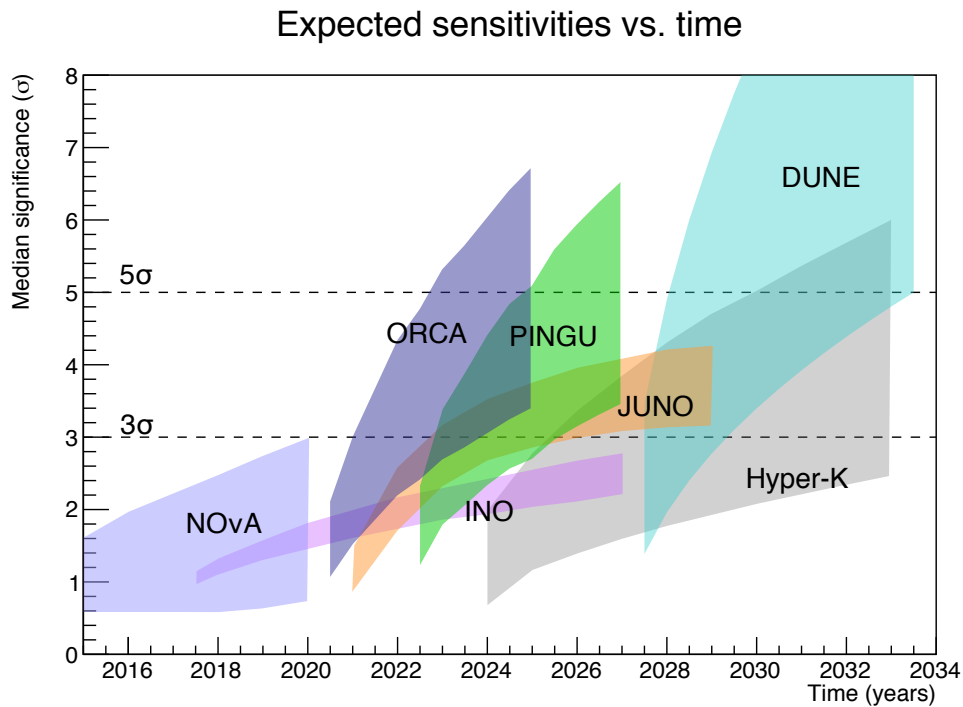


Figure 3.11: Expected median NMH sensitivity in number of sigmas for rejecting the IH if the NH is true for different experiments as a function of calendar year. The width of the bands come from the uncertainties in the true oscillation parameters and different detector performance assumptions. The figure is adopted from the comparison plot in [86] and ORCA and Hyper-Kamiokande are added. Figure produced by S. Bourret.

4 Cherenkov detectors for neutrinos

Neutrino detectors need to encompass large detector volumes in order to detect a significantly large number of neutrinos, as neutrinos interact only weakly with matter. Water- or ice-based Cherenkov detectors are often used to instrument sufficiently large volumes. These type of detectors register the Cherenkov light of charged secondary particles emerging from neutrino interactions with a large array of photosensitive devices. From the arrival times of the Cherenkov photons and the positions of the photosensors, the direction and energy of the incoming neutrino as well as other parameters of the neutrino interaction can be reconstructed.

Neutrino detectors are usually built underground, to reduce the background from muons produced in air showers resulting from cosmic-ray interactions. Possible locations are either in natural environments, such as the deep sea and deep glacial ice, or in deep underground laboratories. The planned KM3NeT/ORCA detector will be located in the Mediterranean deep sea and is described in detail in Sec. 5.

Most existing very large volume neutrino detectors are targeting neutrinos above the energy regime relevant for NMH determination and are often called ‘neutrino telescopes’, as they search for TeV–PeV neutrinos from astrophysical sources. Currently operating neutrino telescopes are the BAIKAL experiment [109] in the Lake Baikal, the ANTARES experiment [110] located offshore the French south coast, the IceCube neutrino observatory [111] in the South Pole glacier ice and recently also the first components of the KM3NeT/ARCA [3] detector were deployed offshore Sicily, Italy. All of these detectors share the same detection principle, which is also the same for the ORCA detector. Their main difference is the photocathode area density, which determines in particular the neutrino energy threshold, and is optimised for the targeted physics goal.

In the following, the detection principle of water/ice-based Cherenkov detectors and the relevant physics determining the signatures of GeV-scale neutrino-induced events in these detectors are discussed. Emphasis is put on the relevant characteristics for Cherenkov detectors designed as three-dimensional arrays of photosensors in the deep sea, such as the ORCA detector. The overall structure of this section and partly also the content is inspired by other PhD theses [112, 113].

4.1 Cherenkov radiation

Charged particles passing through a dielectric medium with a velocity greater than the speed of light in that medium emit Cherenkov radiation [114]. The Cherenkov light is emitted under a characteristic angle θ_{Ch} forming a light front with conical form, as schematically shown in Fig. 4.1. The opening angle of this cone depends on the particle’s velocity $\beta = v/c$ and the refraction index n of the medium:

$$\cos(\theta_{\text{Ch}}) = \frac{1}{\beta n}. \quad (4.1)$$

In seawater with $n_{\text{water}} \approx 1.35$, the *Cherenkov angle* for relativistic particles (i.e. $\beta \approx 1$) approaches $\theta_{\text{Ch}}^{\text{water}} \approx 42^\circ$ and becomes independent of the particle’s energy. In ice with $n_{\text{ice}} \approx 1.32$, the opening angle is slightly smaller $\theta_{\text{Ch}}^{\text{ice}} \approx 41^\circ$.

The number of emitted photons per unit path length dl from a particle with unit charge is given by [11]:

$$\frac{d^2N}{dl d\lambda} = \frac{2\pi\alpha}{\lambda^2} \left(1 - \frac{1}{n^2\beta^2}\right), \quad (4.2)$$

where λ is the photon’s wavelength in vacuum and α is the fine-structure constant. The default Cherenkov light yield N_0 for $\beta = 1$ in a wavelength window $[\lambda_1, \lambda_2]$ is approximately

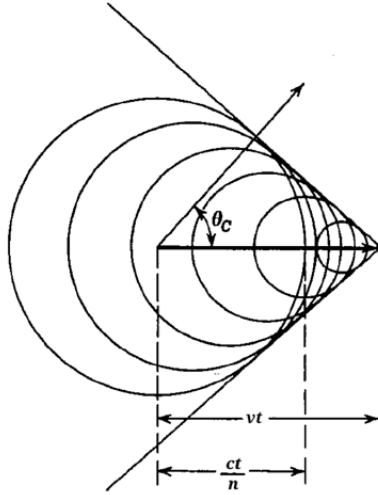


Figure 4.1: Schematic illustration of the Cherenkov effect. Taken from [115].

given by:

$$\frac{dN_0}{dl} = 2\pi\alpha \left(1 - \frac{1}{n^2}\right) \frac{\lambda_2 - \lambda_1}{\lambda_1\lambda_2}. \quad (4.3)$$

Water/ice is only transparent in a narrow band in the visible and ultraviolet spectrum. In the relevant wavelength range of about 300 nm to 600 nm, the number of photons per particle path length is approximately:

$$\left. \frac{dN_0}{dx} \right|_{\text{water}} = 340 \text{ cm}^{-1}, \quad (4.4)$$

$$\left. \frac{dN_0}{dx} \right|_{\text{ice}} = 325 \text{ cm}^{-1}. \quad (4.5)$$

Cherenkov radiation only occurs for particle's velocity above $\beta > 1/n$. For a particle with rest mass m_0 , the Cherenkov threshold energy E_{th} is given by:

$$E_{\text{th}} = \frac{m_0}{\sqrt{1 - 1/n^2}}. \quad (4.6)$$

In water, this corresponds to a threshold in kinetic energy (with $T_{\text{th}} = E_{\text{th}} - m_0c^2$) of $T_{\text{th}}^e \approx 0.25$ MeV for electrons, $T_{\text{th}}^\mu \approx 53$ MeV for muons, and $T_{\text{th}}^p \approx 460$ MeV for protons.

4.2 Muon propagation

A muon propagating through matter can lose energy via various processes: ionisation, bremsstrahlung, pair production and photonuclear interactions. The relative contribution of these processes depends on the muon energy. Below ~ 1 TeV, the energy loss is dominated by ionisation²⁸, which manifests itself as quasi-continuous process along the muon track. Further details can be found in [11].

In the relevant energy range of a few GeV, muons behave like so-called ‘minimum ionising particles’: they experience a roughly constant energy loss per unit track length, and travel on approximately straight lines. Most of the Cherenkov light is emitted by the muon itself, while $\sim 10\%$ – 30% (depending on muon energy) is emitted by quasi-continuously

²⁸ Energy loss due to Cherenkov radiation (see Sec. 4.1) is negligible compared to the energy loss due to ionisation.

produced low-energy δ -electrons along the track. Processes with large energy transfers hardly ever occur.

Therefore, the signature of few-GeV muons in water/ice Cherenkov detectors is a straight *track* with a nearly uniform luminance, which is given by Eq. 4.3. The length of the track is approximately 4 m/GeV in water and slightly longer in ice due to smaller matter density. After slowing down, the muon eventually decays²⁹ at rest into two neutrinos and an electron (see Eq. 3.3, lifetime $\sim 2.2 \mu\text{s}$). The electron initiates an electromagnetic shower (see Sec. 4.3). The Cherenkov light from the end of the muon track (last few metres) is studied in Fig. 9.2.

At muon energies above a few TeV, the muon energy loss starts to be dominated by stochastic processes, i.e. bremsstrahlung, pair production and photonuclear interactions. These so-called ‘catastrophic’ energy losses are visible as luminous electromagnetic showers along the muon track. This peculiarity of muon propagation contributes significantly to the signature observed by neutrino telescopes targeting TeV–PeV neutrinos.

4.3 Electromagnetic showers

Electrons (and positrons) lose energy mainly via bremsstrahlung and ionisation, where bremsstrahlung dominates in water above energies of $\sim 80 \text{ MeV}$ [11]. These radiated photons in turn interact with matter and produce electrons and positrons via pair production (dominant channel above $\sim 27 \text{ MeV}$ [116]) or Compton scatter off electrons. This leads to a cascading process of electrons/positrons producing photons and vice versa, which is called *electromagnetic shower*. Within this shower, Cherenkov light is emitted by all electrons/positrons with energies above their Cherenkov threshold³⁰.

The shower evolution is characterised by the radiation length X_0 , which yields the average distance after that the shower energy is reduced by a factor of $1/e$. In water, X_0 is roughly 36 cm [11]. The average longitudinal profile of the energy deposition as well as the Cherenkov light production in the shower can be well parameterised by [117]:

$$\frac{dE}{dt} = E_{\text{in}} b \frac{(bt)^{a-1} e^{-bt}}{\Gamma(a)}, \quad (4.7)$$

where $t = x/X_0$ is the number of radiation lengths and E_{in} is the incident shower energy. The scale parameter b is approximately constant over energy, whereas the shape parameter a increases linearly with $\log(E)$. Both parameters have been determined for water from simulations by several authors, e.g. [11, 112, 118, 119]. These studies agree within $\sim 10\%$ among each other. In [112], $a = 1.85 + 0.62 \ln(E/\text{GeV})$ and $b = 1.85$ is found. The maximum in the longitudinal shower profile is reached at $t_{\text{max}} = (a - 1)/b$. For shower energies of a few GeV, this maximum and consequently the brightest point in Cherenkov light yield is offset roughly $\sim 1 \text{ m}$ in the shower direction from the initial shower starting position. The lateral extension of energy deposition and Cherenkov light generation around the shower axis is restricted to distances below the Molière radius, which is smaller than 10 cm in water [11].

Compared to muon tracks, showers appear therefore in first approximation as a point-like burst of light in the detector. The total Cherenkov light yield is proportional to the initial shower energy with fluctuations smaller than 1% (see. Sec. 9.3.1). This allows a very precise ‘calorimetric’ energy measurement.

²⁹ In water, a μ^- can also be captured by a nucleus (see Sec. 3.2.5).

³⁰ It is worth noting that photons down to $\sim 0.4 \text{ MeV}$ can produce Compton electrons/positrons above the Cherenkov threshold $T_{\text{th}}^e \approx 0.25 \text{ MeV}$.

Although an electromagnetic shower consists of many electron-positron pairs with rather short path lengths and overlapping Cherenkov cones, the effective angular light distribution still peaks at the Cherenkov angle but is much broader than for muons. For initial shower energies above a few hundreds of MeV, the angular profile is nearly independent of energy and is shown in Fig. 4.2. Due to rotational symmetry of the Cherenkov light emission in conjunction with the point-like emission, an electromagnetic shower induced by a single electron results in a single Cherenkov cone. Also the term ‘Cherenkov ring’ is often used, because a cone appears as ring in a projection onto a plane perpendicular to the shower axis, and for a given point in time the Cherenkov signature is actually a ring (and not a entire cone, which is the time-integrated signal).

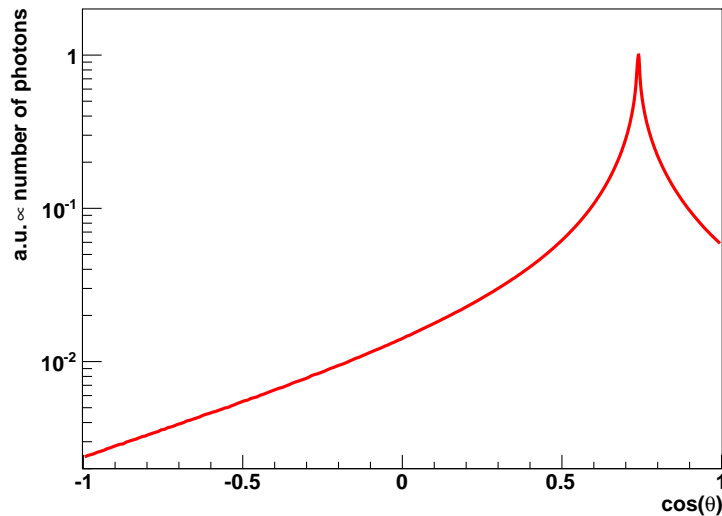


Figure 4.2: Angular profile of Cherenkov light emitted by simulated electromagnetic showers developing in water. The maximum is normalised to unity. Simulations as described in Sec. 6.6. For this plot, the initial electron energy is $E_e = 10$ TeV, but the shape is nearly energy independent.

4.4 Hadronic showers

A set of energetic hadrons develops into a *hadronic shower*. Every neutrino-nucleon interaction has a hadronic system in the final state (see Sec. 2.1), which produces in turn a hadronic shower.

The characteristics of the evolution of hadronic showers and their Cherenkov light emission in water/ice, have been obtained from simulation studies by several authors [118, 119, 120, 121]. However, these studies have focused on energies well above those relevant for the NMH measurement. Therefore, dedicated simulations of hadronic showers in the relevant energy range have been performed, and the most important characteristics are presented in Sec. 7.2. In the following, some general features of hadronic showers are briefly summarised.

The evolution of a hadronic shower is similar to that of an electromagnetic shower, apart from the fact that the shower development is driven by nuclear interactions instead of electromagnetic interactions. In water, the nuclear interaction length is roughly 83 cm [11]. Despite the longer mean free path length, hadronic and electromagnetic showers with the same initial shower energy have very similar longitudinal elongations, as the energy is

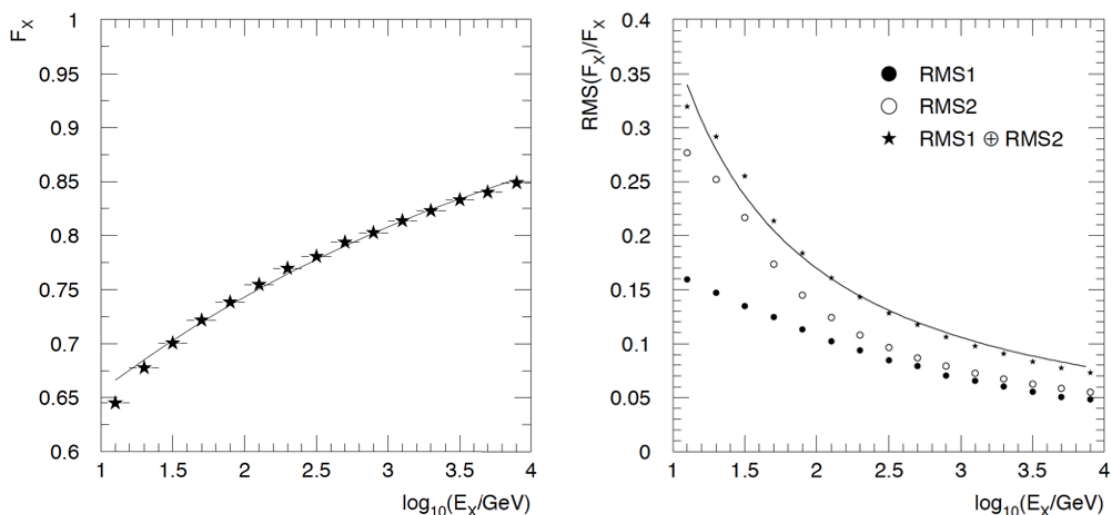


Figure 4.3: Left: Light yield ratio of hadronic and electromagnetic showers as a function of shower energy (labelled E_X here). The line represents a fit using Eq. 4.8. Right: Relative fluctuations (measured in root mean square, RMS) around the average light yield. Contributions from ‘propagation’ (RMS1), ‘hadronic state’ (RMS2) and both combined (RMS1 \oplus RMS2) are shown separately. The line represents a fit to the data. Taken from [121].

on average distributed to more than two hadrons at each interaction. Therefore, hadronic showers appear also as a point-like burst of light in the detector. The light is emitted by all charged particles with energies above their Cherenkov thresholds.

Hadronic showers produce less Cherenkov light than electromagnetic showers with the same initial shower energy. For the energies of interest, the main reason are the higher energy thresholds for Cherenkov radiation of charged hadrons compared to that of electrons due to their higher masses. With increasing energy, the average light yield of hadronic showers approaches that of electromagnetic showers. The reason is that in each secondary interaction a substantial fraction of produced particles are π^0 , which decay dominantly to two photons initiating electromagnetic subshowers within the hadronic shower. The π^0 production represents a “one way street” [122], as every generated π^0 increases the electromagnetic activity in the hadronic shower. Hence, the fraction F_{em} of electromagnetic activity in hadronic showers increases with shower energy. The light yield ratio $F = Y_h/Y_e$ of hadronic and electromagnetic showers is shown in Fig. 4.3 (left). This ratio can be well approximated by a simple phenomenological model introduced in [122] for energy deposition of hadronic showers in calorimeters and adopted to light yield in water/ice Cherenkov detectors in [121]:

$$\begin{aligned} F &= F_{\text{em}} + (1 - F_{\text{em}})f_0 , \\ F_{\text{em}} &= 1 - (E_{\text{in}}/E_0)^{-m} , \end{aligned} \quad (4.8)$$

where E_{in} is the incident shower energy, while f_0 , E_0 and m are parameters of the model depending on the particle species composition, the particle energy spectrum and the detector material. f_0 represents the relative Cherenkov activity of the pure hadronic part in the shower, E_0 can be understood as an effective π^0 production threshold energy, which is roughly at ~ 1 GeV. As the exponent m is positive, F increases with increasing shower energy.

Using particle physics terminology – a water/ice-based Cherenkov detector is a ‘non-compensating calorimeter’, i.e. its response to electromagnetic showers is intrinsically dif-

ferent from the response to hadronic showers. In addition, the latter depends on the π^0 content of the shower and is therefore depending on the shower energy.

Furthermore, hadronic showers also show large event-to-event fluctuations in the Cherenkov light yield. Two sources of fluctuations have to be considered: (i) the variation due to the variety of possible hadronic final states, i.e. number as well as species of particles and their energies, and (ii) the variation due to the possible interactions of shower particles during propagation in the shower development. In the following, these fluctuations are denoted as ‘hadronic state’ and ‘propagation’, respectively. Fig. 4.3 (right) shows the relative fluctuations in Cherenkov light yield of hadronic showers, separated into both sources of fluctuations. The relative fluctuations are particularly large for small hadron energies and decrease with energy. At energies of $E_h = 10$ GeV, the relative fluctuations (RMS/ E_h) are above $\sim 32\%$. The limitations imposed by these intrinsic fluctuations on attainable reconstruction resolutions of water/ice-based Cherenkov detectors for particle energies of 1–20 GeV are studied in detail in Sec. 9.

Hadronic showers consist of a set of energetic particles and each hadronic shower particle with sufficient energy can produce one Cherenkov cone. For energies of a few GeV, the initial hadronic shower particle directions are not collinear and the space angles between them are about $\mathcal{O}(10^\circ)$. Thus, the light emission signature are usually several Cherenkov cones with different intensity depending on the initial hadron types, their momenta and their hadronic interactions in the shower evolution. This leads to a huge variety of different event signatures of hadronic showers with energies of a few GeV.

As example, two simulated ν_e CC events with each $E_\nu \approx 10$ GeV and $y \approx 0.5$, i.e. equal share of energy between the electron and the hadronic shower, are shown in Fig. 4.4. The Cherenkov ring from the electron is clearly visible together with fainter rings from hadronic shower particles.

With increasing shower energy, the initial hadrons become more and more collinear, so that the individual Cherenkov cones overlap and the effective angular light distribution approaches that for electromagnetic showers (see Fig. 4.2). Therefore, neutrino telescopes targeting TeV-PeV neutrinos do normally not distinguish between showers initiated by an electron or a set of hadrons.

4.5 Light propagation

The detector medium significantly influences the observable signature of Cherenkov light, i.e. the number, the arrival times as well as the arrival directions of Cherenkov photons. Two effects have to be considered: absorption and scattering. While the former only affects the number of photons, the latter affects also the photon arrival times and directions. From the event reconstruction perspective, scattering reduces the information content per photon, while absorption reduces the number of photons.

The effect of photon absorption and scattering can also be seen in Fig. 4.4. Comparing the photon intensity at distance of 20 m (middle) and 50 m (bottom), shows the effect of photon absorption. As no cut on photon arrival time is applied, the effect of scattering is clearly visible as blurring of the Cherenkov rings with larger photon travel distances.

The planned detectors ORCA (seawater) and PINGU (ice) mainly differ in the detector medium. Therefore, the differences between seawater and ice are studied in Sec. 8 with regard to the implications for event reconstruction. In the following, only typical values for seawater are given. Wavelength-dependent properties are given in Sec. 8.1.

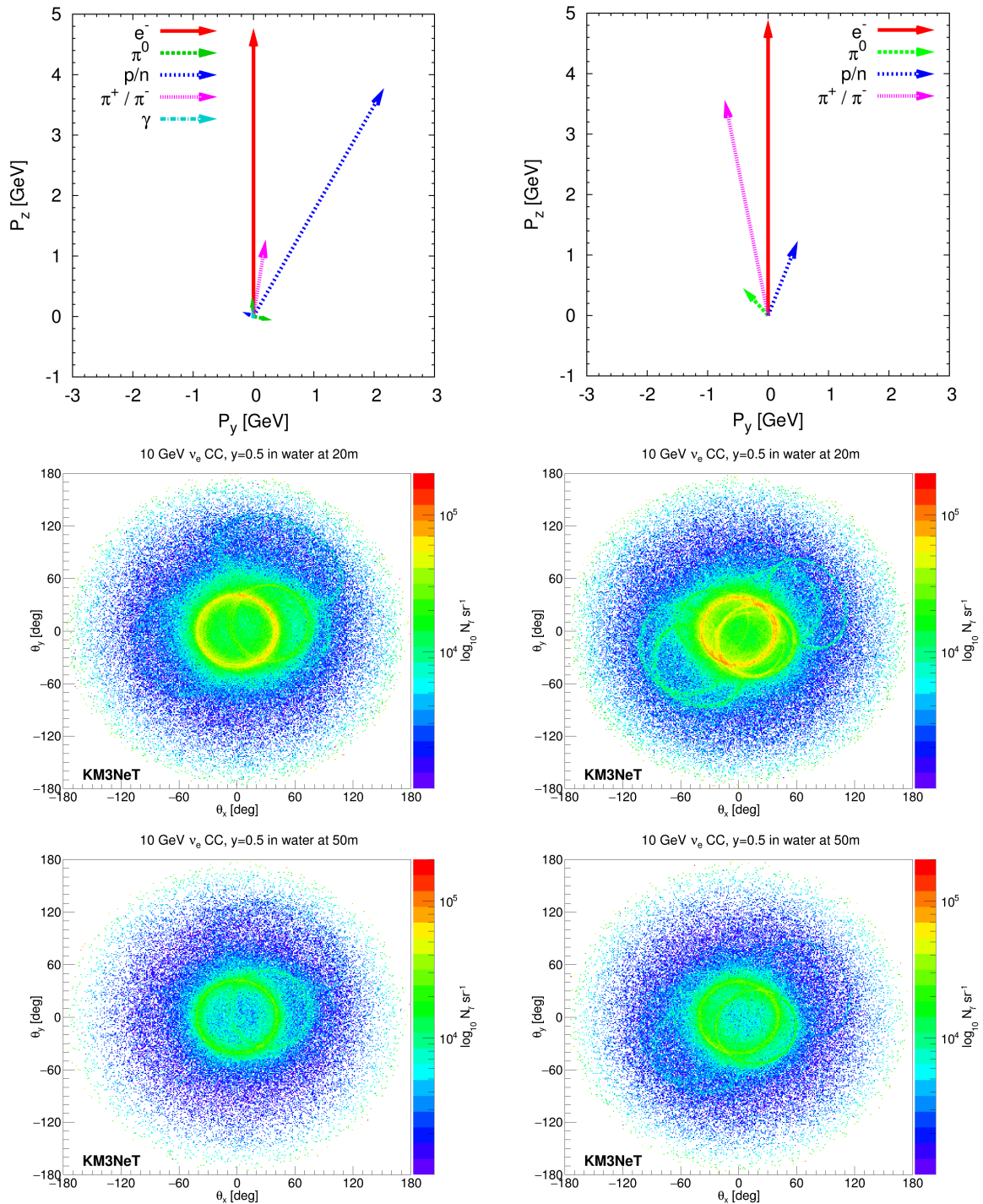


Figure 4.4: Two different simulated ν_e CC events with $E_\nu \approx 10$ GeV and $y \approx 0.5$ in left and right column. Each event is rotated in such a way that the electron is in z -direction. Illustration of the particles produced in the two events (top). Each arrow represents one particle, where arrow direction and length correspond to particle momentum in p_y - p_z plane, and arrow colour indicates particle type. Distributions of all photons recorded on shells at 20 m (middle) and 50 m (bottom) around neutrino interaction vertex in seawater. Angles θ_x and θ_y give the angle in x - and y -direction with respect to the z -direction, respectively. The Cherenkov ring from the electron is centered around $(0, 0)$ with an opening angle of 42° . No cut on photon arrival time is applied. Simulations are performed with GENS_{HWR} (see Sec. 6.1). Figures produced by C. W. James [3].

Absorption

The absorption of light is characterised by the wavelength-dependent *absorption length* λ_a . It corresponds to the total photon path length at which the photon survival probability is reduced by $1/e$. Optically pure seawater shows the highest transparency for photon wavelength of about ~ 440 nm, where typical values of roughly $\lambda_a \approx 70$ m are reached [123]. Measurements in the Mediterranean deep sea have shown slightly lower values of $\lambda_a \approx 60$ m [124, 125].

Scattering

The scattering properties are characterised by the *scattering length* λ_s and the *scattering angle distribution* $p(\theta_s)$. In general, the latter can be described by a mixture of scattering off water molecules (often termed ‘Rayleigh scattering’³¹) and larger particulates (often termed ‘Mie scattering’). While ‘Rayleigh scattering’ is symmetric around $\theta_s = 90^\circ$, scattering off particulates is strongly forward peaked. For further details, see Fig. 8.2. As the particulate-scattering contribution dominates over the relevant wavelength range, in most of the scattering processes the scattering angle is small. Hence, an effective scattering length is defined by:

$$\lambda_s^{\text{eff}} = \lambda_s / [1 - \langle \cos(\theta_s) \rangle], \quad (4.9)$$

where the average scattering angle $\langle \cos(\theta_s) \rangle$ is taken into account. For seawater in the Mediterranean deep sea, typical values of $\lambda_s \approx 55$ m and $\lambda_s^{\text{eff}} \approx 265$ m have been measured for photon wavelength of 470 nm [124].

Speed of light

The speed of the Cherenkov photons, and therefore their arrival times, depend on the wavelength-dependent *group velocity* v_g of the medium. It is convenient to define the group refractive index n_g , so that $v_g = c/n_g$. The group refractive index is related to the (phase) refractive index n by:

$$n_g = \frac{n}{1 + \frac{\lambda}{n} \frac{dn}{d\lambda}}. \quad (4.10)$$

Typical refractive indices for seawater in the Mediterranean deep sea are $n \approx 1.35$ and $n_g \approx 1.4$ for photon wavelength of 440 nm [128]. They depend slightly on the seawater temperature, salinity and pressure. Dispersion of group velocity is rather small, so that the photon arrival time distribution is only slightly disturbed³².

4.6 Light detection

In Cherenkov detectors the light is typically detected using photomultiplier tubes (PMTs), which are hosted together with their associated readout electronics in a spherical glass housing or a separate housing nearby. The former are called *digital optical modules* (DOM). The glass spheres protect the PMT from the environmental influences, while being mostly transparent for Cherenkov light in the relevant wavelength range. Often optical gel is used inside the glass spheres in order to reduce unwanted reflections. Incident photons reaching the PMT’s photocathode are subsequently converted to electrons via the photoelectric effect. The efficiency of this conversion is called *quantum efficiency* (QE). Currently used PMTs show QEs of about $\sim 25\%$ for the relevant photon wavelength range. After several

³¹ This is the scattering off individual molecules, which are much smaller than the photon wavelength. However, in a dense medium such as water the number of scattering centres (water molecules) within one photon wavelength is large, so that the medium can be assumed to be homogeneous and the scattering is induced by inhomogeneities, i.e. statistical density fluctuations. The latter is described by the ‘Einstein-Smoluchowski scattering’ [126, 127].

³²The photon wavelength is usually not measured in the photon detection process.

amplification stages, the electrical charge pulse is read out. Hereby, detected photons are converted into a time and a charge information, which is called a *hit*.

General detector layout

Cherenkov detectors located at the deep sea/ice usually instrument a very large volume with hundreds or thousands of DOMs arranged in a three-dimensional spatial grid. For practical reasons, the DOMs are distributed vertically in space along *strings*. They consist of a cable that is used for data transmission, power transmission and serves as mechanical support structure. In the deep sea, one end of each string is anchored to the sea floor and the other end is held taut by a submerged buoy. The buoyancy reduces the horizontal displacement of the top relative to the base in case of large sea current velocities. In the deep glacial ice, the strings are deployed into vertical holes melted in the ice using a hot water drill.

In general, the energy threshold for neutrino detection is determined by the density of photosensors of the detector instrumentation and the absorption length of the detector medium. Consequently, the targeted energy dictates the photosensors density – or more general the detector layout. Therefore, the optimisation of the ORCA detector layout (see Sec. 3.3.4) in the ‘Letter of Intent’ [3] is in fact a DOM density optimisation under technical and financial constraints.

4.7 Event reconstruction

The information available for event reconstruction are a set of hits associated with the event. Each hit consists of the following pieces of information: position and orientation of the PMT that recored the hit, a timestamp and a pulse charge information.

The task of any event reconstruction is to find the event hypothesis that fits the observed hit pattern best. Many reconstruction algorithms apply a *maximum likelihood method*. These class of methods use a *probability density function* (PDF) to assign a likelihood value to each of the PMTs, according to the expected light pattern for the assumed trial event hypothesis. The product³³ of all likelihood values yields the overall likelihood for the given event hypothesis. By varying the trial event hypothesis the event hypothesis that maximises the overall likelihood is found. The process of finding the maximum likelihood is called *fit*.

As the ‘likelihood landscape’ is usually multi-dimensional with many local maxima, the choice of a good starting point is essential. Often simplified algorithms, called *prefits*, based on geometrical considerations serve as fast first-guess estimates. Many reconstructions also start fits from different starting points and choose the best-fit result in order to cover a larger phase space region of the likelihood landscape.

In order to quantify the reliability of the fit result, many reconstruction algorithms provide *quality parameters*. Based on the reconstruction algorithm output a selection of events satisfying certain quality criteria is made. The strictness of this *event selection* is a trade-off between efficiency and resolution of the reconstruction.

4.8 Background

There are several different types of background sources obscuring the neutrino signature in Cherenkov detectors. Two classes can be differentiated: optical noise and atmospheric muons.

³³ For numerical reasons, most algorithms do not calculate the product of likelihood values P_i , but rather the sum of $\log(P_i)$.

4.8.1 Optical noise

The rate of detected photons is dominated by optical noise. This noise originates from three sources:

- **⁴⁰K decays**

Seawater contains a small amount ($\sim 0.04\%$) of the radioactive isotope Potassium-40 (⁴⁰K), which can decay to ⁴⁰Ca via β -decay (branching ratio 89.3%) or to ⁴⁰Ar via electron capture (branching ratio 10.7%). The resulting electron from the β -decay has a maximal energy of 1.33 MeV, which is sufficient to emit Cherenkov light. The photon emitted by the excited ⁴⁰Ar state has an energy of 1.46 MeV, which can be converted into Compton electrons capable of emitting Cherenkov light. Cherenkov photons from ⁴⁰K decays in seawater form a steady, isotropic optical background that add up to a total rate of about 100 Hz per cm² of photocathode area [113]. In general, the noise rate depends on the salinity and on the absorption length λ_a in the medium.

- **Dark count rate**

The dark count rate is the counting rate by the photosensors measured in the absence of external light sources. It includes the thermally-generated noise of the PMT and usually also the radioactive decays in the glass and the optical gel (mainly ⁴⁰K decay). It contributes to the steady background rate. However, its contribution is usually small compared to the noise rate from ⁴⁰K.

- **Bioluminescence**

The deep sea is inhabited by a large diversity of luminescent organisms, which emit visible light as a result of a chemical reaction [129]. Most species emit light in the photon wavelength range where seawater shows the maximum light transmission. For deep-sea Cherenkov detectors, this light shows two ‘components’. One is a slowly-changing background rate in the entire detector that just overlays the steady background rate from ⁴⁰K decays and dark noise. On top of the baseline rate, light bursts with durations of up to several seconds are observed on neighbouring photosensors. Bright bioluminescence bursts can exceed the ubiquitous background rate up to several tens of metres away from the light-emitting organisms. Bursts are usually emitted in response to a mechanical stimulus, e.g. by colliding with detector structures. Bioluminescence activity shows noticeable seasonal variations.

Further details are given in Sec. 10, where the characteristics of bioluminescence are investigated using ANTARES data. In addition, implications for measuring the NMH with ORCA are discussed.

4.8.2 Atmospheric muons

In the development of cosmic-ray air showers, muons are produced besides neutrinos (see Eq. 3.2). These muons are called atmospheric muons. Most of them are stopped in the overburden above the detector, however, with sufficient energy ($\gtrsim 500$ GeV for 2 km water equivalent, see Sec. 4.2), muons can reach the detector from above. This type of background is the main reason why many detectors are located as deep as possible in the sea, ice or mountain in order to maximise the overburden above the detector that acts as shield against these muons. Nevertheless, for a detector located ~ 2450 m below sea level, such as the ORCA detector (see Sec. 5), the rate of atmospheric muons reaching the detector is about $\sim 10^5$ times higher than the rate of atmospheric GeV-scale neutrinos interacting within the detector volume.

As muons cannot transverse the Earth, no atmospheric muon can reach the detector from below. Thus, all upgoing events have to be induced by neutrinos interacting in the detector or its vicinity. Nevertheless, misreconstructed atmospheric muons can mimic an upgoing event signature and may fake a neutrino-induced signal event. Therefore, a good accuracy in the event selection is needed in order to reduce this background.

4.9 Triggering

Due to the optical noise (see Sec. 4.8.1), the readout of thousands of PMTs creates a huge amount of data that has to be filtered before it can be written to permanent storage elements for analysis. The filtering of interesting events is performed by *trigger* algorithms. These algorithms have to be fast in order to be applied in real time and are either implemented in hardware or software.

For this task, the trigger algorithms usually look for *coincidences* in time between hits on different PMTs, which are close in space. In the deep sea, this strategy is very powerful as the optical noise produces such coincidences relatively rarely. By requiring clusters of pairwise causally connected coincidences the pure noise events can be reduced to a minimum, while keeping most of the events induced by neutrinos in the relevant energy range. As trigger algorithms usually do not differentiate between upgoing and downgoing events, also atmospheric muons reaching the detector from above can fire the trigger. Thus, the trigger rate is often dominated by atmospheric muons and not by neutrino-induced events due to their relative frequency of occurrence.

For the NMH determination, a trigger with an energy threshold as low as the relevant neutrino energy range is essential. Therefore, the trigger efficiency is an important aspect of the ORCA detector performance.

The optimisation of the trigger algorithm configuration used for the ORCA sensitivity calculation (see Sec. 3.3) in the ‘Letter of Intent’ [3] is described in Sec. 11.

5 The KM3NeT/ORCA detector

KM3NeT³⁴ is a future European research infrastructure that will be located at the bottom of the Mediterranean Sea. It will host a network of large-volume Cherenkov detectors and serve as a platform for Earth and Sea science research. The KM3NeT collaboration was formed to build, install and operate this research infrastructure. The KM3NeT detector design builds upon the invaluable return of experience from the first generation of Cherenkov detectors in the Mediterranean Sea: NESTOR [130, 131], NEMO [132, 133] and ANTARES [110]. These detectors have demonstrated the challenges and finally also the feasibility of measuring neutrinos with large-volume Cherenkov detector in the deep sea.

Two of the main objectives of the KM3NeT collaboration are i) the determination of the mass hierarchy of neutrinos with the KM3NeT/ORCA detector and ii) the discovery and subsequent observation of high-energy neutrino sources in the Universe with the KM3NeT/ARCA³⁵ detector [3]. For both detectors, the same technology and neutrino detection principle is employed, namely a three-dimensional array of photosensors that is used to detect Cherenkov light produced by relativistic particles emerging from neutrino interactions (see Sec. 4). The main difference between both detector designs are the density of photosensors, which is optimised for the study of neutrinos in the few-GeV (ORCA) and TeV-PeV energy range (ARCA), respectively.

The ORCA detector will be deployed at the KM3NeT-France site, which is located at $42^{\circ} 48' N$ $06^{\circ} 02' E$ in a depth of 2450 m, about 40 km offshore from Toulon, France. The site is about 10 km west of the existing ANTARES detector. Both locations are shown on a map in Fig. 5.1.

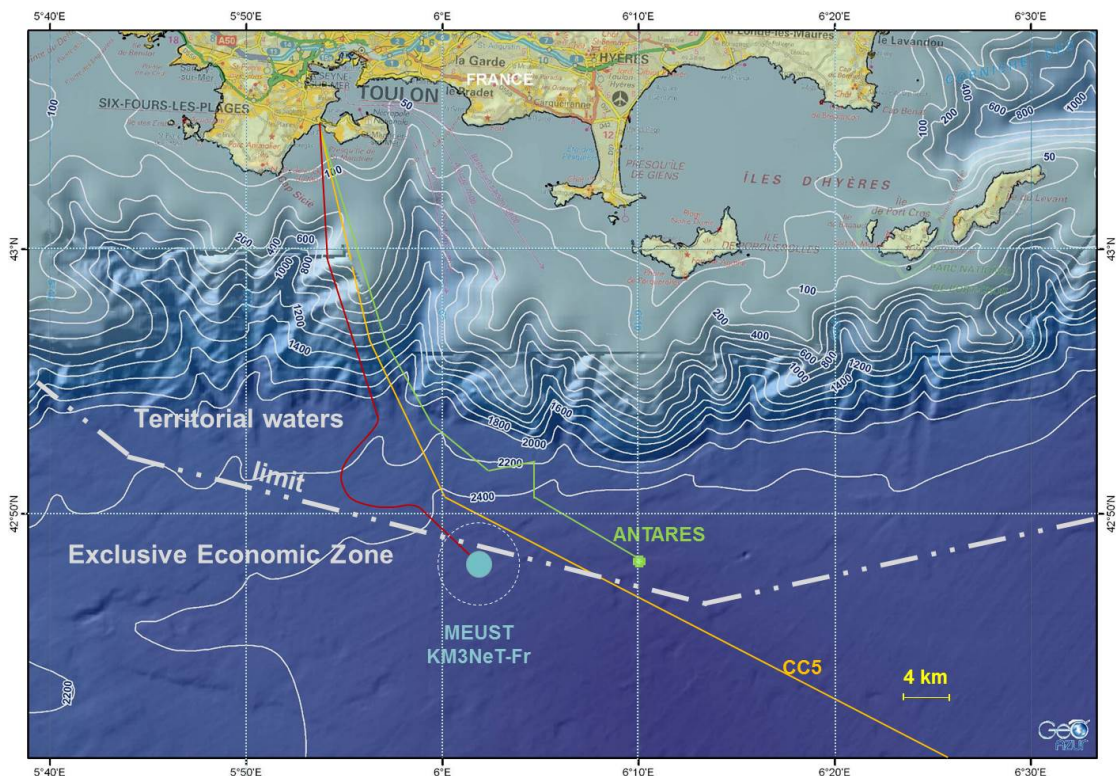


Figure 5.1: Map of the Mediterranean Sea south of Toulon, France. The location of the ORCA detector ('MEUST KM3NeT-Fr') and the ANTARES detector are indicated. Taken from [3].

³⁴KM3NeT is an acronym for 'Cubic Kilometre Neutrino Telescope'.

³⁵Astroparticle Research with Cosmics in the Abyss.

In the following, the planned ORCA detector design is described. Emphasis is put on the relevant information for the detector simulation. The content of this section is based on the ‘Letter of Intent’ [3]. Further information on technical details can be found therein and in the ‘Technical Design Report’ [134].

5.1 Digital optical module

The ‘digital optical module’ (DOM) developed by the KM3NeT collaboration comprises a transparent 17-inch diameter pressure-resistant glass sphere, housing 31 3-inch PMTs, their associated readout electronics and additional sensors. This key element of both KM3NeT detectors is shown in Fig. 5.2.

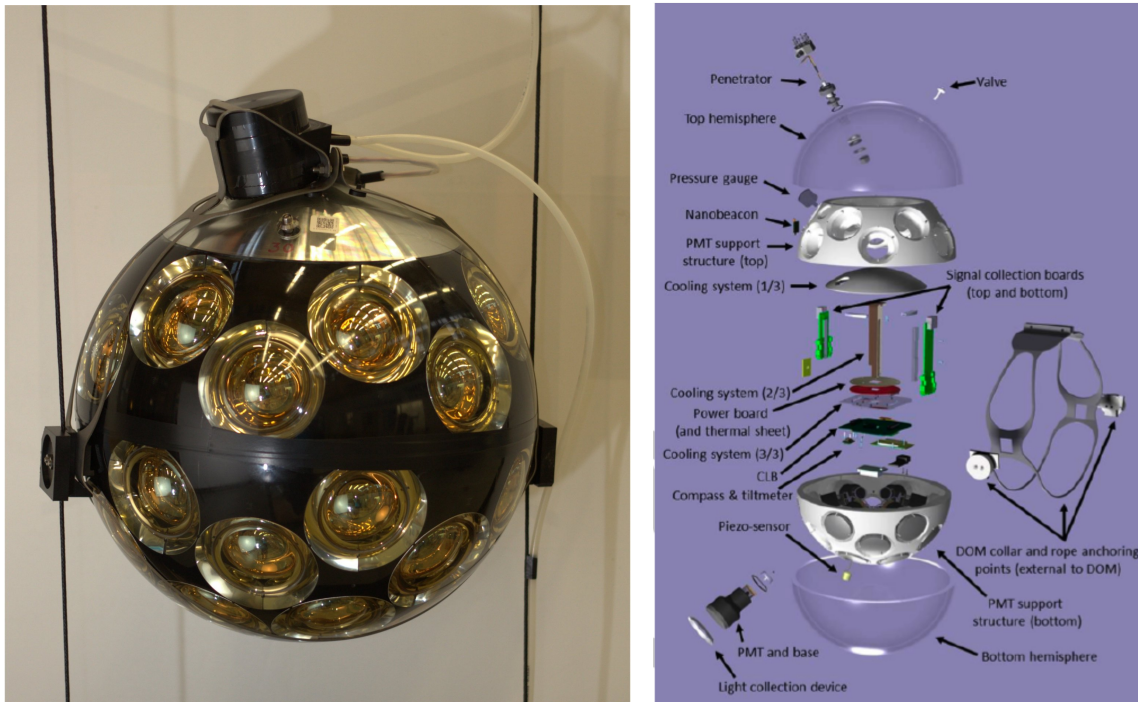


Figure 5.2: Photograph (left) and an exploded view (right) of a DOM. Taken from [3].

The PMTs are arranged in 5 rings with 6 PMTs each and a single PMT at the bottom pointing vertically downwards. In each ring, the PMTs are spaced with 60° in azimuth. Successive rings are staggered by 30° . A support structure holds all PMTs in place. There are 19 PMTs in the lower hemisphere and 12 PMTs in the upper hemisphere of the DOM. Each PMT is surrounded by a reflector ring in order to increase the photon collection efficiency (20-40% depending on photon incident angle) [135]. Optical gel is filled in the cavity between PMT and glass sphere in order to assure optical contact between the components. Further details on the PMT characteristics are given in Sec. A.1.

This multi-PMT design has three main advantages over traditional optical modules hosting only a single large 10-inch PMT (like for example in ANTARES, see Sec. 10.2): i) in total, roughly three times larger photocathode area, ii) almost uniform angular coverage, iii) information on the photon arrival direction. The angular acceptance of a full DOM, i.e. the sum of all 31 PMTs, is shown in Fig. 5.3. By construction, the angular acceptance is (nearly) rotation-symmetric in azimuth. As most PMTs are facing downwards, the largest acceptance is reached for photons coming from below. For photons coming from above, the acceptance is $\sim 42\%$ of that for photons from below. The angular acceptance of a single PMT is shown in Fig. A.2 (Appendix).

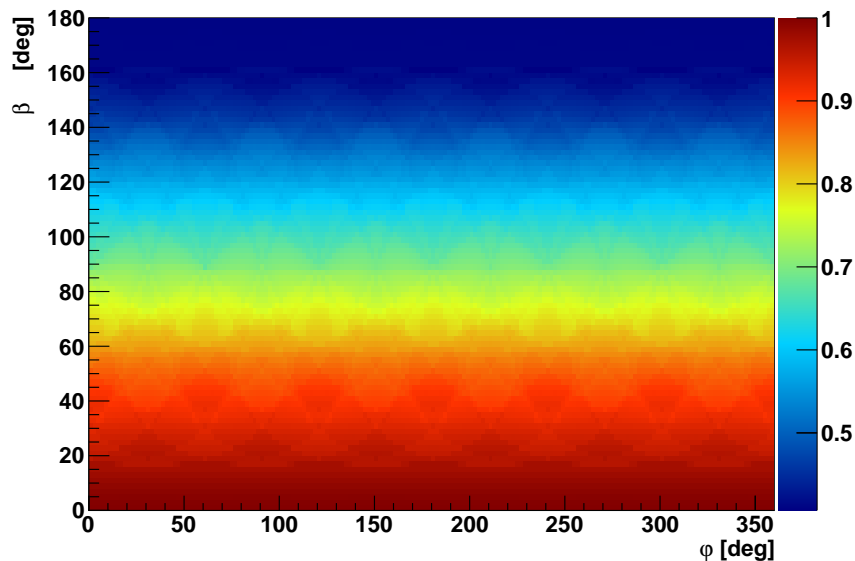


Figure 5.3: Relative angular acceptance of a full KM3NeT DOM (sum of all 31 PMTs) as a function of its orientation angles β (angle measured with respect to negative z -axis, vertical upward-going light corresponds to $\beta = 0^\circ$) and φ (azimuth). The maximum value is normalised to unity. The ring-structure with 6 PMTs can be seen as small differences (repeating every $\varphi = 60^\circ$) in β -bands.

Each PMT has an individual high-voltage base with integrated amplification and tunable discrimination. Its threshold is set at the level of typically 0.3 of the mean single photon pulse height in order to suppress electrical noise. If the electrical charge pulse exceeds this threshold the *time-over-threshold* (ToT) is recorded as well as the photon arrival time using a time-to-digital converter. The ToT serves as a pulse charge information and increases with the number of detected photons. According to the PMT specification, the full width at half maximum of the transit time spread is 4.5 ns (corresponding to a Gaussian with $\sigma \approx 2$ ns). The PMT quantum efficiency is 28% at 404 nm and 20% at 470 nm. Wavelength-dependent quantum efficiencies are shown in Fig. A.1 (Appendix).

In addition to the photosensors, each DOM contains three calibration devices, which are also shown in Fig. 5.2 (right): a LED nano-beacon for time calibration between nearby DOMs, a compass and a tilt meter for orientation calibration, and an acoustic piezo sensor for position calibration. In ANTARES, it has been demonstrated using similar calibration devices that the positions of the photosensors can be monitored with an uncertainty of less than 10 cm [136].

5.2 Detector layout

The ORCA detector is planned to consist of 115 detection strings arranged in a circular footprint. Fig. 5.4 (left) shows the footprint of the simulated benchmark detector (see Sec. 6.3). The minimal horizontal spacing between detection strings is limited due to the deformation of the strings due to the sea current [137], and the string deployment procedure. An average inter-string distance of about 20 m is foreseen. Each string hosts 18 DOMs with a vertical spacing³⁶ of about 9 m, starting about 40 m above the sea floor. The strings

³⁶ In the current ORCA design, a vertical spacing of 9 m between adjacent DOMs is envisaged, which is the result of a detector layout optimisation [3]. In this thesis, parts of this optimisation study are

are held taut by a submerged buoy and are anchored to the seabed by a dead weight. For power supply and data transmission, each string comprises an electro-optical cable, which is connected to the seabed infrastructure. The main electro-optical cable is connected to a shore station in La Seyne-sur-Mer for power supply, control and data acquisition.

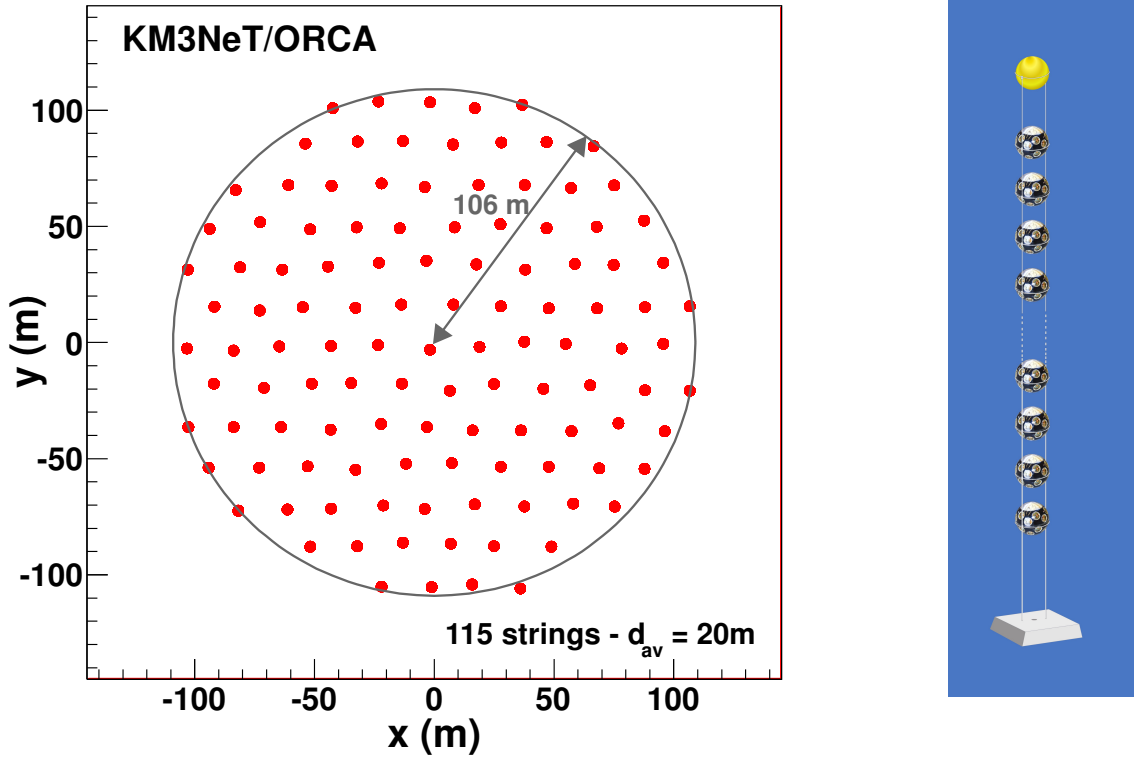


Figure 5.4: Footprint of the ORCA benchmark detector used for simulations (left). Each red dot represents a detection string (right). Taken from [3].

5.3 Data acquisition

The readout of the detector is based on the ‘all-data-to-shore’ concept successfully pioneered by ANTARES [138]. In this, all analogue PMT signals above the threshold are digitised in the DOM and sent to shore via the main electro-optical cable. The data is processed in real time by a PC farm, which is located at the Institute Michel Pacha in La Seyne-sur-Mer.

The total data rate for the ORCA detector is expected to amount to about 25 Gb/s, dominated by optical background (see Sec. 4.8.1). A reduction of a factor of $\sim 10^3$ is required to write the filtered data to disk. Therefore, the interesting events (induced by atmospheric muons or neutrinos) are filtered from the background using dedicated triggers algorithms (see Sec. 4.9). The trigger algorithm utilised for the ORCA detector are described in Sec. 11.1. Each triggered event contains a snapshot of all hits in the detector during the event. For the ORCA detector, the snapshot time window is typically $\pm 1.3 \mu\text{s}$ around the hits that fired the trigger, and is determined by the maximal photon travel time through the entire detector.

described. The benchmark detector simulated for this optimisation has 6 m vertical spacing between DOMs (see Sec. 6.3).

In addition, the singles rates of all PMTs in the detector as well as the status of the DOMs are recorded with a sampling frequency of 10 Hz. This information can be used in the event reconstruction to take into account the actual optical background and the general detector conditions.

5.4 Prototypes and first KM3NeT detection strings

A prototype DOM was installed on an ANTARES string in May 2013. It was operated in-situ for over one year. The observed singles rate are typically 8 kHz per PMT corresponding to 250 kHz per DOM. The rates of two-, three- and fourfold coincidences between PMTs inside the same DOM (within a 20 ns time window) are in good agreement with expectations and are about 340 Hz, 30 Hz and 2.7 Hz, respectively [139].

A test string with three prototype DOMs has been operated at the KM3NeT-Italy site (Capo Passero, 80 km offshore the Sicilian coast) from May 2014 until its decommissioning in July 2015 [140].

In December 2015, the first full string with 18 DOMs in the ARCA-style configuration (36 m vertical spacing between DOMs) has been deployed at the KM3NeT-Italy site and is operated since then. Since May 2016, another string is in operation.

5.5 Timeline for ORCA detector construction

The first ORCA-style string is foreseen to be deployed at the KM3NeT-France site in early 2017. An array comprising 7 detection strings is expected to be concluded and operational by the of 2017. The full-size ORCA detector comprising one detector block of 115 detection strings could be operational towards 2020.

5.6 Additional scientific goals

Besides determining the neutrino mass hierarchy and improving the uncertainties on atmospheric neutrino mixing parameters (see Sec. 3.3), an ORCA-like detector can contribute to several additional physics topics, including: testing unitarity of the neutrino mixing matrix (see Eq. 2.17) by studying $\bar{\nu}_\tau$ appearance [141]; indirect searches for sterile neutrinos and non-standard interactions [142]; indirect searches for dark matter [77]; testing the chemical composition of the Earth's core (Earth tomography) [143]; low-energy neutrino astrophysics [144].

Additionally, the KM3NeT research infrastructure will also house instrumentation for Earth and Sea sciences, such as marine biology, oceanography and geophysics.

6 Simulations

This section describes the simulation tools and the generation of simulated Monte Carlo (MC) events used for the results presented in this thesis. The software packages generate atmospheric neutrinos and atmospheric muons, and simulate the particle interactions within the detector medium, Cherenkov light generation and propagation as well as the detector response including optical noise.

6.1 Simulation tools

Different standard KM3NeT simulation packages are used in this thesis. Each software package is briefly described.

gSeaGen [145] is a software package to generate (anti)neutrino-induced interactions in seawater. It is based on the widely used **GENIE** [31, 146] (version 2.8.4) neutrino event generator. A relativistic Fermi Gas model is assumed for the motion of the target nucleon inside the nucleus (see Sec. 2.1.5).

MUPAGE [147, 148] is a software package to generate downgoing atmospheric muons based on a parameterised description of the underwater flux of atmospheric muons. These parameterisations were obtained from full simulations with **HEMAS** [149] and cosmic-ray data. Multi-muon events are also included.

KM3SIM is part of the **HOURS** software package [150] and simulates the response of a water-based Cherenkov detector. It propagates all particles emerging from a neutrino interaction using tools offered by the **GEANT 4** simulation package [151], generates Cherenkov photon emission, tracks the photons in seawater taking into account photon absorption and scattering (see Sec. 4.5), and simulates the photon detection taking into account the KM3NeT DOM and PMT characteristics. The latter include PMT photocathode area, quantum efficiency and angular acceptance, as well as transmission of light in the optical module glass sphere and in the optical gel. Version v6 is used.

KM3 [152] is the standard **ANTARES** simulation package for the generation and propagation of Cherenkov light by muons and electromagnetic showers in seawater. The code has been modified to take into account the KM3NeT DOM and PMT characteristics. For the photon propagation, the program uses parameterisations obtained from a full **GEANT 3.21** [153] simulation (using the **GEN** simulation package, see below).

GENSHWR is a special version of **GEN**, which is part of the **KM3** simulation package, and simulates the propagation of particles emerging from a neutrino interaction using **GEANT 3.21** as well as generates and tracks Cherenkov photons. The Cherenkov photons can be tracked through the medium and recorded on shells. Compared to the original version of **GEN**, it allows to simulate a set of particles instead of only a single particle. This can be used to simulate entire hadronic showers. Details on **GEANT 3.21** settings are given in Appendix A.2. Within **GEANT 3.21**, hadron tracking is performed by either **GHEISHA** ('**G-GHEISHA**') or **FLUKA** ('**G-FLUKA**')³⁷. If not stated otherwise, **G-GHEISHA** is employed.

³⁷ Note that **G-FLUKA** implemented within **GEANT 3.21** is a preliminary version of **FLUKA** and is different from their independent distributions.

JTE is a software package, which among others implements the adding of hits from randomly distributed optical background noise (see Sec. 4.8) to the hits induced by energetic charged particles, simulates the PMT electronics (i.e. converts the detected photons into a hit time and a ToT), and applies the trigger algorithms. Version r2356 is used.

6.2 Comparison of different simulation tools

The output of the KM3Sim and KM3/GENSHWR simulation tools have been compared over the course of the studies for this thesis. I performed many of these comparisons, revealing some small deficiencies. After correcting them, the simulation results were found to agree quantitatively very well. Obviously, presenting all comparisons would be exhausting, therefore only a brief summary of the comparisons performed by myself is given below.

The light yield from muons simulated with KM3 and KM3Sim was found to agree quantitatively very well (below $\lesssim 3\%$). This comparison can be found in [3]. Further detailed comparisons for muons as well as electrons simulated with different simulation tools have been presented in [154], including comparisons of photon arrival time distributions observed on PMTs/DOMs with defined orientations in a ‘toy detector’ simulation as well as the angular light distributions. Simulation results from different simulation tools for electromagnetic showers are found to be nearly identical.

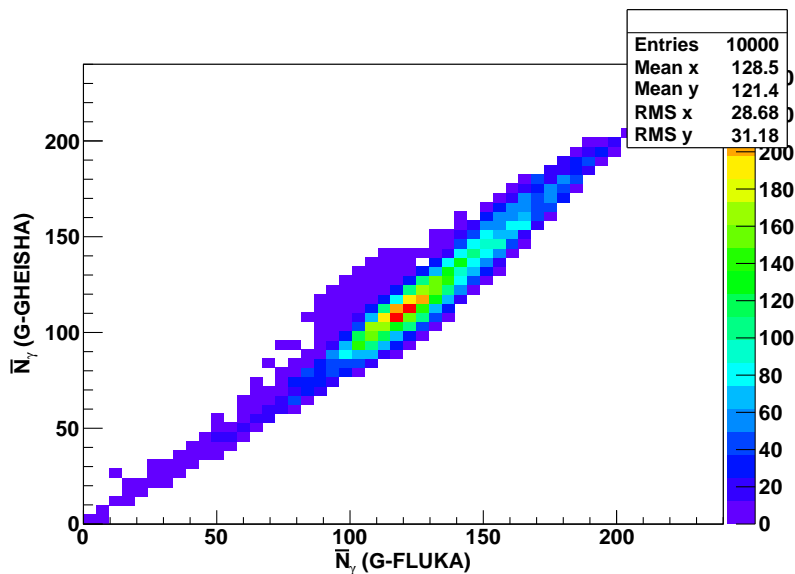


Figure 6.1: Mean number of detected photons \bar{N}_γ from hadronic showers with $E_h = 10$ GeV. Each Cherenkov photon is weighted according to its detection probability (see Sec. 6.6). In total, 10000 hadronic showers extracted from ν_μ CC interactions are simulated 1000 times with G-FLUKA (x -axis) and G-GHEISHA (y -axis). Light yields are averaged over all iterations of the same hadronic final state.

An event-by-event comparison of the light yield of hadronic showers simulated using G-GHEISHA and G-FLUKA, which are employed within GENSHWR, is shown in Fig. 6.1 for hadronic showers with $E_h = 10$ GeV. The resulting distributions of the mean number of detected photons look very similar. G-FLUKA shows on average a $\sim 6\%$ higher light yield than G-GHEISHA. Similarly, about $\sim 13\%$ less fluctuations in the light yield are found for G-FLUKA than for G-GHEISHA. For smaller energies, less discrepancy is found. Differences are found to be larger for simulations of single charged pions than for entire hadronic showers, because the light yield from the electromagnetic component (e, γ, π^0) in hadronic showers is identical between both simulation packages. Fig. 6.2 shows a comparison of

the light yield from π^- when using G-GHEISHA and G-FLUKA. G-FLUKA shows on average a $\sim 18\%$ higher light yield and about $\sim 26\%$ less fluctuations than G-GHEISHA. Fig. 6.3 shows a comparison of the light yield ratio between hadronic and electromagnetic showers as a function of energy for all three different hadron tracking simulation tools. The light yield ratio is fitted with the simple phenomenological model introduced in Eq. 4.8. As GEANT 4 employs internally a model that is based on the GHEISHA package of GEANT 3.21, a nearly identical light yield for these two simulation tools is observed. Nevertheless, this verifies that both simulation packages (KM3Sim and GENSHWR) have a compatible implementation of Cherenkov light production using GEANT-based simulation tools.

As the packages G-GHEISHA and G-FLUKA are available for many years, they have also been compared by others. A useful comparison of these two simulation packages among each other and experimental data was performed in [155].

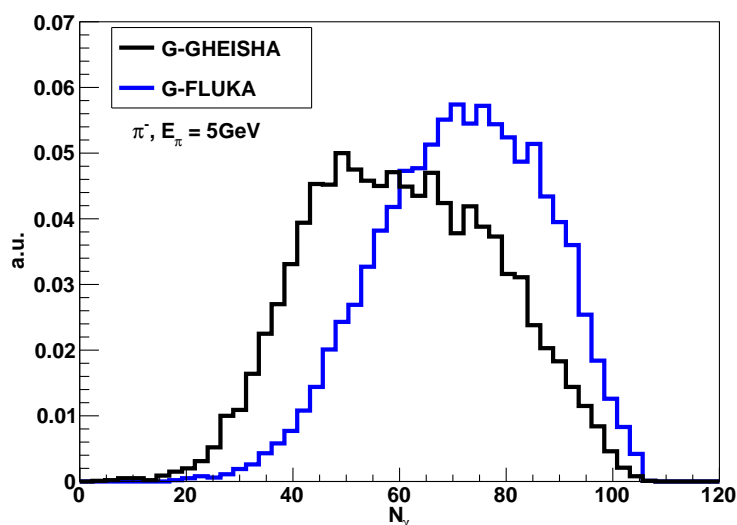


Figure 6.2: Mean number of detected photons \overline{N}_γ from π^- with $E_\pi = 5$ GeV. Each Cherenkov photon is weighted according to its detection probability (see Sec. 6.6). In total, 10000 pions are simulated with G-FLUKA (blue) and G-GHEISHA (black).

6.3 Benchmark detector

The geometry of the benchmark detector used in the simulations follows mostly the detector design described in Sec. 5. It consists of 115 detection string arranged in a circular pattern of radius ~ 106 m, as shown in Fig. 5.4 (left). Each string host 18 DOMs with 6 m vertical spacing between adjacent DOMs. The first DOM is 50 m above the seabed, which is at 2450 m depth. In total, a volume of about 3.6×10^6 m³ (equivalent to ~ 3.7 Mt of seawater) is instrumented.

Optical properties of seawater as described in [156], which is based on the data from [125] for ‘Capo Passero’, are assumed. These optical properties are also shown in Sec. 8.1.

Further details on the PMT and DOM characteristics used in the simulations can be found in Appendix A.1.

6.4 Implementation of different detector configurations

The different investigated detector configurations have the same footprint as the benchmark detector, but different vertical spacings between adjacent DOMs: 6 m, 9 m, 12 m and 15 m.

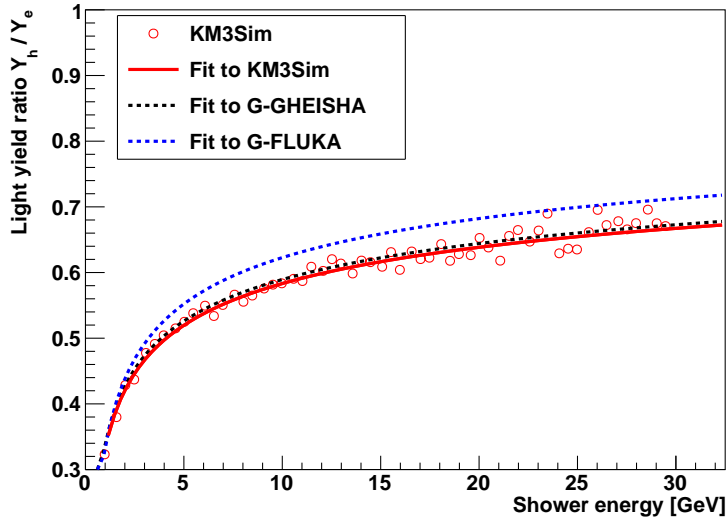


Figure 6.3: Light yield ratio Y_h/Y_e of hadronic showers relative to electromagnetic showers of the same energy. For simulations using G-GHEISHA (black dashed) and G-FLUKA (blue dashed) from GEANT 3.21, the fits from Fig. 7.10 are shown. For simulations using GEANT 4 employed in KM3Sim, data points (red) and the fitted function (red solid) are shown. Eq. 4.8 is used as fit function.

For all configurations, the same simulations as for the benchmark detector (6 m vertical spacing) are used. Different vertical spacings are achieved by masking parts of the detector. For the detector configuration with 9 m vertical spacing, every third DOM on each detection string is masked. In order to make the masked detector as homogeneous as possible, the strings are masked in three different schemes (1st scheme: masking DOM 1, 4, ...; 2nd scheme: masking DOM 2, 5, ...; and 3rd scheme: masking DOM 3, 6, ...). Neighboring strings use different masking schemes. Similar masking procedures are applied for detector configurations with 12 m and 15 m vertical spacing between DOMs.

Doing so the instrumented volume stays the same for all detector configurations, but the DOM density changes. In order to compare the effective volume of the different detector configurations assuming the same number of DOMs for each vertical spacing, the effective volumes of the masked detectors are scaled accordingly (factor of 1, 1.5, 2, 2.5).

This masking procedure of course overestimates the negative effect of events which are not fully contained, because the surface-to-volume ratio for the masked detector configuration is larger than it would be for a full detector with 18 DOMs per detection string. Therefore, the evaluated detector performance is a conservative estimate. Differences in effective volumes and reconstruction resolutions between fully contained events and all events including those that are only partially contained can be inferred from the comparisons in Sec. 12.5.1 and Sec. 12.5.2.

6.5 Event generation for full detector simulation

For the simulation of the benchmark detector, neutrino and antineutrino events are generated with gSeaGen in the energy range from 1 to 100 GeV with an E^{-1} spectrum. These events are weighted³⁸ to reproduce the conventional atmospheric neutrino flux following the ‘Bartol model’ [84]. Atmospheric muon events are generated with MUPAGE. Cherenkov light emission and propagation for neutrino events is simulated using KM3SIM, while for the atmospheric muon events KM3 is used due to runtime constrains.

³⁸ For ν_τ and $\bar{\nu}_\tau$ events, the predicted atmospheric ν_e and $\bar{\nu}_e$ flux is used for weighting.

The PMT electronic is simulated using JTE. For the optical background noise, an uncorrelated single hit rate of 10 kHz per PMT and time-correlated noise on each DOM (500 Hz twofold, 50 Hz threefold, 5 Hz fourfold, 0.5 Hz fivefold) was added. This is a conservative optical background light estimation compared to the rates measured in [139] (8 kHz single, 340 Hz twofold, 30 Hz threefold, 2.7 Hz fourfold). Trigger algorithms and the optimisation of the trigger configuration is discussed in Sec. 11. These simulations are the ‘official’ ORCA simulations, which are also used in the ‘Letter of Intent’ [3].

6.6 Detector-geometry-independent simulations

For the detailed investigation of events induced by GeV-scale neutrino interactions in Sec. 7, Sec. 8 and Sec. 9, different GENSHWR simulations independent of a specific detector geometry are used.

In many of these simulations an idealised ORCA-like detector with an unspecific detector geometry is considered. Such a detector is characterised only by the wavelength-dependent probability of detecting each Cherenkov photon. Each photon is weighted according to its detection probability when it is emitted, such that tracking of individual photons does not have to be performed explicitly. This idea was originally introduced by C. W. James.

Probabilities of Cherenkov photon detection [157]

Ignoring surface effects and self-shadowing, a photon with wavelength λ propagates until it is either absorbed or detected, so that the detection probability $p_{\text{det}}(\lambda)$ is given by:

$$\begin{aligned} p_{\text{det}}(\lambda) &= \frac{b_{\text{det}}(\lambda)}{b_{\text{det}}(\lambda) + b_{\text{abs}}(\lambda)} \\ &\approx \frac{b_{\text{det}}(\lambda)}{b_{\text{abs}}(\lambda)}, \end{aligned} \quad (6.1)$$

where $b_{\text{abs}}(\lambda)$ is the probability of absorption per unit photon path length, and $b_{\text{det}}(\lambda)$ is the probability of detection per unit length. The latter is determined by the detector’s PMT density ρ_{PMT} and the solid-angle-averaged PMT effective area $\bar{A}(\lambda)$:

$$b_{\text{det}}(\lambda) = \rho_{\text{PMT}} \bar{A}(\lambda). \quad (6.2)$$

For the ORCA benchmark detector (see Sec. 6.3), ρ_{PMT} is approximately $\sim 0.015 \text{ PMT/m}^3$. Using this, and the effective area of the KM3NeT PMTs (see Sec. A.1), the probability of detection p_{det} is given in Fig. 6.4.

An equivalent measure for the probability p_{uns} of detecting an unscattered photon (i.e. before being either absorbed or scattered) can be defined similarly to Eq. 6.1:

$$p_{\text{uns}}(\lambda) \approx \frac{b_{\text{det}}(\lambda)}{b_{\text{abs}}(\lambda) + b_{\text{scat}}(\lambda)}, \quad (6.3)$$

where $b_{\text{scat}}(\lambda)$ is the probability of scattering per unit length. In Fig. 6.4, $p_{\text{uns}}(\lambda)$ is also shown.

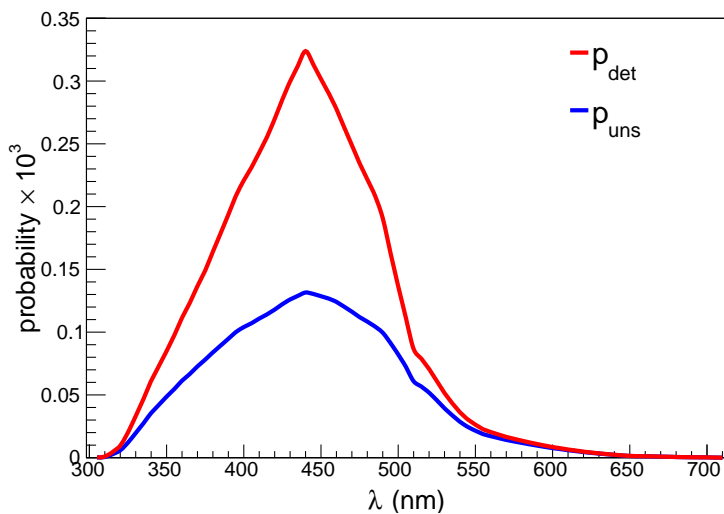


Figure 6.4: Probabilities of detection, p_{det} and p_{uns} , for all photons (i.e. before being absorbed, see Eq. 6.1) and unscattered photons (i.e. before being scattered or absorbed, see Eq. 6.3) as a function of photon wavelength λ . Average PMT density of the ORCA benchmark detector (see Sec. 6.3) and optical properties of seawater described in [156] (shown in Sec. 8.1 for ‘Capo Passero’) are assumed. Figure provided by C. W. James [158].

Part II

Fundamental investigations for ORCA-like detectors

This part investigates the Cherenkov light signatures observed in water/ice-based Cherenkov detectors, aimed at laying the groundwork for the event reconstruction methods developed in Part III of this thesis. Importantly, the studies are independent of the particulars of the KM3NeT/ORCA detector geometry, and several key results apply to other detection media, such as ice. This allows for any future developments, and giving intrinsic limitations on the reconstruction resolutions attainable with this kind of detector.

Most investigations presented in this part have been performed by myself, and are partly published in the ‘Letter of Intent’ [3] of KM3NeT/ORCA. The investigations of intrinsic resolution limitations were performed in collaboration with C. W. James and are currently being prepared for publication [158].

7 Phenomenology of few-GeV electron neutrino events

Few-GeV $\bar{\nu}_e$ CC events constitute a very important event class for the NMH determination with atmospheric neutrinos (see Sec. 3.2.3). In these events, the outgoing electron initiates an electromagnetic shower and the hadronic system develops into a hadronic shower. While the signature of electromagnetic showers show only very little fluctuation, hadronic showers can appear very different depending on the decay modes of individual particles in the shower.

In this section, the properties of hadronic showers are extensively investigated and differences between them and electromagnetic showers are elaborated. These event signature differences in megaton-scale water Cherenkov detectors, such as KM3NeT/ORCA, have not been extensively studied in the literature so far, since existing detectors, such as ANTARES and IceCube/DeepCore, do not have the capabilities to observe these differences due to insufficient photocathode area density. After characterising the kinematics of hadronic showers and the outgoing electrons in $\bar{\nu}_e$ CC interactions in Sec. 7.1, electromagnetic and hadronic showers themselves as well as their Cherenkov light signatures are characterised in detail in Sec. 7.2. Based on these signatures, several aspects of reconstructing $\bar{\nu}_e$ CC events are considered in Sec. 7.3, including possible reconstruction strategies. The shower reconstruction method developed in Sec. 12 is a realisation of one of the discussed strategies and accounts for many of the presented shower characteristics.

As this detailed event signature characterisation is an important groundwork for neutrino event reconstruction in general and in particular for few-GeV $\bar{\nu}_e$ CC events, relevant parts were also presented in the ‘Letter of Intent’ [3]. In the following, parts of the ‘Letter of Intent’ [3], for which I am responsible, are copied in verbatim. Also plots, for which I am responsible for, are labelled ‘KM3NeT’ and copied without further indication.

In the following, the energy E_h and momentum \vec{p}_h of a hadronic shower are defined through four-momentum conservation applied to the neutrino interaction vertex in the laboratory frame:

$$(E_h, \vec{p}_h) = (E_\nu, \vec{p}_\nu) - (E_l, \vec{p}_l). \quad (7.1)$$

where (E_ν, \vec{p}_ν) is the original neutrino four-momentum, and (E_l, \vec{p}_l) the four-momentum of the outgoing lepton. This definition of E_h and \vec{p}_h is chosen because it is most relevant for reconstructing the original neutrino properties.

7.1 Neutrino interaction characterisation

This section describes the relevant neutrino CC interaction characteristics as they are simulated by **gSeaGen** (see Sec. 6.1) with internally using **GENIE** (version 2.8.4). All distributions are very similar for GeV-scale $\bar{\nu}_e$ and $\bar{\nu}_\mu$ CC events, as electron and muon mass are negligible at these neutrino energies. However, the interaction characteristics for ν and $\bar{\nu}$ CC events are very different (see Sec. 2.1.2), and are therefore shown separately.

7.1.1 Interaction mode

The relative contribution of each neutrino interaction mode is shown in Fig. 7.1 as a function of neutrino energy. As already discussed in Sec. 2.1.4, the DIS interaction mode dominates above a few GeV. Differences with predictions by another neutrino event generator shown in Fig. 2.5 are comparatively small and within the uncertainties of neutrino cross section measurements (cf. Sec. 2.1.6).

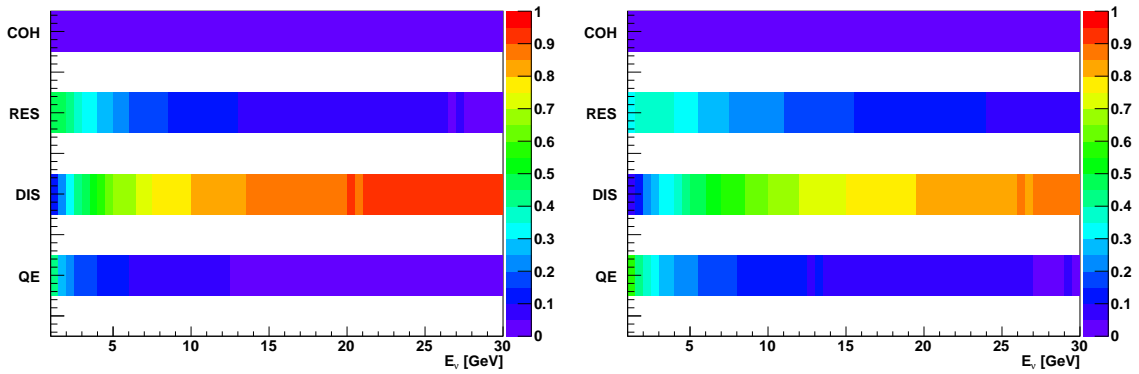


Figure 7.1: Relative contribution of each neutrino interaction mode as a function of neutrino energy E_ν for ν CC (left) and $\bar{\nu}$ CC (right) interactions. Each energy bin is normalised to unity. Interaction modes: quasi-elastic scattering (QE), resonant production (RES), deep inelastic scattering (DIS) and coherent scattering (COH). The COH contribution is below $\lesssim 1\%$ at the relevant energies.

7.1.2 Interaction kinematics

Fig. 7.2 shows the distributions of interaction inelasticity y (or Bjorken y , see Eq. 2.6) as a function of neutrino energy E_ν for ν_μ and $\bar{\nu}_\mu$ CC events separately. For $\bar{\nu}_e$ CC events, the distributions look very similar. At energies below $E_\nu \lesssim 10$ GeV and low y the different strengths of the interaction modes are visible. The average inelasticity is higher for neutrinos ($\langle y \rangle \approx 0.5$) than for antineutrinos ($\langle y \rangle \approx 0.35$). For a better comparability, the y distributions of ν and $\bar{\nu}$ CC events with $E_\nu = 5$ GeV and $E_\nu = 10$ GeV are shown in Fig. 7.3. As DIS dominates at these energies, the y distributions look similar to those to Fig. 2.4 for pure DIS events. The additional structure at $E_\nu \times y \lesssim 1$ GeV is caused by the quasi-elastic and the resonant production modes. Note that the relative differences between ν and $\bar{\nu}$ CC events increases with larger y values.

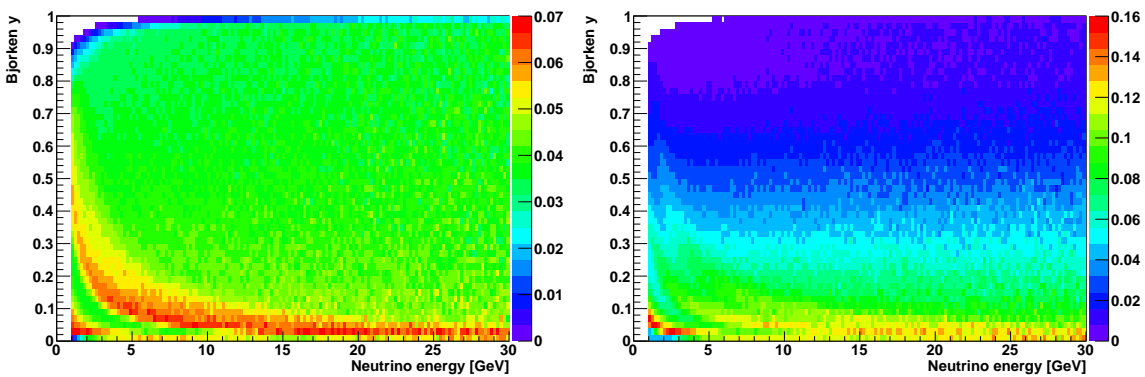


Figure 7.2: Distributions of inelasticity y as a function of neutrino energy for ν_μ CC (left) and $\bar{\nu}_\mu$ CC events (right). The integral of each column of bins in energy is normalised to unity.

The inelasticity y of a neutrino interaction critically determines the interaction kinematics, as can be seen in Fig. 7.4 (left). The scattering angle $\phi_{\nu,l}$ between the incoming neutrino and the outgoing lepton increases with y . Fig. 7.4 (right) shows the median scattering angle $\phi_{\nu,l}$ as a function of neutrino energy and inelasticity. The influence of different interaction modes is visible for $E_\nu \times y \approx 0.3$. The recoil mass is larger for QE than for other interaction modes, leading to larger scattering angles $\phi_{\nu,l}$.

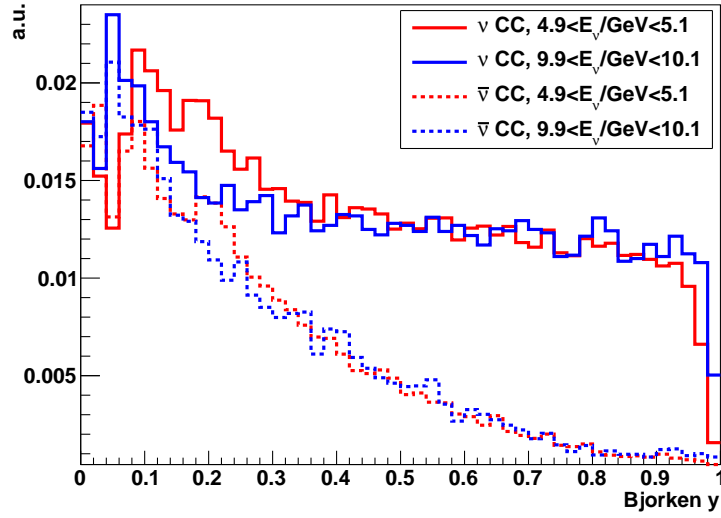


Figure 7.3: Distributions of interaction inelasticity y for ν_μ CC (solid lines) and $\bar{\nu}_\mu$ CC events (dashed lines) with $E_\nu \approx 5$ GeV (red) and $E_\nu \approx 10$ GeV (blue). The cross-section weighted sum of ν_μ and $\bar{\nu}_\mu$ CC events is normalised to unity. The dip in the last bin for $y \rightarrow 1$ is caused by the finite muon mass.

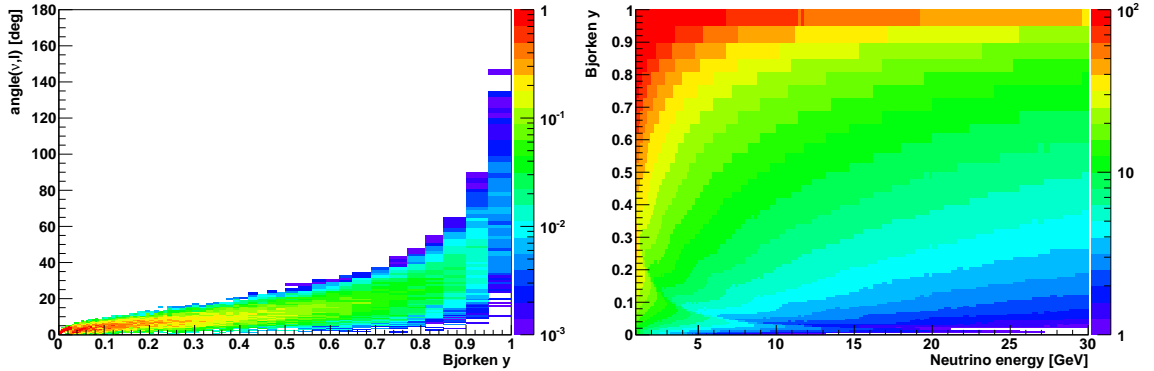


Figure 7.4: Scattering angle $\phi_{\nu,l}$ between incoming neutrino and outgoing lepton versus inelasticity y for ν_μ CC events with $E_\nu = 10$ GeV. The integral of each column of bins in y is normalised to unity (left). Median scattering angle $\phi_{\nu,l}$ in degrees as a function of neutrino energy and inelasticity y (right). For $\bar{\nu}_\mu$ CC events, the distributions look nearly identical.

Fig. 7.5 shows the angle $\phi_{l,h}$ between the outgoing lepton and the hadronic shower. The angle $\phi_{l,h}$ is minimal for $y = 0.5$ with a mean value of roughly 25° for $E_\nu = 10$ GeV. For $y \rightarrow 0$ ($y \rightarrow 1$), the angle between the incoming neutrino and the outgoing hadronic shower (lepton) becomes larger, leading to larger $\phi_{l,h}$. For increasing neutrino energies, the angle $\phi_{l,h}$ becomes smaller.

7.2 Characterisation of electromagnetic and hadronic showers

The relevant characteristics of hadronic showers are described below and are compared to that of electromagnetic showers. Hadronic showers are extracted from $\nu_{e,\mu}$ CC events, if not stated otherwise. Differences with hadronic showers from $\bar{\nu}_{e,\mu}$ CC or $\bar{\nu}$ NC events are discussed. However, the average event signature is very similar for the same shower energy.

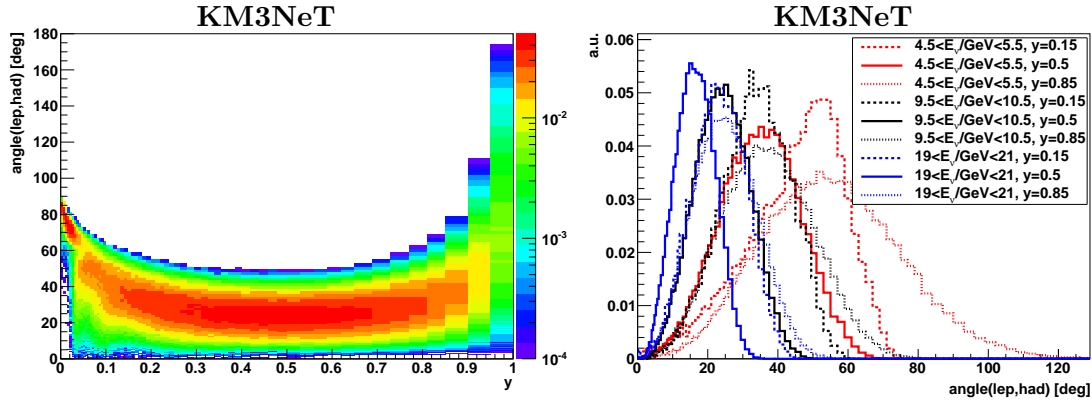


Figure 7.5: Opening angle $\phi_{l,h}$ between the outgoing lepton and the hadronic shower versus inelasticity y in ν_μ CC events with $E_\nu \approx 10$ GeV. The features at $0 < y < 0.2$ are due to different neutrino interaction modes. The integral of each column of bins in y is normalised to unity (left). Distributions of angle $\phi_{l,h}$ in ν_μ CC events for different inelasticities y and neutrino energies ranges (right).

7.2.1 Hadronic shower composition

Each hadronic shower consists of a set of particles, mainly hadrons, emerging from the interaction vertex. The kinetic energy distributions for the different particle species are shown in Fig. 7.6 for $E_h \approx 5$ GeV. The dominant particle species are pions, protons and neutrons. As expected, the contribution of π^+ in ν CC events is very similar to that of π^- in $\bar{\nu}$ CC events. The excess of low-energy protons and neutrons comes from the ‘breakup’ of the nucleus. Their kinetic energies are constrained to about 200 MeV due to the motion of the target nucleon inside the nucleus (see Sec. 2.1.5).

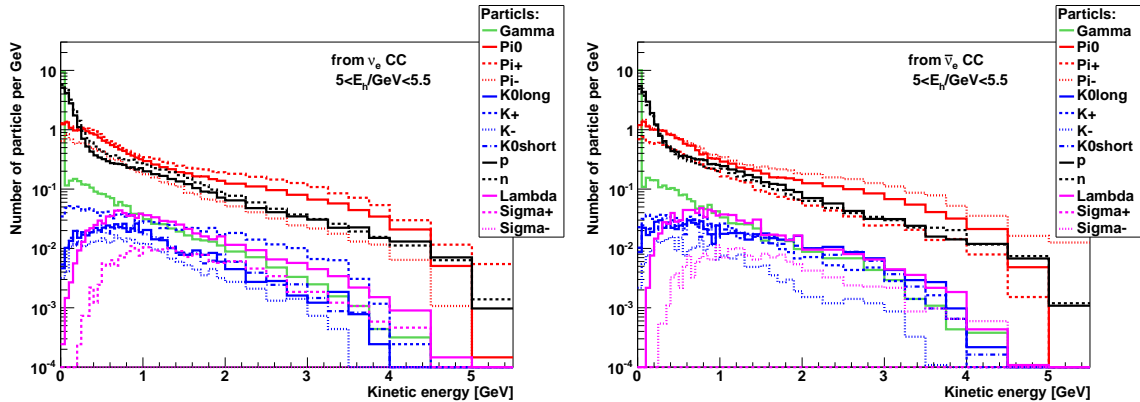


Figure 7.6: Kinetic energy distributions for different particle species in hadronic showers extracted from ν CC (left) and $\bar{\nu}$ CC events (right) with $5 \text{ GeV} < E_h < 5.5 \text{ GeV}$.

7.2.2 Cherenkov light production

In order to characterise the Cherenkov light production, it is sufficient to simulate only the particle shower and calculate the expected Cherenkov photon properties, so tracking of individual photons through the detector medium is not needed. Using the GENSHWR simulation package with G-GHEISHA for hadron tracking (see Sec. 6.1), the emitted photons³⁹

³⁹ For the sake of clarity, in all light yield considerations for hadronic showers the delayed Cherenkov light signal from the electromagnetic showers induced by the electrons produced in muon decays are taken

are weighted according to their detection probabilities in an idealised ORCA-like detector, as described in Sec. 6.6.

Each shower is simulated multiple times (1000 times) with different random number seeds. Variations in the mean properties averaged over different random number seeds correspond to the fluctuations due to different hadronic final states ('hadronic state'), while the total variation in all simulated hadronic showers (different hadronic final states and different random number seeds) is the quadratic sum of both fluctuation sources 'hadronic state' and 'propagation' (see Sec. 4.4).

The longitudinal and transverse light emission profiles of electromagnetic and hadronic showers are shown in Fig. 7.7 and Fig. 7.8. For the energies of interest, the brightest point

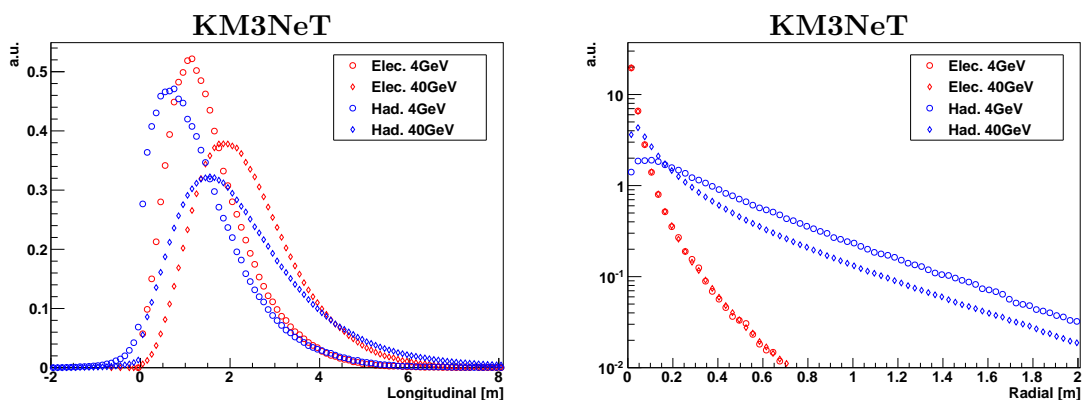


Figure 7.7: Light emission profiles of electromagnetic showers from electrons (red) and hadronic showers (blue) with 4 GeV and 40 GeV energy, depicted in shower direction (left, longitudinal) and perpendicular to the shower direction (right, transverse).

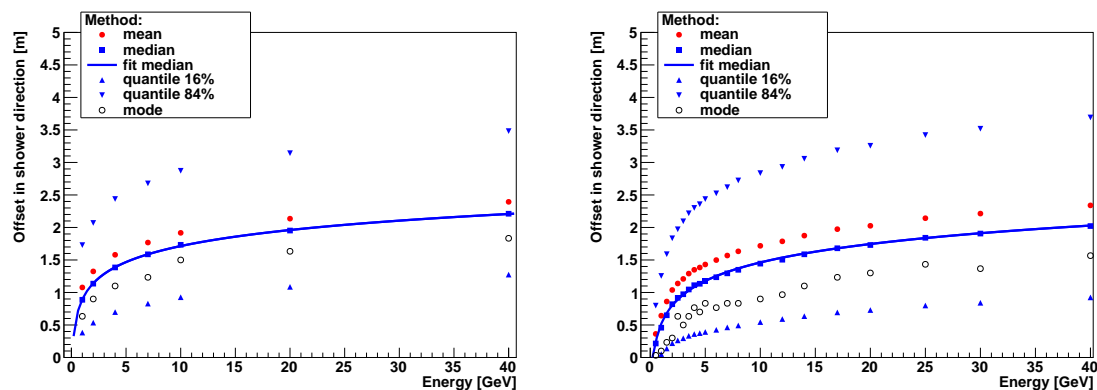


Figure 7.8: Light emission profiles characterised by the mean (red dots), median (blue squares), 16% and 84% quantiles (blue triangles) and mode (black circles) as a function of shower energy for electromagnetic showers from electrons (left) and hadronic showers (right). A fit to the medians using Eq. 7.3 is also shown (blue line).

into account. It might make more sense to discard these photon signal, as it is superimposed by optical noise in seawater. However, this delayed light contributes on average only a few percent to the total light yield in hadronic showers. For example, hadronic showers with $E_h = 5$ GeV show on average a reduced light yield of about 0.55 compared to electromagnetic showers (see Fig. 7.10) and produce on average ~ 2.5 muons (see Tab. 7.2), which initiate a ~ 40 MeV electromagnetic shower each when they decay, resulting in a $\sim 4\%$ light yield contribution.

of a shower is offset roughly 1–2 m in the shower direction. The transverse extension of hadronic and electromagnetic showers is negligible compared to the longitudinal. The longitudinal extension of the showers increases with $\log(E)$ and the median longitudinal emission position $\text{med}[L]$ is well described by:

$$\text{med}[L]_e = 0.90 + 0.36 \ln(E/\text{GeV}), \quad (7.2)$$

$$\text{med}[L]_h = 0.52 + 0.41 \ln(E/\text{GeV}). \quad (7.3)$$

For electromagnetic showers, this is in agreement (within 10%) with the findings of [112] at much higher target energies (cf. Sec. 4.3).

The expected number of detected Cherenkov photons N_γ in an idealised ORCA-like detector with the instrumentation density of the ORCA benchmark detector (see Sec. 6.6) for electrons as well as hadronic showers with $E_e = E_h = 5 \text{ GeV}$ is shown in Fig. 7.9. For electrons, the total number of detected photons is on average $N_e = 20.8 \times E_e/\text{GeV}$ with very few fluctuations. Hadronic showers produce less light than electromagnetic showers and show large fluctuations for the reasons discussed in Sec. 4.4. These intrinsic fluctuations are further discussed in Sec. 9 and limits imposed on the energy and direction resolution are deduced. Differences between hadronic showers extracted from ν CC, $\bar{\nu}$ CC and NC events are below a few percent for energies above $E_h \gtrsim 2 \text{ GeV}$ ⁴⁰.

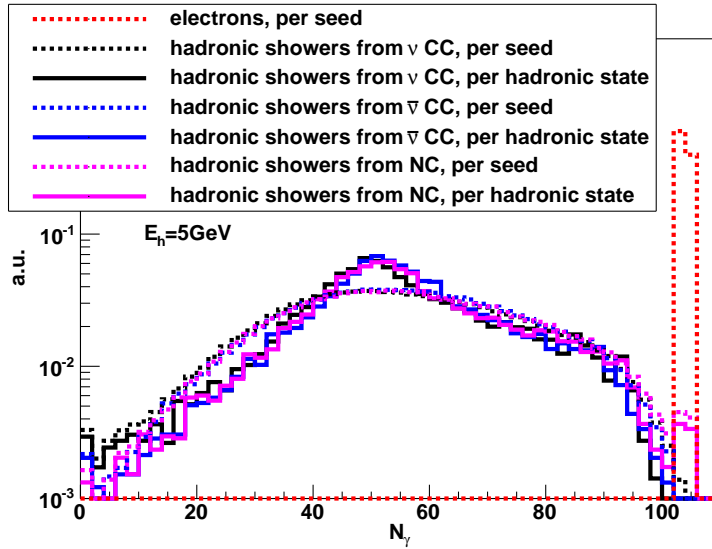


Figure 7.9: Expected number of detected photons N_γ for electrons (red) as well as hadronic showers extracted from ν CC (black), $\bar{\nu}$ CC (blue) and NC events (purple) with $E_e = E_h = 5 \text{ GeV}$. Distributions are shown for all simulated events with different random number seeds for particle propagation (dashed) and averaged over all iterations of the same hadronic final state (solid).

Fig. 7.10 shows the ratio of light yield produced by hadronic showers and electromagnetic showers as a function of shower energy. The light yield ratio f_h is well described by Eq. 4.8 and a fit yields:

$$f_h(E_h) = 1 - 0.681 \left(\frac{E_h}{0.863 \text{ GeV}} \right)^{-0.207}. \quad (7.4)$$

⁴⁰ Below $E_h \lesssim 2 \text{ GeV}$, the light yield from hadronic showers extracted from ν CC events is slightly reduced compared to those from $\bar{\nu}$ CC and NC events, because the positive charge excess in the nuclei (protons) leads due to charge conservation to more π^+ compared to π^0 in the hadronic final state resulting in a smaller light yield, as shown in Fig. 7.11. This difference in charged pion production becomes also visible in the number of produced muons in hadronic showers at these energies (see Sec. 7.2.3).

A $\sim 6\%$ larger light yield is found for G-FLUKA than for G-GHEISHA. The light yield from both hadron tracking models is compared on an event-by-event basis in Fig. 6.1.

The obtained values for the light yield ratio in Fig. 7.10 are in agreement with the results of [121] shown in Fig. 4.3 (left), however, the fitted parameters in the function f_h differ. This discrepancy might be caused by the significantly different target energy ranges.

As expected, the light yield for a given hadronic final state depends strongly on the electromagnetic component (e^\pm , γ and mainly π^0) in the set of final-state particles, as can be seen from Fig. 7.11.

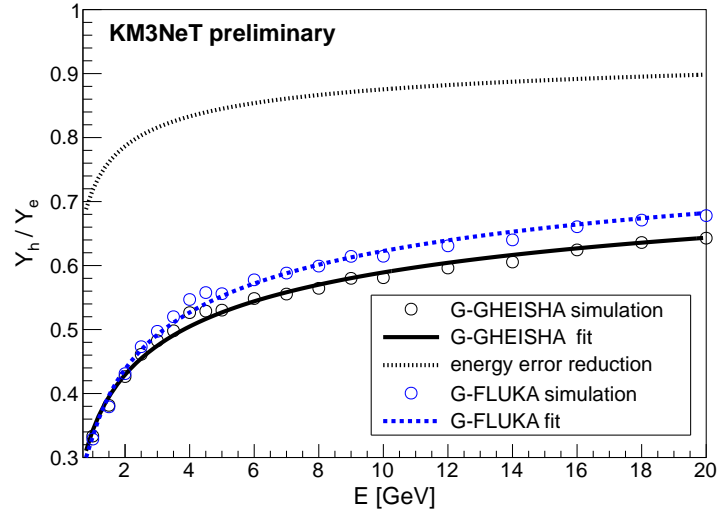


Figure 7.10: Light yield ratio Y_h/Y_e of hadronic showers extracted from ν CC events relative to electromagnetic showers of the same energy, showing data points and the fitted function. Simulations using G-GHEISHA (black) and G-FLUKA (blue) are shown. Also shown is the resulting reduction in relative reconstructed energy errors (see Sec. 9.4.1) compared to relative N_γ fluctuations for G-GHEISHA (black dotted line).

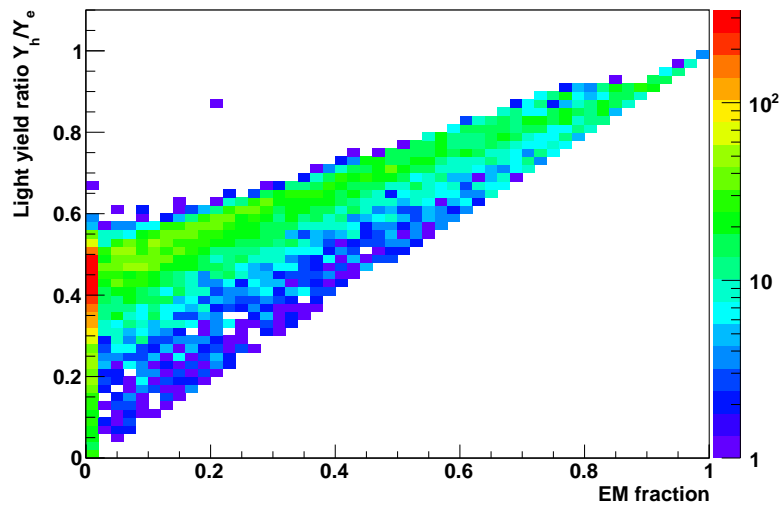


Figure 7.11: Light yield ratio Y_h/Y_e of hadronic and electromagnetic showers versus the fraction of electromagnetic component (sum of energy of all e^\pm , γ and π^0) in the set of final-state particles for hadronic showers with $E_h = 5$ GeV. For each hadronic final state, the light yield is averaged over 1000 simulation iterations.

Another interesting quantity is the ‘beamness’ B of the Cherenkov light emitted by showers. A convenient measure for this is the ratio of the magnitude of the vectorial sum of all emitted photon directions $\vec{\gamma}$ weighted by their wavelength-dependent detection probability for unscattered⁴¹ photons p_{uns} (Eq. 6.3) over the sum of all unscattered photon detection probabilities:

$$B = \frac{|\sum_i (\vec{\gamma}_i p_{\text{uns}})|}{\sum_i (|\vec{\gamma}_i| p_{\text{uns}})}. \quad (7.5)$$

The denominator is the number of detected unscattered photons. A literally beamed emission (all photon collinear) corresponds to $B = 1$, while an isotropic emission corresponds to $B = 0$. For practical reasons, B is calculated from the track segments producing Cherenkov light within the shower instead of the Cherenkov photons themselves⁴².

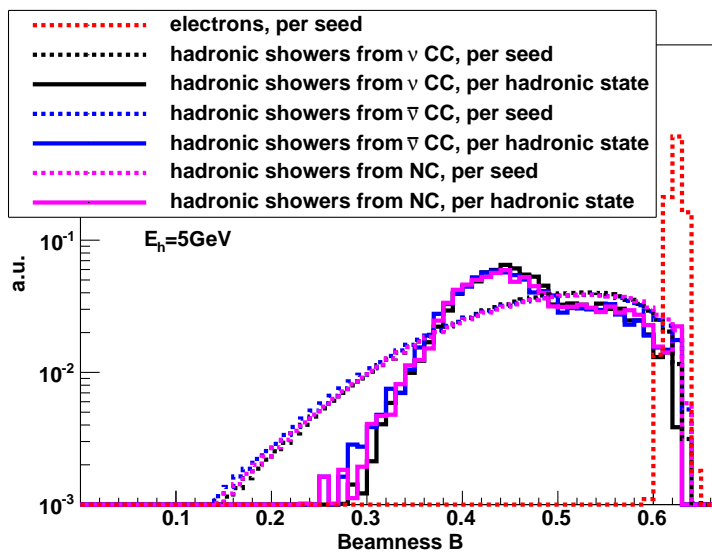


Figure 7.12: Beamness B (Eq. 7.5) for electrons (red) as well as hadronic showers extracted from ν CC (black), $\bar{\nu}$ CC (blue) and NC events (purple) with $E_e = E_h = 5$ GeV. Distributions are shown for all simulated events with different random number seeds for particle propagation (dashed) and averaged over all iterations of the same hadronic final state (solid). The bump at $B \approx 0.44$ is caused by events with no electromagnetic component in the set of final-state particles, cf. Fig. 7.14.

Fig. 7.12 shows the beamness B for electrons and hadronic showers with $E_{e,h} = 5$ GeV. Electrons show (nearly) constant beamness of $B \approx 0.624$. This value is the integral of the effective angular light distribution in Fig. 4.2, as the mean photon direction is (nearly) collinear to the initial electron direction. Hadronic showers show a broader distribution with a lower mean value ($B \approx 0.47 \pm 0.10$ for $E_h = 5$ GeV) than electrons due to the space angles between the different initial particle directions. The maximal reachable beamness for hadronic showers is that of electrons. As in the case of light yield, differences between hadronic showers extracted from ν CC, $\bar{\nu}$ CC and NC events are negligible for $E_h \gtrsim 2$ GeV. The mean and RMS of the B distributions are shown in Fig. 7.13 as a function of shower

⁴¹ Here, unscattered photons are used, because they maintain information on their emission direction.

⁴² Using the number of emitted photons $N_i(\lambda)$ and the Cherenkov angle $\theta_i^{\text{Ch}}(\lambda)$, which both depend on the photon wavelength λ , associated to each particle track segment i as well as its direction d_i , the beamness B is approximated by:

$$B = \frac{|\sum_i \sum_\lambda p_{\text{uns}} \vec{d}_i N_i \cos(\theta_{\text{Ch}})|}{\sum_i \sum_\lambda p_{\text{uns}} |\vec{d}_i| N_i \cos(\theta_{\text{Ch}})}. \quad (7.6)$$

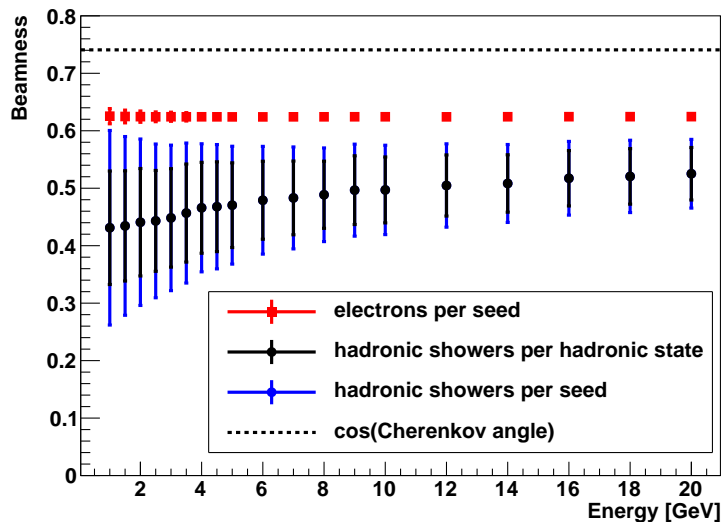


Figure 7.13: Mean beamness B for electrons (red) and hadronic showers (black) as a function of energy. Error bars represent the RMS for all simulated events (black) and averaged over all iterations of the same hadronic final state (blue). For comparison, $\cos(\theta_{\text{Ch}}) \approx 0.74$ is also shown (black dashed line).

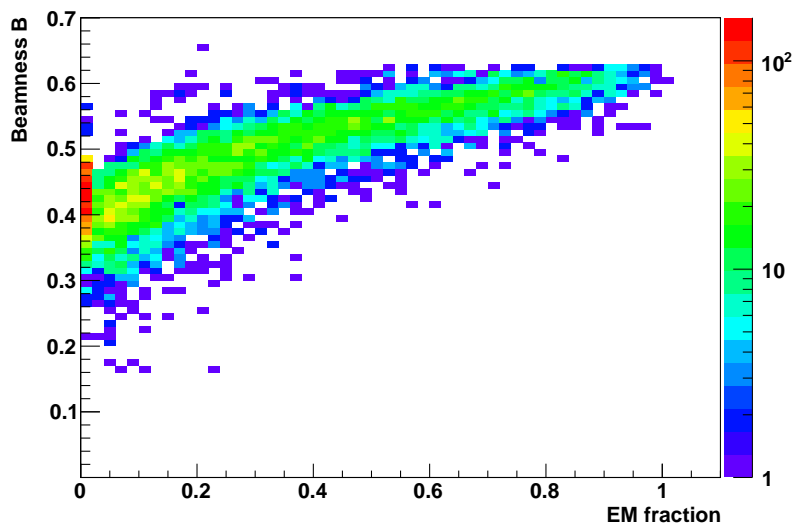


Figure 7.14: Beamness B versus fraction of electromagnetic component (sum of energy of all e^\pm , γ and π^0) in the set of final-state particles for hadronic showers with $E_h = 5$ GeV. For each hadronic final state, the light yield is averaged over 1000 simulation iterations.

energy. As expected, the beamness B for a given hadronic final state is also strongly correlated with the electromagnetic component (e^\pm , γ and mainly π^0) in the set of final-state particles, as shown in Fig. 7.14.

7.2.3 Muons from hadronic showers

Most muons in hadronic showers are produced via charged pions (and to a smaller amount via charged kaons). A significant contribution of muons with path lengths in excess of the hadronic shower extension, i.e. with energies above ~ 1 GeV, could complicate and probably

deteriorate the event classification capabilities needed for the NMH determination (see Sec. 3.2.4). However, as shown in the following, GeV-scale muons from hadronic showers affect only about $\sim 1\%$ of the events. For this study, the GENSHWR simulation package with G-GHEISHA for hadron tracking is used.

In Fig. 7.15 the Cherenkov photon emission positions along and perpendicular to the hadronic shower direction are shown for simulated hadronic showers with $E_h \approx 5$ GeV and $E_h \approx 20$ GeV. Each Cherenkov photon is weighted with its wavelength-dependent detection probability (see Sec. 6.6). In total, 3400 (4000) hadronic showers extracted from ν CC events are superimposed. For both shower energies, only a few muon tracks can be seen that emit light significantly beyond the hadronic shower extension.

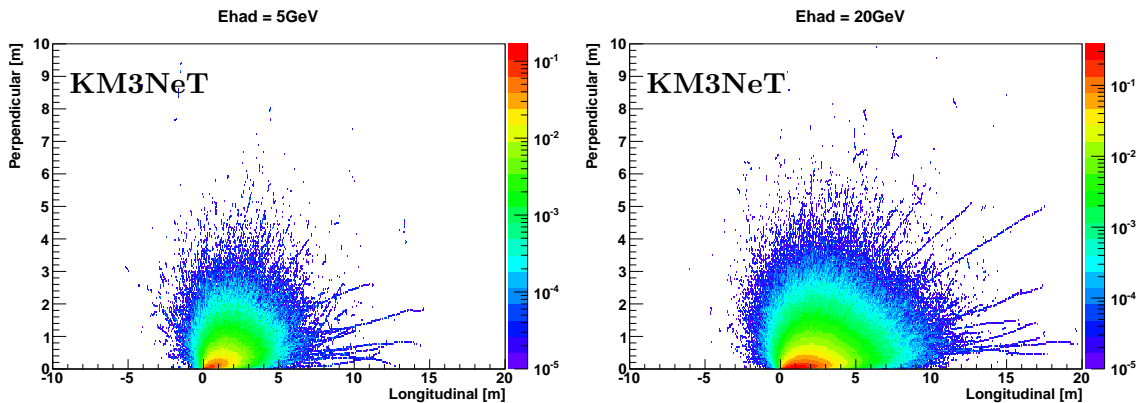


Figure 7.15: Simulated Cherenkov photon emission positions along and perpendicular to the direction of hadronic showers extracted from ν CC events. Left: 3400 superimposed hadronic showers with $E_h \approx 5$ GeV. Right: 4000 superimposed hadronic showers with $E_h \approx 20$ GeV.

In order to study the muon production from charged pions in greater detail, 10000 charged pions with energies of $E_\pi = 2, 5, 10$ GeV have been simulated in seawater. Pions with energies in the GeV range will likely interact before they decay, as the hadronic interaction length for pions in water is approximately ~ 1 m. The mean number of muons $\langle N_\mu \rangle$ and the fraction of simulated events with at least one muon $f_{\mu \geq 1}$ are summarised in Tab. 7.1. The energy spectra and cumulative energy distributions of the most energetic muon are shown in Fig. 7.16. For all three pion energies, the fraction of events producing a muon with more than 1 GeV (2 GeV) is below 2% (1%).

Simulation	$\langle N_\mu \rangle$	$f_{\mu \geq 1}$
π^+ 10 GeV	2.79	0.96
π^+ 5 GeV	1.44	0.84
π^+ 2 GeV	0.93	0.73
π^- 10 GeV	2.22	0.89
π^- 5 GeV	0.91	0.61
π^- 2 GeV	0.42	0.38

Table 7.1: Mean number of muons $\langle N_\mu \rangle$ and fraction of simulated pions producing at least one muon $f_{\mu \geq 1}$.

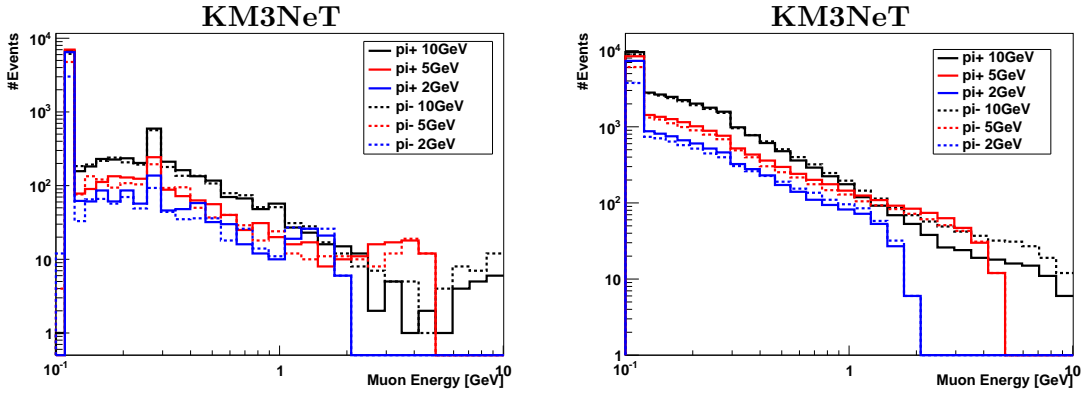


Figure 7.16: Energy spectra (left) and cumulative energy distributions (right) of the most energetic muon from simulated charged pions with energies of $E_\pi = 2, 5, 10$ GeV. In total, 10000 events for each pion energy are simulated. The peak visible at $E_\mu \approx 250$ MeV is due to the decay (at rest) of kaons produced in pion-induced hadronic interactions.

The number of produced muons in hadronic showers might also be interesting for event reconstruction purposes. As shown before, these muons themselves are usually below their Cherenkov threshold ($E_{\text{th}}^\mu \approx 157$ MeV) and are therefore invisible to Cherenkov detectors. Each muon eventually decays ($\tau \approx 2.2 \mu\text{s}$) producing an electron ($E_e \approx 40$ MeV) that initiates an electromagnetic shower. Although the photosensor density of the planned ORCA detector might not be sufficient to distinguish these delayed electrons from random background noise (on average ~ 1 detected photon per muon decay for the ORCA benchmark detector), more-densely instrumented detectors might be able to efficiently do so. Fig. 7.17 shows the number of muons produced in hadronic showers with $E_h = 1, 2, 5, 10$ GeV that are extracted from ν CC, $\bar{\nu}$ CC and NC events. The mean number of muons $\langle N_\mu \rangle$ are summarised in Tab. 7.2.

For energies below a few GeV, hadronic showers extracted from ν CC events have a significantly higher probability to produce a muon than hadronic showers extracted from $\bar{\nu}$ CC and NC events. This is caused by the positive charge excess in the nuclei (protons), which due to charge conservation leads to more produced π^+ in the hadronic final state, and leads to a higher probability for π^- to get absorbed during propagation than for π^+ . This feature is for example exploited in Super-Kamiokande to separate ν and $\bar{\nu}$ events on a statistical basis [93]. For energies above a few GeV, the muon multiplicity is very similar in all three hadronic shower types. Fig. 7.18 shows the number of produced muons in hadronic showers with $E_h = 5$ GeV versus their light yield. Larger light yields come along with less produced muons, as the light yield is strongly correlated with the electromagnetic component in the hadronic showers (see Fig. 7.11), which does not produce any muons.

E_h	Hadronic showers extracted from		
	ν CC	$\bar{\nu}$ CC	NC
10 GeV	4.04	3.34	3.66
5 GeV	2.44	1.80	2.08
2 GeV	1.27	0.68	0.93
1 GeV	0.75	0.19	0.38

Table 7.2: Mean number of muons $\langle N_\mu \rangle$ in simulated hadronic showers.

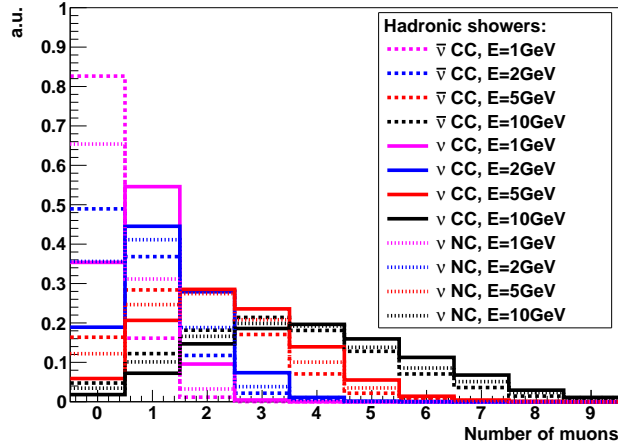


Figure 7.17: Number of muons produced in hadronic showers with $E_h = 1, 2, 5, 10$ GeV that are extracted from ν CC (solid), $\bar{\nu}$ CC (dashed) and ν NC (dotted) events. For each energy, 10000 different hadronic final states are simulated.

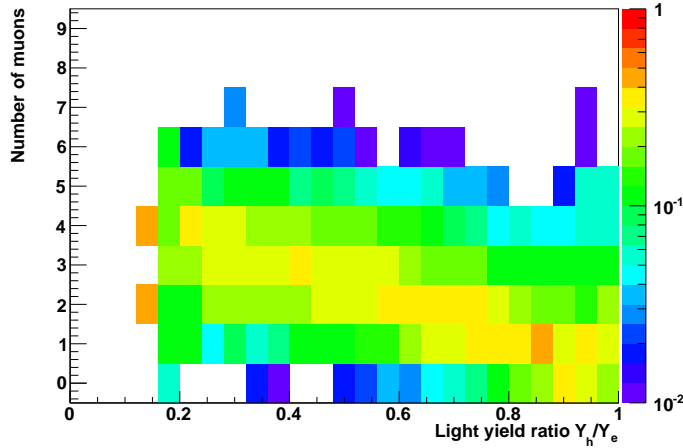


Figure 7.18: Number of muons produced versus light yield ratio Y_h/Y_e for hadronic showers with $E_h = 5$ GeV that are extracted from ν CC events. In total, 10000 different hadronic final states are simulated. Each light-yield-ratio bin is normalised to unity.

7.2.4 Detected light characteristics

In the following, Cherenkov photons are generated as well as tracked through seawater, taking into account absorption and scattering. In order to have sufficient photon statistics also for large photon path lengths, photons are not explicitly absorbed, but they are weighted according to the probability of absorption before being detected. Simulations are performed with the **GENSHWR** simulation package and hadronic showers are extracted from ν CC events. Photons are recorded either when traversing shells with radii of 10 m, 20 m, 30 m, 40 m, 50 m, 70 m and 100 m around the shower event or when traversing small spheres with 21.6 cm radii (DOM sphere), which are located on those shells. The initial shower vertex position is shifted according to Eq. 7.3 opposite to the shower direction, so that the expected brightest point is located at the centre of the photon-recording shells. For each recorded photon, the average detection probability is calculated from its traveled distance and the incident angle on the DOM sphere taking into account the average coverage of the DOM surface with photocathode area and the PMT quantum efficiencies.

Due to the small extension of electromagnetic and hadronic showers (few metres) and the favourable optical properties of seawater (large scattering length and small scattering angles), many photons arrive at nearly the same time and with a small time residual t_{res} :

$$t_{\text{res}} = t_{\text{hit}} - t_{\text{vtx}} - d/c_{\text{water}}, \quad (7.7)$$

where d is the distance between the shower vertex position \vec{x}_{vtx} and the photon detection position, t_{vtx} is the vertex time, t_{hit} is the photon detection time and c_{water} is the speed of light in water (see Sec. 4.5). The vertex position and time are here defined as the brightest point and its corresponding time in the shower evolution and not by the neutrino interaction itself.

The t_{res} distributions for electromagnetic and hadronic showers are shown in Fig. 7.19. Even at distances of 100 m (roughly the height of the benchmark detector) most of the photons arrive within a few nanoseconds. Additionally, the arrival time is (to first order) independent of the angle θ between shower direction and the vector from the vertex to the photon detection position, as can be seen in Fig. 7.20.

The averaged angular light distributions for photons with $t_{\text{res}} < 20$ ns from electromagnetic and hadronic showers with $E_e = E_h = 5$ GeV are shown in 7.21. For both shower types, the probability to detect at least one photon on a DOM (DOM-hit probability) is maximal at the Cherenkov angle of $\theta = 42^\circ$, but it is more peaked for electromagnetic

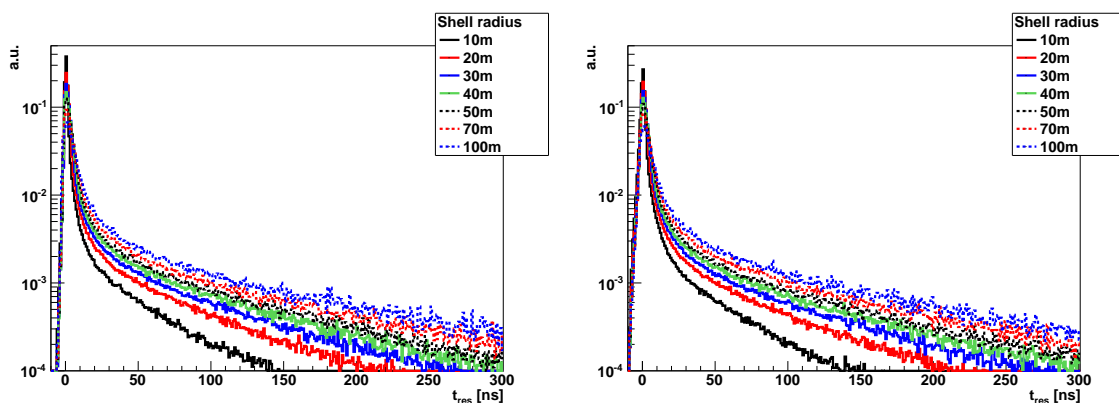


Figure 7.19: Distributions of time residuals t_{res} for photons from electromagnetic (left) and hadronic showers (right) with $E_e = E_h = 5$ GeV. Photons are recorded on shells with different radii. Distributions are averaged over 1000 showers and normalised to unity.

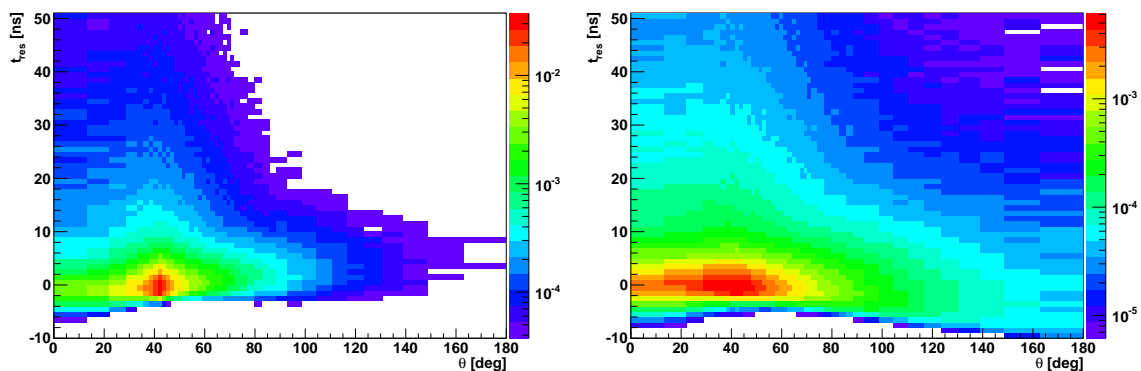


Figure 7.20: Photon detection probability as a function of time residual t_{res} and angle θ between shower direction and the vector from the vertex to the photon detection position for electromagnetic (left) and hadronic shower (right) with $E_e = E_h = 5$ GeV at a distance of 50 m away from the vertex.

than for hadronic showers due to the angular spread between different particles in hadronic showers. Note that the light distribution for a single hadronic shower event will not be as smooth as shown in these plots due to the distinct Cherenkov cones from each individual particle (cf. Fig. 4.4). Fig. 7.22 shows the distribution of expected number N_γ^{DOM} of detected photons per DOM under different angles θ . For $\theta = 42^\circ$, the N_γ^{DOM} distribution for electromagnetic showers is well described by a Poissonian (i.e. no fluctuations at the source), while for hadronic showers it looks like an exponential spectrum. This exponential spectrum is basically the kinetic energy spectrum of single particles in the hadronic shower (cf. Fig. 7.6). If a DOM lies on a Cherenkov cone, N_γ^{DOM} is to first order proportional to the particle's kinetic energy. If a DOM is far off any Cherenkov cone, then only scattered light (Poisson statistics) can be seen, explaining the Poisson-like feature at $N_\gamma^{\text{DOM}} \rightarrow 0$.

As most of the photons reach the DOMs on nearly a straight path (almost never large angle scattering, see Fig. 8.2), photons hardly ever hit the DOM backside. This is shown in Fig. 7.23. This feature can be exploited for the suppression of noise, which is isotropically distributed on the DOM.

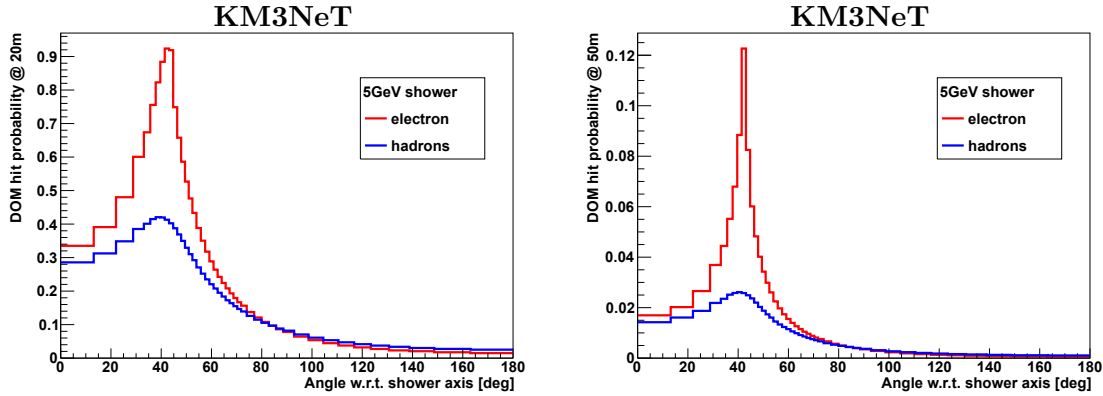


Figure 7.21: DOM-hit probability (average probability to detect at least one photon in an entire multi-PMT optical module) at a distance of 20 m (left) and 50 m (right) away from showers with $E_e = E_h = 5$ GeV as a function of the angle θ between shower direction and the vector from vertex to DOM centre. A cut on the photon arrival time with $t_{\text{res}} < 20$ ns is applied.

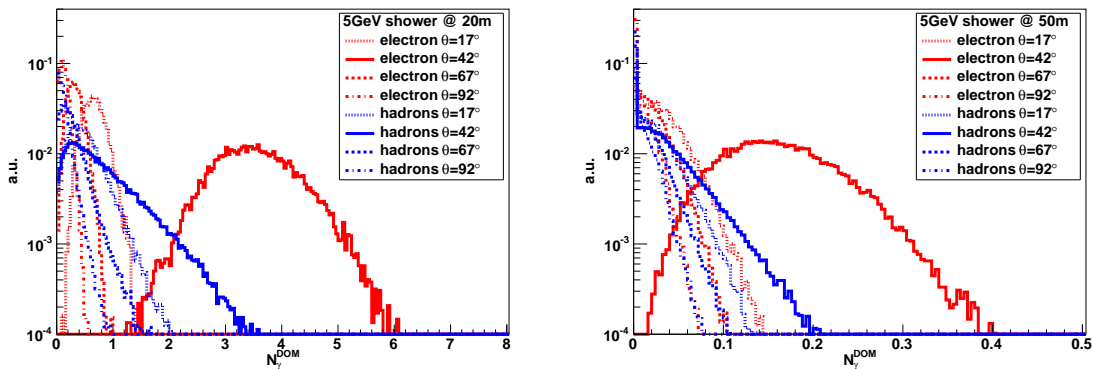


Figure 7.22: Distributions of expected number N_γ^{DOM} of detected photons per DOM at a distance of 20 m (left) and 50 m (right) away from showers with $E_e = E_h = 5$ GeV for different angle θ between shower direction and the vector from vertex to DOM centre.

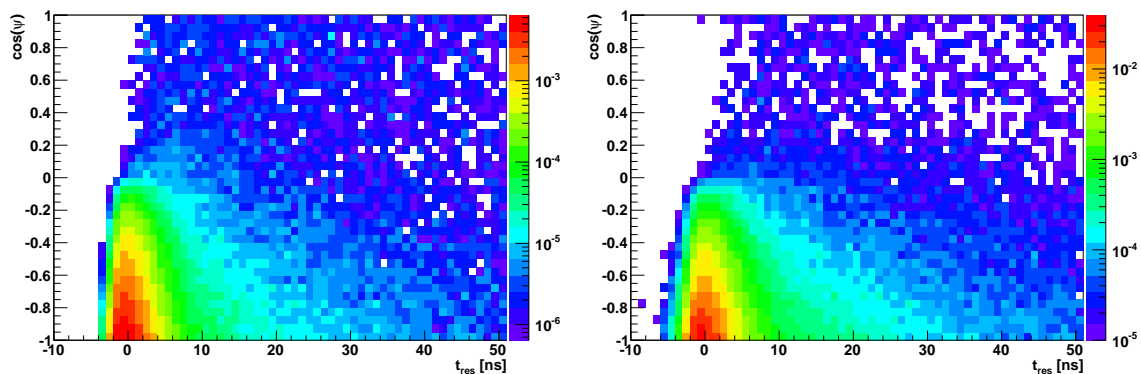


Figure 7.23: Photon detection probability as a function time residual t_{res} and angle ψ between the vector normal to the DOM surface and the vector from vertex to DOM centre for DOMs under the Cherenkov angle $\theta = 42^\circ$ and at a distance of 50 m away from electromagnetic (left) and hadronic showers (right) with $E_e = E_h = 5$ GeV.

7.3 Considerations for event reconstruction

7.3.1 Sensitivity to interaction inelasticity

Electromagnetic showers induced by single electrons and hadronic showers with energies of a few-GeV show different Cherenkov light emission characteristics and signatures in the detector, as discussed above. Due to the large scattering length in seawater, these differences are conserved over sufficiently large distances, so that information from a large detector volume can contribute to the discrimination between both shower types. In $\bar{\nu}_e$ CC events, in which both an outgoing electron and a hadronic shower are present at the same time and the Cherenkov signals are partly overlapping, the angular separation $\phi_{e,h}$ (see Fig. 7.5) of both showers can help to distinguish between them. This can make an estimation of the interaction inelasticity y in $\bar{\nu}_e$ CC events feasible. Additionally, it might allow for a partial separation of ν_e CC, $\bar{\nu}_e$ CC and $\bar{\nu}$ NC events on a statistical basis.

However, with an ORCA-like detector⁴³ it seems impossible to distinguish a shower induced by a single electron from a shower induced by a single hadron, since both resulting Cherenkov light cones are of similar intensity for the same particle energy. This can for example be seen in the simulated example event in Fig. 4.4 (right), in which the electron ($E_e = 4.77$ GeV) and the pion ($E_\pi = 3.71$ GeV) induce Cherenkov cones of similar intensity.

The most intense Cherenkov cone in $\bar{\nu}_e$ CC events is seen in most cases from the electron, as can be inferred from the distributions of the inelasticity parameter y in Fig. 7.3, and keeping in mind that the hadronic shower energy E_h is often shared between many hadrons with different directions. An approximate measure for the intensity of a Cherenkov cone E_x^{ch} induced by a particle x with energy E_x can be defined as:

$$E_x^{\text{ch}} = \begin{cases} E_x - m_p, & \text{if particle } x \text{ is a baryon} \\ E_x, & \text{else} \end{cases} \quad (7.8)$$

where m_p is the proton mass.

In the example event in Fig. 4.4 (right), the most intense Cherenkov cone is from the electron ($E_e^{\text{ch}} = E_e$) and the relative intensity is $E_e/E_\nu = 4.77 \text{ GeV}/9.82 \text{ GeV} = 0.49$, while the leading Cherenkov cone in the hadronic shower E_h^{ch} is from the pion ($E_\pi^{\text{ch}} = E_\pi$) with

⁴³ Detectors with an average photocathode area density – and consequently photon detection probability – similar to that of the planned ORCA detector.

a relative intensity of about $E_\pi/E_\nu = 3.71 \text{ GeV}/9.82 \text{ GeV} = 0.38$. The distributions of E_e/E_ν , the leading E_h^{ch}/E_ν in the hadronic shower and the leading $E_{\text{tot}}^{\text{ch}}/E_\nu$ of the total event are shown in Fig. 7.24 (top) for $\bar{\nu}_e$ CC events with $E_\nu \approx 10 \text{ GeV}$. Additionally, the distribution of leading $E_h^{\text{ch}}/E_\nu = E_{\text{tot}}^{\text{ch}}/E_\nu$ in $\bar{\nu}_e$ NC events with $E_h \approx 10 \text{ GeV}$ is shown Fig. 7.24 (bottom).

Generically, the measurable inelasticity y_{lead} from the leading Cherenkov cone is given by:

$$y_{\text{lead}} = 1 - E_{\text{tot}}^{\text{ch}}/E_{\text{vis}}, \quad (7.9)$$

where E_{vis} is the visible energy of the event and is defined as the difference between the energy of the incoming neutrino E_ν^{in} and the outgoing neutrino(s) E_ν^{out} from the primary neutrino interaction (NC events) or τ -decay ($\bar{\nu}_\tau$ CC events):

$$E_{\text{vis}} = \begin{cases} E_\nu^{\text{in}}, & \text{for } \bar{\nu}_e \text{ CC} \\ E_\nu^{\text{in}} - \sum E_\nu^{\text{out}}, & \text{for } \bar{\nu}_e \text{ NC and } \bar{\nu}_\tau \text{ CC.} \end{cases} \quad (7.10)$$

Therefore, it is expected that all measured events will show an inelasticity of $y_{\text{lead}} \lesssim 0.8$, as $E_{\text{tot}}^{\text{ch}}/E_\nu \gtrsim 0.2$ for all neutrino interaction types (see Fig. 7.24). This is even the case for NC events, which are in principle very similar (cf. Sec. 7.2.2) to $\bar{\nu}_e$ CC events with the same neutrino energy as the hadronic energy in the NC events and an inelasticity of $y = 1$.

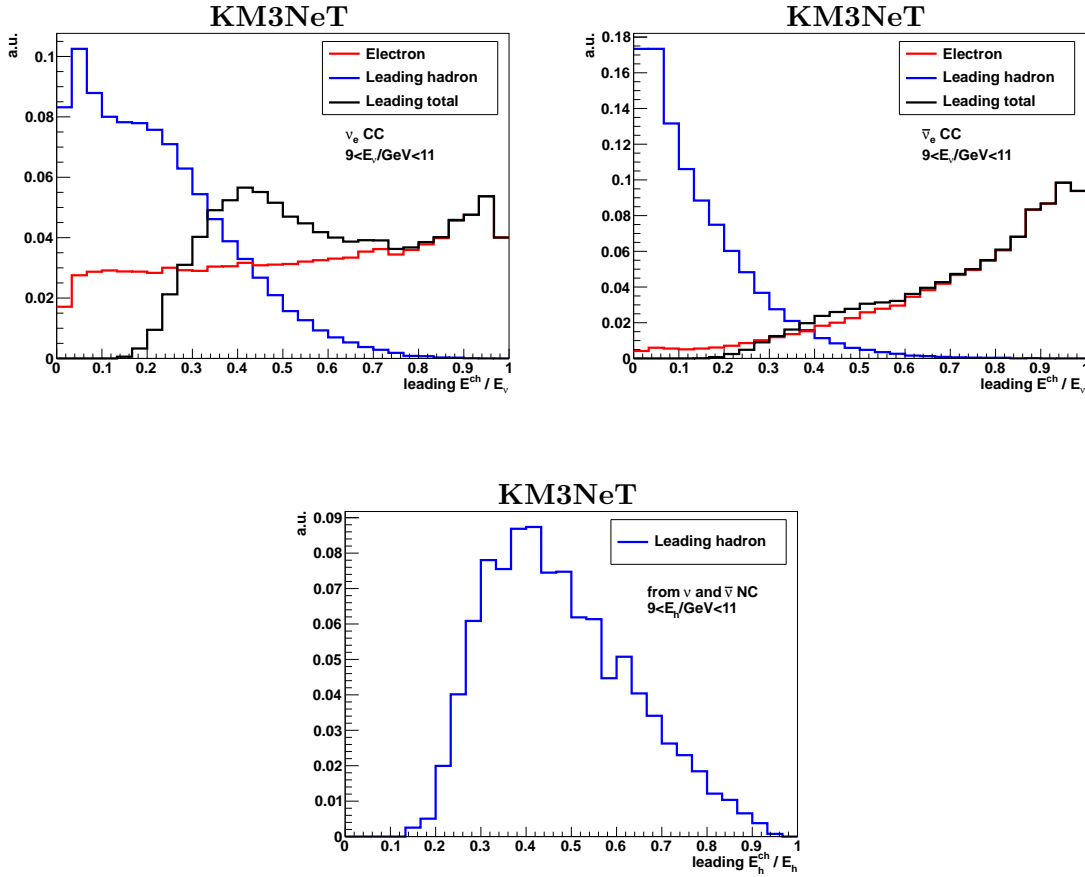


Figure 7.24: Distributions of E_e/E_ν (red), the leading E_h^{ch}/E_ν in the hadronic shower (blue) and the leading $E_{\text{tot}}^{\text{ch}}/E_\nu$ of the total event (back). Top left (right): ν_e CC ($\bar{\nu}_e$ CC) events with $9 \text{ GeV} < E_\nu < 11 \text{ GeV}$. Bottom: NC events with $9 \text{ GeV} < E_h < 11 \text{ GeV}$.

7.3.2 Leading particle direction

Assuming that the Cherenkov cone with the highest intensity can be identified, the direction of the particle producing that cone can be used as a neutrino direction estimate and the difference between this direction and the neutrino direction is a resolution estimate. Fig. 7.25 shows the median space angle between the neutrino direction and the direction of the electron, leading hadron (associated to E_h^{ch}) as well as the leading particle (associated to $E_{\text{tot}}^{\text{ch}}$) in the whole $\bar{\nu}_e$ CC event. For ν_e CC events, comparatively often (26%) $E_h^{\text{ch}} > E_e$, and the leading hadron direction is closer to the neutrino direction than the electron direction due to momentum conservation, while for $\bar{\nu}_e$ CC events, rather rarely (7%) a hadron can produce the most intense Cherenkov cone.

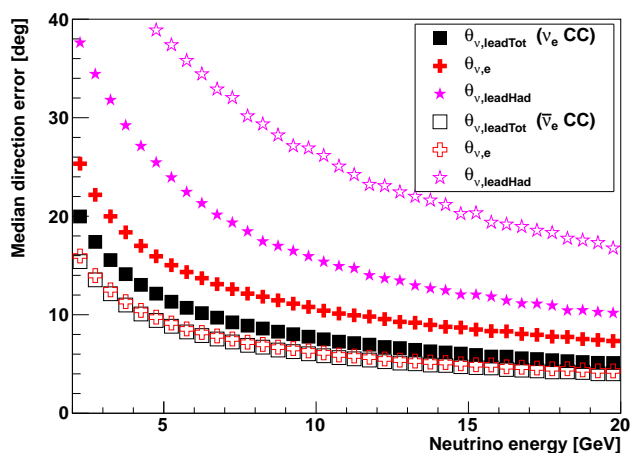


Figure 7.25: Median space angle between the neutrino direction and the direction of the electron (red crosses), the leading hadron (purple stars) and the total leading particle (black squares) for ν_e CC (solid markers) and $\bar{\nu}_e$ CC events (hollow markers) as a function of neutrino energy.

7.3.3 Possible reconstruction strategies

Based on the presented phenomenology of $\bar{\nu}_e$ CC events, different neutrino reconstruction strategies are possible (ordered by complexity):

1. Multi-cone

With sufficient photon statistics it might be possible to reconstruct several distinct Cherenkov cones from different particles in the event, which would allow to use all available information in the Cherenkov signal. Such a reconstruction strategy is for example pursued in Super-Kamiokande. However, for the planned ORCA detector, this approach seems infeasible for few-GeV neutrinos due to the insufficient photosensor density. Nevertheless, such an approach might become feasible for higher neutrino energies or more-densely instrumented detectors, and should be studied in the future.

2. Leading cone plus remaining shower

By identifying the brightest Cherenkov cone, which is most probably from the electron, and assuming a single collective signature for the remaining particles, which are usually all hadrons, it might be possible to reconstruct an electron-like object and a hadronic-shower-like object. Both objects have an associated energy and direction, which allow to reconstruct the relevant neutrino interaction properties (energy, direction and inelasticity y). Prospects for this strategy are investigated in Sec. 9.

3. Leading cone plus angular profile

Similar to the previous approach, but without identifying the direction of the hadronic-shower-like object. Obviously, the direction resolution is in this case limited approximately as per Fig. 7.25. Nevertheless, the inelasticity y is accessible from the spread of the angular profile around the reconstructed direction. A realisation of this reconstruction strategy is developed in Sec. 12.

4. Single shower with fixed angular profile

If it is not possible to identify a substructure in the shower, the only feasible reconstruction strategy is to reconstruct just one collective shower signature (energy and direction). Prospects for this strategy are investigated in Sec. 9.5.4. The disadvantage of this simple reconstruction strategy is that the inelasticity y is inaccessible.

7.3.4 Important detection distances

In principle, each DOM (whether hit or not hit) corresponds to one measurement in space-time. The number of detected photons on a single DOM can also be used in reconstruction as an intensity measurement. However, from the event reconstruction perspective, n detected photons on one DOM are not as useful as n DOMs with one detected photon each. From the latter, a direction can be reconstructed, while not from the former.

It is clear that very close to a vertex the ‘sampling rate’ is very small, because the number of DOMs at small vertex-DOM distances d is low. The number of DOMs at a given distance scales with d^2 . In addition, close-by DOMs are associated with a large angular error on θ due to a small lever arm and the limited resolution of the position. With increasing distance the angular error associated to a DOM decreases, i.e. a hit DOM far away from the vertex contains more information on the direction than a close-by hit DOM. This can also be interpreted as ‘pixel size’ – large pixels for close-by DOMs and small pixels for far-away DOMs. On the other hand, before reaching DOMs very far away from the vertex most photons get absorbed. Therefore, intermediate distances are most important for event reconstruction.

In order to determine the important range of vertex-DOM distances, it is advisable to take a look at the DOM-hit probabilities weighted with d^2 in order to take the ‘sampling rate’ into account. The expected number of hit DOMs in the ORCA benchmark detector at different distances is shown in Fig. 7.26. It is obvious that the relevant distances are roughly 20–70 m for few-GeV showers.

Another interesting back-of-the-envelope calculation is the signal-to-noise ratio. Assuming 15 PMTs facing the interaction vertex (ignoring PMTs on the backside of the DOM, cf. Fig. 7.23) and a 10 kHz/PMT single noise rate, results a $\sim 0.3\%$ ($\sim 0.75\%$) probability to get at least one noise hit within a time window of 20 ns (50 ns). At the Cherenkov angle $\theta = 42^\circ$, the signal-to-noise ratio is about 40 (16) for electrons with $E_e = 5$ GeV at a distance of 50 m, and the signal exceeds the noise level up to ~ 100 m. The noise level is also shown in Fig. 7.26.

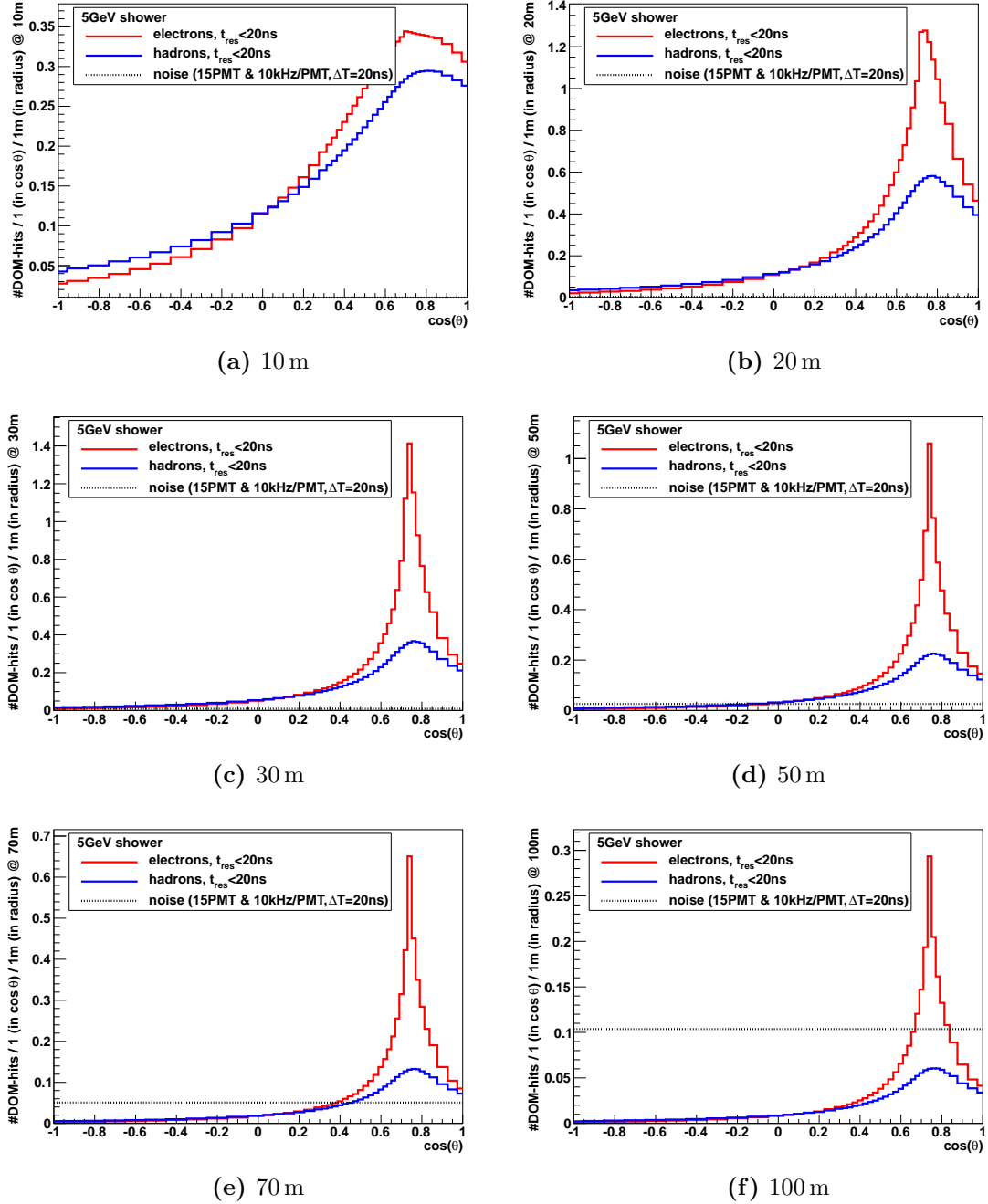


Figure 7.26: Number of hit DOM per 1 in $\cos(\theta)$ and 1m in shell radius (vertex-DOM distance) for different distances away from the vertex of showers with $E_e = E_h = 5 \text{ GeV}$ as a function of $\cos(\theta)$. DOM density as in the ORCA benchmark detector (see Sec. 6.3) is assumed, and detector surface effects are ignored, i.e. an infinitely large detector is assumed. Additionally, the noise level is shown for 15 PMTs (DOM hemisphere facing the shower) with a noise rate of 10 kHz/PMT and for a time window of $\Delta T = 20 \text{ ns}$.

8 Comparison of seawater and ice as detector media

The differentiation of the Cherenkov signature of a single electron from that of a hadronic shower is an important capability for reconstructing few-GeV $\bar{\nu}_e$ CC events. It allows to gain sensitivity to the interaction inelasticity y and to apply more advanced reconstruction methods. In deep-sea water, the identification of individual sufficiently bright Cherenkov cones in few-GeV $\bar{\nu}_e$ CC events seems to be feasible, as discussed in Sec. 7.3.

Since ice and seawater both consist of dominantly H_2O , the physics of the primary neutrino interaction and the subsequent particle propagation are very similar. Differences in Cherenkov light emission are also small, as discussed in Sec. 4.1. Hence, the main differences in reconstruction capabilities come from optical properties of both media.

In this section, the optical properties of average PINGU ice are introduced and differences with seawater are discussed. Then, the Cherenkov light signature of electromagnetic showers induced by single electrons and hadronic showers in an ice-based detector is investigated and the feasibility of differentiating their signatures is qualitatively discussed in comparison with that of a seawater-based detector.

In order to study the Cherenkov light signature in ice, the ice properties had to be implemented in **GENSHWR**. This was done in collaboration with C. W. James and is described in [159]. While C. W. James did the actual implementation in the program code, I gathered together the relevant information on the ice model used by the IceCube collaboration to simulate the detector response of PINGU. Using these simulations, I performed the comparison of the Cherenkov light signatures in both media presented below.

8.1 Comparison of optical properties

While deep-sea water is believed to be an isotropic medium, deep glacial ice at the South Pole is not. It has a layered structure, i.e. the optical properties change with depth. Measurements of depth-dependent ice properties have been performed with the IceCube detector, and a model for the optical properties of ice within the instrumented volume has been derived in [160, 161].

For simplicity and technical reasons⁴⁴, the ice properties [160, 161] are averaged over the depth of the PINGU detector (2107–2450 m) in order to compare the optical properties of ice and seawater. If a single value is required (e.g. temperature in temperature-dependent quantities, such as absorption length or refractive index), a depth of 2278.5 m is assumed. Details on the implementation of the ice model in **GENSHWR** are given in [159].

The resulting average absorption and scattering lengths as well as the group and phase refractive indices are shown in Fig. 8.1. The scattering angle distribution is shown in Fig. 8.2. For comparison, also shown are the values for seawater used in the simulations for ANTARES (as described in [162]) and KM3NeT (as described in [156], which is based on data from [125]). The ‘KM3NeT water’ is used in all simulations of seawater presented in this thesis. While the scattering angle distribution is assumed to be independent of the photon wavelength in the applied ice model [161], it is wavelength-dependent in the applied seawater model [162]. In seawater, the relative contribution from statistical (thermodynamical) fluctuations in seawater optical properties increases at smaller wavelength and leads to more-frequent large-angle scattering [162].

There are three main differences in optical properties between seawater and average PINGU ice: (i) in ice, the absorption length is significantly larger, so that an ice-based Cherenkov detector detects on average more photons for the same photocathode density;

⁴⁴ Photon propagation in **GENSHWR** (see Sec. 6.1) can only handle one set of optical properties.

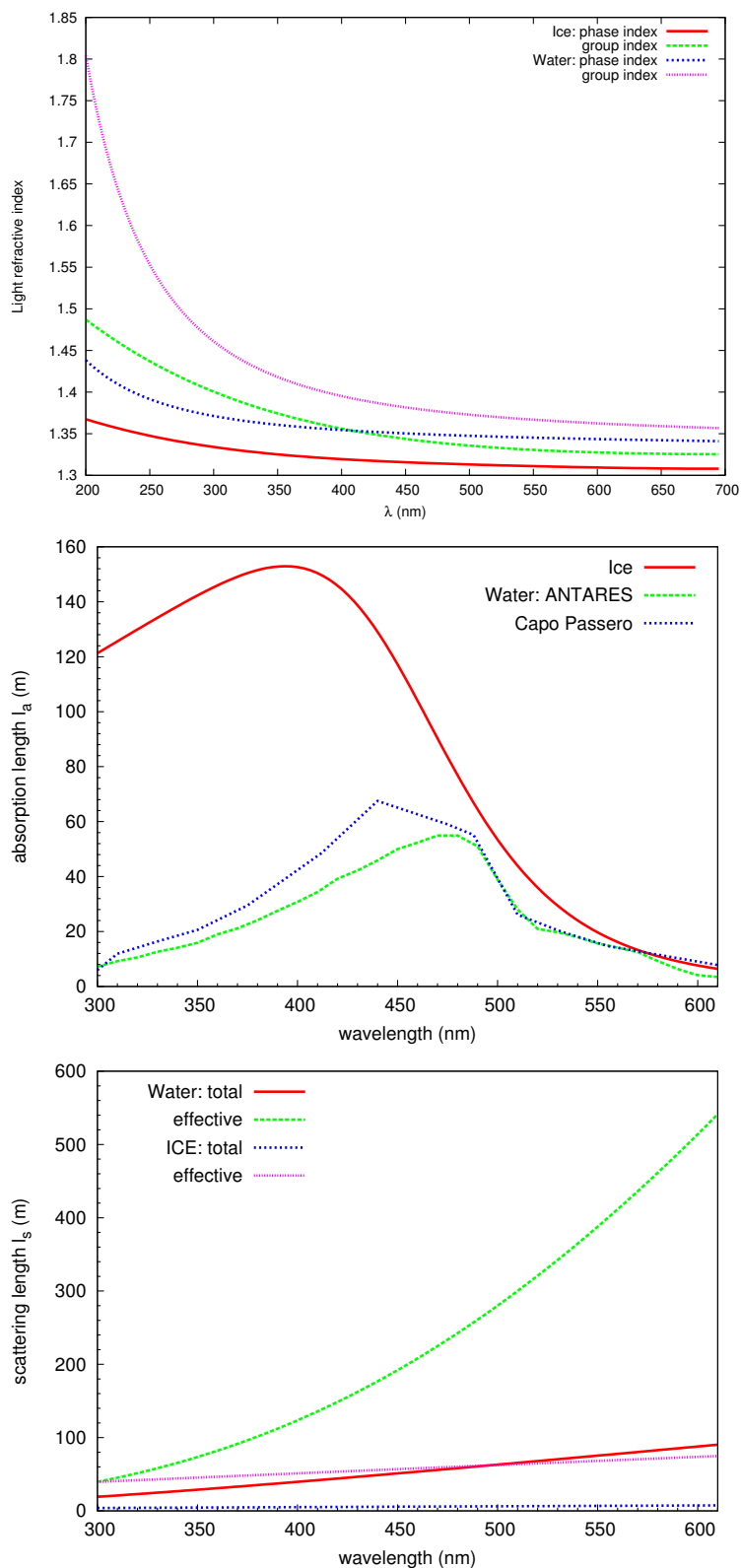


Figure 8.1: Optical properties as a function of photon wavelength λ for average PINGU ice, ANTARES seawater and KM3NeT seawater (denoted ‘Capo Passero’). ANTARES and KM3NeT seawater only differ in absorption length. Top: phase and group indices of refraction. Middle: absorption length λ_a . Bottom: scattering length λ_s and effective scattering length λ_s^{eff} (Eq. 4.9). Figures provided by C. W. James [159].

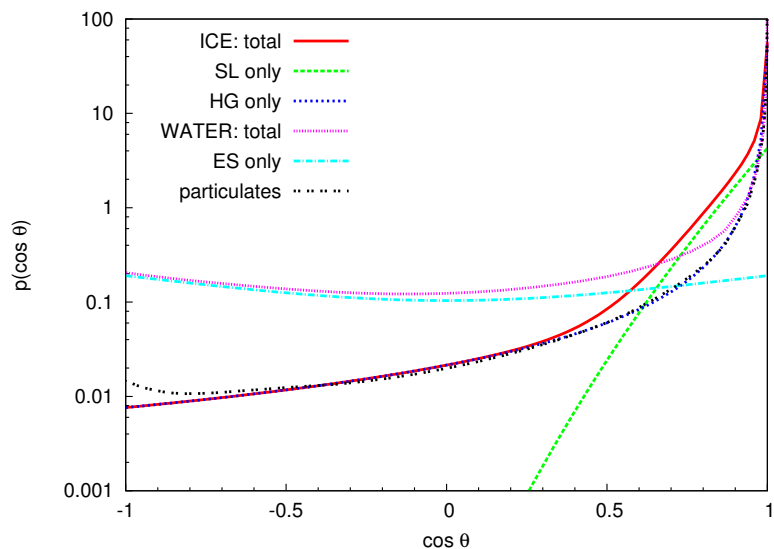


Figure 8.2: Normalised scattering angle distribution $p(\cos\theta_s)$ at a photon wavelength of $\lambda = 400$ nm for average PINGU ice and seawater. Total distribution and contributions from individual functions are shown: Henley-Greenstein (HG), Simplified Liu (SL), Einstein-Smoluchowski (ES) and particulates contributions. Figure provided by C. W. James [159].

(ii) in seawater, the scattering length is significantly larger, so that less photon scattering occurs; and (iii) the scattering angle distribution in seawater is much narrower for forward scattering than in ice.

Despite (iii), the average scattering angle is much larger in seawater ($\langle\cos(\theta_s)\rangle_{\text{water}} \approx 0.7$ at 400 nm) than in ice ($\langle\cos(\theta_s)\rangle_{\text{ice}} \approx 0.9$ at 400 nm) due to the contribution from particulates in seawater. This leads to a smaller difference between seawater and ice in effective scattering length than total scattering length (see Eq. 4.9). Nevertheless, water is much more suitable for resolving fine structures, such as single Cherenkov cones, because large-angle scattering is irrelevant (easy identifiable by photon arrival time) and only the frequent $\mathcal{O}(10^\circ)$ scattering in ice is harmful.

8.2 Comparison of event reconstruction capabilities

For all following plots, the same procedures as in Sec. 7.2.4 are followed, i.e. also for ice, all recorded photons are weighted according to their detection probabilities assuming KM3NeT DOMs and PMTs (see Sec. A.1). For the calculation of time residuals t_{res} (see Eq. 7.7) in ice, $n_{\text{ice}} = 1.356$ is assumed.

Photon arrival time

The time residual t_{res} distribution – especially its spread – is a very important aspect for event reconstruction. It directly impacts the vertex resolution, and indirectly also provides information about the expected direction resolution, as scattered (i.e. delayed) photons have partly lost their direction information. Fig. 8.3 shows the t_{res} distributions at different distances away from electromagnetic showers simulated in ice. With increasing distance, the t_{res} distributions smear out towards later photon arrival times. At a distance of 50 m, the most probable photon arrival time is already ~ 15 ns later than expected from the speed of light in ice. These distributions should be compared with those for seawater in Fig. 7.19. Cumulative t_{res} distributions normalised to the total number of emitted photons for electromagnetic showers in ice and seawater are shown in Fig. 8.4.

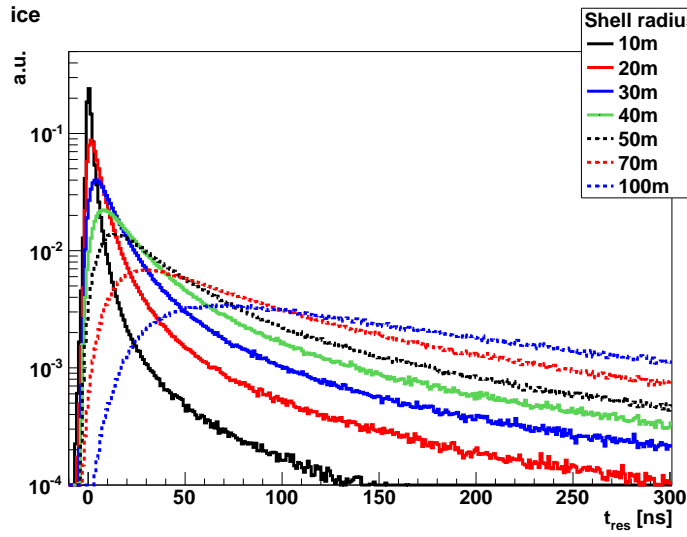


Figure 8.3: Distributions of time residuals t_{res} for photons from electromagnetic showers with $E_e = 5$ GeV. Photons are propagated through ice and recorded on shells with different radii. Distributions are averaged over 1000 showers and normalised to unity.

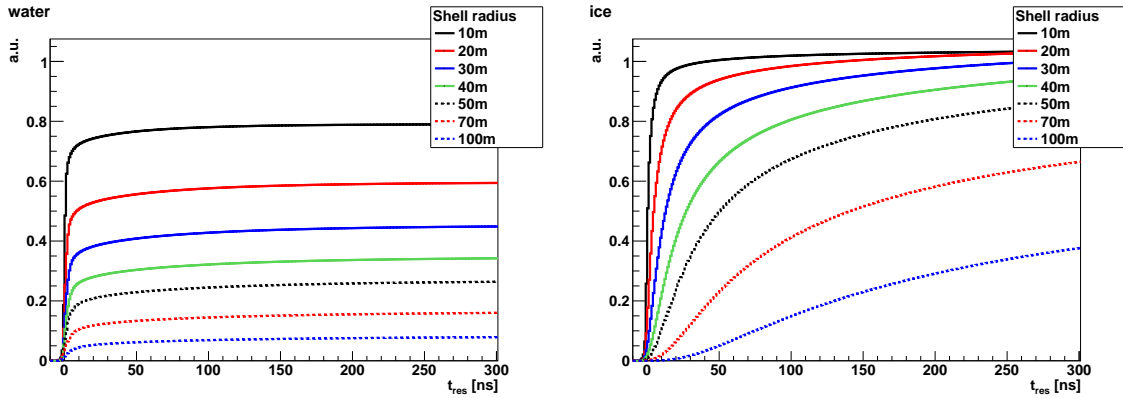


Figure 8.4: Cumulative distributions of Fig. 7.19 for seawater (left) and Fig. 8.3 for ice (right) normalised to total number of emitted photons.

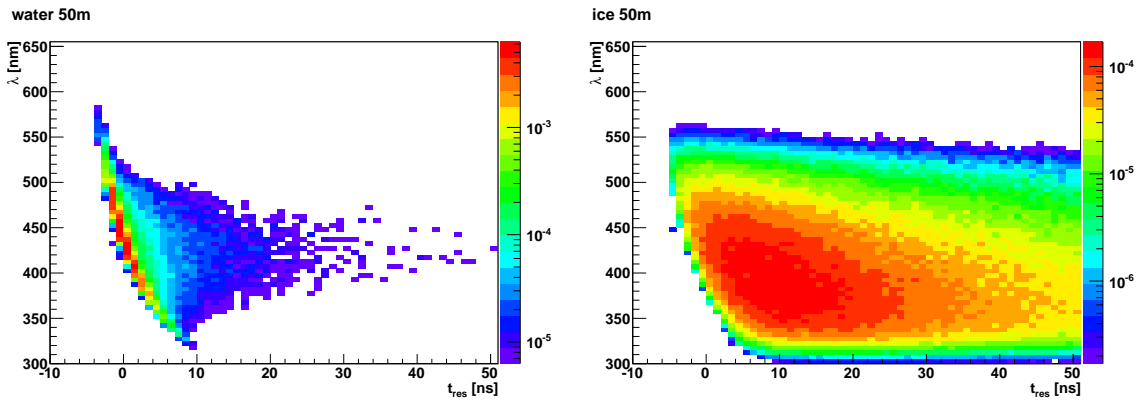


Figure 8.5: Photon detection probability as a function of photon wavelength λ and time residual t_{res} for DOMs under Cherenkov angle $\theta = 42^\circ$ and at a distance of 50 m away from electromagnetic showers with $E_e = 5$ GeV simulated in seawater (left) and ice (right).

Due to the larger absorption length, the absolute number of photons reaching a certain distance is much larger in ice than in seawater. The same photon statistics as in seawater within $t_{\text{res}}^{\text{water}} < 10$ ns is reached in ice within $t_{\text{res}}^{\text{ice}} < 5$ ns (17 ns, 50 ns) for 20 m (50 m, 100 m).

In ice, The spread in photon arrival times is dominantly caused by scattering and the contribution from dispersion is negligible, whereas in water dispersion dominates. This becomes evident from Fig. 8.5.

Angular light distribution

The angular light distribution – especially its spread around the Cherenkov peak – directly affects the expected direction resolution of a detector. The narrower the angular light distribution, the better the direction of a single particle can be reconstructed.

Fig. 8.6 shows the photon arrival time against the angle θ between shower direction and the vector from the vertex to the photon detection position for electromagnetic showers simulated in ice. Fig. 8.6 (right) should be compared with the corresponding distributions for seawater in Fig. 7.20 (left). One-dimensional representations are given in Fig. 8.7, where the average DOM-hit probability for different t_{res} ranges is shown for electromagnetic and hadronic showers. These distributions should be compared with the corresponding distributions for seawater in Fig. 7.21.

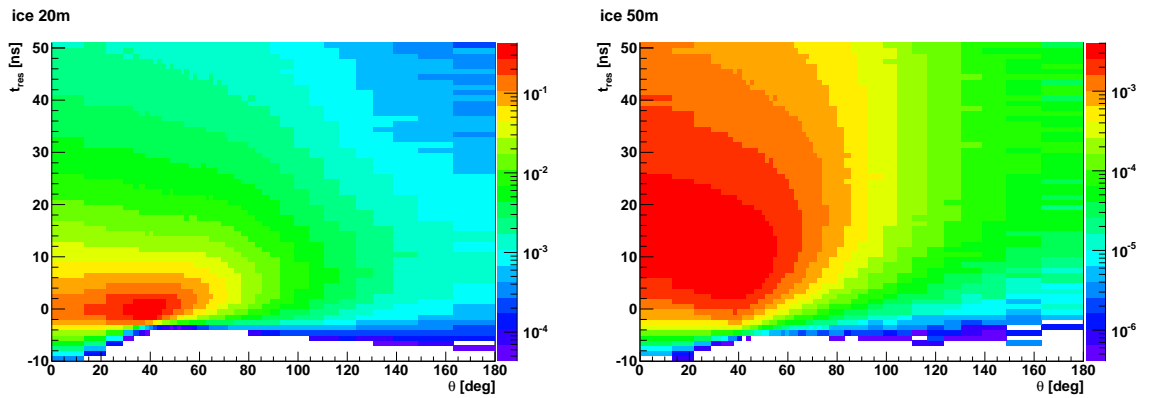


Figure 8.6: Photon detection probability as a function of time residual t_{res} and angle θ between shower direction and the vector from vertex to photon detection position for a distance of 20 m (left) and 50 m (right) away from electromagnetic showers with $E_e = 5$ GeV simulated in ice.

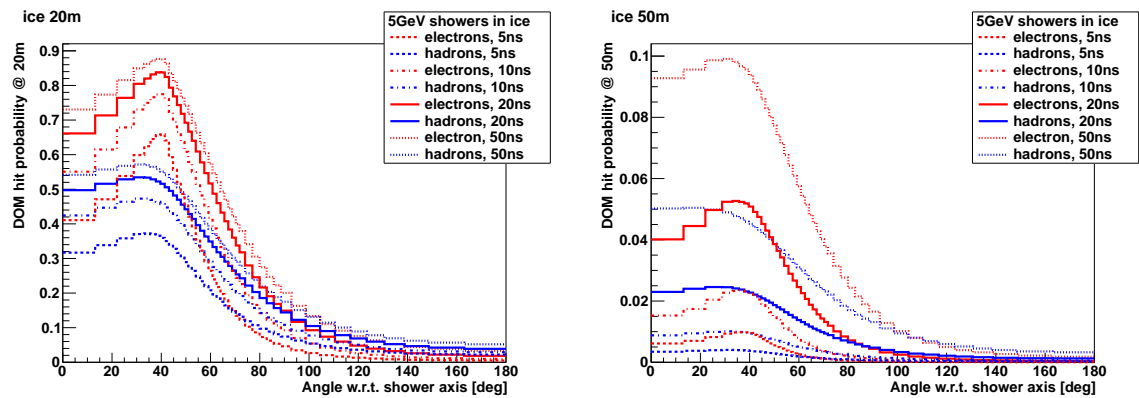


Figure 8.7: DOM-hit probability (average probability to detect at least one photon in an entire multi-PMT optical module) at a distance of 20 m (left) and 50 m (right) away from electromagnetic and hadronic showers with $E_e = E_h = 5$ GeV as a function of angle θ between shower direction and the vector from vertex to photon detection position. Showers are simulated in ice. Distributions are shown for different cuts on photon arrival time: t_{res} smaller 5 ns, 10 ns, 20 ns and 50 ns.

In ice, even at relatively short distances of 20 m the Cherenkov peak of an electromagnetic shower is smeared out considerably. The Cherenkov peak itself becomes visible only for photons with time residuals smaller than a few nanoseconds. Compared to seawater, many fewer of these unscattered photons are available (cf. Fig. 7.21 and Fig. 8.7). After these first few unscattered photons only one big ‘blob’ is observable in ice. Nevertheless, the scattered photons still carry some directional information, as the typical scattering angle is about $\cos^{-1}(0.9) \approx 25^\circ$ (see Fig. 8.2). The observable light signature in ice looks more like a filled cone (opening angle larger than the Cherenkov angle due to scattering) with a diffuse edge, whereas in seawater the light signature is the surface of a cone (opening angle similar to Cherenkov angle).

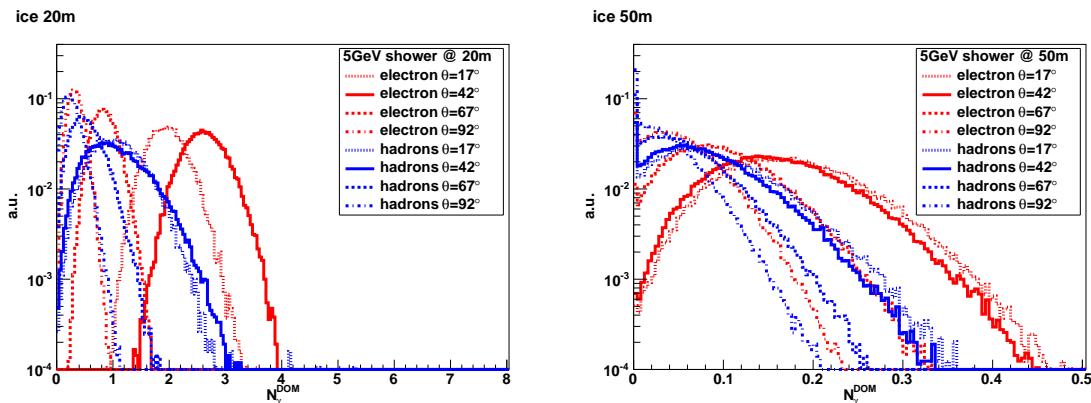


Figure 8.8: Distributions of expected number N_{γ}^{DOM} of detected photons per DOM at a distance of 20 m (left) and 50 m (right) away from electromagnetic and hadronic showers with $E_e = E_h = 5$ GeV simulated in ice.

On the other hand, due to photon scattering the number of photons detected on a certain DOM becomes randomised. Hence, the N_{γ}^{DOM} distributions for ice are more Poisson-like than for seawater. For ice, these distributions are shown in Fig. 8.8 and can be compared with those for seawater in Fig. 7.22. Consequently, detector signatures in ice show less event-to-event fluctuations⁴⁵, as the ice prevents the detector to resolve the substructure of the event signature anyway.

The directionality information from multi-PMT DOMs might help in ice, because the time residual distribution depends on the PMT orientation, as can be seen in Fig. 8.9. However, also in ice, most of the photons arrive from the hemisphere facing the event, so that the possible improvement might not be too large. For comparison, the corresponding distributions for seawater are shown in Fig. 7.23.

8.3 Validation of ice simulation

In order to validate the simulation results obtained using **GENSHWR** for ice, the resulting time residual distributions have been checked against those obtained using **clsim**, a simulation tool widely used within IceCube. Here, both simulation packages are input with the same optical properties. Simulations using **clsim** were performed by T. Kittler.

Fig. 8.10 compares the time residual distributions for DOMs at a distance of 100 m away from the vertex and two different angle θ between the shower direction and the vector from the vertex to the DOM. The shapes of the distributions look very similar⁴⁶. This validates the **GENSHWR** simulations and the results presented in the previous sections.

⁴⁵ The event-to-event fluctuations in total light yield are of course (nearly) identical in ice and water, as discussed in Sec. 9.6.

⁴⁶ The different relative time offsets between the distributions for $\theta = 0^\circ$ and $\theta = 90^\circ$ can be explained by

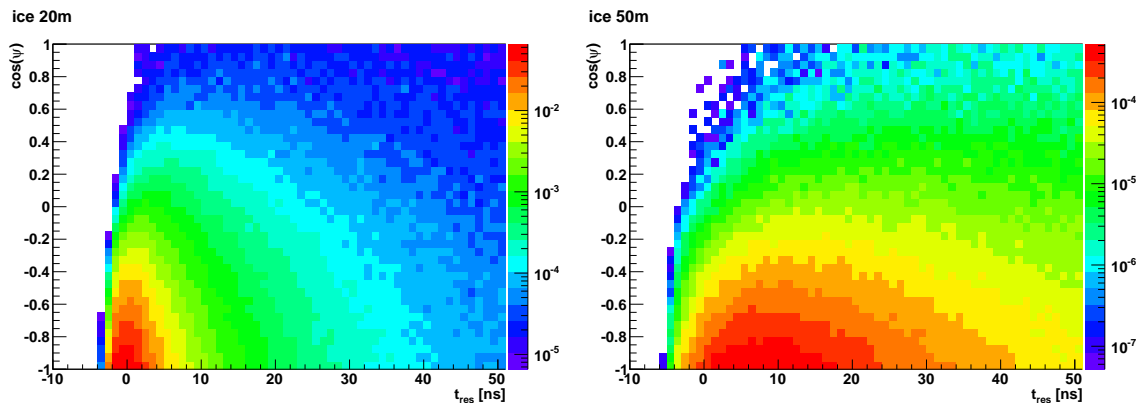


Figure 8.9: Photon detection probability as a function of time residual t_{res} and angle ψ between the vector normal to the DOM surface and the vector from the vertex to the DOM centre for DOMs under an angle of $\theta = 42^\circ$ and at a distance of 20 m (left) and 50 m (right) away from the vertex of electromagnetic showers with $E_e = 5$ GeV simulated in ice.

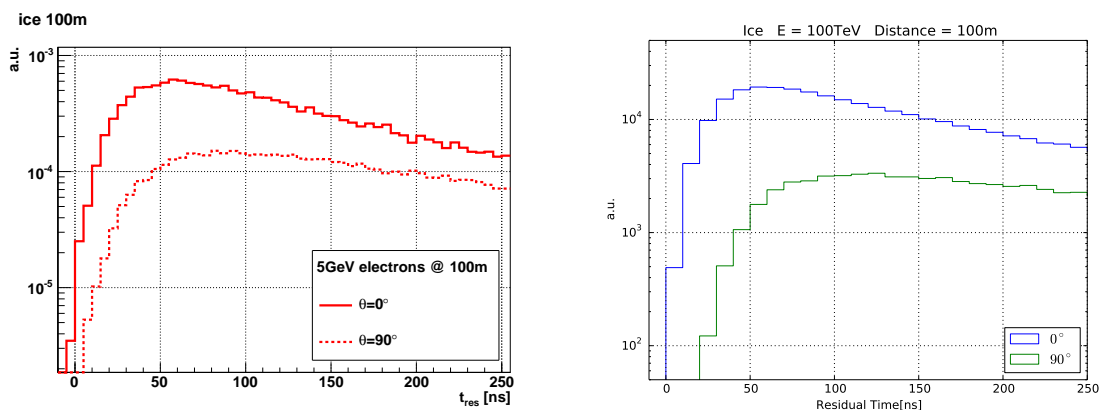


Figure 8.10: Distributions of time residuals t_{res} for DOMs located in ice at a distance of 100 m away from the vertex and under two different angles ($\theta = 0^\circ$ and $\theta = 90^\circ$) with respect to the shower axis. The GENSHWR simulation package is used to simulate electrons with 5 GeV (left) and the clsim simulation package is used to simulate ν_e CC events with $E_\nu = 100$ TeV (right). While the left plot is normalised to unity, the right plot shows photon counts. Both simulation packages use the average PINGU ice properties outlined in Sec. 8.1. Right figure provided by T. Kittler.

8.4 Conclusions

Based on the presented results, the identification of individual energetic particles in few-GeV $\bar{\nu}_e$ CC events via their distinct Cherenkov cones seems more feasible with a seawater-based detector than with an ice-based detector due to the optical properties of both media.

For ice, it seems very likely that one is able to reconstruct roughly the overall direction of few-GeV $\bar{\nu}_e$ CC events, but is not able to distinguish different energetic particles with typical opening angles of $\mathcal{O}(10^\circ)$, as their Cherenkov light signatures are hardly distinguishable from each other due to the frequent photon scattering with typical scattering angles of $\mathcal{O}(10^\circ)$. Hence, differentiating between electromagnetic showers initiated by single electrons and hadronic showers seems to be challenging – consequently also the determination of interaction inelasticity y .

the different initial particle energies leading to different shower elongations. For electrons with $E_e = 5$ GeV and $E_e = 100$ TeV, the difference in longitudinal shower elongation is about ~ 3.3 m (cf. Sec. 4.3), which corresponds to a time differences of about ~ 14 ns in ice.

This conclusion becomes even more evident when considering the depth-dependent inhomogeneities in ice and the uncertainties on optical properties in the immediate vicinity⁴⁷ of each DOM. This anisotropy deteriorates the achievable vertex and direction reconstruction accuracy in ice. Note that for direction reconstruction a very good vertex (position and time) accuracy is an essential precondition for identifying unscattered photons (via small t_{res}) as well as for ‘defining’ the angle θ between shower direction and the vector from the vertex to the photon detection position.

For seawater, the feasibility of differentiating between electromagnetic showers initiated by single electrons and hadronic showers is presented and discussed in Sec. 7.3.

For the assumed photosensor densities of ORCA and PINGU (planned with very similar photocathode area densities), it seems probable that only a seawater-based detector can identify substructures in few-GeV $\bar{\nu}_e$ CC events, which allows to apply one of the more sophisticated reconstruction strategies discussed in Sec. 7.3.3 (strategy 1, 2 and 3). A ice-based detector of that photosensor density is reduced to follow the most simple reconstruction strategy in Sec. 7.3.3 (strategy 4).

⁴⁷ It is known that the ‘hole ice’ shows very different optical properties than the ‘bulk ice’ [161].

9 Intrinsic limits on resolution of few-GeV neutrinos

In the few-GeV energy regime, intrinsic fluctuations in particle behaviour – and consequently in the Cherenkov photon signature – are important. These intrinsic fluctuations impose limitations on the attainable reconstruction accuracy.

These limitations are investigated to answer two basic questions. First, how do intrinsic fluctuations limit the reconstruction accuracy of a detector where every single photon is detected? While this requires making some basic assumptions about the methods used in the reconstruction, the answer to this question will indicate the optimum that could be achieved by any detector. Second, given that only a finite number of photons will be detected, what is the best possible reconstruction accuracy in the case of an ideal use of the information carried by these photons?

After introducing the applied methods in Sec. 9.1, limits on energy and direction resolution of muons (Sec. 9.2), electrons (Sec. 9.3), and hadronic showers (Sec. 9.4) are derived for an ORCA-like detector. By combining these results, limits on the reconstruction accuracy for the initial neutrinos are deduced in Sec. 9.5.

The intrinsic fluctuations and the derived limits on the reconstruction accuracy have been investigated in collaboration with C. W. James. Preliminary studies on muon tracks and hadronic showers have been performed by M. Pleinert [163] and T. Rauch [164]. The following section is based on a paper draft [158] written by C. W. James and myself. Preliminary results were also presented at the ‘34th International Cosmic Ray Conference’ [165].

In the paper draft [158], C. W. James mainly worked on the fluctuations and resolution limits for electrons as well as hadronic showers, and he wrote the corresponding parts. I was responsible for the results for muon tracks and in particular for the combination of the results on individual components (muons, electrons and hadronic showers) to resolution limits on the initial neutrino and the interaction inelasticity, and I wrote the corresponding parts. In addition, I contributed to the considerations on the light yield of hadronic showers (my contributions are presented in Sec. 7.2.2), and the discussions on the ‘1D’ vs ‘2D’ method for direction reconstruction of electromagnetic showers (see Sec. 9.3.2). In the following, the paper draft [158] is partly copied in verbatim.

9.1 Methods

For the work in this section, a simplified procedure is used to determine the best possible reconstruction accuracy of an ORCA-like detector. In this simplified procedure, both optimistic and idealising assumptions are made, so that the resulting intrinsic limits on the reconstruction accuracy will be better than that of a real detector.

Cherenkov detectors determine the properties of neutrino interaction events by measuring photons. Ideally, photons from each of the components occurring in neutrino interactions – muons, electrons and hadronic showers – could be uniquely identified, so that the ability to reconstruct the initial neutrino properties would only be limited by the resolution of each component when considered in isolation. This idealisation is used throughout. However, in Sec. 9.5.4 this assumption is relaxed for $\bar{\nu}_e$ CC events in order to investigate the effects on the neutrino resolution both with and without the components resolved.

Additionally, it is optimistically assumed that ‘unscattered’ photons can be identified perfectly. Unscattered photons are usually used in direction reconstructions, as these photons carry directional information of the particle that emitted them.

9.1.1 Sources of intrinsic fluctuations

Intrinsic limitations on energy and direction resolution come from multiple sources of fluctuations in the Cherenkov photon signatures. The fluctuations due to the stochastic nature of energetic particle behaviour during ‘propagation’ and due to different hadronic final states – or ‘hadronic states’ for short – are already introduced in Sec. 7.2.2. The ‘all-photon limit’, in which every single emitted photon is detected unscattered, is the combination of reconstruction errors from both sources of fluctuations.

In any real detector, only a small fraction of all emitted photons is detected. This ‘photon sampling’ effect limits the ability to determine event properties from the information carried by the detected photons. In the idealised detector assumed for these studies, the sampled photon fraction is only characterised by the wavelength-dependent probability of detecting each photon, as introduced in Sec. 6.6. For this, the photocathode area density of the ORCA benchmark detector (see Sec. 6.3) is assumed throughout.

The ‘overall limit’ is the combination of all three sources of fluctuations (propagation, hadronic state, and photon sampling)⁴⁸.

Not considered effects

The methods used here to derive the limiting resolutions differ significantly from the performance evaluation procedure based on full detector simulations (e.g. in Sec. 12), which include several further effects: optical background noise (see Sec. 4.8.1); discrimination between signal events and atmospheric muon (see Sec. 4.8.2); timing- and charge-calibration uncertainties; events only partially contained inside the instrumented volume; ‘clumpiness’⁴⁹ of detection elements.

9.1.2 Simulations

The `GENSHWR` simulation package (see Sec. 6.1) is used for particle propagation in seawater and Cherenkov photon generation. These photons are weighted according to their detection probabilities in an idealised ORCA-like detector, as described in Sec. 6.6. The photocathode area density of the ORCA benchmark detector (with 6 m vertical spacing between DOMs, see Sec. 6.3) is assumed. Differences between using `G-GHEISHA` or `G-FLUKA` for hadron tracking serve as a measure of systematic uncertainties. The difference are found to be small, apart from a $\sim 6\%$ smaller light yield for `G-GHEISHA` than for `G-FLUKA` (see Sec. 6.2 and Fig. 7.10). If not stated otherwise, results are presented for `G-GHEISHA`.

Simulations of both muons and electrons are performed at discrete energies between 1 GeV and 20 GeV, while hadronic showers are extracted from $\bar{\nu}_\mu$ CC events simulated using `gSeaGen`, as described in Sec. 6.5. Selected hadronic showers have a required energy E_h within 1% of the nominal values. The simulation statistics is summarised in Tab. 9.1.

9.1.3 Characterising fluctuations

Usually, events are reconstructed using maximum-likelihood methods. Uncertainties in this procedure are estimated by considering fluctuations in simulated truth for given observables. As each particular analysis might apply its own data selection and quality criteria, this ‘inverse problem’ is not analysis-independent. For both generality and simplicity,

⁴⁸ In previous works, such as [165], other naming conventions were used: ‘hadronic states’ was termed ‘vertex composition’, ‘all-photon limit’ was termed ‘perfect detector’, and ‘overall limit’ was termed ‘finite detector’.

⁴⁹ Clumpiness means the fact that photon-collection area is concentrated in small regions, i.e. PMTs, which in turn might be grouped in optical modules. This makes the photon detection non-uniform and results in strong correlations between the photons that are detected.

Component	events/energy	repetitions/event
Muons	1	1000
Electrons	1	1000
Hadronic showers	1000	1000 G-FLUKA, 1000 G-GHEISHA
Energies [GeV]:	1, 1.5, 2, 2.5, 3, 3.5, 4, 4.5, 5, 6, 7, 8, 9, 10, 12, 14, 16, 18, 20	

Table 9.1: Description of the simulations for each component. Each repetition uses a different random number seed. For hadronic showers, each event represents a different hadronic final state.

only fluctuations in the ‘forward problem’ are considered, i.e. the variation in observable quantities for a given simulated truth. No event selection is applied.

In the following, the fluctuations relating to energy reconstruction errors ΔE are characterised by the RMS, as in most cases the underlying distributions are found to be sufficiently Gaussian-like. However, fluctuations relating to direction reconstruction errors tend to show large non-Gaussian tails. It is therefore more appropriate to characterise resolutions using quantiles. In this section, direction reconstruction errors $\Delta\theta$ are given such that the range $[0^\circ, \Delta\theta]$ contains 68.27% of the data, i.e. the same fraction covered by $\pm 1\sigma$ of a Gaussian.

9.1.4 Breaking the limits

Although optimistic assumptions are made throughout, under certain circumstances resolutions better than the limits presented here might be achieved. Understanding the reasons will help interpret the results. Possible reasons are:

- Event selection procedures can lead to preferentially selecting events with intrinsically good properties, e.g. neutrino interactions with a small inelasticity y , or hadronic final states producing a high light yield. The reconstruction accuracy will be improved on such a selected subset of events, but at the expense of a reduction in effective volume.
- More sophisticated reconstruction methods than that assumed here can of course lead to a better reconstruction accuracy. The limits hold only for the assumed reconstruction methods.
- The usage of scattered photons in the direction reconstructions could improve the achievable resolutions, as scattered photons retain some directional information. However, for scattered photons it will be more difficult to resolve the source of the photons, i.e. if they come from the hadronic shower or the lepton. This photon source identification is optimistically assumed here, and without this ability the resolutions are worse (see Sec. 9.5.4).

9.2 Muons

Muons are produced in $\bar{\nu}_\mu$ CC interactions. The characteristics of propagating muon are discussed in Sec. 4.2.

9.2.1 Energy resolution

In the considered energy range, muons behave very similarly to minimum ionising particles. Therefore, their signature in the water/ice Cherenkov detectors is a straight track with a nearly uniform luminance. This behaviour leads to two obvious methods of energy

reconstruction: (i) the track length of the muon, measured by estimating the start- and endpoints of a track; and (ii) the total Cherenkov light yield of the muon, measured by simply counting the number of detected photon.

Track length measurement

Assuming optimistically in all cases that the starting point of a muon track can be resolved perfectly using information from the accompanying hadronic shower, the general strategy of a muon track length measurement is to detect the endpoint of a muon track using information from unscattered photons, i.e. by back-projecting the hits onto the track assuming the Cherenkov angle. The best possible resolution of the endpoint is therefore derived by assuming that the true emission positions of detected unscattered photons can be reconstructed.

In the all-photon limit, it is assumed that the track endpoint can be determined precisely. Relative fluctuations in the muon track length L_μ itself correspond then directly to a relative error in the energy reconstruction. If $\bar{L}_\mu(E_\mu)$ is the expected track length of a muon initially at energy E_μ , and $\sigma_{L_\mu}(E_\mu)$ is the standard deviation of L_μ , then the relative energy resolution in the all-photon limit $\Delta E_{\mu,L}^{\text{all}}/E_\mu$ is given by:

$$\Delta E_{\mu,L}^{\text{all}}/E_\mu = \frac{\sigma_{L_\mu}(E_\mu)}{\bar{L}_\mu(E_\mu)}. \quad (9.1)$$

Distributions of relative track length L_μ/\bar{L}_μ for 3 and 10 GeV muons are shown in Fig. 9.1.

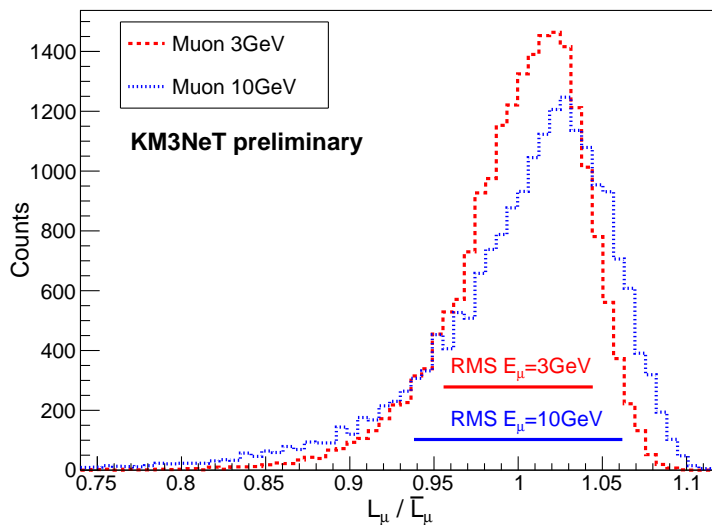


Figure 9.1: Distributions of relative track length L_μ/\bar{L}_μ for muons with initial energies of 3 GeV (red) and 10 GeV (blue). Horizontal bars represent the RMS of the data.

In the overall limit, the relatively small number of sampled unscattered photons will limit the resolution of the muon path, and the track length measurement is reduced to a determination of the distance from the starting point to the position where the last detected, unscattered photon is emitted by the muon. Fig. 9.2 shows the expected number of detected unscattered photons from the last few metres of the muon track. The corresponding uncertainty due to photon sampling $\Delta L_\mu^{\text{samp}}$ is estimated from the variation about the mean offset between the position of last emission and the true muon endpoint. For the assumed photon detection probability, from the last 73 cm of the muon track 1.15

detected unscattered photons are expected⁵⁰, as shown in Fig. 9.3. This corresponds to roughly ~ 0.1 GeV uncertainty on the muon energy.

This uncertainty is independent from the variation in the true length of the muon track, and the overall limit on the relative energy resolution $\Delta E_{\mu}^{\text{over}}/E_{\mu}$ is given by:

$$\Delta E_{\mu,L}^{\text{over}}/E_{\mu} = \frac{\sqrt{(\sigma_{L_{\mu}}^{\text{all}})^2 + (\Delta L_{\mu}^{\text{samp}})^2}}{L(E_{\mu})}. \quad (9.2)$$

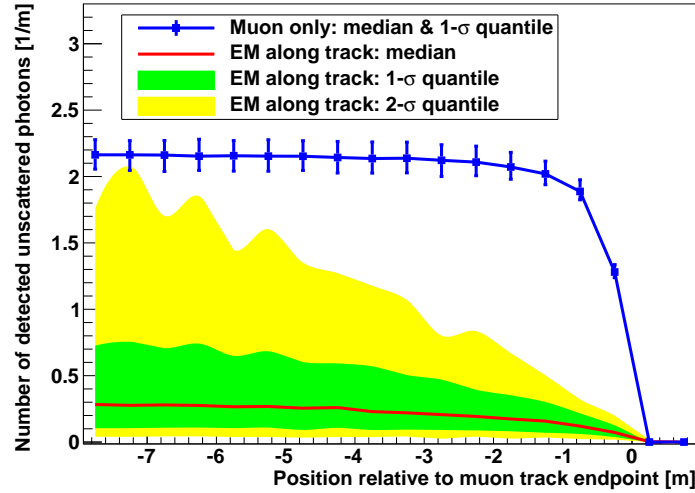


Figure 9.2: Expected number of detected unscattered photons (see Sec. 6.6 for detection probability) as a function of the position along muon track relative to muon endpoint. The amount of Cherenkov photons from the muon itself and from electromagnetic showers (EM) initiated by the muon are shown separately. The ‘oscillating structure’ in the 1- σ and 2- σ quantiles of the electromagnetic shower contribution are artefacts of the representation of statistical fluctuations.

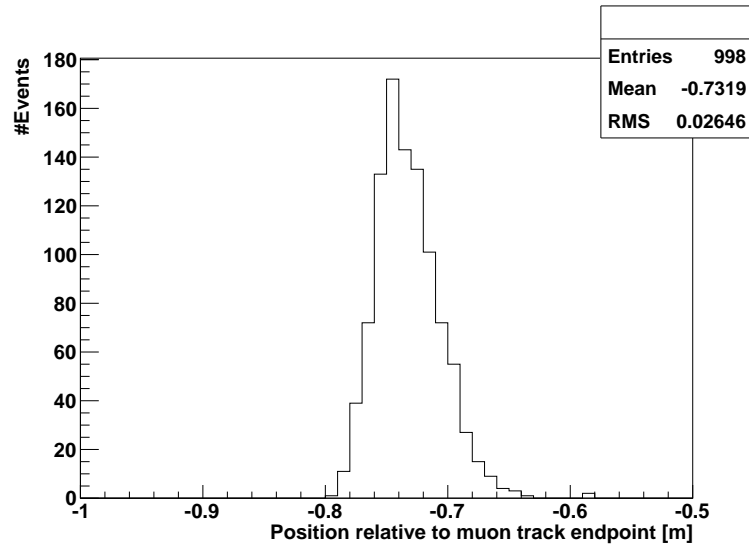


Figure 9.3: Distribution of positions along the muon track relative to the muon endpoint at which 1.15 detected unscattered photons, corresponding to 1 Gaussian- σ , are expected from the remaining part of the muon track.

⁵⁰ For a Poissonian P , it holds that $1 - P(N = 0, \lambda = 1.15) \approx 68.27\% = 1$ Gaussian- σ .

Total light yield

In the case of the total Cherenkov light yield measurement in the all-photon limit, relative fluctuations in the total number of emitted photons $N_\mu(E_\mu)$ correspond directly to a relative error in energy reconstruction. If $\bar{N}_\mu(E_\mu)$ is the mean number of emitted photons from a muon initially at energy E_μ , and $\sigma_{N_\mu}(E_\mu)$ is the standard deviation of N_μ , then the relative energy resolution in the all-photon limit $\Delta E_{\mu,N}^{\text{all}}/E_\mu$ is given by:

$$\Delta E_{\mu,N}^{\text{all}}/E_\mu = \sigma_{N_\mu}/\bar{N}_\mu. \quad (9.3)$$

The average number N_μ^{samp} of detected photons increases almost linearly with energy. For the assumed photon detection probability, $N_\mu^{\text{samp}}(E_\mu) = 22.0 \times (E_\mu - E_\mu^{\text{th}})/\text{GeV}$, where E_μ^{th} is the energy threshold for Cherenkov radiation in seawater (see Sec. 4.1). The resulting Poisson variations add an extra uncertainty $\Delta E_{\mu,N}^{\text{samp}}$:

$$\Delta E_{\mu,N}^{\text{samp}}/E_\mu = [N_\mu^{\text{samp}}(E_\mu)]^{-0.5}. \quad (9.4)$$

The two sources of variation are independent, and can be added in quadrature to find the overall uncertainty. As opposed to the track length measurement, all detected photons count, whether or not they are scattered.

Comparison

All-photon and overall limits on the relative muon energy resolution for both energy estimates (muon track length and total light yield) are shown in Fig. 9.4. In the case of the all-photon limit, fluctuations in total photon emission are almost negligible, whereas those in muon track length are not, so that the total light yield method is most accurate. In the case of the overall limit, the resulting uncertainty due to Poisson fluctuations about the average number of total detected photons is much larger than the uncertainty due to detection of the endpoint of the track, so that even when combined with intrinsic track length fluctuations the muon track length method is more accurate below $E_\mu \lesssim 13 \text{ GeV}$.

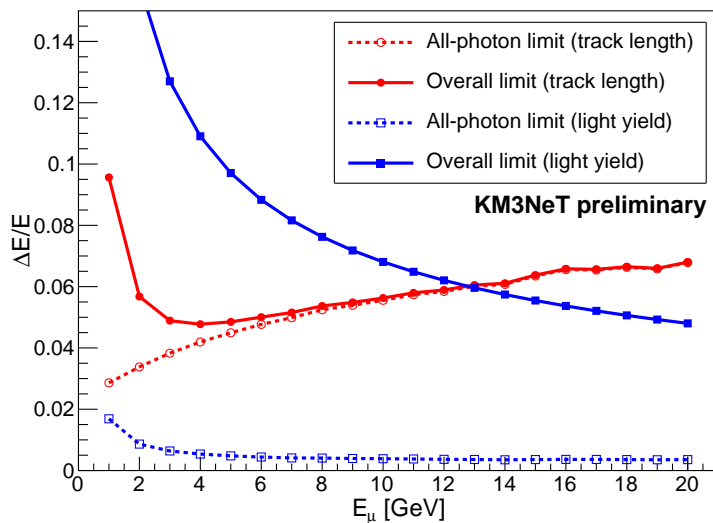


Figure 9.4: Limits on relative muon energy resolution as a function of muon energy for muon track length method (red) and total light yield method (blue). Resolutions are shown for all-photon limit (hollow marker and dashed lines) and overall limit (filled marker and solid lines).

9.2.2 Direction resolution

In the case of the all-photon limit, under the assumption that the precise emission points of each photon can be reconstructed, in theory it would be possible to measure the initial direction of the muon track immediately after the neutrino interaction, giving perfect direction resolution. Here, a single constraint is introduced to obtain intrinsic limits: that the muon track fit assumes a linear muon path over its entire length, so that the linearity of the track itself limits the accuracy of the fit.

The effects of photon sampling on the intrinsic limit to the direction resolution is unclear, since only a few unscattered photons (with perfect timing and position resolution) need to be detected in order to fully constrain a track fit. It might be possible to obtain such limits by considering the timing uncertainty of the PMTs, or the dispersion characteristics of seawater – however, such limits will be very small indeed, as verified by the very good direction resolution of muon tracks in ANTARES. Hence, only the intrinsic fluctuations from the straightness of a muon track itself are considered, and applied equally to both the all-photon and overall limits.

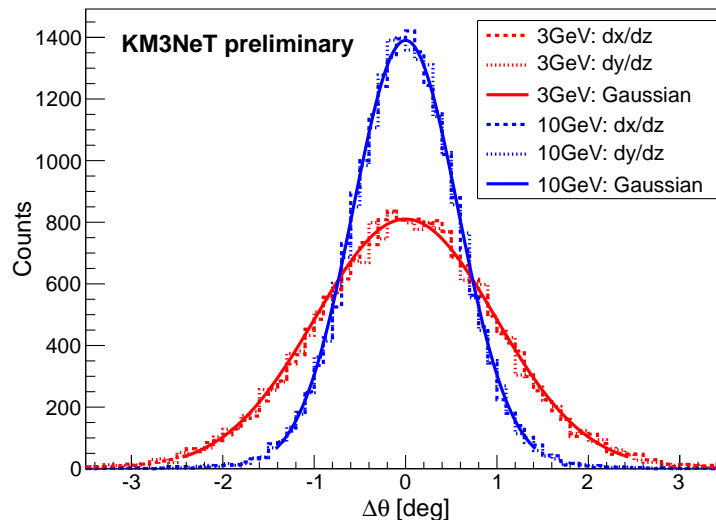


Figure 9.5: Slopes dx/dz (dashed) and dy/dz (dotted) from fits to muons which began traveling along the z -axis with initial energies of 3 GeV (red) and 10 GeV (blue). Gaussians (solid) are shown for comparison.

The slopes dx/dz and dy/dz from fits to the true muon path (which always begins traveling along the z -axis) are used as the errors of such a muon track fit. Their distributions for initial muon energies of 3 and 10 GeV are shown in Fig. 9.5, and compared to Gaussian distributions. The resulting angular error in two dimensions $\Delta\theta^{\text{all, over}}$ is both the all-photon and overall limit, and is shown as a function of muon energy in Fig. 9.6. Note that these angular errors are dominated by multiple scattering, although the straight-line fitting procedure results in a different angular error than more common measures of multiple scattering angles in [11].

9.3 Electrons

Electrons are produced in $\bar{\nu}_e$ CC interactions. The characteristics of the initiated electromagnetic showers are discussed in Sec. 4.3. For the reconstruction accuracy limits, only fluctuations in the number and direction of emitted photons are considered. Uncertainties due to the shower elongation are expected to be small and are neglected.

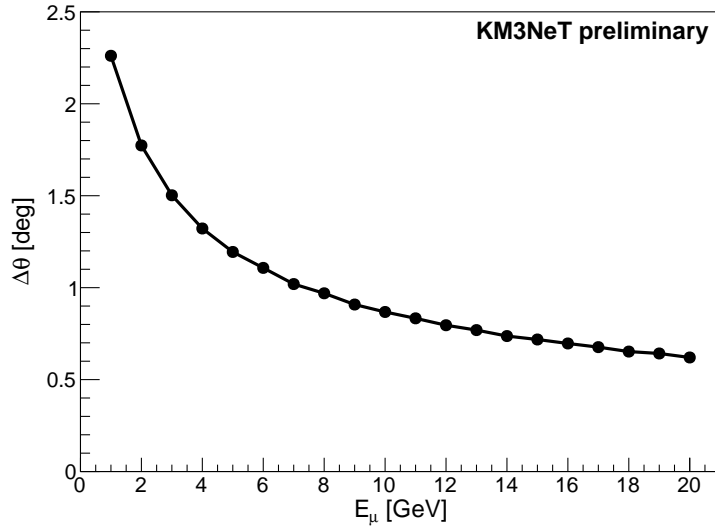


Figure 9.6: Limits on the muon direction resolution as a function of muon energy E_μ .

9.3.1 Energy resolution

The energy of an electron is usually estimated from the number of detected photons, as the light yield scales almost linearly with the initial electron energy. Resulting fluctuations are calculated analogously to the ‘total light yield’ method for the muons in Sec. 9.2.1.

The limiting relative energy resolution $\Delta E_e/E_e$ is shown in Fig. 9.7. In the overall limit, the dominant fluctuation comes from photon sampling, i.e. Poisson fluctuations in the total number of detected photons, which is $N_e^{\text{samp}}(E_e) = 20.8 \times E_e/\text{GeV}$ for the assumed photon detection probability.

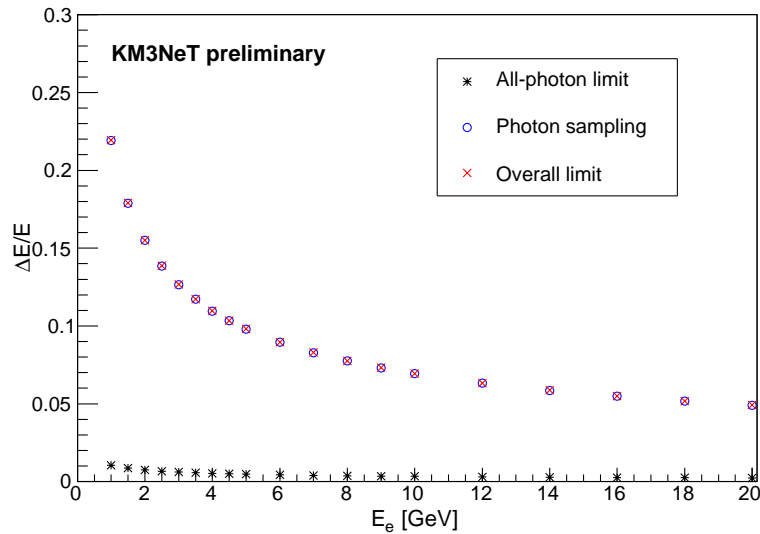


Figure 9.7: Relative energy errors $\Delta E/E$ as a function of electron energy E_e . All-photon limit (black), errors due to photon sampling (blue), and overall limit (red) are shown separately. Figure provided by C. W. James [158].

9.3.2 Direction resolution

The direction of an electromagnetic shower induced by an electron is usually reconstructed by fitting a trial shower axis to the observed photon signature. As discussed in Sec. 4.3, the photon signature of an electromagnetic shower is rotational symmetric around the shower axis and can be described by a one-dimensional function. Following the ‘forward problem’ guideline (see Sec. 9.1.3), fluctuations in the mean values of observed angular distribution are used to deduce limiting resolutions. This reconstruction approach is called ‘1D’ method.

Resulting limits are shown in Fig. 9.8. For comparison, the limit resulting from averaging the photon directions is also shown. This ‘2D’ method is used for reconstructing hadronic shower directions in Sec. 9.4.2. Reconstruction errors due to photon sampling dominate over the entire energy range. The resolution for the ‘1D’ method is significantly better than that for the ‘2D’ method due to exploiting the rotational emission symmetry. For $E_e = 5$ GeV, resolution limits of about 3.5° (10.5°) are obtained for the ‘1D’ (‘2D’) method.

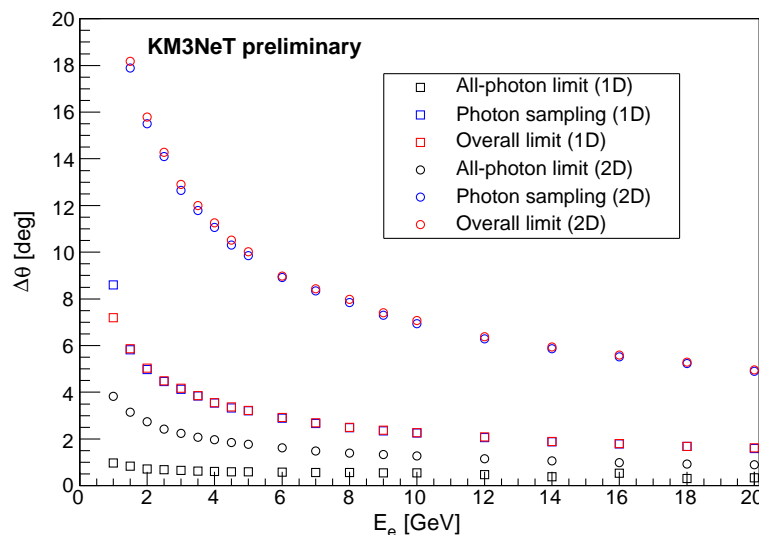


Figure 9.8: Angular errors $\Delta\theta$ as a function of electron energy E_e . All-photon limit (black), errors due to photon sampling (blue), and overall limit (red) are shown separately. Both the ‘1D’ method described in Sec. 9.3.2 (squares) and the ‘2D’ method described in Sec. 9.4.2 (circles) are used. Figure provided by C. W. James [158].

9.4 Hadronic showers

Hadronic showers are produced in every neutrino interaction, except for $\bar{\nu}_e$ scattering on atomic electrons. The energy E_h and direction \hat{p}_h of a hadronic shower are defined through four-momentum conservation applied to the neutrino interaction vertex (see Eq. 7.1). The characteristics of the mean properties of the emitted Cherenkov light are already discussed in Sec. 7.2.2, in particular, no significant differences are observed between hadronic showers extracted from ν CC, $\bar{\nu}$ CC and $\bar{\nu}$ NC events. Fluctuations in the Cherenkov light signature are used to estimate the limiting resolutions.

Compared to muons and electrons, hadronic showers suffer from the additional source of fluctuations due to different hadronic final states. The contributions from ‘propagation’ and ‘hadronic state’ are therefore estimated separately, as described in Sec. 7.2.2.

9.4.1 Energy resolution

The energy of a hadronic shower is also estimated from the number of detected photons. However, unlike in the case of electrons, the light yield from hadronic showers increases faster than linear with shower energy in the relevant energy range (see Sec. 4.4 and Sec. 7.2.2). This leads to a reduction of the relative energy error $\Delta E_h/E_h$ compared to the relative fluctuations in the number of detected photons $\Delta N_\gamma/N_\gamma$. The reduction factor is shown in Fig. 7.10.

The resulting relative energy resolution is shown in Fig. 9.9. Fluctuations due to hadronic final state dominate over the considered energy range, and the effect of photon sampling is relatively small, so that the overall limiting resolution is only slightly larger than the all-photon limit.

Intrinsic fluctuations of hadronic showers were also investigated in [121] for energies above 10 GeV, with results shown in Fig. 4.3 (right). The results for ‘propagation’ and ‘hadronic state’ are broadly similar taking into consideration that Fig. 4.3 (right) does not account for the energy reduction factor.

A further improvement in energy resolution for hadronic showers might be possible by including other observables than light yield. One such variable is for example the beamness B introduced in Sec. 7.2.2. However, this possibility is not considered here.

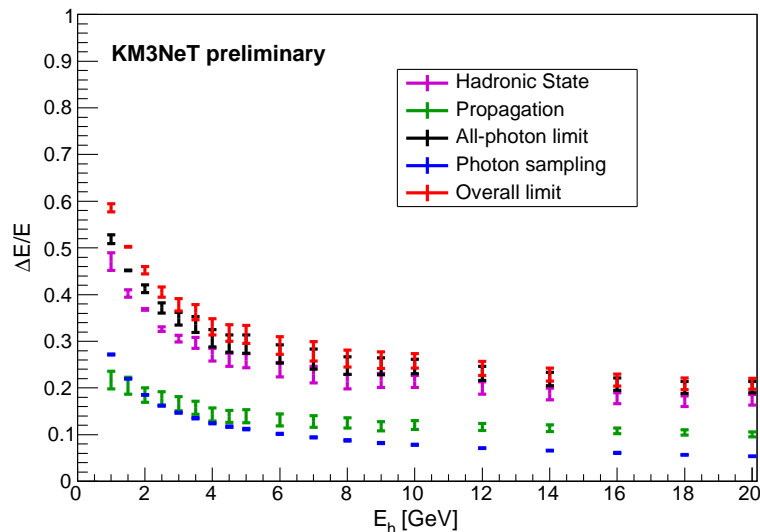


Figure 9.9: Relative energy errors $\Delta E/E$ as a function of hadronic shower energy E_h . Errors due to hadronic state (red), particle propagation (green), their combined effect in the all-photon limit (blue), and the additional variation introduced due to photon sampling (purple) in the overall limit (black) are shown separately. The means are calculated from the average between the G-GHEISHA and G-FLUKA results, and the error bars cover the range between them. Figure provided by C. W. James [158].

9.4.2 Direction resolution

Unlike in the case of electrons, the Cherenkov photon signature from a hadronic shower in the considered energy range is not rotationally symmetric around the shower axis, as hadronic showers typically consists of many non-collinear particles emerging from the neutrino interaction. Details on hadronic shower phenomenology are given in Sec. 7.2. A relatively robust method to estimate the hadronic shower direction is to use the mean photon direction in two dimensions. This reconstruction approach is denoted by ‘2D’ method.

The ‘2D’ method has to be applied if the individual particles in the hadronic shower cannot be resolved, such that it is not possible to follow a ‘multi-cone’ reconstruction approach (see Sec. 7.3.3). Neglecting the latter approach seems to be a reasonable assumption about the photocathode density of the planned ORCA detector.

The resulting direction resolution is shown in Fig. 9.10. In the all-photon limit, the fluctuations due to particle propagation dominate above $E_h \gtrsim 3$ GeV. The effect of photon sampling is significantly above the all-photon limit over the entire energy range, so that the overall limit is significantly higher than the all-photon limit.

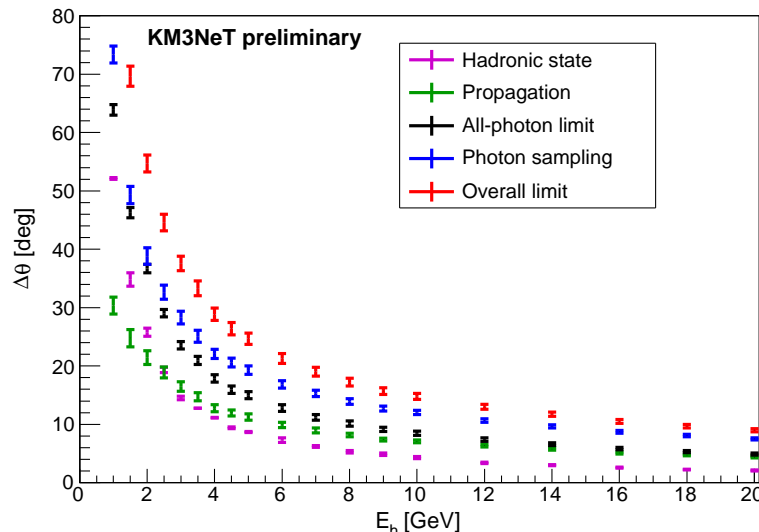


Figure 9.10: Angular errors $\Delta\theta$ (right) as a function of hadronic shower energy E_h . Errors due to hadronic state (red), particle propagation (green), their combined effect in the all-photon limit (blue), and the additional variation introduced due to photon sampling (purple) in the overall limit (black) are shown separately. The means are calculated from the average between the G-GHEISHA and G-FLUKA results, and the error bars cover the range between them. Figure provided by C. W. James [158].

9.5 Resolutions of electron and muon neutrino charged-current events

Using the results for muons, electrons, and hadronic showers of the previous sections, limits on the reconstruction accuracy of $\vec{\nu}_e$ CC and $\vec{\nu}_\mu$ CC events in the energy range of 1–20 GeV can be deduced⁵¹.

First, the degree of correctness of how the hadronic shower results are combined with the results on muons and electrons to resolutions limits on the initial neutrino, in particular its direction, is discussed. Then, three different methods for reconstructing the initial neutrino properties are investigated. Finally, the resolution of the neutrino interaction inelasticity y is deduced.

9.5.1 Selecting hadronic showers

For the studies of the intrinsic limits on neutrino energy and direction, pre-simulated hadronic showers extracted from $\vec{\nu}_\mu$ CC events are ‘implanted’ into other neutrino in-

⁵¹ The reconstruction accuracy for NC events from all flavours can be more-simply deduced from the interaction kinematics and the limits on hadronic showers. Brief investigations have shown that the intrinsic energy and direction resolutions of hadronic showers induced by Z^0 bosons are very similar to that induced by W^\pm bosons (cf. Sec. 7.2.2).

teractions than those that the hadronic showers are originally extracted from. Only the energy of the selected hadronic shower is required to be similar to the hadronic energy ($E_h = y \times E_\nu$) in the neutrino interaction. While this is computationally efficient, it neglects any potential correlations between neutrino interaction parameters – such as E_ν , y and Q^2 (Eq. 2.2) – and the particular properties of the hadronic final state (other than E_h) that might be correlated both with energy/direction reconstruction errors of the hadronic shower. These correlations are lost when selecting hadronic final states using E_h only.

In order to investigate this, the correlation between different properties are calculated. The correlation between the mean photon direction (\sim shower direction, see Sec. 9.4.2) and Q^2 is found to be small, with correlation coefficient $|c| < 0.05$. The correlation between N_γ and Q^2 is slightly larger ($c \approx -0.15$). This is still much smaller than the correlation between N_γ and the mean photon direction ($c \approx -0.5$, see Fig. 9.11), which is accounted for in the results of Sec. 9.5.

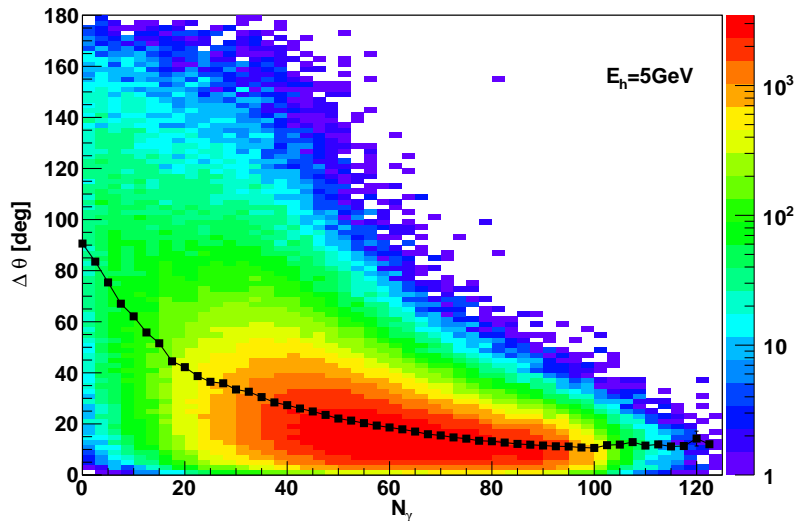


Figure 9.11: Angular error $\Delta\theta$ in the ‘overall limit’ (see Sec. 9.1.1) as a function of the expected number of detected Cherenkov photons N_γ for hadronic showers with $E_h = 5$ GeV. Black markers represent the mean $\Delta\theta$ per N_γ bin. In total, 1000 hadronic final states are simulated with 1000 repetitions. The correlation coefficient is about $c \approx -0.5$.

Fig. 9.12 compares the angular error $\Delta\theta$ obtained using the method described in Sec. 9.5.2 with that using the exact hadronic final state from each interaction, i.e. accounting for all correlations. A very good agreement is achieved.

A further approximation is required when $E_h (= y E_\nu)$ or $E_{e,\mu}$ does not equal one of the simulated energies of Tab. 9.1, in which case the expected properties $\Delta E/E$, $\Delta\theta$ must be interpolated between simulated values. When $E < 1$ GeV, the values of $\Delta\theta^{\text{all}}$ and $\Delta E^{\text{all}}/E$ are conservatively set to their values at 1 GeV. In the case of energy resolution in the overall limit, uncertainties due to photon sampling are extrapolated according to the photon statistics ($\sqrt{N_\gamma}$). Uncertainties due to muon track length determination are assumed to be independent of initial muon energy. The effects of these approximations are included in Fig. 9.12 for $E_\nu = 3$ GeV, $y = 0.2$ and $y = 0.8$. The agreement with full simulations is only slightly worse.

As the effect of the neglected correlations is small, they are ignored for the intrinsic limits for neutrino reconstruction accuracy.

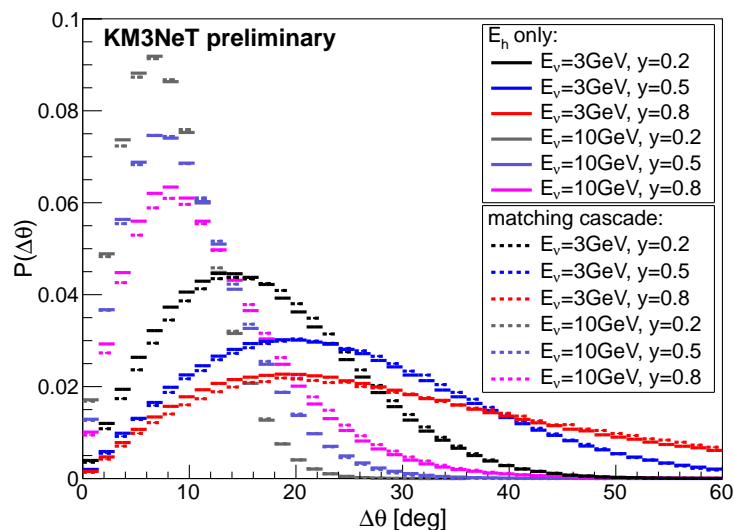


Figure 9.12: Comparison of angular error $\Delta\theta$ calculated using the method described in Sec. 9.5.2, where hadronic showers are selected using E_h only, with that when simulating the particular hadronic final state matching each neutrino interaction.

9.5.2 Using naive energy and momentum conservation

The neutrino energy E_ν and normalised direction \hat{p}_ν can be reconstructed using the interaction kinematics of Eq. 7.1, i.e. by combining the estimated electron/muon properties ($E_{e,\mu}$, $\hat{p}_{e,\mu}$) with that of the hadronic shower (E_h , \hat{p}_h) using naive energy and momentum conservation (neglecting masses):

$$E_\nu = E_{e,\mu} + E_h, \quad \hat{p}_\nu \approx \frac{1}{E_\nu} (E_{e,\mu} \hat{p}_{e,\mu} + E_h \hat{p}_h). \quad (9.5)$$

Note that the assumption about the hadronic shower momentum magnitude $|\vec{p}_h|$ not being reconstructable requires using the relative energies to weight the reconstructed directions of each component. Here, Eq. 9.5 assumes $E_h = |\vec{p}_h|$, whereas necessarily $|\vec{p}_h| > E_h$ from the definition of Eq. 7.1. Fig. 9.13 shows the ratio $E_h/|\vec{p}_h|$ as a function of E_h . Fluctuations in this ratio can be considered as intrinsically limiting fluctuations. It has been decided to not correct Eq. 9.5 for the expected ratio. While $|\vec{p}_h| > E_h$ suggests a greater weighting of \hat{p}_h , the larger error on \hat{p}_h compared to $\hat{p}_{e,\mu}$ suggests that the coefficient of \hat{p}_h should be down-weighted, with the total effect likely being small. The general situation, of choosing arbitrary weights between $\hat{p}_{e,\mu}$ and \hat{p}_h , is illustrated in Fig. 9.14.

For each simulated neutrino event, the MC truth values of the parameters $E_{e,\mu}$, $\hat{p}_{e,\mu}$, E_h , and \hat{p}_h are taken from the **gSeaGen** simulations (see Sec. 7.1 for a characterisation of **gSeaGen** events), while the errors in reconstructing them are calculated by considering the leptonic and hadronic components separately, i.e. it is assumed that the photons from the lepton can be identified. For muon tracks, resolutions from the track length measurement (Sec. 9.2.1) are used. For electrons, resolutions from the ‘1D’ method (Sec. 9.3.2) are used. Correlations between energy and direction errors for each component are taken into account. However, the exact hadronic final states of each neutrino interaction are not used, but other pre-simulated hadronic showers are ‘implanted’. In Sec. 9.5.1, it is shown that the differences between this procedure and the correct procedure of simulating the exact hadronic final state from each interaction (computationally significantly less efficient) is small, so they are here ignored. Nevertheless, neutrino limits depending on components,

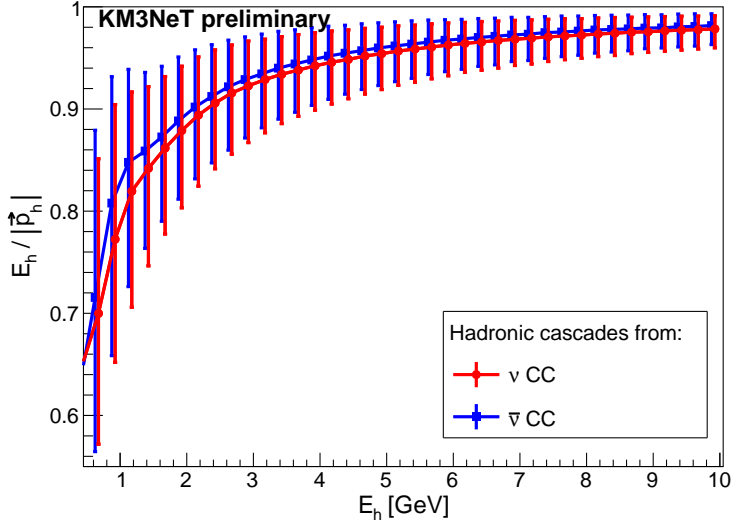


Figure 9.13: Ratio $E_h/|\vec{p}_h|$, calculated according to Eq. 7.1, as a function of E_h for hadronic showers extracted from both ν CC and $\bar{\nu}$ CC events separately. Error bars represent 16% and 84% quantiles.

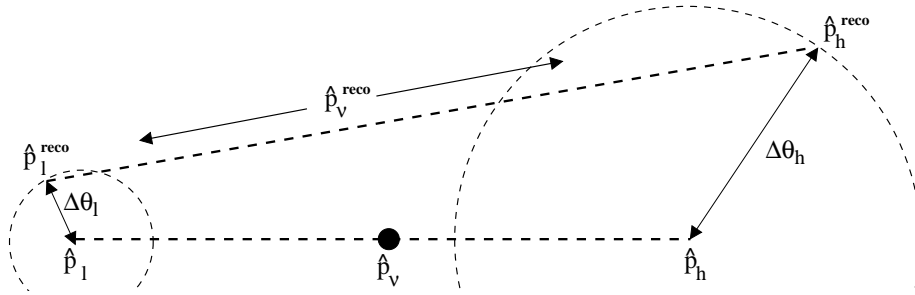


Figure 9.14: Sketch illustrating the reconstruction of a neutrino direction \hat{p}_ν . The true lepton \hat{p}_l and hadronic directions \hat{p}_h are reconstructed in directions \hat{p}_l^{reco} and \hat{p}_h^{reco} with characteristic errors $\Delta\theta_l$ and $\Delta\theta_h$. The reconstructed neutrino direction $\hat{p}_\nu^{\text{reco}}$ must then lie on the vector defined by these two points. Sec. 9.5.2 and 9.5.3 essentially differ in the method for choosing a point on this vector. Figure provided by C. W. James [158].

especially hadronic showers, with $E < 1$ GeV should be taken with caveats, as extrapolated results have to be used (see Sec. 9.5.1).

Fig. 9.15 and Fig. 9.16 show the resulting limits on the neutrino energy E_ν and direction resolution for $\bar{\nu}_e$ CC and $\bar{\nu}_\mu$ CC events as a function of E_ν and inelasticity y . Due to the large differences between resolutions for electrons/muons and hadronic cascades, the neutrino resolutions depend strongly on inelasticity y . With increasing y the contribution from the hadronic shower increases and consequently the resolution of the neutrino gets worse due to the larger errors for hadronic showers than for electrons/muons. In addition, the resolutions are very similar for $\bar{\nu}_e$ and $\bar{\nu}_\mu$ CC events, apart from the overall limit on direction resolution, which is slightly different and is shown separately. For direction resolution in Fig. 9.16, the 68.27% quantiles of the scattering angle $\phi_{\nu,l}$ between neutrino and lepton is also shown. The feature in direction resolution visible at $E_\nu \times y \approx 0.3$ is due to a change in recoil mass (different interaction modes) and therefore different $E_h/|\vec{p}_h|$, as already mentioned in Sec. 7.1.2.

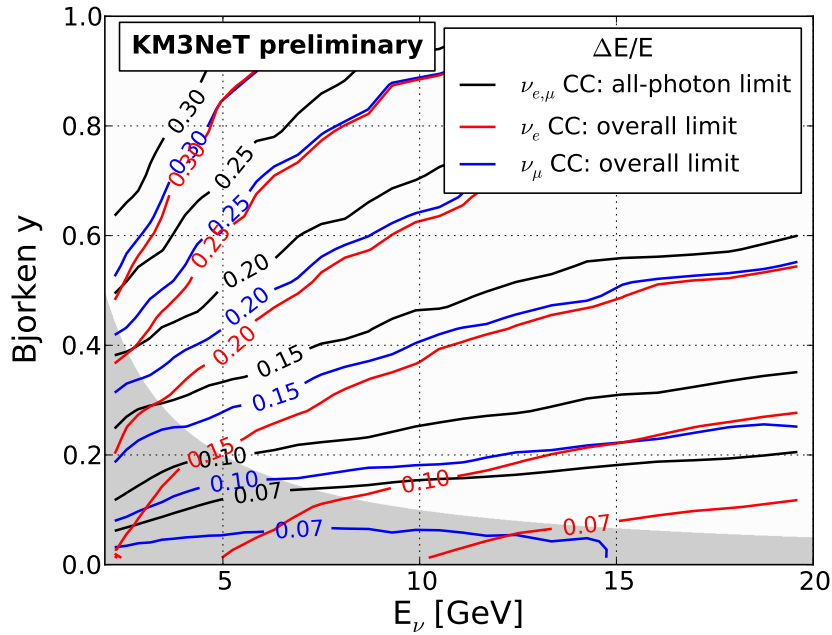


Figure 9.15: Limitations on relative neutrino energy resolution as a function of neutrino energy E_ν and inelasticity (Bjorken y). Resolutions are shown as contour lines for $\vec{\nu}_{e,\mu}$ CC in all-photon limit (black), for $\vec{\nu}_e$ CC in overall limit (red), and for $\vec{\nu}_\mu$ CC in overall limit (blue). The region with $E_h < 1$ GeV (grey shading) has been calculated using extrapolated results, and should be taken with caveats.

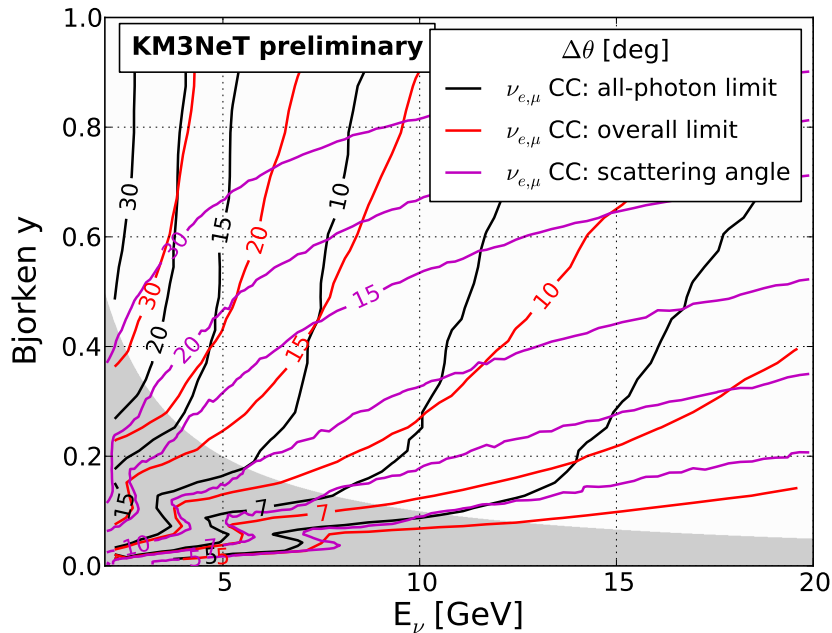


Figure 9.16: Limitations on neutrino direction resolution for $\vec{\nu}_{e,\mu}$ CC events as a function of neutrino energy E_ν and inelasticity (Bjorken y). Resolutions for all-photon limit (black) and overall limit (red) are separately shown as contour lines. This is compared to the intrinsic scattering angle between the outgoing lepton and the neutrino (purple). See Fig. 9.15 for explanations of grey shading area.

Fig. 9.17 and Fig. 9.18 show the neutrino energy and direction resolutions for ν_e CC, $\bar{\nu}_e$ CC, ν_μ CC and $\bar{\nu}_\mu$ CC events as a function of E_ν integrated over the according inelasticity distributions. Both energy and direction resolutions are better for $\bar{\nu}_{e,\mu}$ CC than for $\nu_{e,\mu}$ CC events, since the former have on average smaller inelasticity. Energy resolution for $\bar{\nu}_\mu$ CC is slightly better than for $\bar{\nu}_e$ CC because the track length measurement shows less fluctuations than the light yield measurement for electrons. For comparison, in case of measuring only the lepton energy (and ignoring the hadronic cascade energy comparatively), the neutrino energy resolution is significantly worse and is nearly energy-independent with about $\Delta E/E \sim 0.5$ (~ 0.3) for $\nu_{e,\mu}$ ($\bar{\nu}_{e,\mu}$) CC events. These relative fluctuations correspond

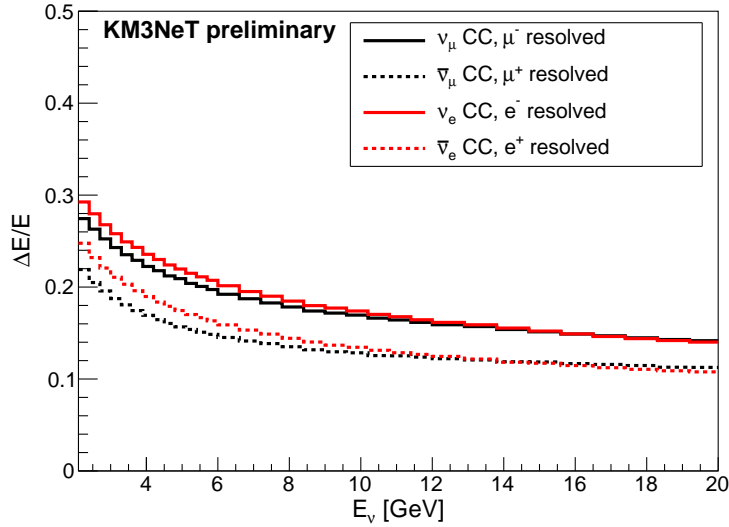


Figure 9.17: Relative energy resolution for $\nu_\mu/\bar{\nu}_\mu$ CC (black) and $\nu_e/\bar{\nu}_e$ CC (red) events. Neutrinos are shown as solid lines and antineutrinos as dashed lines.

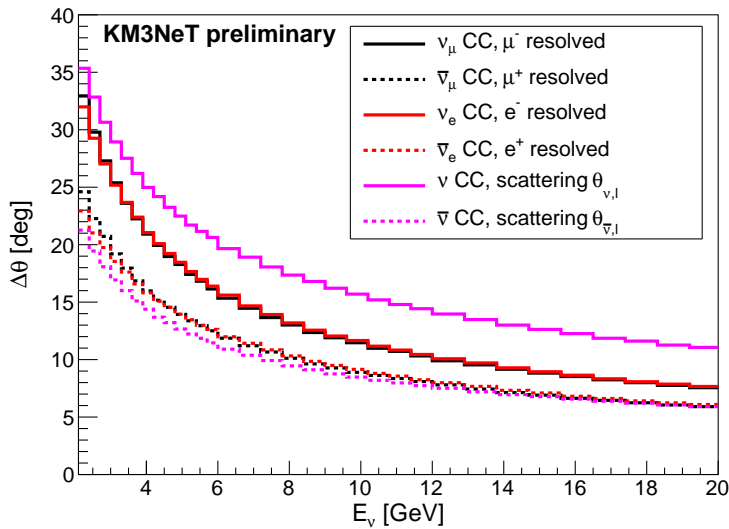


Figure 9.18: Direction resolution for $\nu_\mu/\bar{\nu}_\mu$ CC (black) and $\nu_e/\bar{\nu}_e$ CC (red) events. Neutrinos are shown as solid lines and antineutrinos as dashed lines. For comparison, the scattering angles $\phi_{\bar{\nu},l}$ between the (anti)neutrino and lepton are shown as purple lines.

to the variation in the inelasticity y distributions. While the direction resolution for $\nu_{e,\mu}$ CC events is significantly better than the scattering angle $\phi_{\nu,l}$ between neutrino and lepton, the direction resolution for $\bar{\nu}_{e,\mu}$ CC events is slightly worse than $\phi_{\bar{\nu},l}$.

Using the hadronic shower for direction reconstruction is limited dominantly by the large error $\Delta\theta_h$ on the direction of the hadronic shower. This can be inferred from Fig. 9.19, where the neutrino direction resolution limits are compared for different cases of using reconstructed energies and directions as well as MC truth properties. Compared to using reconstructed energies and directions, the usage of MC truth energies does not improve the resulting neutrino direction resolution⁵², while the usage of MC truth directions leads to a significant improvement. The inability to reconstruct $|\vec{p}_h|$ and assuming $E_h = |\vec{p}_h|$ in Eq. 9.5 has only a significant effect for low E_h , i.e. at low inelasticity y and low E_ν , as already expected from Fig. 9.13. Consequently, these two further factors are subordinated in most of the relevant phase space region: the fluctuation of E_h^{reco} , which leads to errors in $\hat{p}_\nu^{\text{reco}}$ through Eq. 9.5; and the inability to reconstruct $|\vec{p}_h|$, which necessitates an assumption about $E_h/|\vec{p}_h|$. An improvement therefore might be made by using \hat{p}_h^{reco} only to define the plane of the interaction – this is investigated in the next section.

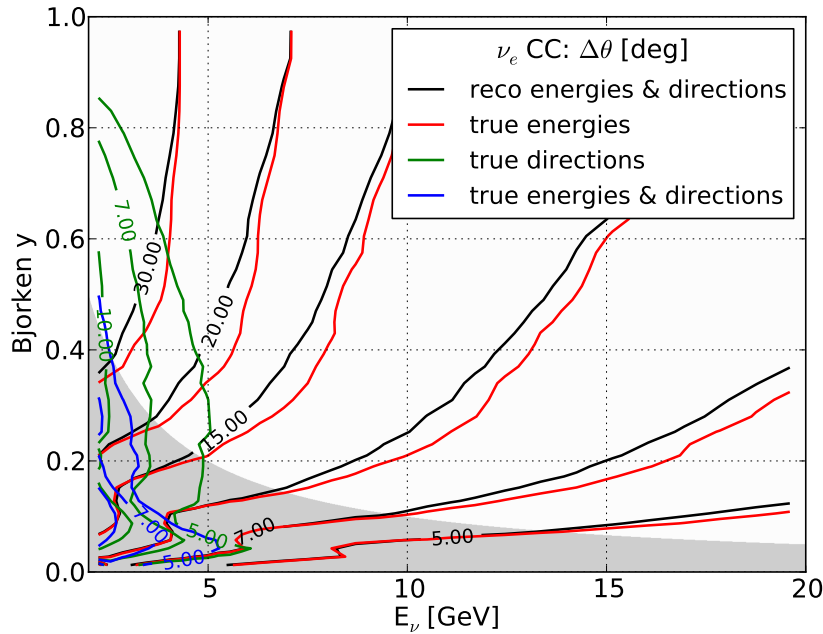


Figure 9.19: Limitations on neutrino direction resolution for ν_e CC events as a function of neutrino energy E_ν and inelasticity (Bjorken y) are shown as contour lines for different cases: using reconstructed energies and directions (black), using MC truth energies for E_e and E_h (red), using MC truth directions for \hat{p}_e and \hat{p}_h (green), and using MC truth E_e , E_h , \hat{p}_e and \hat{p}_h (blue). If reconstructed energies or directions are required, the ‘overall limits’ (see Sec. 9.1.1) are used. For $\bar{\nu}_e$ CC and $\bar{\nu}_\mu$ CC events, limiting resolutions look very similar.

⁵² When using MC truth energies, in particular E_h , and reconstructed directions, the neutrino direction becomes even slightly worse (up to $\sim 10\%$) compared to using the reconstructed energies for the weights in Eq. 9.5, because N_γ and $\Delta\theta$ are correlated for a fixed E_h (correlation coefficient $c \approx -0.5$, see Fig. 9.11), so that faint hadronic showers with small N_γ and large $\Delta\theta$ are naturally down weighted when using reconstructed energies ($\propto N_\gamma$).

9.5.3 Using expected neutrino-lepton scattering angle

An alternative neutrino direction reconstruction method is to use the expected median scattering angle $\text{med}[\phi_{\nu,l}]$ between neutrino and lepton. Such a method will tend to improve the resolution on \hat{p}_ν if the relative scatter in the angle $\phi_{\nu,l}$ about $\text{med}[\phi_{\nu,l}]$ is small compared to the combined fluctuations in energy error of the lepton and the hadronic shower as well as the ratio $E_h/|\vec{p}_h|$. Here, $\text{med}[\phi_{\nu,l}]$ is calculated from the reconstructed energies $E_{e,\mu}^{\text{reco}}$ and E_h^{reco} by setting $\text{med}[\phi_{\nu,l}(E_{e,\mu}^{\text{reco}}, E_h^{\text{reco}})]$ to $\text{med}[\phi_{\nu,l}(E_{e,\mu}^{\text{true}}, E_h^{\text{true}})]$, following the ‘forward problem’ guideline.

Fig. 9.20 shows the neutrino direction resolution limits for ν_e CC events⁵³ as a function of E_ν and inelasticity y , relative to those shown in Fig. 9.16. For a large region of parameter space in the E_ν - y plane, this method provides a better neutrino direction reconstruction (ratio < 1), with up to $\sim 25\%$ improvement. It does not perform well at large y due to an intrinsically large scatter in $\phi_{\nu,l}$ (see Fig. 7.4).

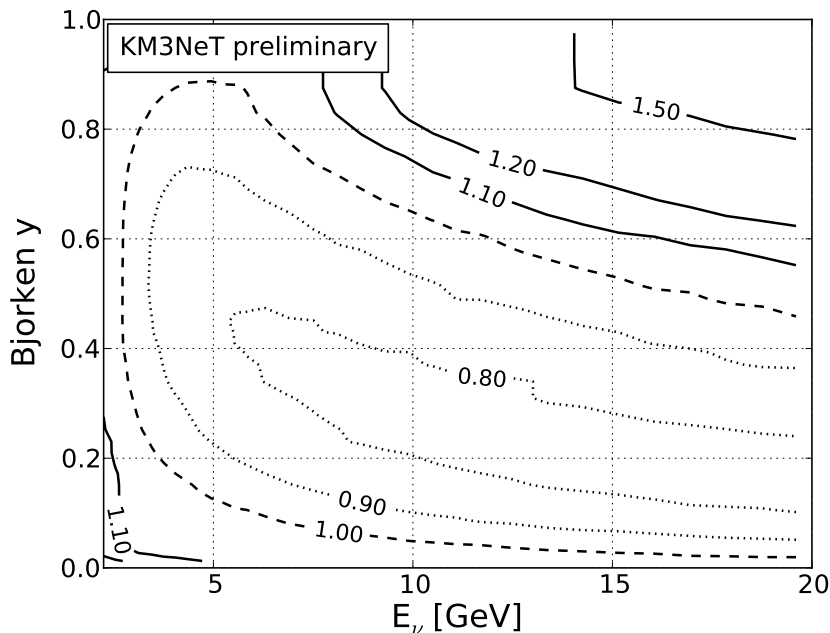


Figure 9.20: Ratio of neutrino direction resolution limits for applying the expected neutrino-lepton scattering angle method over the limits for applying the energy/momentum conservation method for ν_e CC events in the overall limit as a function of E_ν and inelasticity (Bjorken y).

9.5.4 Treating electron neutrino events as one single shower

If the detector is not able to distinguish between photons from the electron and the hadronic shower in $\vec{\nu}_e$ CC events, the reconstruction must treat all photons as coming from one single shower. This corresponds to reconstructing the direction from all photons using the ‘2D’ method introduced in Sec. 9.4.2. Since this method simply averages the directions of all detected unscattered photons, it can be reproduced by using the ‘2D’ results on isolated components and using the number N_γ of detected photons from each component as weights in the combination. Any such reconstruction must necessarily assume an inelasticity y distribution, which governs the relationship between N_γ and original E_ν . Here, this distribution is taken from ν_e CC and $\bar{\nu}_e$ CC events in the ratio 2.5:1, approximately corresponding to the interaction rate of atmospheric neutrinos in this energy range.

⁵³ For $\bar{\nu}_e$ and $\vec{\nu}_\mu$ CC events, the ratios of both resolution limits look very similar.

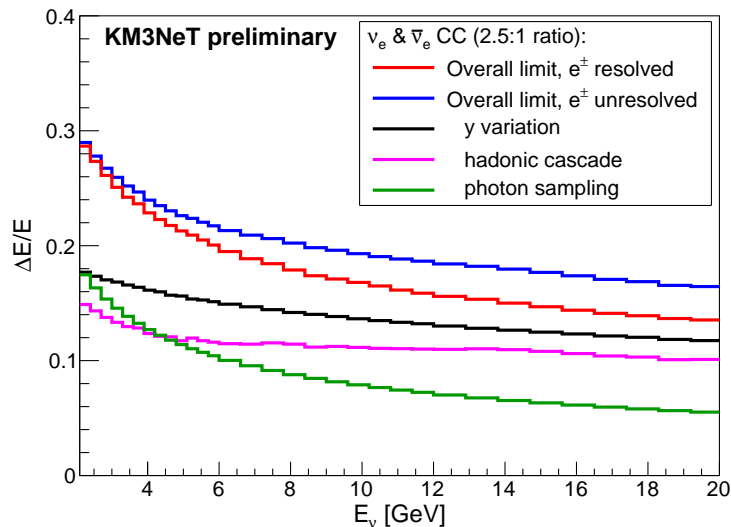


Figure 9.21: Relative neutrino energy resolution for ν_e CC and $\bar{\nu}_e$ CC events (ratio 2.5:1) in the overall limit, assuming that photons from the outgoing e^\pm can (red) and cannot (blue) be resolved. For the unresolved case, contributions from variation due to unknown inelasticity y (black), hadronic cascade (purple) and photon sampling (green) are shown separately.

In Fig. 9.21, the resulting limits on the neutrino energy resolution for ν_e CC and $\bar{\nu}_e$ CC events (ratio 2.5:1) are compared to those obtained when the photons from the electron/positron can be resolved. Due to the lack of knowledge about the source of the photons, the energy resolution $\Delta E/E$ worsens from 16.8% to 19.3% for $E_\nu = 10$ GeV. This deterioration emphasises the importance of the capability to identify the electron in $\bar{\nu}_e$ CC events in order to allow for more advanced reconstruction procedures.

In the unresolved photon source case, contributions from different sources of variation are separately shown in Fig. 9.21. The variation due to the unknown interaction inelasticity y is calculated by fixing the number of photons from the electron and hadronic showers to their mean values (Sec. 9.3.1 and Sec. 9.4.1, respectively) and varying y using the truth distribution. The variation due to photon sampling is given by the average Poisson error on N_γ (summed over both components). The remaining variation is attributed to the contribution from the hadronic showers (hadronic state and propagation) and is calculated by subtracting both previously mentioned contributions in quadrature from the total energy resolution. Additionally, when the photon source is unresolved, the energy resolution for a mixed composition of ν_e and $\bar{\nu}_e$ becomes worse than a simple linear combination of their individual results would suggest, since fluctuations of N_γ about the joint mean are necessarily larger. The light yield of $\bar{\nu}_e$ CC events is about $\sim 10\%$ larger than that of ν_e CC events at $E_\nu = 5$ GeV and difference between both decreases slightly with energy, as can be seen in Fig. 9.22.

Variations in inelasticity y affect the ‘ e^\pm unresolved’ case most obviously by smearing the relation between E_ν and the expected N_γ for that energy, but is still non-zero in the ‘ e^\pm resolved’ case, where fluctuations in y imply that hadronic and electromagnetic energies must be estimated independently. This is why the resolutions for both cases are identical at low energies: when E_ν is small, almost all light comes from the outgoing e^\pm ; the hadronic energy E_h is not directly observable; and both cases reduce to measuring E_e only, and relating that to E_ν based purely on the expected value of y .

In case of direction resolution, when the photon source is unresolved, mainly neutrino

interactions with low $y \lesssim 0.25$ get worse (see Fig. 9.23), as the electron cannot be reconstructed using the more accurate ‘1D’ method (see Sec. 9.3 for a comparison of ‘1D’ and ‘2D’ method for electrons). Without the additional knowledge about the source of the photons, the direction resolution deteriorates from 11.6° (9.2°) to 11.8° (10.3°) for ν_e CC ($\bar{\nu}_e$ CC) at $E_\nu = 10$ GeV, as shown in Fig. 9.24.

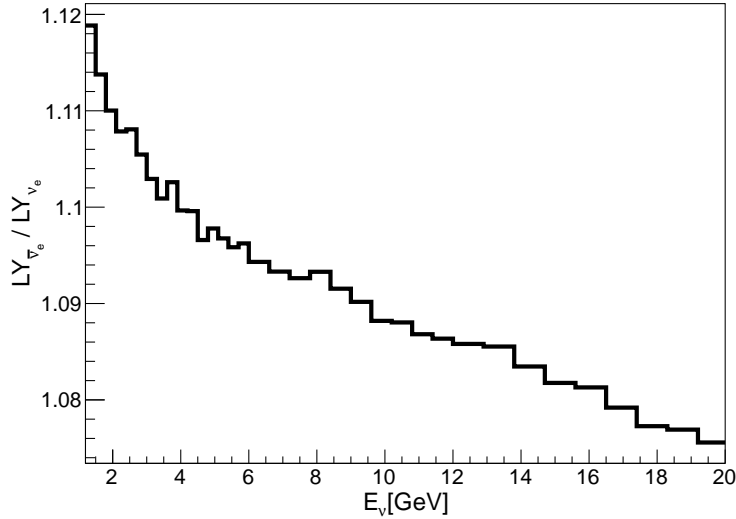


Figure 9.22: Light yield ratio of ν_e and $\bar{\nu}_e$ CC events as a function of neutrino energy E_ν . This is calculated by convoluting the light yield ratio of hadronic and electromagnetic showers (see Fig. 7.10, G-GHEISHA) with the inelasticity y distribution of ν_e and $\bar{\nu}_e$ CC events (see Fig. 7.2).

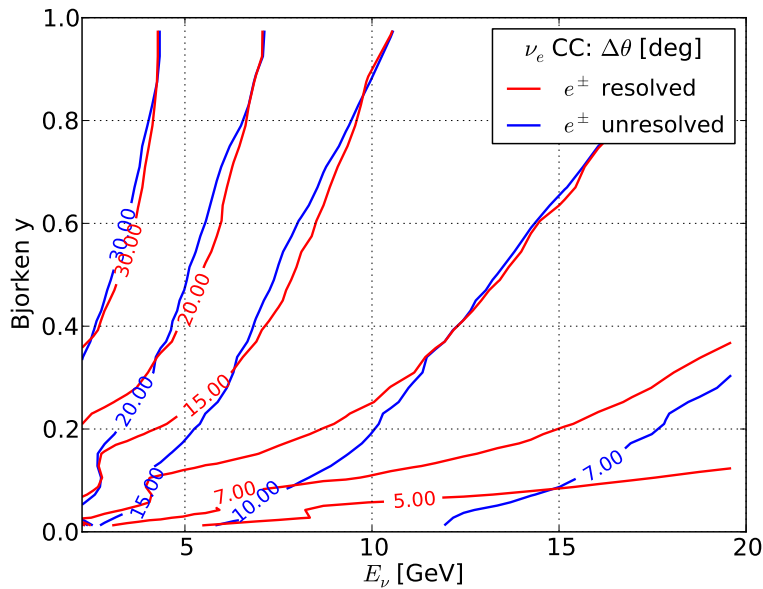


Figure 9.23: Limitations on the neutrino direction resolution for ν_e CC events as a function of neutrino energy E_ν and inelasticity (Bjorken y) for the case that photons from the e^\pm can be resolved and using the ‘1D’ method for the electron (red) and the case of not resolving photons from the e^\pm and using the ‘2D’ method applied to all detected photons (blue).

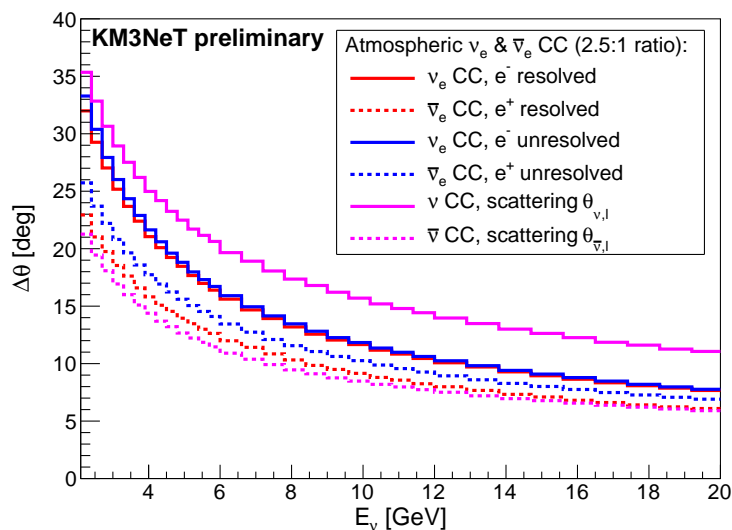


Figure 9.24: Direction resolution for ν_e and $\bar{\nu}_e$ CC events in the case that the photons from the e^\pm can be resolved and using the ‘1D’ method for the electron (red) and the case of not resolving the photons from the e^\pm and using the ‘2D’ method applied to all detected photons (blue). Neutrinos are shown as solid lines and antineutrinos as dashed lines. For comparison, the 68.27% quantile of the scattering angle $\phi_{\nu,l}$ between neutrino and lepton is shown as purple lines.

9.5.5 Interaction inelasticity resolution

The different differential cross sections of ν CC and $\bar{\nu}$ CC interactions allow to statistically separate both interaction types, which will add significance to the NMH measurement (see Sec. 3.2.5). The relative energy resolutions obtained in Sec. 9.2, Sec. 9.3 and Sec. 9.4 can be readily converted into resolution limits on the interaction inelasticity y , using:

$$y_{\text{reco}} = \frac{E_h^{\text{reco}}}{E_h^{\text{reco}} + E_{e,\mu}^{\text{reco}}}. \quad (9.6)$$

Fig. 9.25 shows both the MC truth y_{true} distributions for ν_μ CC as well as $\bar{\nu}_\mu$ CC events and the y_{reco} distributions in the overall limit for $E_\nu = 5$ GeV. The dip in the last bin for $y \rightarrow 1$ is caused by the finite muon mass. For $\bar{\nu}_e$ CC events, the distributions are very similar. Despite the relatively poor resolution of E_h , the differences between the y_{reco} and y_{true} distributions are small. This is partly due to the lack of structure in the y distribution, particularly for $\nu_{e,\mu}$. The other effect is definitional: from Eq. 9.6, the error in y_{reco} tends to zero with both E_h and E_e .

The statistical separation between the y distributions from neutrinos $P_\nu(y)$ and antineutrinos $P_{\bar{\nu}}(y)$ can be characterised by the correlation coefficient c , by defining the separation power s as:

$$s \equiv 1 - c = 1 - \frac{\int_0^1 P_\nu(y) P_{\bar{\nu}}(y) dy}{\sqrt{\int_0^1 P_\nu^2(y) dy \int_0^1 P_{\bar{\nu}}^2(y) dy}}. \quad (9.7)$$

Perfect separation is indicated by $s = 1$, while no separation corresponds to $s = 0$. Following the same procedure as in Sec. 9.5.2, the separation power as a function of E_ν both with and without reconstruction errors is shown in Fig. 9.26. The separation power of $\bar{\nu}_e$ CC and $\bar{\nu}_\mu$ CC events is nearly identical due to very similar energy resolutions. Above 5 GeV, the relative reduction in separation power for both all-photon and overall reconstruction limits is 5% or less compared to using the y_{true} distributions.

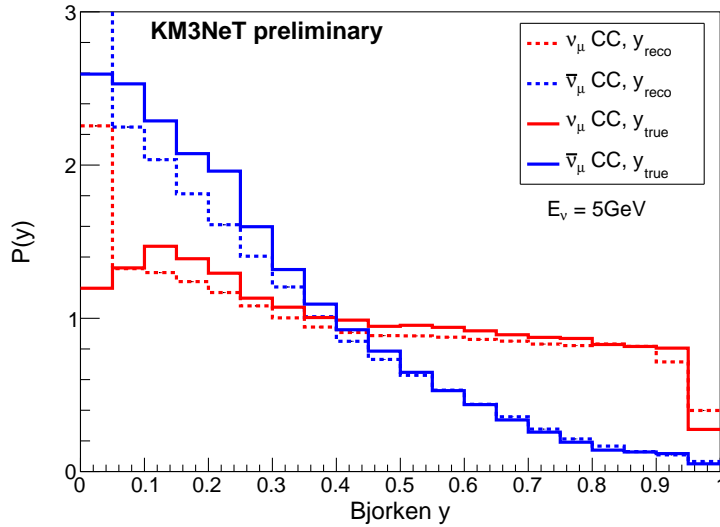


Figure 9.25: Probability distributions P of inelasticity (Bjorken y) for ν_μ CC (red) and $\bar{\nu}_\mu$ CC (blue) events taken from **gSeaGen** simulations (see Sec. 6.1), both with (y_{reco} , dashed) and without (y_{true} , solid) reconstruction errors applied.

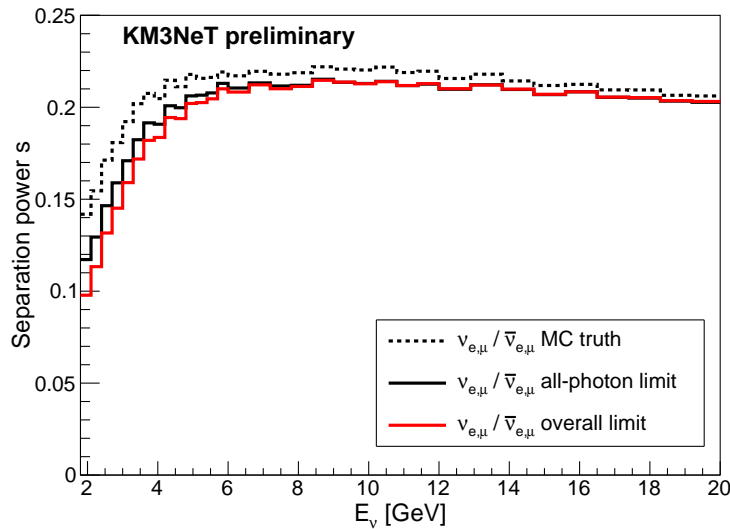


Figure 9.26: Separation power s (Eq. 9.7) between $\nu_{e,\mu}$ and $\bar{\nu}_{e,\mu}$ for using MC truth y_{true} and reconstructed y_{reco} in the all-photon limit and overall limit.

9.6 Conclusions, implications and discussion

The limits derived here from intrinsic fluctuations in Cherenkov photon signatures indicate the best reconstruction accuracies achievable with an ORCA-like detector. While leptons show comparatively small fluctuations and therefore good reconstruction accuracies (electrons 10%/3.5° and muons 5%/1° in energy/direction resolution for $E_{e,\mu} = 5$ GeV), hadronic showers are subject to much larger fluctuations resulting in significantly worse reconstruction resolutions (34%/26° for $E_h = 5$ GeV).

Despite the optimistic and idealising assumptions, the resulting limits for shower-like

neutrino events are close to the resolutions obtained using a full detector simulation and applying a full shower reconstruction, as is discussed in Sec. 12.5.2. This justifies the assumptions made here.

The main result is that the energy reconstruction resolution of few-GeV neutrinos is primarily dictated by the intrinsic fluctuations in the number of emitted Cherenkov photons, and the uncertainty due to detecting only a small fraction of them plays only a minor role. The dominant fluctuations in light yield are due to different final-state hadrons in conjunction with the variation of inelasticity y in neutrino interactions (see Fig. 9.21). The neutrino direction resolution is dominated by the large errors in hadronic shower direction reconstruction, which is mainly driven by photon statistics.

The major implications of these studies are:

- **Optimal photocathode density for NMH determination**

Assuming a fixed number of total photocathode area (or equivalent number of DOMs and therefore money), a larger and sparser detector layout (i.e. reducing the available photon statistics) than the assumed ORCA benchmark detector might be more optimal for the NMH determination. This would increase the number of detected events at only a very little deterioration in energy resolution. As the energy resolution is more relevant for the NMH determination in the $\bar{\nu}_e$ channel ($\Delta E^{\text{limit}}/\Delta E^{\bar{\nu}_e \text{ NMH}} \gg \Delta\theta^{\text{limit}}/\Delta\theta^{\bar{\nu}_e \text{ NMH}}$, see Sec. 3.2.3), the deterioration in direction resolution due to less detected photons is of little consequence.

This conclusion is in agreement with the results of the ORCA detector layout optimisation (based on a full simulation of the detector including backgrounds and applying full event reconstructions) performed in the ‘Letter of Intent’ [3] as well as in Sec. 13.2.3. In other words, the results presented here explain the underlying reason for the outcome of the detector layout optimisation.

Historically, this conclusion was obtained before the ORCA detector layout optimisation was performed, and was in fact the reason why sparser and not denser detector layouts were considered.

- **Sensitivity to physical uncertainties**

The downside of the sensitivity to the intrinsic fluctuations in the emitted Cherenkov light signature is that experiments such as ORCA are sensitive to systematic uncertainties in the neutrino interaction and hadronisation process. This consideration underlines the fact that further work on improving these models are essential for reducing the systematic uncertainties for the NMH measurement with an ORCA-like detector.

On the other hand, if an ORCA-like detector is affected by systematic uncertainties in modelling these processes, then the data collected with such a detector might help to constrain these models. However, this would require dedicated studies.

- **No significant degradation in neutrino-antineutrino separation power**

Despite the relatively poor resolution of the hadronic shower energy, the separation power between ν CC and $\bar{\nu}$ CC events is not significantly degraded in case of using the intrinsic limits compared to using MC truth energies. Hence, also the possible improvement in NMH sensitivity due to $\nu/\bar{\nu}$ separation is not significantly affected.

- **Strong correlation between energy and direction errors**

Due to the large differences in resolutions between leptons and hadronic showers, the neutrino resolutions depend strongly on the interaction inelasticity y and are therefore different for ν CC and $\bar{\nu}$ CC events. Consequently, energy and direction resolutions are strongly correlated via the inelasticity y .

In addition, the results obtained here using idealised reconstruction methods contain useful pointers as how to best reconstruct events in a real ORCA-like detector. On the one hand, the studies here simply verify why existing methods have found to be optimal, e.g. that the muon energy reconstruction is best-performed by estimating the track length and not the total light yield (see Fig. 9.4). On the other hand, new methods are presented that are expected to be able to improve the reconstruction performance. The neutrino direction reconstruction method presented in Sec. 9.5.3 can improve the achievable resolution in large regions of the E_ν - y phase space, in particular for energies relevant for the NMH determination (see Fig. 9.20).

Furthermore, the difference in direction resolution between the ‘2D’ and ‘1D’ methods for electrons (see Fig. 9.8) highlights the importance of being able to fit a Cherenkov cone to such events. This suggests that the possibility of doing so also for a subset of hadronic showers producing a significant cone structure (due to several collinear particles, or one leading particle) should be investigated. The effect on the neutrino direction resolution due identifying the leading particle in the hadronic shower is discussed in Sec. 7.3.1.

All more sophisticated energy and in particular direction reconstruction methods require the differentiation between photons from the outgoing lepton and the hadronic shower. Most of the limiting resolutions derived here make this assumption. Without this capability the resolutions get worse (see Sec. 9.5.4). This emphasises the importance of resolving the outgoing lepton in $\bar{\nu}_{e,\mu}$ CC interactions, a capability that is demonstrated to be feasible for ORCA also in $\bar{\nu}_e$ CC events (see Sec. 12).

Applicability to ice-based Cherenkov detectors

The limits derived here are based on simulations assuming seawater and reconstruction methods most applicable for the proposed ORCA detector. Nevertheless, some results are applicable to Antarctic glacial ice, and therefore also hold for PINGU. Cherenkov light emission characteristics are very similar in ice and seawater, as discussed in Sec. 4.1 and Sec. 8. Therefore, the all-photon limits are almost directly applicable to ice-based Cherenkov detectors.

Different detector media mainly influence the light propagation (see Sec. 4.5) and therefore the detected light signature (see Sec. 7 and Sec. 8). However, neutrino energy resolution limits are dominated by the fluctuations due to different hadronic final states, and are not limited by the detected photon statistics. Therefore, in-ice experiments do not profit significantly in energy resolution from the larger photon statistics due to less photon absorption. For direction resolution, the effect of photon sampling in ice is more difficult to estimate than in seawater. The smaller scattering length in ice reduces the amount of unscattered photons dramatically, which requires the reconstruction method to use also the directional information contained in scattered photons. The methods applied here do not allow to include this information, so that a dedicated study would be required. The increased scattering in ice makes it also more difficult to resolve the individual components (muons, electrons and hadronic showers), as discussed for electrons in Sec. 8. Therefore, the method for improving the reconstruction accuracy suggested in Sec. 9.5.3 might not be applicable, and the ‘ e^\pm unresolved’ limits in Sec. 9.5.4 are likely more applicable.

Comparison to estimates in the literature

The NMH sensitivity of PINGU – and hence approximately ORCA – have been estimated by several authors, e.g. [2, 107, 166]. A specific comparison of each assumed value for reconstruction resolution in these works would be rather tedious. Nevertheless, several broad aspects are worthwhile commenting on.

First, none of the authors [2, 107, 166] takes into account the differences between ν and $\bar{\nu}$, or the correlations between energy and direction resolutions.

Second, the assumed neutrino energy resolutions are sometimes incompatible with the limit derived here, i.e. they are likely too optimistic in the relevant energy range. The neutrino energy resolution assumed in [2] is $\Delta E/E = 20\%$ and ranges from 15% ('optimistic') to 35% ('conservative') in [107], while energy resolutions below $\sim 20\%$ tend to become incompatible with the limits for neutrino energies relevant for measuring the NMH (see Fig. 9.21).

In [166], different effects governing neutrino resolutions are also investigated. However, the authors do not consider the fluctuations in hadronic showers due to different hadronic final states or particle propagation. Additionally, they overestimate the light yield of hadronic showers⁵⁴ and consequently underestimate the contribution due to variation in interaction inelasticity y . However, the neglected effects contribute significantly to the limiting resolutions of neutrino energy. As a consequence, the energy resolutions assumed in [166] are incompatible with the limits derived here.

Third, all authors assume neutrino direction resolutions well within the limits derived here. However, direction errors are often [2, 107] assumed to be Gaussian in zenith angle and not in space angle, which simplifies the resolution parameterisations, but seems to be physically unmotivated, at least in optically isotropic media, such as seawater.

⁵⁴ In [166], a light yield ratio of hadronic and electromagnetic showers of 80% is assumed independent of energy. This value is significantly too large for the considered energies (see Fig. 7.10).

Part III

Developments and investigations towards ORCA

In this part the expected performance of the future KM3NeT/ORCA detector is determined. For this, a new shower reconstruction algorithm is developed, existing trigger algorithms are optimised, and a detector configuration optimisation is performed. In addition, the influence of optical background due to bioluminescence is investigated.

All developments and investigations presented in this part were performed by myself, and are published in the ‘Letter of Intent’ [3] of KM3NeT/ORCA, where my results are employed as a key ingredient to estimate ORCA’s sensitivity to the neutrino mass hierarchy.

10 Bioluminescence studies

ANTARES has proven that it is feasible to operate an underwater Cherenkov detector in the Mediterranean Sea despite different optical background sources (see Sec. 4.8.1), in particular time-dependent bioluminescence activity. There is no doubt that this is in principle also feasible with the technology used for the planned KM3NeT/ORCA detector, where only the interplay between the significantly denser instrumentation and the optical background rates due to bioluminescence needs to be reconsidered.

It is known that bioluminescent organisms can emit a burst of light when mechanically stimulated, for example by colliding with mechanical structures. Hence, the rate of stimulated bioluminescence bursts in the detector volume depends to first order on the total amount of mechanical structure of the detector. A detector with the same amount of mechanical structure but within a smaller detector volume, i.e. higher instrumentation density, will stimulate the same amount of bursts but within a smaller volume and consequently the average photon flux from these bursts within the detector volume is higher, leading to higher hit rates. Therefore, the mean background hit rate also depends on the detector instrumentation density.

It is known that depending on the environmental conditions the bioluminescence bursts can contribute significantly to the total hit rates in ANTARES. It is therefore necessary to investigate the bioluminescence at the location of the planned ORCA detector and try to estimate its impact on the feasibility of measuring the neutrino mass hierarchy with ORCA. As the ORCA site is very close to the ANTARES site, it can be assumed that the bioluminescent organisms are very similar at both sites, so that the data from ANTARES can be used to estimate the expected bioluminescence characteristics in ORCA.

Two questions are tried to answer in this section. First, how large is the expected increase in background hit rates from bioluminescence bursts compared to the ubiquitous background from ^{40}K decays for the planned ORCA detector? Second, which volume of the detector is affected, i.e. ‘blinded’, by each typical bioluminescence burst, and do these bursts impact the detector layout optimisation of ORCA? For this purpose, the class of bioluminescence bursts that dominates the total number of burst-induced hits in ANTARES are investigated in detail, in order to allow for an extrapolation from the characteristics observed in ANTARES to the expected characteristics in ORCA.

Although it is not expected that bioluminescence can produce correlated photons that could form large clusters of causally connected hits in the detector and could therefore confuse the identification of neutrino-induced events, it is important to scrutinize this hypothesis. For this, the ANTARES data is here.

A brief overview of the main known characteristics of bioluminescence is given in Sec. 10.1. Relevant information on the ANTARES detector and its data acquisition is summarised in Sec. 10.2, and the characteristics of hit rates and bioluminescence in ANTARES are described in Sec. 10.3. The dominant class of bioluminescence bursts in ANTARES is characterised in Sec. 10.4, and the expected influence of these bursts on the planned ORCA detector is discussed in Sec. 10.4.8. In Sec. 10.5, the short-scale variability of bioluminescence bursts is studied. The rate of coincident hits in ANTARES during bioluminescent bursts is investigated in Sec. 10.6. Finally, implications deduced for ORCA are discussed in Sec. 10.7.

10.1 Bioluminescence

The deep sea is inhabited by a remarkable diversity of life forms, ranging from bacteria to larger animals, such as fish and jellyfish. Most of these organisms are luminescent, i.e. they emit visible light as a result of a chemical reaction [129].

In the absence of sunlight, bioluminescence is an efficient means of attracting or distracting attention. It serves many functions for marine organisms: offence (illumination or luring prey), defence (deterrence or blinding predators), communication and propagation of species (attracting or recognising mates). Many animals have light-emitting organs, others release a cloud of luminescent secretion or use bacterial symbionts for light production. The light is typically produced by the oxidation of a light-emitting molecule – generically called luciferin – in conjunction with a catalysing enzyme. Highly developed species have often additional structures to control the light intensity and its angular distribution [129].

Bioluminescence is observable in situ and in the laboratory, whereas the characteristics of emitted light in the laboratory may not reflect how they appear under natural circumstances. The light emission characteristics depend strongly on the specific species. Luminescent bacteria can emit a faint glow over periods as long as several days, while animals that produce the light themselves or use bacteria emit bursts that range from a few tens of milliseconds up to several seconds. An important feature is that the emission of light can be stimulated mechanically or photonically. Most organisms give a single burst in response to a single stimulus, although some species emit a series of flashes. Burst characteristics vary widely, but common to most species is a delay after stimulation, followed by a rapid rise in the intensity of light emitted and a slow decay, with more or less complex substructures [167]. The burst intensity ranges from 10^9 to 10^{13} photons per burst [168]. Emission maxima of most species correspond to photon wavelengths of $\lambda = 450\text{--}490$ nm [169], identical to the maximum light transmission in seawater (cf. Fig. 8.1). In this photon wavelength regime, bright bursts can exceed the ubiquitous light background from ^{40}K decays (see Sec. 4.8.1) up to several tens of metres away from the light source. The number density of bursting organisms decreases rapidly with depth and depends on the location. In the Mediterranean Sea, bioluminescence activity decreases towards the East [168].

10.2 ANTARES detector and its data acquisition

The ANTARES detector is located 40 km offshore from Toulon in the Gulf of Lion at a depth of 2475 m. Its location is also shown in Fig. 5.1. It is an underwater Cherenkov detector (see Sec. 4) that has been designed to search for cosmic neutrinos.

The detector consists of 12 detection strings, each equipped with 75 optical modules (OMs) that are arranged in groups of three on 25 storeys. A storey is shown in Fig. 10.1. Each OM houses a 10-inch PMT that points downwards at 45° . The OMs of each storey have an angular spacing of 120° and are held in place by a support structure that also contains the electronics. Adjacent storeys have a vertical spacing of 14.5 m and the first storey is located 100 m above the seabed. The strings are separated from each other by a typical distance of ~ 70 m. The construction of the detector started in 2007 with the first five detection strings. The full detector configuration of 12 strings was completed in May 2008 and is operated since then. Further details can be found in [110] and references therein.

Data acquisition

During data taking the analogue signals from the PMTs are processed by an analogue ring sampler (ARS) within the electronic module on the storey. If the signal exceeds a threshold of 0.3 photoelectrons, the signal within a time window of 25 ns is integrated. Then, a second ARS takes over. Each ARS has a dead time of about 250 ns after its integration time. Only after the integration time of the second ARS, the dead time of the first plays a role. The data collected by the two ARSs within a *time slice* (TS) of 104.858 ms is buffered and then sent to shore, following the ‘all-data-to-shore’ concept [138].

The ubiquitous optical background noise precludes to store all raw data (~ 0.5 GB/s) for the entire operation time of the detector of $\mathcal{O}(10)$ year). As a protection against biolu-



Figure 10.1: An ANTARES storey with three OMs. Taken from [170].

minescence bursts, data from PMTs with hit rates exceeding 500 kHz are not sent to shore. This is referred to as *high rate veto* (HRV). A similar cutoff occurs when a PMT registers an excessive hit rate for a long period, overfilling the buffer (Xoff). The OM is in Xoff until the buffer is emptied. Both HRV and Xoff lead to time slices with no hits, i.e. a hit rate of zero. HRV and Xoff cannot be distinguished from the data.

Within the continuous data stream, trigger algorithms are looking for ‘physics events’, i.e. sufficiently large clusters of causally correlated hits (see Sec. 4.9). In addition, there are two further ‘triggers’. First, a minimum bias trigger fires on average every 10 s. Time difference Δt between consecutive triggers follows an exponential decay: $P(\Delta t) = \exp(-\Delta t/10 \text{ s})$. Second, sometimes the entire data stream, i.e. all registered hits, of a short time period is written to tape without filtering, e.g. if an external alert is received. For *gamma ray burst* (GRB) alerts, periods of two minutes are usually stored (happens on average about twice per day).

The continuous data stream is split in *runs* with typical durations of about 2 h before April 2013, and up to about 8 h since then. In addition to all hits within a triggered event, a summary of all environmental conditions including the mean rates of every OM in a TS are stored for each TS containing at least one triggered event.

10.3 Characteristics of hit rates and bioluminescence in ANTARES

The hit rates measured in ANTARES show large variations due to bioluminescence. Two different bioluminescence ‘components’ are observed. One is a slowly-changing baseline rate in the entire detector that just overlays the background rate from ^{40}K decays and dark noise. Baseline rates range typically from 50 kHz to about 120 kHz depending on the contribution from bioluminescence. Variation between different OMs are about 15% due to differences in the photon detection efficiencies. On top of the baseline rate, light bursts with durations of up to several seconds can be seen on neighbouring OMs. It is believed

that the former is caused by large clouds of luminescent bacteria (single cell organisms), while the latter is caused mainly by larger luminescent organisms that are mechanically stimulated when colliding with the detector structures or moved by the turbulences behind the detector structures [171].

Bioluminescence activity shows noticeable seasonal variations. The highest bioluminescence activity is usually seen during the spring season, where background rates can increase up to several hundred kHz per PMT. This basically prevents regular data taking in these periods and the detector is switched off. These periods seem to be connected with the vertical movement of nutrient-rich water from warmer layers down to the depths of the detector [172].

In addition, a strong correlation with the velocity of the local sea current is observed [171, 172]. The sea current changes due to convection of water layers, the circulation in the Gulf of Lion (main direction either East-West or West-East along the deep basin borderline – change of sea current direction within $\mathcal{O}(h)$ and then often stable for several days or weeks), and due to the water motion induced by the Earth’s rotation (periodicity ~ 17.5 h [173]). The sea current velocity measured in ANTARES as a function of date is shown in Fig. 10.2. Sea current velocities are typically a few centimetres per second and can reach maximum velocities of 20–30 cm/s, whereas sea current velocities above 12 cm/s are observed less than 5% of the time [137].

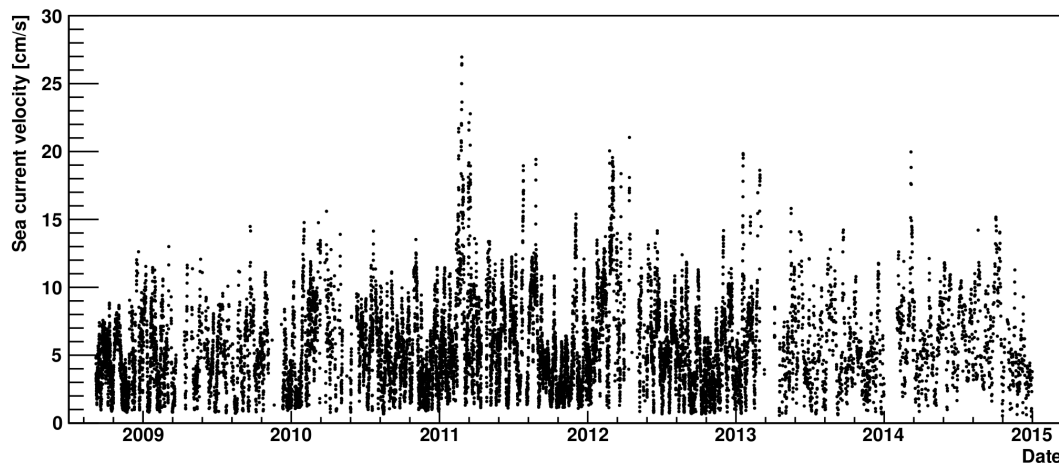


Figure 10.2: Sea current velocity measured in ANTARES as a function of date. Data taken from the ANTARES database.

10.4 Investigation of the dominant class of bioluminescence bursts

In this section, the characteristics of the class of bioluminescence bursts that dominates the total number of burst-induced hits in ANTARES are investigated. The duration, intensity and frequency of occurrence of these bursts are determined and studied as a function of date (2008–2014) as well as sea current velocity.

In addition, the influence of these bursts on the hit rates in ANTARES are estimated and extrapolated to the planned ORCA detector (see Sec. 5).

10.4.1 Data selection

Data recorded due to the minimum bias trigger and an external GRB trigger is independent of the actual environmental conditions, in particular of the optical background noise rates

date	GRB trigger (ANTARES run)	baseline rate [kHz]	mean rate [kHz]	burst fraction [%]	sea current velocity [cm/s]
2007/12/08	grb_61_298308 (30541)	51	60	13	4.9
2008/11/02	grb_110_247349683 (36826)	60	173	31	6.7
2009/12/31	grb_110_283928195 (45523)	53	58	6	1.1
2010/01/01	grb_110_283999191 (45538)	52	81	13	3.6
2010/06/20	grb_110_298695091 (49437)	94	320	45	6.3
2010/07/02	grb_110_299767472 (49795)	62	246	48	7.3

Table 10.1: Details on the six GRB-triggered data sets used for the bioluminescence studies. The *mean rate* is the average of all hit rates, the *baseline rate* describes the continuous component of the background hit rates (measured by fitting a Gaussian to the rising left tail of hit rate histograms) and the *burst fraction* quantifies the fraction of time with high hit rates ($> 20\%$ over baseline rate) [174]. Mean rate, baseline rate and burst fraction are taken from the ANTARES database.

and consequently bioluminescence activity. Therefore, these unbiased data samples are used for the presented bioluminescence studies.

For the full data stream recorded due to a GRB trigger, each single recorded hit is used to allow for monitoring hit rates on the millisecond time scale. Only six GRB-triggered data sets (total ~ 10 minutes) from different years are analysed. Details are given in Tab. 10.1, in particular the average detector conditions during the time the data was recorded.

For the data recorded due to the minimum bias trigger, rates from the TS summaries are used. Runs from 2008–2014 that fulfill the following two requirements are analysed: (i) more than 400 minimum bias triggers (corresponding to a minimum run duration of about 4000 seconds) in order to avoid large statistical fluctuations and (ii) the average baseline rate in the entire detector calculated for the first half and second half of the run differs by less than 5% in order to avoid significant changes in the bioluminescence conditions during a run. For 2008–2010, the minimum bias triggered data was processed by the standard data production chain, while the data was processed by myself for the presented bioluminescence analysis for 2011–2014. Due to problems with the data production of longer runs, not all runs taken since April 2013 are included here.

For all studies, rates equal to zero⁵⁵, i.e. HRV and Xoff (see Sec. 10.2), are interpreted as 500 kHz (HRV threshold value). Entire TS where more than 50% of all OMs are in HRV or Xoff are discarded, because this often indicates problems in the data acquisition and is not caused by bioluminescence activity. Individual OMs that fail in the course of a run or that show baseline rates below 20 kHz are discarded for the entire run.

⁵⁵ For technical reasons, all rates below 10 kHz are interpreted as HRV and Xoff.

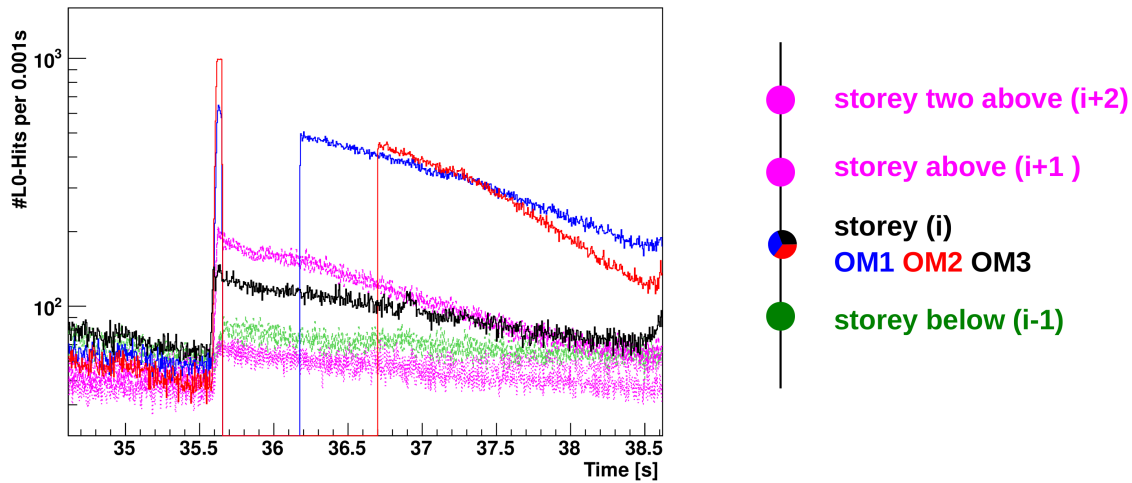


Figure 10.3: Number of hits per millisecond (values correspond to rates in kHz) for different OMs on adjacent storeys as a function of time. The time is given with respect to the start of the GRB-triggered data (grb_61_298308, see Tab. 10.1). Colors represent rates on different OMs and storeys, as explained in the sketch on the right hand side. For storey $i-1$, $i+1$ and $i+2$, rates observed by different OMs on the same storey are displayed with the same colors. The lower (higher) purple lines are from the storey $i+2$ ($i+1$).

10.4.2 Inspection of an example bioluminescence burst

An example of a burst from the dominant class of bioluminescence bursts is shown in Fig. 10.3. The hit rates of OMs on different storeys are shown as a function of time for a time interval of about four seconds. The source of this burst is located very close to storey i that shows the highest rates, because the photon flux drops rapidly with distance d (roughly $\propto \exp(-d/\lambda_{\text{att}}(d)) \cdot d^{-2}$, see Eq. 12.6). Most probably the bursting organism was stimulated by the ‘interaction’ (e.g. collision or turbulences) with the mechanical structures of this storey. Since too high rates are not transmitted (see Sec. 10.2), two OMs on storey i are in HRV or Xoff, i.e. their rates are zero and not displayed in Fig. 10.3. It is very likely that these two OMs are facing the light-emitting organism. The burst is also visible on the storeys above (storey $i+1$ and $i+2$) and below (storey $i-1$). The same burst is seen by all displayed storeys, because it starts at the same time and shows the same time profile. During the burst, rates are significantly enhanced above the baseline rates. The baseline can be inferred from the rates before the start of the burst. The maximum is reached few tens of milliseconds after the rates start to rise and is about a factor 3 above the baseline for all OMs on the storey above ($i+1$). Due to the angular acceptance and mounting of the OMs, the rates are higher for OMs on the storey above than below. The OMs on the storey above are oriented about 45° away from the light source, while the OMs on the storey below are oriented about 135° away⁵⁶.

As different OMs on the same storey above and below see exactly the same rates, it is clear that the light source has to be located close to the vertical detection string. The

⁵⁶ Fig. 10.4 suggests a difference of ~ 30 between the increase in rate for the storey above compared to that below, while the observed difference in Fig. 10.3 is only a factor ~ 10 . This difference indicates that the assumed scattering and absorption properties are wrong, the emitted light has a different wavelength, the light is not emitted isotropically, or shadowing plays a role. This inconsistency is ignored in the following.

three OMs on storey i show very different rates indicating that the light source has to be close by. This confirms the hypothesis that the light source has to be close to storey i .

Note that the light from the bursting organism can be shadowed by close-by detector elements depending on where the light-emitting organism is located relative to the detector elements. This reduces the hit rates observed by the OMs on the storeys above and below.

The photon emission rate of the bursting organism can be estimated from the rates R recorded on the storeys above (and below). Assuming that the light source is located at the position of storey i , the light is emitted isotropically, the effect of shadowing due the mechanical structure of storey i is negligible, and the emitted light is monochromatic with wavelength $\lambda = 450$ nm, the rate R_{source} of photons emitted by the source is given by:

$$R_{\text{source}} = \frac{R - B}{P(d, \theta)}, \quad (10.1)$$

where B is the baseline rate and $P(d, \theta)$ is the photon detection probability that depends on the distance d between the OM and the light source as well as the OM orientation θ with respect to the light source. The angle θ is here defined such that an OM facing the light source has $\theta = \pi$ ($\cos(\theta) = -1$). This probability is shown in Fig. 10.4.

Using the rates observed by the OMs on the storey above ($d = 14.5$ m, $\cos(\theta) = -1/\sqrt{2}$), the maximum emitted photon flux is about $F_{\text{source}}^{\text{max}} \approx 150$ kHz/ $(1.8 \times 10^{-6}) \approx 8 \times 10^{10}$ s $^{-1}$. The burst has a duration of a few seconds and in total about $\sim 2 \times 10^{11}$ photons are emitted, so that the average emitted photon flux is about $\sim 0.5 \times 10^{10}$ s $^{-1}$. As is shown in the following, this is a relatively bright burst with a typical duration.

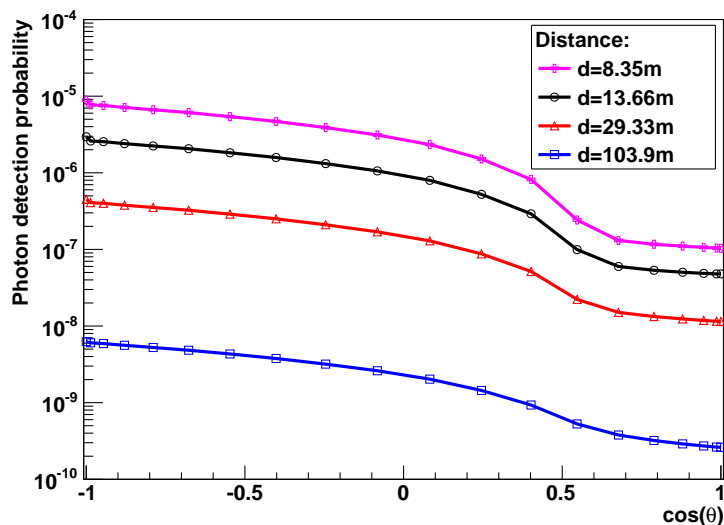


Figure 10.4: Detection probability for photons with a wavelength of $\lambda = 450$ nm as a function of OM orientation θ for different distances of an ANTARES OM from a point-like photon source. An isotropic light emission is assumed. Head-on incidence corresponds to $\cos(\theta) = -1$. No cut on photon arrival time is applied. Simulations performed by C. W. James using the GEN simulation package (see Sec. 6.1).

10.4.3 Duration

The duration of bioluminescence bursts is studied first in GRB-triggered data (see Sec. 10.2), where all hits are available. Here, rates are averaged over time intervals of 10 ms, i.e. about 600 ± 25 hits for a rate of 60 kHz. With this data it is possible to study also very short bursts with durations down to a few tens of milliseconds.

A simple definition of the start of a burst is when the rate exceeds three times the baseline rate. Similarly, the burst end is defined when the rate drops below two times the baseline rate. The difference in thresholds for burst start and end are chosen to avoid very short bursts due to random fluctuations. Of course, this very simple burst duration definition ignores the fact that two independent burst can overlap and counts overlapping bursts as a single longer one.

Fig. 10.5 (top) shows the distribution of the observed burst durations, and the duration-weighted counterpart is shown in Fig. 10.5 (bottom). The bottom plot shows the probability that a given OM observes for a given point in time an increased hit rate due to a burst with a certain duration. Five out of the six considered GRB-triggered data sets show very similar distributions of burst durations, while mainly the absolute normalisation is

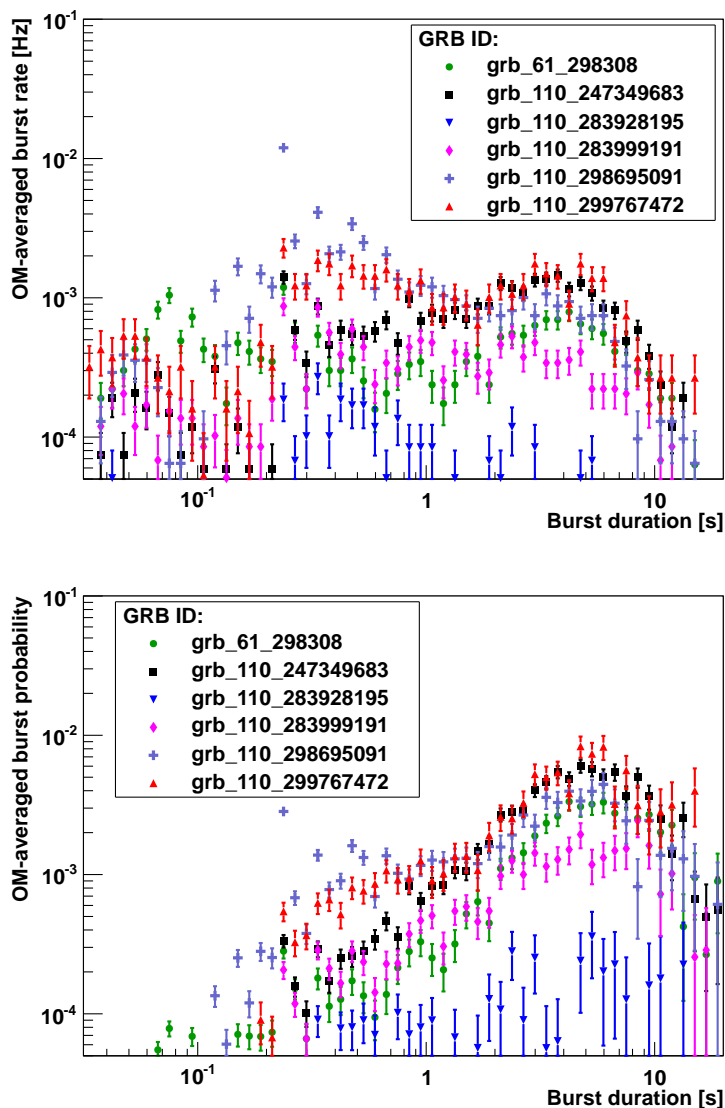


Figure 10.5: Distributions of burst durations observed during the six considered GRB-triggered data sets (see Tab. 10.1) shown as different colors: OM-averaged burst rate (top) and the OM-averaged burst probability (bottom). The bottom plot is calculated from the top one by multiplying each bin content with the corresponding burst duration. Spikes at multiples of the TS duration (104.858 ms) are artefacts of the data acquisition (HRV or Xoff, see Sec. 10.2).

different. The other GRB-triggered data set shows in total a very small number of bursts, because the sea current velocity was very low during that time (see Tab. 10.1) and the sea velocity determines how often bursts occur, as is discussed in Sec. 10.4.5.

From Fig. 10.5 (bottom), it is obvious that the most important bursts are those with durations of about 2–10 seconds. This is the dominant class of bioluminescence bursts. As is shown below, this is not only the case for the relatively short time intervals (about two minutes) of the considered GRB-triggered data sets, but over many years.

A peculiar series of very bright light bursts with durations of $\mathcal{O}(100\text{ ms})$ occurred in one of the GRB-triggered data sets (grb_110_298695091), explaining the accumulation of short burst durations for this data set in Fig. 10.5. Further details for these bursts are discussed in Appendix B.1.

The average burst duration can also be studied using the hit rates stored in the TS summary of minimum bias triggered events. This is done by looking at the correlation between the rates of the same OM at different times. For this, the probability is calculated that an OM that is in HRV or Xoff, i.e. too high rates for data transmission (see Sec. 10.2), at a time t_0 shows a rate above a certain threshold at a later time t_1 ($t_1 > t_0$). The rate threshold ΔR_{th} is defined with respect to the baseline of the OM in the analysed run.

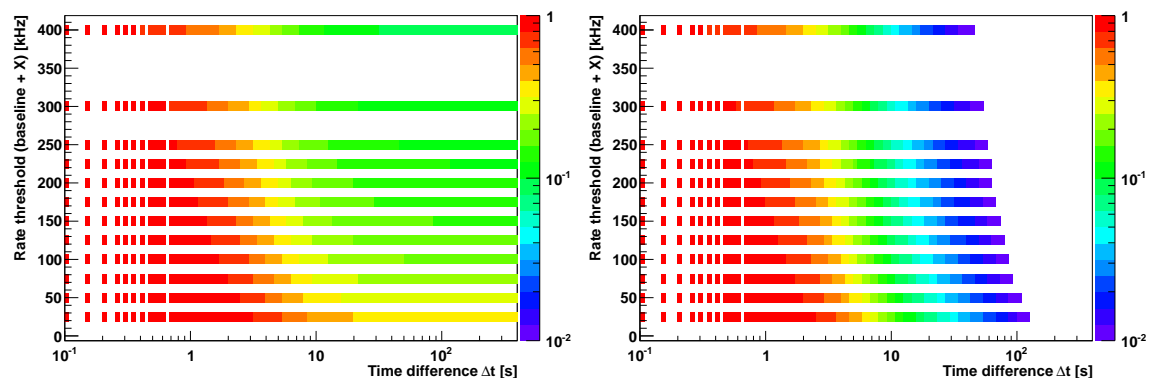


Figure 10.6: Left: Probability to observe a rate above a certain threshold ΔR_{th} with respect to baseline rate after a time difference Δt with respect to the time when an OM was in HRV or Xoff: i.e. observed too high rates (see Sec. 10.2). Right: In addition, subtracting the constant probability C for $\Delta t > 100\text{ s}$ and normalising the distribution for each threshold with $1/(1 - C)$. Here, rates from the TS summary of minimum bias triggered events are used. Data is averaged over many different runs from 2008–2014 (see Sec. 10.4.1).

Fig. 10.6 (left) shows this probability as a function of time difference Δt and rate threshold ΔR_{th} . Data is averaged over all considered runs (see Sec. 10.4.1), spanning nearly seven years of data taking. A short time after an OM is in HRV or Xoff, this OM has a high probability to observe significantly higher rates than the baseline rate, or being still in HRV or Xoff. After a few seconds the correlation is basically lost and the probability to observe a rate above a certain threshold is constant. This is the average probability to observe such a rate at any given time. As expected from the slow decay of the burst intensity (see Fig. 10.3), the correlation decreases at shorter Δt for higher ΔR_{th} . In Fig. 10.6 (right), the constant probability at large Δt is subtracted, and normalised appropriately. This gives the inter-time correlation of an average burst, assuming that bursting organisms are not clustered, i.e. they are uncorrelated in space and time⁵⁷.

⁵⁷ Preliminary studies show that this assumption is justified to first order. However, as bioluminescence bursts have to serve any purpose – probably communication (see Sec. 10.1) – there should be a spatial

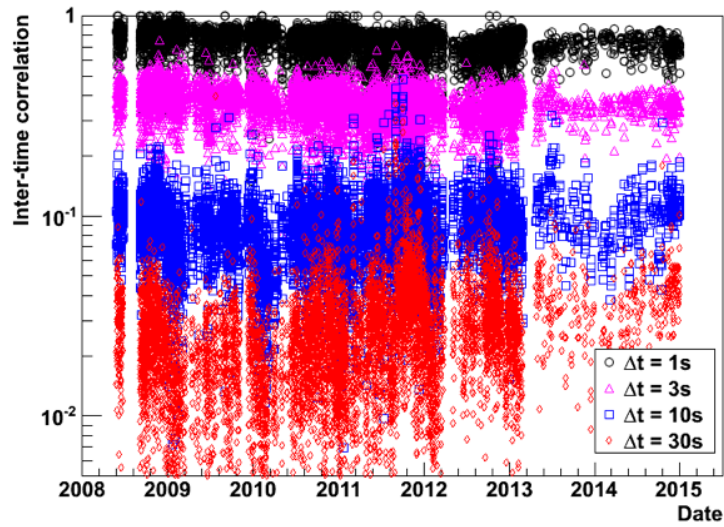


Figure 10.7: Average inter-time correlation as a function of date. The bin contents for $\Delta R_{\text{th}} = 200$ kHz and four different time differences Δt (1 s, 3 s, 10 s and 30 s) of distributions like in Fig. 10.6 (right) are shown for each run. Data after April 2013 is sparser, as not all runs taken during that time are considered (see Sec. 10.4.1).

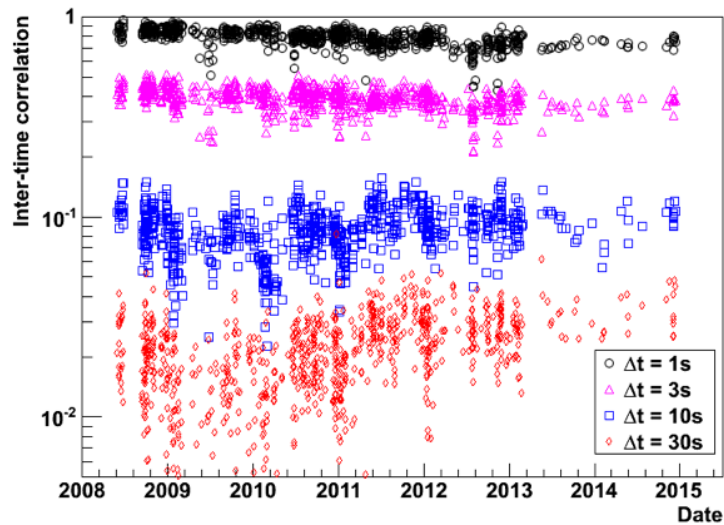


Figure 10.8: Same as Fig. 10.7, but only for runs with sea current velocities $6 \text{ cm/s} < v < 7 \text{ cm/s}$.

Remarkably, this inter-time correlation looks rather similar in most studied runs, as shown in Fig. 10.7. The probability to observe a rate that is $\Delta R_{\text{th}} > 200$ kHz above the baseline rate for different time differences Δt is similar over seven years. The scatter is mainly caused by the influence of the sea current velocity. Restricting the sea current velocity v to a small interval reduces the scatter significantly, as can be seen in Fig. 10.8, where only runs with $6 \text{ cm/s} < v < 7 \text{ cm/s}$ are shown. The correlation is roughly constant over time. Over the analysed seven years there is an overall trend to smaller correlations

correlation between bursting organisms. This could in principle be studied with a dedicated analysis of the available data.

for $\Delta t = 1$ s and 3 s, which is very likely caused by the drop in photon detection efficiency observed in calibration studies [175]. However, it is unclear why the correlation increases over the years for $\Delta t = 10$ s and 30 s.

Using this inter-time correlation, the mean burst duration T_{burst} can be calculated in each run. This is done by integrating over one slice of fixed threshold rate in Fig. 10.6 (right):

$$T_{\text{burst}} = 2 \times \sum_i (\Delta t_i - \Delta t_{i-1}) \times c_i, \quad (10.2)$$

where Δt_i is the time differences of bin i and c_i is the corresponding inter-time correlation. The factor 2 comes from the fact that the same inter-time correlation is present in positive as well as negative time differences. Here, the threshold of $\Delta R_{\text{th}} = 400$ kHz above the baseline rate is used, which is in principle equivalent to HRV or Xoff, so that the resulting duration is the mean duration that an OM is in HRV or Xoff. Fig. 10.9 shows this mean burst duration as a function of sea current velocity. In nearly all studied runs the mean duration in HRV or Xoff is about 2–10 s. This result is compatible with the mean burst duration found with a different method in GRB-triggered data (cf. Fig. 10.5 bottom). A larger sea current velocity carries away the light-emitting organisms faster from the OM, so that the photon flux reaching the PMT drops faster. This might explain the decrease of mean burst duration for larger sea current velocities. The reason for the drop of mean burst duration for smaller sea current velocities is unclear. A possible explanation is discussed in Sec. 10.4.7.

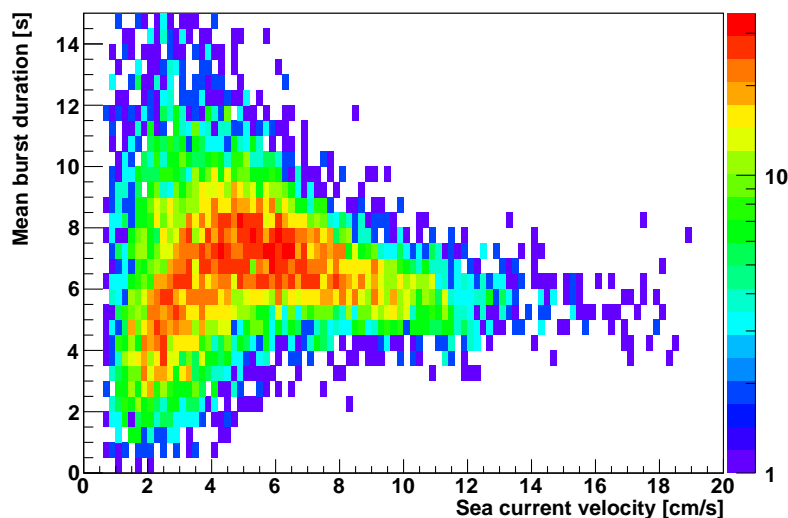


Figure 10.9: Mean duration of bioluminescence burst (calculated from inter-time correlations, see Eq. 10.2) as a function of the sea current velocity.

10.4.4 Intensity

The general strategy to determine the intensity of a bioluminescence burst is to use the rates observed by OMs on the storey above the storey where the burst originates from. The storey hosting OMs that are in HRV or Xoff, i.e. very high rates (Sec. 10.2), is likely very close to the bursting organisms. A ‘tag and probe’ method is applied here. First, a burst is tagged based on the rates observed by an OM on storey i , and then the increase in rate above the baseline observed by the ‘probe OM’ on the storey above ($i+1$) is used

as a measure for the burst intensity. The same strategy is also applied and discussed for the example burst in Sec. 10.4.2.

The intensity of bioluminescence bursts is studied first in GRB-triggered data (see Sec. 10.4.1). The same definitions are used for the start and end of a burst as in Sec. 10.4.3. In addition, the ‘tag OM’ is required to be at least for one TS in HRV or Xoff, the rate observed by the probe OM in the 50 ms before the burst start is required to be compatible ($\pm 20\%$) with the baseline rate and different probe OMs on the storey above are required to observe similar rates in order to minimise the chance that during the burst on the tag OM another independent burst on the probe OMs occurs and distorts the estimated intensity of the tagged burst. The increase in rate above the baseline rate within the first 200 ms after the burst start (expected intensity maximum, see Fig. 10.3) and within the full burst duration are shown in Fig. 10.10 for all bursts with durations of 2 to 8 seconds. For comparison, also the rates observed in the same time intervals on random OMs far away from the tag OM are shown. A significant increase in the rates on the probe OMs is observed compared to the far-away OMs. The amount of increase follows roughly an exponential decay, reaching maximal rates of up to ~ 150 kHz above the baseline, corresponding to ~ 3 times the baseline rate. The example burst in Fig. 10.3 is therefore one of the brightest bursts in the about ten minutes of detector lifetime spanned by the considered GRB-triggered data sets.

Fig. 10.11 shows the rate increase above the baseline rate on the probe OM within the first 200 ms after the burst start versus the burst duration on the tag OM. Bursts with durations of few seconds predominantly lead to a significant increase in rate on the storey above. A small correlation between burst duration and burst intensity is observed. However, it is unclear if there is only a small correlation at the source of the light, i.e. the bursting organisms, or if the possible stronger correlation is lost due to the applied method (e.g. shadowing can decrease the observed burst intensity on the probe OM).

The average burst intensity can also be studied using the hit rates stored in the TS summary of minimum bias triggered events. This is done in a similar manner as for the

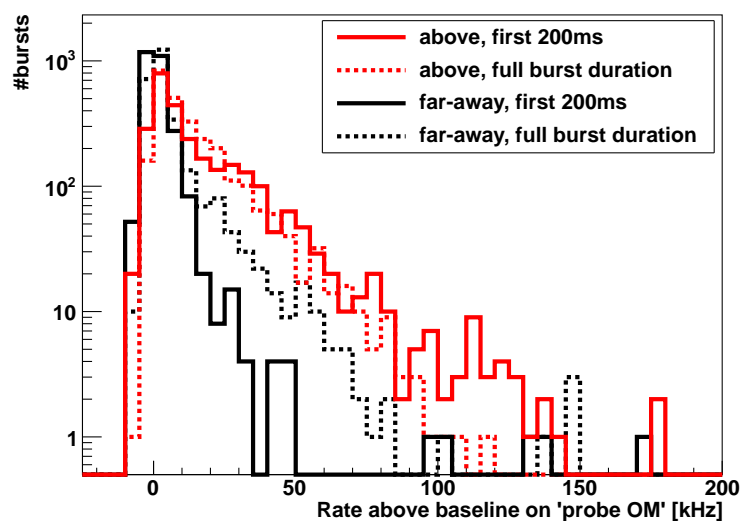


Figure 10.10: Increase of rates above the baseline rate on the probe OMs on the storey above (red) and random far-away OMs (black) within the first 200 ms after the start of a bioluminescence burst (solid) and within the full burst duration (dashed) for all bursts with durations of 2–8 s. Method and further requirements for the tag OM and probe OM are explained in the text.

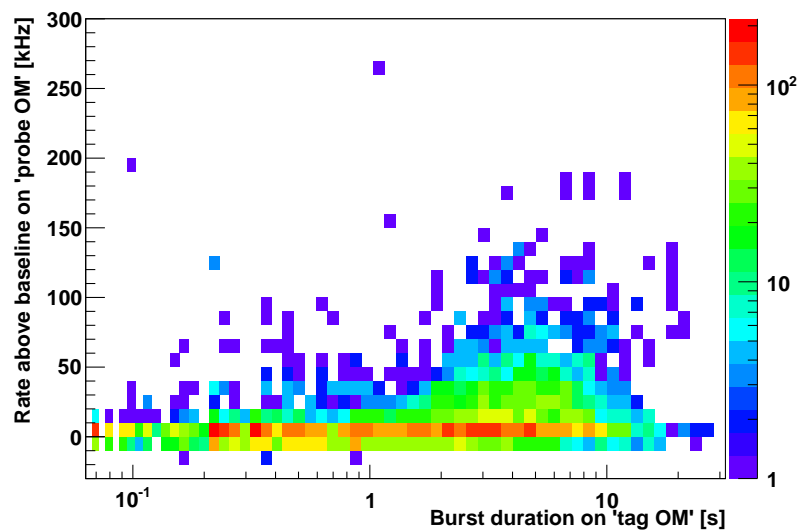


Figure 10.11: Increase of rate above the baseline rate on the probe OM within the first 200 ms after bioluminescence burst start versus the burst duration on the tag OM. Outliers may be caused by an overlapping burst from a bioluminescent organism close to the probe OM.

burst duration (cf. Sec. 10.4.3), but instead of correlations in time on the same OM, now correlations in space for the same time are investigated. As before, a burst is tagged on one storey by requiring an OM to be in HRV or Xoff and the burst intensity is determined using the rate observed by a probe OM on the storey above.

If P_t is the probability that the tag OM is HRV or Xoff during a given run, P_p is the probability that the probe OM observes rates above a certain threshold ΔR_{th} relative to its baseline rate, and P_{tp} is the probability that both events happen at the same time (i.e. same TS), then the Pearson correlation coefficient⁵⁸ r is given by [176]:

$$r = \frac{P_{tp} - P_t P_p}{\sqrt{P_t - P_t P_t} \sqrt{P_p - P_p P_p}}. \quad (10.3)$$

This correlation is shown in Fig. 10.12 for different rate threshold values ΔR_{th} on the probe OM and for different distances between the tag OM and the probe OM (in storey difference Δ_{storey} , i.e. units of inter-storey distance). All considered runs (see Sec. 10.4.1) are analysed and the average correlations are shown. The correlation drops with larger distances and with higher rate thresholds. The distance dependency behaves as expected from the photon detection probabilities (see Fig. 10.4), e.g. the correlation $r(\Delta R_{th} = 400 \text{ kHz}, \Delta_{storey} = 1)$ is nearly identical to $r(\Delta R_{th} = 75 \text{ kHz}, \Delta_{storey} = 2)$, because $P(d = 14.5 \text{ m}, \cos(\theta) = -1/\sqrt{2})/P(d = 29 \text{ m}, \cos(\theta) = -1/\sqrt{2}) \approx 5.4 \approx 400 \text{ kHz}/75 \text{ kHz}$.

This inter-storey correlation looks similar in most studied runs over seven years, as shown in Fig. 10.13. Again, the scatter is mainly caused by the influence of the sea current velocity v . Fig. 10.14 shows the inter-storey correlation for $6 \text{ cm/s} < v < 7 \text{ cm/s}$. An overall drop in the correlation coefficients is observed since mid 2010. This coincides with the drop in photon detection efficiency observed in calibration studies [175]. With the applied threshold definition, this photon detection efficiency drop is not taken into account.

⁵⁸ Note that the definition of the Pearson correlation coefficient is adjusted for binary decisions, where the expectation value of x and x^2 are identical.

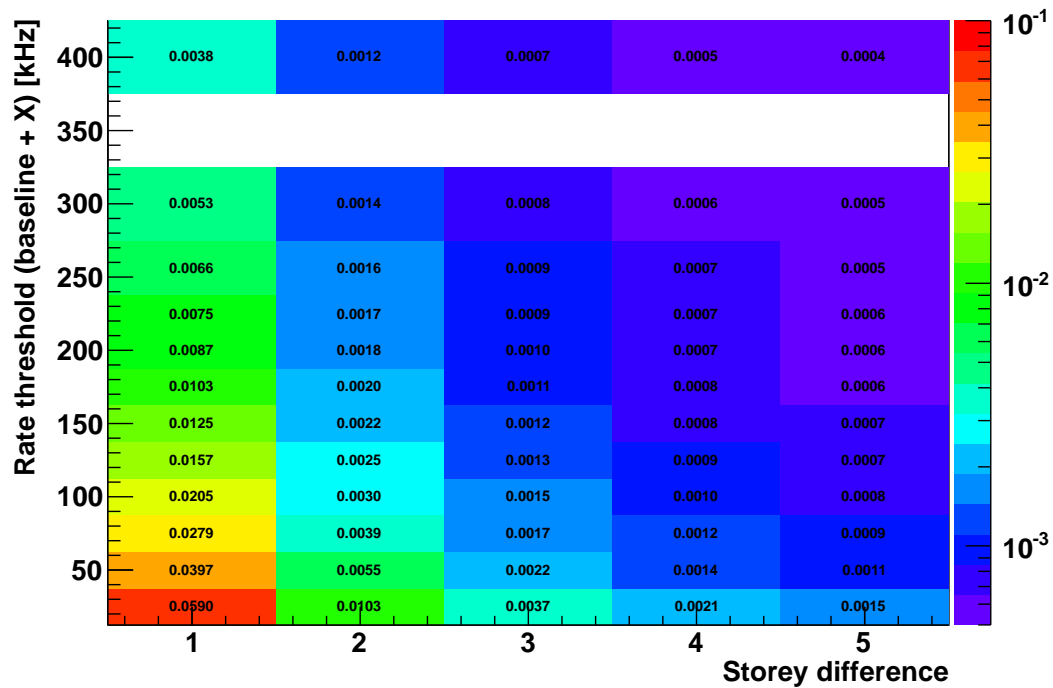


Figure 10.12: Inter-storey correlation coefficients (Eq. 10.3) as a function of distances between the tag OM and the probe OM (given in units of inter-storey distance, i.e. 14.5 m) and rate threshold ΔR_{th} on the probe OM relative to its baseline rate. The tag OM is required to be in HRV or Xoff (see Sec. 10.2). Data is averaged over many different runs from 2008–2014 (see Sec. 10.4.1).

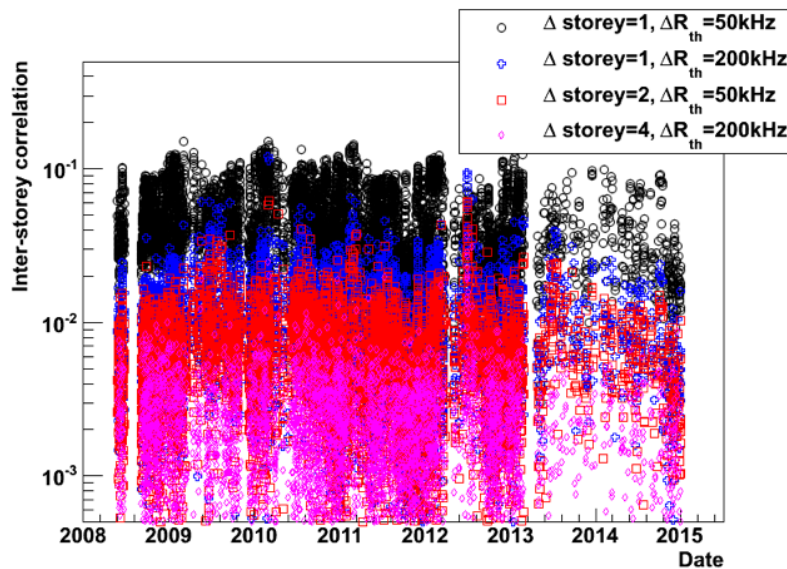


Figure 10.13: Inter-storey correlation coefficients (Eq. 10.3) as a function of date. The correlation coefficients for four different combinations of rate threshold ΔR_{th} and inter-storey distance Δstorey of distributions like in Fig. 10.12 are shown for each selected run (see Sec. 10.4.1).

Using the correlation coefficients, the mean burst intensity can be estimated. Assuming that bursts do not overlap, the mean burst intensity I_{burst} is given by integrating over the correlation coefficients r_i (Eq. 10.3) for different rate thresholds ΔR_i of the storey above (column with $\Delta_{\text{storey}} = 1$ in distributions like Fig. 10.12) and taking into account the photon detection probability $P(d = 14.5 \text{ m}, \cos(\theta) = -1/\sqrt{2})$ from Fig. 10.4:

$$I_{\text{burst}} = P(d = 14.5 \text{ m}, \cos(\theta) = -1/\sqrt{2}) \times \sum_i (\Delta R_i - \Delta R_{i-1}) \times r_i. \quad (10.4)$$

Fig. 10.15 shows this mean burst intensity estimator as a function of sea current velocity. The estimated mean burst intensity increases with the sea current velocity. The cause

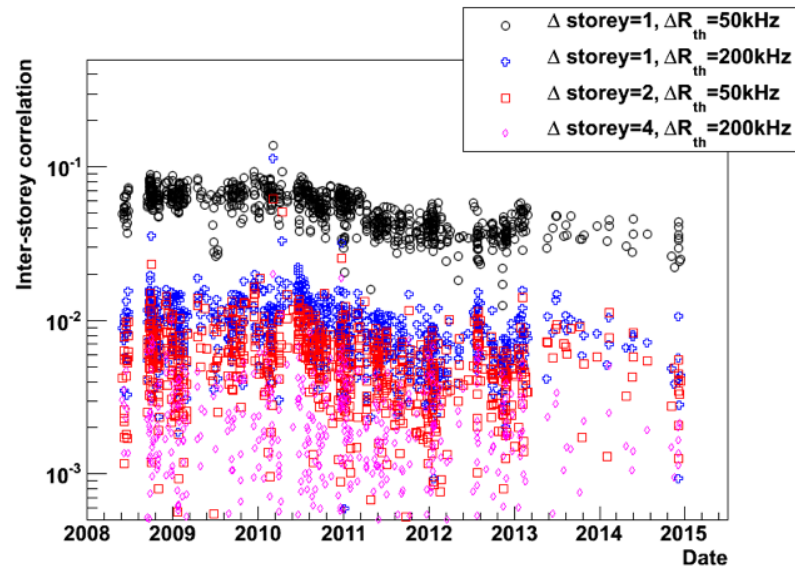


Figure 10.14: Same as Fig. 10.13, but only for runs with sea current velocities $6 \text{ cm/s} < v < 7 \text{ cm/s}$.

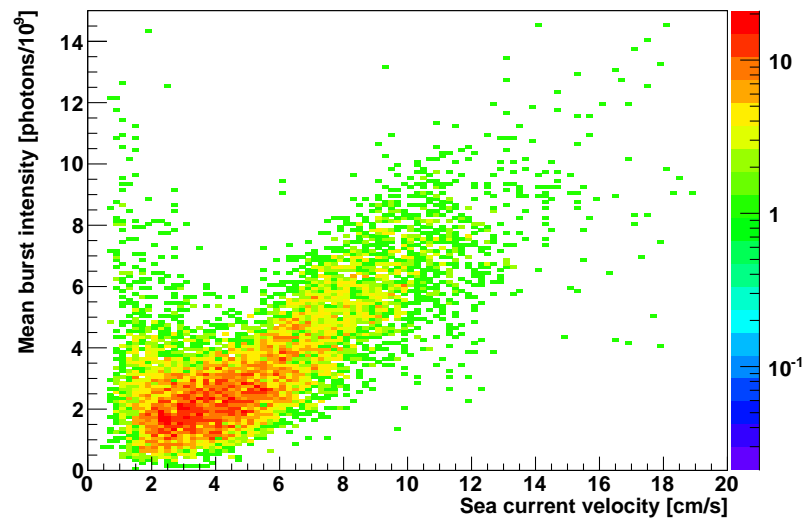


Figure 10.15: Mean burst intensity estimated from the inter-storey correlation coefficients (explained in the text) as a function of sea current velocity.

of this increase is unclear. It could be a bias in the method, the light output per burst depends on the strength of the stimulus (and therefore on the sea current velocity), or a combination of both. A possible bias in the applied method could be introduced due to the fact that a higher sea current velocity leads on average to: (i) selecting only the brighter first seconds of the burst (as discussed in Sec. 10.4.3), (ii) less shadowing as the light-emitting organism is carried away faster from the detector elements, and (iii) more bursts in general (as is discussed in Sec. 10.4.5), so that the non-overlapping burst assumption might be less justified. However, it is unclear how to disentangle these effects.

The scatter in Fig. 10.15 for a given sea current velocity can partly be explained by the drop in photon detection efficiency over the seven years of data taking mentioned before.

10.4.5 Frequency of occurrence

The frequency of occurrence of bursts from the dominant class of bioluminescence bursts can be deduced from the probability $P_{\text{HRV},\text{Xoff}}$ that an OM is in HRV or Xoff (see Sec. 10.2) at a given time. Assuming that a burst does only lead to HRV and Xoff for the OMs on one storey (closest to bursting organism) and does not lead to HRV or Xoff on adjacent storeys, the $P_{\text{HRV},\text{Xoff}}$ is directly proportional to the frequency of occurrence of bursts, because the mean duration in HRV or Xoff per burst is similar in all runs with the same sea current velocity v (see Fig. 10.9). Fig. 10.16 shows that $P_{\text{HRV},\text{Xoff}}$ is proportional to v^2 . For an exemplary sea current velocity of $v = 7 \text{ cm/s}$, $P_{\text{HRV},\text{Xoff}} \sim 0.06$ and the mean burst duration is $\sim 7 \text{ s}$ (see Fig. 10.9), so that a burst happens on average every $\sim 120 \text{ s}$.

During each run, the number of occurring bioluminescence bursts is randomly distributed. As the intensity of bioluminescence bursts is usually not bright enough to lead to HRV or Xoff on the OMs above the storey that stimulated the light emitting organism (see Sec. 10.4.4), the number of OMs in HRV or Xoff in each TS follows roughly a Poissonian distribution, as shown in Fig. 10.17 for five runs.

Note that the probability for overlapping bursts is rather low, as $P_{\text{HRV},\text{Xoff}} \ll 1$ for most of the time. Hence, the non-overlapping assumption made before is justified.

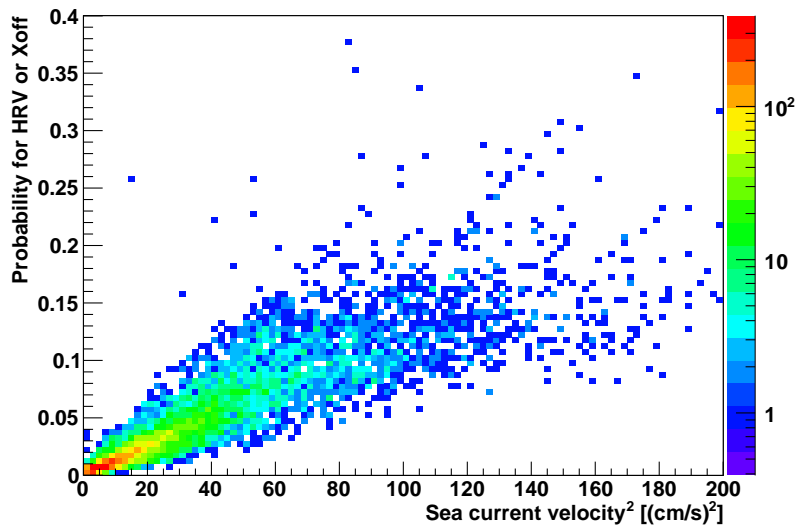


Figure 10.16: Probability $P_{\text{HRV},\text{Xoff}}$ that an OM is in HRV or Xoff as a function of sea current squared for all selected runs (see Sec. 10.4.1).

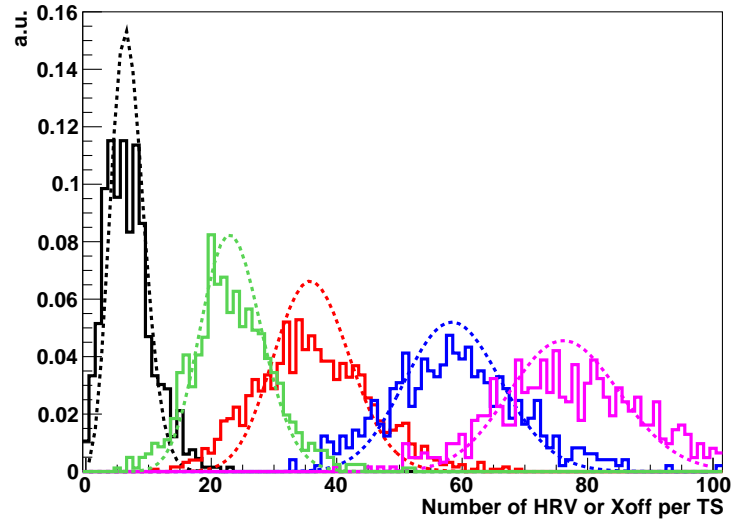


Figure 10.17: Distributions of the number of OMs in HRV or Xoff per TS (solid) for five runs. Poissonian distributions with the same mean values (dashed) are shown for comparison.

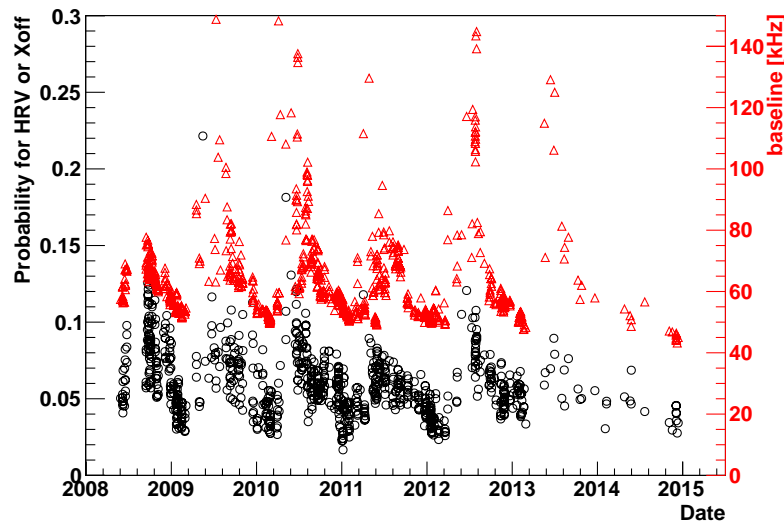


Figure 10.18: Probability $P_{\text{HRV},\text{Xoff}}$ that an OM is in HRV or Xoff (black circles, left axis) and baseline rate (red triangles, right axis) as a function of date for all selected runs (see Sec. 10.4.1) with $6 \text{ cm/s} < v < 7 \text{ cm/s}$. The baseline rate is taken from the ANTARES database.

Fig. 10.18 shows $P_{\text{HRV},\text{Xoff}}$ as a function of date for runs with sea current velocities $6 \text{ cm/s} < v < 7 \text{ cm/s}$. After the spring season, $P_{\text{HRV},\text{Xoff}}$ is high (~ 0.15) and decreases until it increases again in the next spring season. The difference in $P_{\text{HRV},\text{Xoff}}$ right after the spring season (high values) and before the next spring season (low values) is about a factor of 2–3. For comparison, the baseline rate averaged over all working OMs in the detector for the same runs is also shown in Fig. 10.18. A clear correlation between baseline rate and $P_{\text{HRV},\text{Xoff}}$ is observed. For better comparability, Fig. 10.19 shows the baseline rate versus $P_{\text{HRV},\text{Xoff}}$ for runs with $6 \text{ cm/s} < v < 7 \text{ cm/s}$ between summer 2008 and spring 2009. A linear dependence between baseline rate and $P_{\text{HRV},\text{Xoff}}$ is observed.

Correlation plots between the probability $P_{\text{HRV},\text{Xoff}}$ that an OM is in HRV or Xoff, the mean burst intensity and the mean burst duration are shown in Appendix B.2. In addition, further comparisons of $P_{\text{HRV},\text{Xoff}}$ and baseline rate as a function of date for different winter seasons are also shown in Appendix B.2.

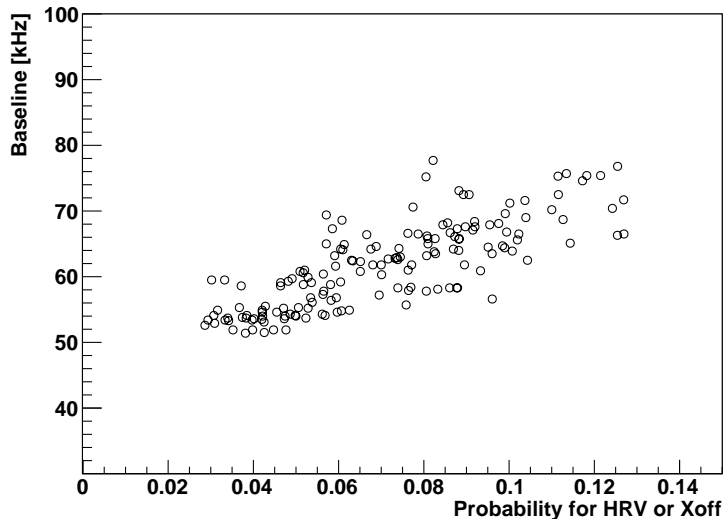


Figure 10.19: Baseline rate versus probability $P_{\text{HRV},\text{Xoff}}$ that an OM is in HRV or Xoff for all selected runs (see Sec. 10.4.1) with $6 \text{ cm/s} < v < 7 \text{ cm/s}$ between summer 2008 and spring 2009.

10.4.6 Contribution from non-local bursts to the mean hit rate

Using the results of the previous sections, the contribution from bioluminescence bursts, which are not stimulated by the detector structures in the local vicinity, to the mean hit rate can be calculated. For the sake of clarity, all bursts are considered that do not originate from the storey that hosts the OM in question. As discussed before, bursting organisms in the local vicinity often lead to hit rates that are too high for the data acquisition so that no data is transmitted to shore (HRV or Xoff, see Sec. 10.2), while bursts on adjacent storeys are visible as an increase in rate, but do usually not lead to HRV or Xoff.

This contribution to the mean rate is given by the product of the probability $P_{\text{HRV},\text{Xoff}}$ that an OM is in HRV or Xoff, the burst intensity (tagged by HRV or Xoff, see Sec. 10.4.4) and the average probability that an emitted photon is detected by any of the OMs in the entire detector except for the storey where the burst originates from. The latter probability is calculated by summing over the photon detection probabilities for all individual OMs (see Fig. 10.4) assuming that a bursting organism is located at the position of a given storey. By averaging over all storey positions, the average photon detection probability for the entire detector is obtained. For the ANTARES detector, this average photon detection probability is about 8.1×10^{-6} under the same assumptions made for Fig. 10.4. The OMs on the storey above the burst contribute about 2/3 to the total detection probability.

The resulting contribution of non-local bursts to the mean rate is shown in Fig. 10.20 as a function of sea current velocity cubed v^3 . The mean extra rate increases roughly linearly with v^3 . For exemplary sea current velocities of $v = 7 \text{ cm/s}$ ($v = 12 \text{ cm/s}$), the mean extra rate due to non-local bursts is about 3 kHz (14 kHz), corresponding to about 5% (25%) of the baseline rate. In 95% of the time, the sea current is below $v < 12 \text{ cm/s}$ [137], and therefore the contribution of non-local bursts to the mean rate is below 25%.

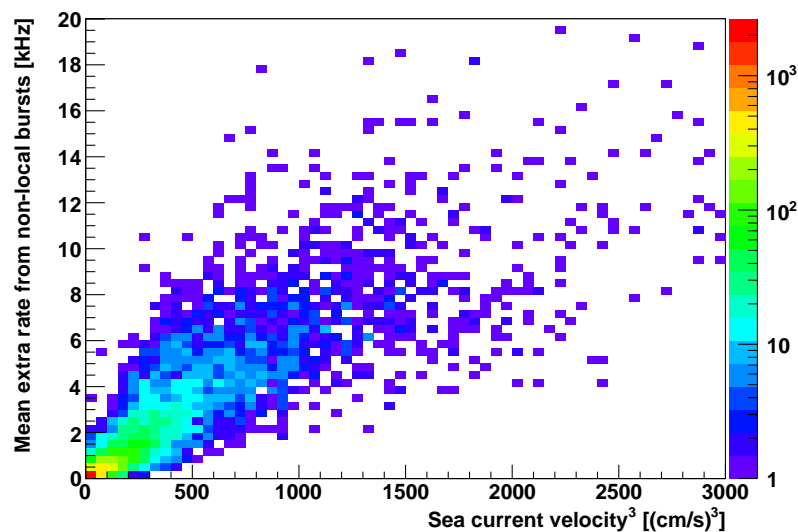


Figure 10.20: Mean extra rate from non-local burst (explained in the text) as a function of sea current velocity cubed for all selected runs (see Sec. 10.4.1).

10.4.7 Biological interpretations

The clear correlation between the baseline rate and the frequency of occurrence of bursts from the dominant class of bioluminescence bursts (see Sec. 10.4.5) suggests that there is common biological cause⁵⁹. Possible sources for this are the population size of the organisms or their bioluminescence activity, or a combination of both. Dedicated studies are needed to advance the biological understanding.

A possible ‘application’ of the correlation between the baseline rate and the probability $P_{\text{HRV},\text{Xoff}}$ that an OM is in HRV or Xoff (Sec. 10.2) might be to determine the contribution from ^{40}K decays to the baseline rate. From this, the absorption length can be derived. The rate that would be observed for $P_{\text{HRV},\text{Xoff}} = 0$ is dominated by the background light from ^{40}K decays (see Fig. 10.19). The correlation between baseline rate and $P_{\text{HRV},\text{Xoff}}$ might therefore allow to disentangle the contributions due to ^{40}K decays (and dark rate) from the contributions due to bioluminescence. Of course, there might be a bioluminescence background that does not correlate with $P_{\text{HRV},\text{Xoff}}$. Thus, such interpretation should be taken with caveats, and further investigations are needed to draw valid conclusions.

The distributions of burst durations shown in Fig. 10.5 (top) suggest that there might be two main classes of bursts. One class with durations of about a few seconds – the dominant class of burst studied here – and one class with shorter burst durations of a few hundred milliseconds or below. In addition, the inspection of individual time profiles of several bursts recorded in GRB-triggered data suggests that the shape of time profiles of shorter $\mathcal{O}(100\text{ ms})$ and longer bursts $\mathcal{O}(\text{s})$ is different. The drop of the mean burst duration for smaller sea current velocities in Fig. 10.9 can be explained if the two classes of bursting organisms respond differently to increasing sea current velocities, so that a transition between the two burst durations occurs in the mean burst duration.

⁵⁹ It can be assumed that the baseline rate calculation as it is done for the values in the ANTARES database [174] is only slightly affected by more frequent bursts, because the procedure was designed to cope with this difficulty.

The frequency of occurrence of bursts (see Sec. 10.4.5) could in principle be used to calculate the number density of bursting organisms of the dominant class of bioluminescence bursts. The only missing ingredient is the effective ‘burst-stimulating cross section’ of a storey.

Assuming that the number density of bursting organisms is independent of (short-term) changes of the sea current velocity v , the observed v^2 dependence of the probability $P_{\text{HRV}, \text{Xoff}}$ supports the hypothesis that bioluminescence bursts are mechanically stimulated by the shear forces in the turbulence flow around the mechanical detector structures.

10.4.8 Extrapolations for ORCA detector

As the ORCA site and the ANTARES site are very close to each other (~ 10 km, see Fig. 5.1), the results for the dominant class of bursts in ANTARES can be used to estimate the effect of these bursts on the ORCA detector.

The extrapolation from the frequency of occurrence of bioluminescence bursts observed in ANTARES to the expected burst rate in ORCA requires to make assumptions about the relative differences between the effective ‘burst stimulating cross section’ of an ANTARES storey and a KM3NeT DOM. The physical size of a KM3NeT DOM is significantly smaller than an ANTARES storey, so that the frequency of burst is expected to be significantly reduced. As an ANTARES storey consists of three 17-inch glass spheres, which have each the same size of a KM3NeT DOM, and a support structure, which is in total size at least as large as one KM3NeT DOM, it is assumed in the following that a factor of 4 times less bursts are stimulated by a KM3NeT DOM than by an entire ANTARES storey.

Two main implications for ORCA can be deduced:

- The contribution from non-local bursts to the mean rate in ORCA will be small but non-negligible compared to the baseline rate. For the ORCA detector, the average photon detection probability for non-local bursts is about 8.5×10^{-5} (calculated as in Sec. 10.4.6), and therefore about 10 times larger than in ANTARES. However, due to the reduced frequency of occurrence of bursts per DOM/storey in ORCA compared to ANTARES by a factor of ~ 4 , the contribution from non-local bursts to the mean rate in ORCA will be ~ 2.5 times larger than in ANTARES. For a sea current velocity of $v = 7$ cm/s ($v = 12$ cm/s), the mean extra rate due to non-local bursts is expected to be about $\sim 15\%$ ($\sim 70\%$) of the baseline rate in ORCA. Hence, in about $\gtrsim 95\%$ of the time ($v < 12$ cm/s [137]) the contribution to the mean rate from non-local bursts is smaller than the contribution from the baseline.
- PMTs on adjacent DOMs ($d = 9$ m) that face a bursting organism during the time of its highest photon emission rate (first seconds after the burst starts, see example burst in Fig. 10.3) will show too high rates to be transmitted to shore, while PMTs on next-to-adjacent DOMs ($d = 18$ m) as well as neighbouring strings ($d \gtrsim 20$ m) will be within the limitations. For example, the PMT pointing directly downwards ($d = 9$ m, $\cos(\theta) = -1$) to the DOM below will observe ~ 5 times more light relative to the baseline in ORCA⁶⁰ than an OM in ANTARES ($d = 14.5$ m, $\cos(\theta) = -1/\sqrt{2}$) if a burst occurs on the DOM/storey below. For the next-to-adjacent DOM, the PMT oriented directly to the light source will show a relative increase in rate comparable with that of an OM in ANTARES if a burst occurs on the storey below.

As a burst from the dominant class of bioluminescence bursts only leads to HRV or Xoff (i.e. too high rates, see Sec. 10.2) on the OMs on the storey that is closest to

⁶⁰ For the rough estimate done here, the angular acceptance of PMTs used in KM3NeT are assumed to be the same as in ANTARES. Only the effective area is scaled down by a factor ~ 10 due to the larger PMTs for an ANTARES OM (10-inch) than for a KM3NeT DOM (3-inch).

the bursting organisms, but does not lead to HRV or Xoff on adjacent storeys in ANTARES, it can be expected that each such burst in ORCA will lead to hit rates above the limitations for ~ 2 full DOMs (the full DOM where the burst is close by, the lower DOM hemisphere of the DOM above and the upper DOM hemisphere of the DOM below). As the frequency of occurrence of bursts per DOM/storey is reduced in ORCA compared to ANTARES by a factor ~ 4 , the fraction of lost data due not transmitting data of PMTs that are exposed to too high rates can be expected to be a factor ~ 2 smaller in ORCA than in ANTARES.

It should be stressed that both points should be taken with caution, as they are based on several assumptions (including that shadowing light from bursting organisms is identical for ANTARES and ORCA, and that an ANTARES storey stimulates a factor 4 times more bursts compared to a KM3NeT DOM due to its physical size).

However, once the first ORCA string is deployed at the KM3NeT-France site, the rather rough estimates can be refined with the data from a rather short period of time. The studies of the dominant class of bioluminescence bursts in ANTARES show that the characteristics of these bioluminescence bursts are rather stable over time, when taking into account the sea current velocity and the time since the last spring season. Note that the effect of shadowing of light from bursting organisms due to close-by detector elements is smaller and can be better controlled with the ORCA than with ANTARES detector, because of the reduced physical size of the detector elements and the ability for reconstructing the position of close-by bursting organisms with multi-PMT DOMs.

10.5 Short-scale variability

The GRB-triggered data (see Sec. 10.2) allow to study the short-scale variability (millisecond time scale) of bioluminescence bursts, as all individual hits are available. Here, rates are averaged over time intervals of 1 ms, i.e. about 60 ± 8 hits for a rate of 60 kHz.

Fig. 10.21 shows the probability to observe a certain difference between hit counts in

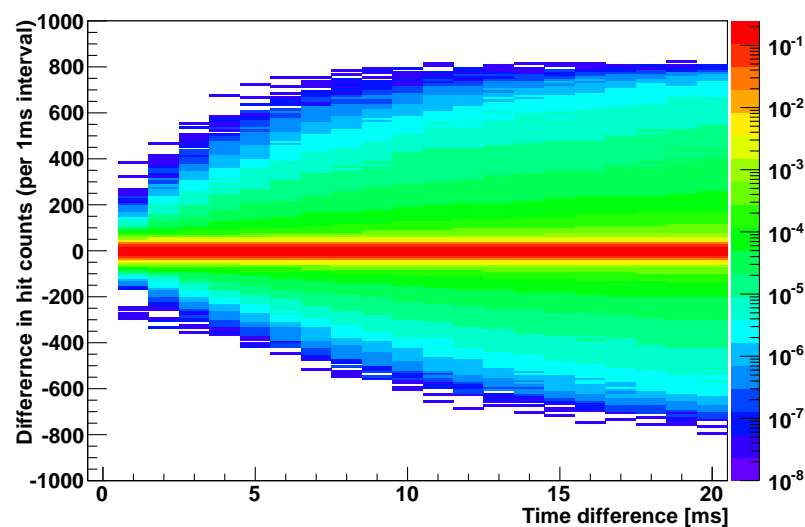


Figure 10.21: Probability to observe a difference between hit counts in two trial time intervals (1 ms duration) as a function of time difference between the two trial time intervals. The rate of the later trial time interval is subtracted from the earlier one. All data from the six considered GRB-triggered data sets (listed in Tab. 10.1) is superimposed.

two different trial time intervals (1 ms duration) as a function of time difference between the two trial time interval. Two observations can be made. First, the rise of a burst is more rapid than its decay, because the maximal slope for increasing rates (positive hit count difference) is larger than for decreasing rates (negative hit count difference). This is in consistency with the literature [167] (see Sec. 10.1). Second, the maximum change in rate is $\lesssim 150$ kHz per millisecond.

10.6 Coincident hits from bioluminescent burst

Hits from Cherenkov light emitted by secondary particles emerging from neutrino interactions are identified as large clusters of causally connected hits (see Sec. 4.9 and Sec. 11). This strategy is based on the assumption that most optical background hits are not correlated (on nanosecond time scale). The relatively faint ^{40}K decays ($\sim\text{MeV}$ compared to targeted neutrino energy of $\sim\text{GeV}$) produce rarely two or more hits from the same ^{40}K decay, which are correlated.

In order to investigate if bioluminescent organisms produce a significant amount of correlated light, the rate of coincidence hits during bioluminescence bursts can be compared to the expectation from random coincidences. If no additional coincidences are observed, bioluminescent bursts do not comprise correlated light.

As the variability timescale of the light intensity from bioluminescent bursts is of the order of a few milliseconds (see Sec. 10.5), rates are calculated for time intervals of 10 ms. This time intervals can be studied with the ANTARES detector when the full data stream is recorded due to GRB triggers (see Sec. 10.2). The time window to define a local coincidence between two different OMs on the same storey is chosen to be $\Delta T = 20$ ns, which is the typical value used in ANTARES⁶¹.

For OMs on the same storey, the coincidence rates are dominated by random coincidence (~ 100 Hz for $\Delta T = 20$ ns). Correlated coincidences from the same ^{40}K decay are about one order of magnitude smaller (~ 10 Hz) and the rate of coincident hits from atmospheric muons is negligible.

As the fraction of correlated coincidences is small and the dead time of OMs is negligible, the rate from random coincidences R_{ij}^{rand} between a given pair of OMs, i and j , is well approximated by:

$$R_{ij}^{\text{rand}} = m \times R_i \times R_j, \quad (10.5)$$

where R_i and R_j are the rates of OM i and j , respectively. For $\Delta T = 20$ ns, the proportionality constant is $m = 0.04/\text{MHz}$.

Fig. 10.22 shows the coincidence rate as a function of the product of the singles rates for the six considered GRB-triggered data sets. No significant excess of coincidences on top of the random coincidences is observed. Hence, there is no indication that a significant amount of coincident light is produced in bioluminescence bursts.

This conclusion is drawn based on the data from about 10 min of data (from different years, see Tab. 10.1), so it is not excluded that there are bioluminescent organisms that can produce coincident light. However, there is no obvious reason, why this should be different at any other time. The burst duration and intensity of the dominant class of bursts deduced from the same 10 min of data is also compatible with the results obtained from the seven years of data taking (see Sec. 10.4).

⁶¹In ANTARES, the coincidence time window is typically larger than in KM3NeT due to the inter-OM distance (~ 1 m).

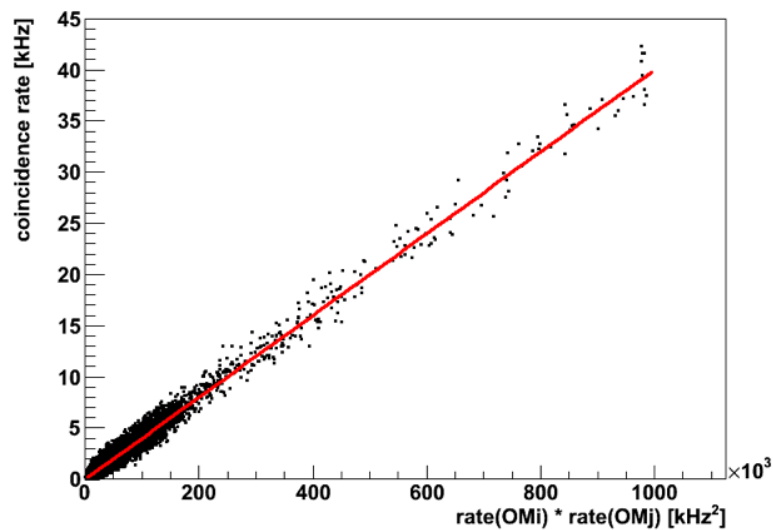


Figure 10.22: Coincidence rate between OMs on the same storey as a function of the product of the singles rates of the two OMs (black dots). Rates are calculated in time intervals of 10 ms and coincidences are defined using $\Delta T = 20$ ns. All data from the six considered GRB-triggered data sets (listed in Tab. 10.1) is superimposed. For comparison, the expectation (Eq. 10.5) from random coincidences is shown (red line).

10.7 Conclusions and implications for ORCA

The new methods developed to study bioluminescence bursts in ANTARES allow a better understanding of the characteristics (duration, intensity and frequency of occurrence) of the class of bursts that dominates the total number of burst-induced hits in ANTARES (see Sec. 10.4). This opens new opportunities to study the organisms that produce these bursts.

From the results of the presented investigations, several implications can be drawn for ORCA. The major implications are:

- For most of the time, the contribution from non-local bursts (bioluminescence bursts that do not originate from the DOM in question) to the mean rate in ORCA will be small but non-negligible compared to the baseline rate. This contribution scales with sea current velocity squared v^2 and is in about 95% of the time smaller than the baseline rate (see Sec. 10.4.8). For typical sea current velocities of $v = 7$ cm/s, the contribution is $\sim 15\%$. Hence, the typical mean extra rate is accounted for in the simulations for ORCA (measured single rates 8 kHz [139] and simulated 10 kHz, see Sec. 6.5).
- A burst from the dominant class of bioluminescence bursts will affect in ORCA only the adjacent DOMs on the same detection string but not the next-to-adjacent DOMs or the DOMs on neighbouring strings. As the effect of each such burst is limited to only a small volume of the detector, such bursts will not significantly reduce the effective instrumentation density (i.e. density of ‘active’ DOMs). Due to the significantly reduced mechanical structure per unit photocathode area in KM3NeT/ORCA compared to ANTARES, the approximate magnitude of this effect will be about a factor ~ 2 smaller than in ANTARES, where the fraction of data not transmitted to shore due to bioluminescence bursts (HRV or Xoff, see Sec. 10.2) is about 6% for the typical sea current velocities of $v = 7$ cm/s (see Fig. 10.16). Hence, bioluminescence

bursts are not expected to reduce the effective photocathode area density, and do not significantly influence the ORCA detector layout optimisation.

- Bioluminescence bursts do not produce a significant amount of coincident hits apart from random coincidences (see Sec. 10.6). Therefore, bioluminescence can be modelled as uncorrelated (single) hits in the simulation. This was also assumed before, but here it is shown that this assumption is justified.
- As the bursts from the dominant class of bioluminescence bursts show durations of a few seconds (see Sec. 10.4.3), a sampling frequency of 10 Hz is sufficient for recording the hit rate summaries⁶², as planned for the ORCA data acquisition (see Sec. 5.3). This sampling rate does not allow to monitor the rise of these bursts (variability on the scale of a few milliseconds or tens of milliseconds, see Sec. 10.5), however, the hit rates during most of the burst duration are changing smoothly and can be well interpolated from consecutive hit rate summaries.

As already mentioned in Sec. 10.4.8, it should be stressed again that the rather rough estimates for the first two points are based on several assumptions, so that they should be taken with caution. However, once the first ORCA string is deployed at the KM3NeT-France site, the estimates can be refined with the data from a rather short period of time. As shown in Sec. 10.4, the characteristics of the dominant class of bioluminescence bursts in ANTARES are rather stable over time, when taking into account the sea current velocity and the time since the last spring season.

The fact that the estimated influence of bioluminescence bursts is small but non-negligible shows that studies of the bioluminescence background for ORCA are important. However, the presented studies reveal that bioluminescence background will not compromise the feasibility of the neutrino mass hierarchy measurement with ORCA. Nevertheless, the operation of an ORCA-like detector with significantly denser instrumentation than that of the benchmark detector (e.g. for measuring the CP-violating phase δ_{CP} with atmospheric neutrinos [177]) might maybe not be feasible with the current KM3NeT technology at the ANTARES/ORCA site or its vicinity. As the KM3NeT-Italy site (Capo Passero, 80 km offshore the Sicilian coast) is significantly deeper and towards the East in the Mediterranean Sea, the bioluminescence activity is smaller than at the ANTARES/ORCA site [168]. The methods developed here should therefore also be applied to the first KM3NeT/ORCA strings in order to study the bioluminescence bursts at this location. A comparison of the characteristics of bioluminescence bursts at the ARCA site and the ANTARES/ORCA site will also be interesting for marine biologists.

⁶² Similar to the summary data for each TS in ANTARES (see Sec. 10.2).

11 Trigger studies

Triggering is an important aspect of the NMH determination with the KM3NeT/ORCA detector. For this measurement, the relevant neutrino events are close to the energy threshold of the planned ORCA detector. As only triggered events are permanently stored and are available for offline analysis, the trigger efficiency influences the effective volume and hence the needed operation time to determine the NMH. The amount of events for too loose trigger conditions becomes not processable due to the optical background in seawater (see Sec. 4.8.1 and Sec. 4.9).

In the following, the trigger algorithms available in the detector simulation tool JTE are briefly summarised in Sec. 11.1. Then, the optimisation procedure of the trigger configuration for the different detector layouts is described in Sec. 11.2. Finally, the trigger performance of the configuration found to be optimal is presented in Sec. 11.3. In addition, possible improvements in the general trigger strategies are outlined in Sec. 11.4.

The trigger configurations found to be optimal are applied in Sec. 12 as well as Sec. 13, and in the ‘Letter of Intent’ [3], in which the trigger performance and the optimisation are also briefly described. In the following, parts of the ‘Letter of Intent’ [3], to which I significantly contributed, are copied in verbatim. Also plots, for which I am responsible for, are labelled ‘KM3NeT’ and copied without further indication.

11.1 Trigger algorithms

The trigger algorithms are designed to extract interesting events from the real-time data stream using time-position correlations that follow from causality. There are two standard trigger algorithms in the JTE software package (version r2356, see Sec. 6.1). They are designed to detect track- and shower-like event signatures. Both trigger algorithms are described in the following along with the hit selection common to them.

11.1.1 Basic idea

The basic idea of all trigger algorithms is that interesting events produce (large) clusters of causally connected hits, while background light is uncorrelated. The relatively faint ^{40}K decays ($\sim\text{MeV}$ compared to targeted neutrino energy of $\sim\text{GeV}$) produce rarely two or more correlated hits from the same ^{40}K decay and photons from bioluminescent organisms are also not correlated, as suggested by the investigations in Sec. 10.6

A set of hits which are pair-wise causally connected form a *cluster*. If a sufficiently large cluster is found the event is triggered. Smaller clusters are discarded. In general, two hits i and j are causally connected if they satisfy

$$|t_i - t_j| \leq |\vec{x}_i - \vec{x}_j|/c_{\text{water}} + T_{\text{extra}}, \quad (11.1)$$

where $t_{i(j)}$ and $\vec{x}_{i(j)}$ are time and position of hit i (j), and $c_{\text{water}} = n_g/c$ is the speed of light in water. The extra time margin T_{extra} accounts for timing uncertainties as well as photon scattering and is typically set to about 10–20 ns.

In order to reduce the trigger rate due to pure noise and reduce computing time, the triggers exploit the simple fact that the hit probability decreases with distance away from the photon emission position. This is implemented by assuming a maximal photon travel distance. This reduces the number of DOMs to be considered and the maximal allowed time window for causally connected hits. Hence, an improvement of the signal-to-noise ratio compared to the general causality relation (Eq. 11.1) can be obtained. Depending on the assumed event topology, the relations that follow from causality, i.e. the matching condition for clustering, are different for the shower trigger and muon trigger.

In general, finding the largest cluster is a NP-complete problem. That means that there exists no efficient algorithm to find the maximal cluster. To solve the problem completely one has to check all possible combinations of hits, thus the complexity is of order $\mathcal{O}(N_{\text{hits}}!)$. Under certain assumptions, the cluster can be found in polynomial time. An algorithm that solves the clustering problem in $\mathcal{O}(N_{\text{hits}}^2)$ is implemented in JTE. It is the same algorithm that is implemented in the ANTARES trigger [178].

11.1.2 Hit definitions

A *L0 hit* refers to a single digitised hit that is transferred to shore, i.e. all analogue pulses above a threshold, as described in Sec. 5.1. A *L1 hit* refers to a coincidence of two (or more) L0 hits from different PMTs in the same DOM within a certain time window. Due to the favourable light scattering properties of deep-sea water, the time window can be very small with typical values of about $\Delta T \approx 10$ ns (see Sec. 7.2.4). For this time window and the noise rates assumed in simulations (10 kHz/PMT single noise rate and 500 Hz/DOM time-correlated noise, see Sec. 6.5), the estimated L1 rate per DOM is 1.4 kHz, of which 900 Hz are due to random coincidences from uncorrelated noise hits, i.e. from photons produced by different ^{40}K decays. The uncorrelated part can be reduced by making use of the orientations of the PMTs. A *L2 hit* refers to a L1 hit, for which additionally the angle θ_{L2} between the hit PMTs is smaller than a certain value. Typically, PMT opening angles smaller than $\theta_{\text{L2}} < 90^\circ$ are chosen, as coincident hits are expected to be emitted at roughly the same location and time, and travel unscattered on straight lines to the DOM. This additional requirement reduces the uncorrelated part of the L2 due to noise by a factor of about⁶³ two compared to L1 hits.

In the following, both trigger algorithms operate on the L2 hit selection.

11.1.3 Shower trigger

The shower trigger is rather simple, as it assumes a point-like emission signature. Consequently, assuming a maximum photon travel distance limits the maximum distance D_{max} between hit DOMs. The maximal allowed time difference ΔT_D between two causally connected hits with distance D is then given by:

$$\Delta T_D = \begin{cases} D/c_{\text{water}} + T_{\text{extra}}, & \text{if } D < D_{\text{max}}/2, \\ (D_{\text{max}} - D)/c_{\text{water}} + T_{\text{extra}}, & \text{if } D > D_{\text{max}}/2. \end{cases} \quad (11.2)$$

Note that the time window becomes smaller again for $D > D_{\text{max}}/2$. If the number of L2 hits forming the largest cluster is greater than the defined value N_{L2}^{shower} the event is triggered.

11.1.4 Muon trigger

The muon trigger is a bit more complicated, as a track-like event signature requires the assumption about a muon direction. Usually, an infinitely long track is assumed. For a given direction, an intersection of a cylinder with the 3D array of DOMs can be considered. The diameter of this cylinder, called road width R_{max} , corresponds to the maximal photon travel distance times $2\sin(\theta_{\text{Ch}})$. The relation for the maximal allowed time difference between causally connected hits can be found in [179].

An adequate solution to trigger a muon track event consists of a scan of the sky combined with a directional filter [3]. For the directional filtering, a muon track direction is

⁶³The factor is actually roughly 1.9 and a bit smaller than 2, as the PMT density on the DOMs is not uniform.

assumed. A set of about 200 directions is usually used to cover the full sky. If for any direction the number of L2 hits forming the largest cluster is greater than N_{L2}^{muon} the event is triggered.

11.2 Trigger configuration studies

The main goal of these trigger configuration studies is to find the trigger configuration that shows the best performance while fulfilling some external requirements (data acquisition, calibration uncertainties, etc.). For these studies, the benchmark detector (see Sec. 6.3) is used, if not stated otherwise. Neutrino events are weighted to reproduce the conventional atmospheric neutrino flux following the Bartol model [84].

Trigger configurations are evaluated based on the expected trigger rates and *trigger efficiency*. The trigger efficiency ϵ is defined as:

$$\epsilon = \frac{N^{\text{selected \& triggered}}}{N^{\text{selected}}}, \quad (11.3)$$

where N^{selected} is the number of all selected events and $N^{\text{selected \& triggered}}$ is the number of selected events that fired the trigger. The total trigger rate is usually limited by the bandwidth capabilities of the data acquisition system. Trigger rates from neutrino interactions $\mathcal{O}(\text{mHz})$ are negligible compared to rates from atmospheric muons $\mathcal{O}(40 \text{ Hz})$.

In the following, trigger efficiencies for neutrino events are determined without adding optical background in order to obtain results independent from the assumed noise level.

11.2.1 Optimisation strategy

The configurations of the shower and muon trigger are optimised by finding the configuration of each trigger that shows the largest trigger efficiency while requiring a maximal trigger rate of 10 Hz due to pure noise for the assumed noise rates (see Sec. 6.5). In the end, both triggers are run in parallel and one of them must fire to trigger an event (logical *OR*). Thus, the total trigger rate of both triggers together is dominated by atmospheric muons ($\sim 40 \text{ Hz}$) and not by noise ($\sim 20 \text{ Hz}$).

The definition of L1 ($\Delta T = 10 \text{ ns}$) as well as L2 hits ($\theta_{L2} < 90^\circ$), and the extra time margin ($T_{\text{extra}} = 10 \text{ ns}$) for both triggers are fixed and have not been tuned. Both time windows are imposed by possible timing uncertainties due to time calibration (few nanoseconds) as well as position calibration ($\sim 10 \text{ cm}$ corresponding to about $\sim 0.5 \text{ ns}$) of the PMTs, and dispersion as well as scattering of the photons ($\sim 6 \text{ ns}$ for 50 m photon travel distance, see Fig. 8.5).

Then, the only configurable parameters of the shower (muon) trigger are the minimum cluster size N_{L2}^{shower} (N_{L2}^{muon}) and the maximal distance parameter D_{max} (R_{max}), respectively. For each given minimum cluster size, there is a corresponding distance parameter such that the expected trigger rate due to pure noise is 10 Hz. Reasonable⁶⁴ combinations are $N_{L2}^{\text{shower}} = 3$ & $D_{\text{max}} = 40 \text{ m}$ as well as $N_{L2}^{\text{shower}} = 4$ & $D_{\text{max}} = 70 \text{ m}$ for the shower trigger, and $N_{L2}^{\text{muon}} = 4$ & $R_{\text{max}} = 35 \text{ m}$ as well as $N_{L2}^{\text{muon}} = 5$ & $R_{\text{max}} = 60 \text{ m}$ for the muon trigger.

In order to answer the question which of these trigger combinations performs best, the trigger efficiency is compared for upgoing $\vec{\nu}_e$ CC and $\vec{\nu}_\mu$ CC events, which would end

⁶⁴ Triggers with $N_{L2} = 2$ would show too high rates. Even, the rate of two causally connected L2 hits on adjacent DOMs is about $\mathcal{O}(100 \text{ Hz})$. In order to obey the requirement of maximal 10 Hz trigger rate due to noise for the muon trigger, $N_{L2}^{\text{muon}} = 3$ would require a maximal road width of about $R_{\text{max}} \approx 10 \text{ m}$, which is obviously too small.

up in the final event selection⁶⁵ of the shower and track reconstructions. This is shown in Fig. 11.1 and Fig. 11.2, respectively. As this study was performed before the reconstructions were finalised for the ‘Letter of Intent’ [3], preliminary versions of these reconstructions were used for selecting events. The shower reconstruction is described in Sec. 12 and the track reconstruction is described in [3].

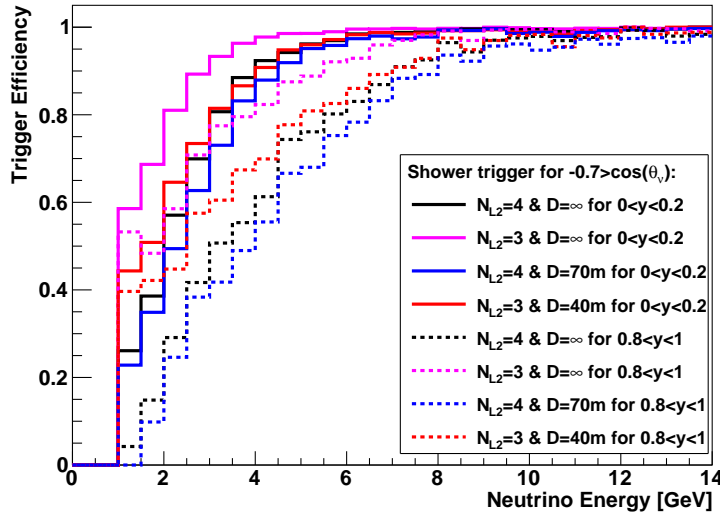


Figure 11.1: Trigger efficiency ϵ (Eq. 11.3) for $\bar{\nu}_e$ CC events with $\cos(\theta_\nu) < -0.7$ triggered with different shower trigger configurations (different colours) as a function of neutrino energy. Only reconstructable events are considered and events are weighted according to the Bartol atmospheric neutrino flux model. Events with low (solid) and high (dashed) inelasticity y are shown separately. For comparison, also shown are trigger configurations with $D_{\max} = \infty$ (black and purple), which would result in trigger rates significantly above the requirement of maximal 10 Hz from pure noise.

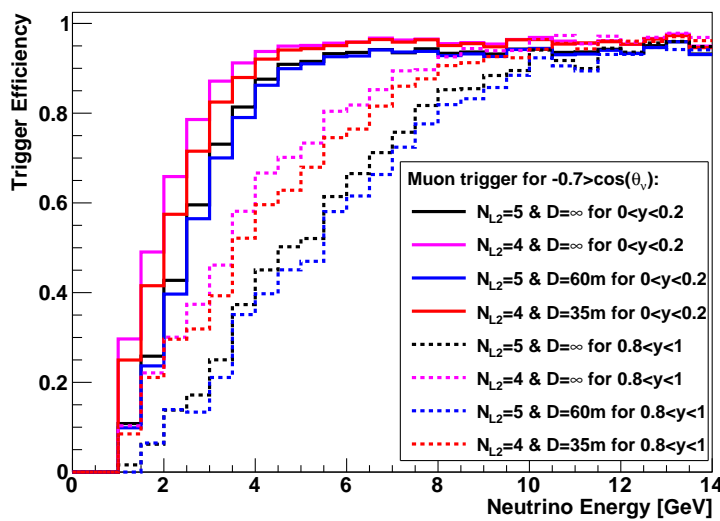


Figure 11.2: Same as Fig. 11.1 but for $\bar{\nu}_\mu$ CC events triggered with different muon trigger configurations.

⁶⁵ Of course, the ‘re-triggering’ requirement on the final hit selection from Sec. 12.1.3 is not applied for this investigation.

For both triggers, the configuration with smaller N_{L2} along with a small value for the distance parameter show higher trigger efficiencies than larger N_{L2} along with a larger value for the distance parameter. This is the case for $\vec{\nu}_e$ CC and $\vec{\nu}_\mu$ CC events with low as well as high inelasticity y . This general feature is also observed for horizontal events and for detector configurations with larger vertical spacings between DOMs.

The optimal configuration of the shower and muon trigger for the benchmark detector is then:

$$N_{L2}^{\text{shower}} = 3 \ \& \ D_{\text{max}} = 40 \text{ m} \quad \text{and} \quad N_{L2}^{\text{muon}} = 4 \ \& \ R_{\text{max}} = 35 \text{ m}. \quad (11.4)$$

These two triggers are applied in parallel (logical *OR*). The other three combinations⁶⁶ of muon and shower trigger configurations have also been tested [180], but showed smaller efficiencies than those in Eq. 11.4. The efficiencies for triggering reconstructable $\vec{\nu}_{e,\mu}$ CC events with $\cos(\theta_\nu) < -0.7$ are shown in Fig. 11.3. An efficiency of $\epsilon = 0.9$ is reached at about $E_\nu \approx 4 \text{ GeV}$ (7 GeV) for $0 < y < 0.2$ ($0.8 < y < 1$). The trigger efficiency for low- y events saturates at smaller energies than for high- y events as hadronic showers produce on average less Cherenkov light than electromagnetic showers (see Sec. 7.2.2).

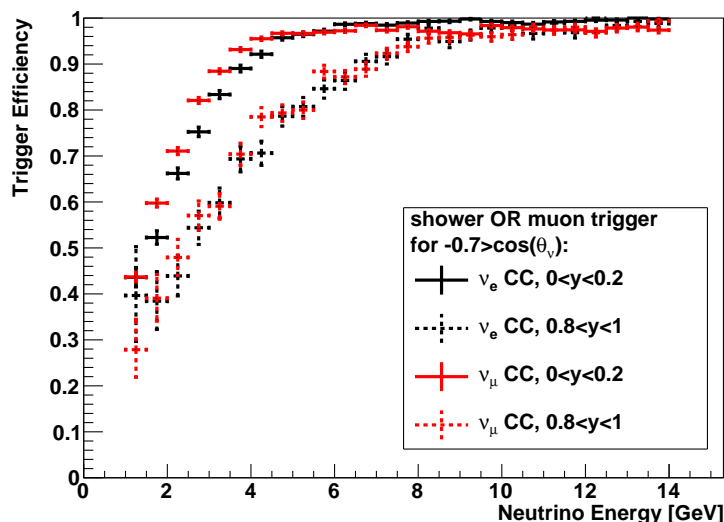


Figure 11.3: Trigger efficiencies (Eq. 11.3) for reconstructable $\vec{\nu}_e$ CC (black) and $\vec{\nu}_\mu$ CC events (red) with $\cos(\theta_\nu) < -0.7$. Shower and muon trigger run in parallel. Events with low (solid) and high (dashed) inelasticity y are shown separately. Error bars represent statistical errors.

11.2.2 Complementarity of shower and muon trigger

Fig. 11.4 shows the fraction of reconstructable $\vec{\nu}_\mu$ CC events which are exclusively (logical *XOR*) triggered by the muon and shower trigger, respectively. The fraction is defined with respect to all triggered events when running both triggers in parallel (logical *OR*). The relative gain in trigger efficiency due to each individual trigger can be read from this.

The shower trigger is significantly more efficient than the muon trigger, particularly for low neutrino energies. This is the case for events with low as well as high y . For $y \rightarrow 1$, this is obvious, as the event is more shower-like than track-like. For $y \rightarrow 0$, this is not obvious, as the muon trigger is designed for track-like event signatures. The handicap of the muon trigger is that an infinitely long track is assumed, which is obviously not optimal for few-GeV muons with track length of a few (tens of) metres. A consequence of the infinite track

⁶⁶ Other combinations are ($N_{L2}^{\text{shower}} = 3$, $D_{\text{max}} = 40 \text{ m}$, $N_{L2}^{\text{muon}} = 5$ & $R_{\text{max}} = 60 \text{ m}$), ($N_{L2}^{\text{shower}} = 4$, $D_{\text{max}} = 70 \text{ m}$, $N_{L2}^{\text{muon}} = 4$ & $R_{\text{max}} = 35 \text{ m}$) and ($N_{L2}^{\text{shower}} = 3$, $D_{\text{max}} = 40 \text{ m}$, $N_{L2}^{\text{muon}} = 5$ & $R_{\text{max}} = 60 \text{ m}$).

assumption is that for the muon trigger a configuration with a larger minimum cluster size ($N_{L2}^{\text{muon}} = 4$) than for the shower trigger ($N_{L2}^{\text{shower}} = 3$) has to be chosen. The requirement of this additional L2 hit shifts the turn-on of the trigger efficiencies to higher neutrino energies.

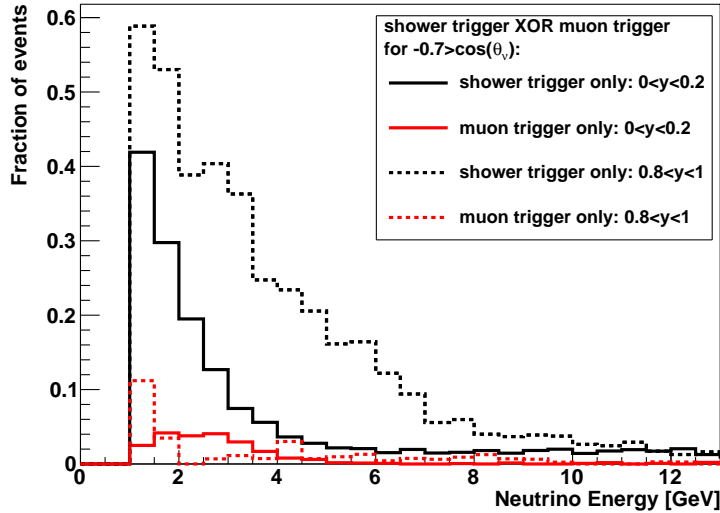


Figure 11.4: Fraction of events that are exclusively triggered by the shower (black) or muon (red) trigger in reconstructable $\bar{\nu}_\mu$ CC events with $\cos(\theta_\nu) < -0.7$ as a function of neutrino energy. Events with low (solid) and high (dashed) inelasticity y are shown separately.

11.3 Trigger performance

Up to now the optimal trigger configuration of shower and muon trigger have been discussed for the benchmark detector with 6 m vertical spacing between DOMs. For the other considered vertical spacings (see Sec 6.4), the maximal distance parameters (R_{max} and D_{max}) of both triggers is adjusted such that each of the triggers has a rate of about ~ 10 Hz from pure noise, i.e. following the same optimisation strategy as before.

The performance of the triggers can be summarised by the *effective volume* and the *event purity*. In general, the effective volume V_{eff} is defined as:

$$V_{\text{eff}} = V_{\text{gen}} \times \frac{N_{\text{sel}}}{N_{\text{gen}}}, \quad (11.5)$$

where V_{gen} is the volume in which simulated neutrinos are generated, N_{gen} is the total number of generated neutrinos, and N_{sel} is the number of selected neutrinos. Here, N_{sel} is the number of triggered neutrino events. The event purity is the fraction of triggered events that contain atmospheric muons, i.e. non-noise events. Trigger rates from neutrino-induced events are negligible.

11.3.1 Trigger rate and event purity

The rate of atmospheric muon events is evaluated at a depth of 2475 m using the simulations described in Sec. 6.5, and amounts to about 36 Hz (6 m) to 55 Hz (15 m) depending on the vertical spacing between DOMs. In order to estimate the trigger rates, dedicated simulations for each vertical spacing are performed, i.e. the strategy of detector masking (see

detector configuration vertical spacing [m]	trigger configuration		trigger rates [Hz]		event purity
	R_{\max} [m]	D_{\max} [m]	pure noise	atm. muons	
6	35	40	19	36	0.65
9	39	43	18	41	0.69
12	42	46	19	47	0.71
15	44	50	20	55	0.73

Table 11.1: Expected trigger rates from pure noise and atmospheric muons for the optimal trigger configurations for different detector configurations with 6 m, 9 m, 12 m and 15 m vertical spacing between DOMs.

Sec. 6.4) is not applied⁶⁷. Trigger rates from pure noise and atmospheric muons are summarised in Tab. 11.1 for the different vertical spacings and optimal trigger configurations. The trigger event purity is between 65% and 73%.

It should be noted that during periods of high bioluminescence (see Sec. 10), the trigger conditions (minimum cluster size and maximal distance parameters R_{\max} and D_{\max}) can be tightened in order to reduce the output data rate and match the bandwidth limitations.

11.3.2 Effective volume

The effective volume at trigger level for the benchmark detector is shown for different neutrino flavours in Fig. 11.5. The effective volume is smaller for $\bar{\nu}$ NC and $\bar{\nu}_\tau$ CC than for $\bar{\nu}_{e,\mu}$ CC events, since the outgoing neutrinos are invisible to the detector, and is larger for $\bar{\nu}_{e,\mu}$ CC than for $\nu_{e,\mu}$ CC events due to the lower average inelasticity and the resulting higher average light yield (see Sec. 7.2.2).

Effective volumes depend also on the neutrino direction. This is shown in Fig. 11.6 for ν_e CC events. Other neutrino flavours show a similar zenith-angle dependency. For

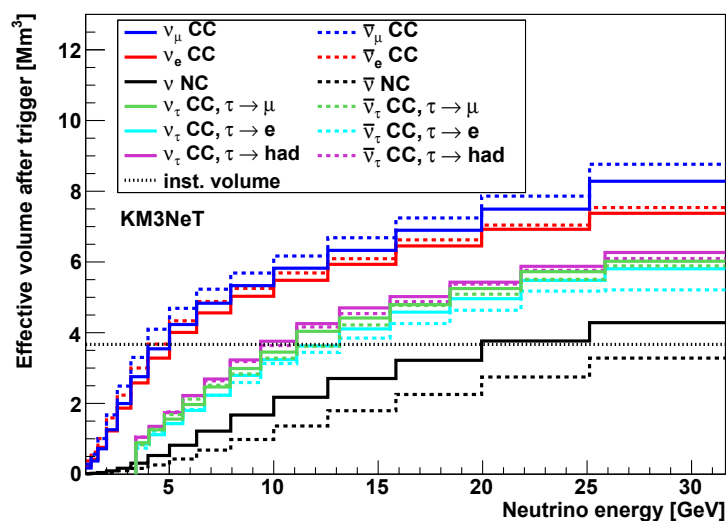


Figure 11.5: Effective volume at trigger level for the benchmark detector with 6 m vertical spacing between DOMs as a function of neutrino energy for upgoing ($\cos(\theta_\nu) < 0$) neutrinos of different flavours.

⁶⁷ A few minutes of detector lifetime are sufficient to estimate the trigger rates from atmospheric muons.

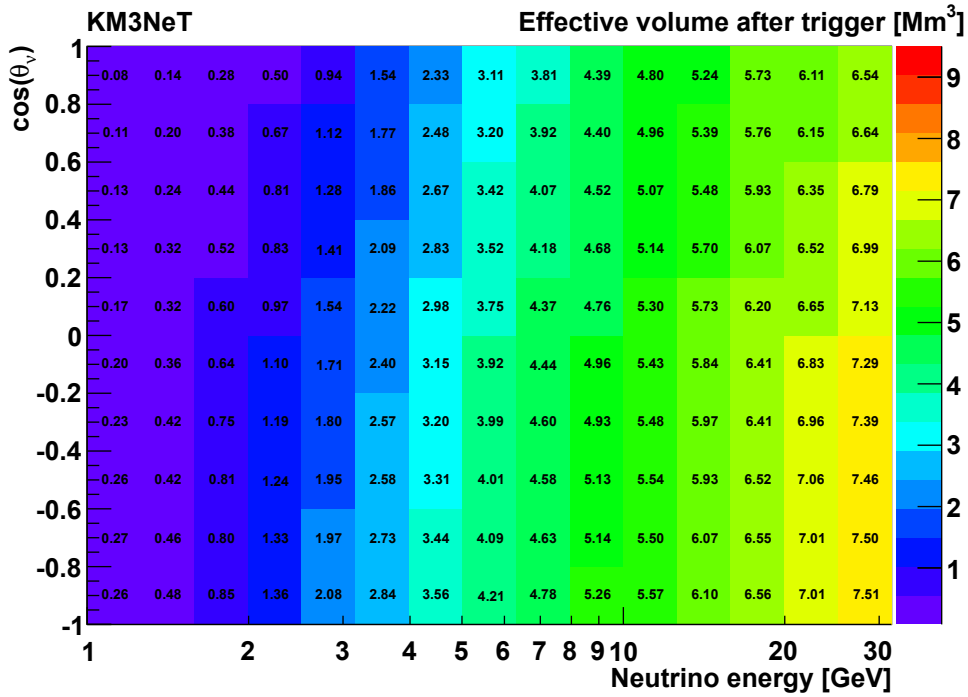


Figure 11.6: Effective volume at trigger level for ν_e CC events as a function of E_ν and $\cos(\theta_\nu)$.

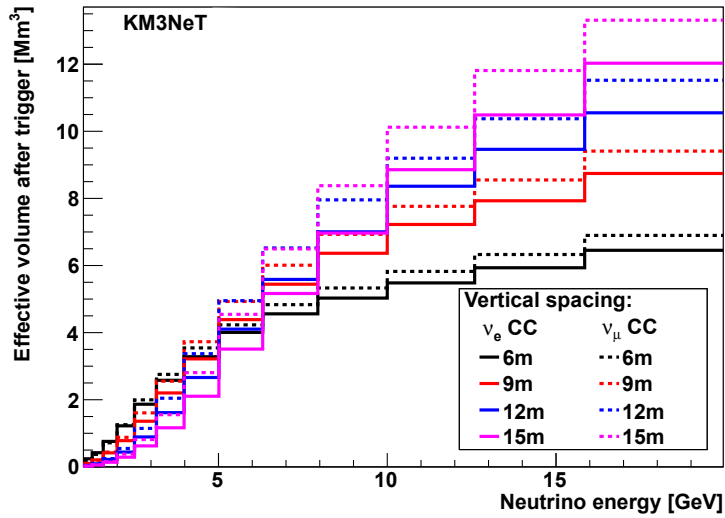


Figure 11.7: Effective volume at trigger level for the benchmark with different vertical spacings between the DOMs (6 m/9 m/12 m/15 m) as a function of neutrino energy for upgoing $\bar{\nu}_e$ CC (solid lines) and $\bar{\nu}_\mu$ CC events (dashed lines).

vertically upgoing events ($\cos(\theta_\nu) \rightarrow -1$), the effective volume starts to rise at lower energies than for horizontal events ($\cos(\theta_\nu) \approx 0$), as more PMTs are oriented down- than upward in a DOM.

The effective volumes at trigger level of $\bar{\nu}_e$ CC and $\bar{\nu}_\mu$ CC events for different vertical spacings between DOMs are shown in Fig. 11.7. For 9 m, 12 m and 15 m vertical spacing, the simulation of the benchmark detector with a 6 m spacing is masked and the resulting effective volumes are scaled to the same number of DOMs per detection string, as described

in Sec. 6.4. Detector configurations with a smaller vertical spacing between DOMs and therefore higher photocathode photosensor density perform better at lower neutrino energies, while larger vertical spacing allow a larger volume to be instrumented (with the same amount of DOMs) and show therefore larger effective volumes for higher neutrino energies.

11.4 Conclusions and suggestions for improvements

The possible gain that might be achievable with more sophisticated trigger algorithms can be deduced from Fig. 11.3. At neutrino energies relevant for the NMH determination, a significant fraction of $\bar{\nu}_{e,\mu}$ CC events would be reconstructable, but are not able to fire the trigger with the considered configuration. For $E_\nu = 4$ GeV, up to $\sim 40\%$ ($\sim 10\%$) more events with $y > 0.8$ ($y < 0.2$) might be reconstructable than triggered. For a sparser detector configuration than the benchmark detector with 6 m vertical spacing between the DOMs – such as the current ORCA detector design with 9 m vertical spacing – this fraction will even increase, since the trigger turn-on is shifted to larger energies due to the reduced photosensor density.

As discussed in Sec. 11.2.2, the strategy of the shower trigger is also appropriate for few-GeV $\bar{\nu}_\mu$ CC events, because muon track lengths are small compared to photon travel distances. Fig. 11.1 shows also the efficiency for a shower trigger configuration of $N_{L2}^{\text{shower}} = 3$ together with $D_{\text{max}} = \infty$, i.e. the maximal achievable efficiency for any trigger algorithm that requires a minimum cluster size of $N_{L2}^{\text{shower}} = 3$. However, about $\sim 10\%$ of the reconstructable $\bar{\nu}_e$ CC events with $E_\nu \approx 3$ GeV and $\cos(\theta_\nu) < -0.7$ have less than $N_{L2}^{\text{shower}} \leq 2$. These events are reconstructable due to a sufficiently large number of hit DOMs with only a single hit PMT. Fig. 11.8 shows the number of hit DOMs versus the number of L1 hits for reconstructable $\bar{\nu}_e$ CC events with $E_\nu \approx 3$ GeV.

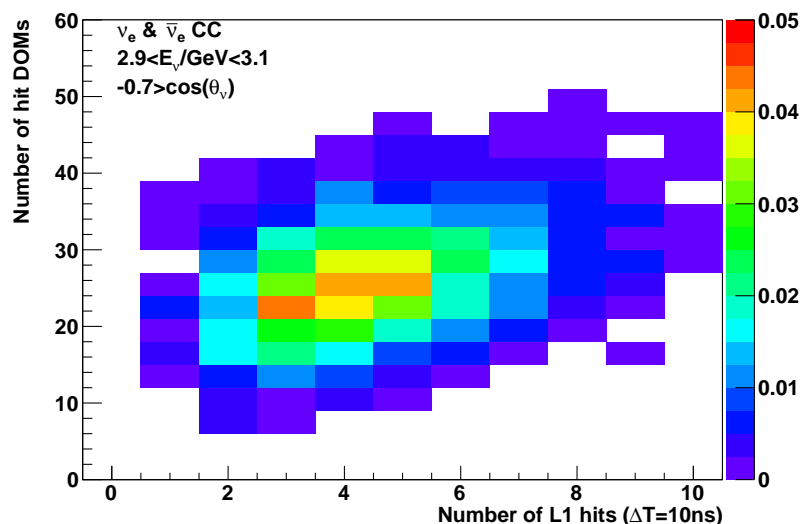


Figure 11.8: Number of hit DOMs versus number of L1 hits for reconstructable $\bar{\nu}_e$ CC events with $2.9 \text{ GeV} < E_\nu < 3.1 \text{ GeV}$ and $\cos(\theta_\nu) < -0.7$.

Based on these considerations, trigger algorithms incorporating L0 hits should be considered. The ultimate solution would be the clustering with all L0 hits. This might be not practicable due to run-time constraints. A possibility might be to follow for all clusters with $N_{L2}^{\text{shower}} = 2$ (or 3) one of the following two procedures:

- Scoring the L1 hits based on all causally connected hits (including L0) in the vicinity (including neighbouring strings) and include these scores in the trigger decision. A

possible scoring scheme has been invented for the hit selection applied in the shower reconstruction and is described in Appendix C. Using this scoring scheme, a considerable improvement in identifying signal-like hits is suggested by Fig. C.2 (Appendix).

- Applying a fast vertex fit based on all hits (including L0) in the vicinity of causally connected L1 hits and include the hit time residuals (Eq. 7.7) in the trigger decision.

It might be worth to investigate if an efficient algorithm can be developed that implements one of these strategies and fulfills the run-time constraints. In addition, the possibility to use GPUs ('graphics processing units') for time sorting should be investigated, as it might allow clustering with all L0 hits.

12 Shower reconstruction

This section describes the methodology and performance of the reconstruction strategy that has been developed as part of this thesis for shower-like events in the KM3NeT/ORCA detector. The reconstruction is optimised for $\bar{\nu}_e$ CC events, which play a crucial role for the envisaged NMH measurement, good direction and energy resolutions are therefore mandatory.

The reconstruction algorithm is a realisation of the 3rd strategy in Sec. 7.3.3 and incorporates most of the phenomenology of few-GeV $\bar{\nu}_e$ CC events discussed in Sec. 7. Besides the energy and direction of the incoming neutrino, also the interaction inelasticity y is reconstructed.

First, the reconstruction algorithm is described in Sec. 12.1, and the event selection criteria are outlined in Sec. 12.2. Then, the reconstruction performance for signal and background events is presented in Sec. 12.3, and the advantages due to also reconstructing the interaction inelasticity y are quantified in Sec. 12.4. In Sec. 12.5, the attained performance is compared to the intrinsic limits derived in the previous sections and to the performance of PINGU, the competitor of the ORCA experiment.

As being one of the key ingredients for the NMH measurement with ORCA, the shower reconstruction methodology and performance are described in the ‘Letter of Intent’ [3]. A preliminary version of the reconstruction was also presented at the ‘34th International Cosmic Ray Conference’ [181]. In the following, parts of the ‘Letter of Intent’ [3], where I am responsible for, are copied in verbatim. Also plots, for which I am responsible for, are labelled ‘KM3NeT’ and copied without further indication.

12.1 Shower reconstruction algorithm

A neutrino induced shower-like event is characterised by 8 parameters: vertex position \vec{x}_{vtx} and time t_{vtx} , energy E , direction \hat{e}_s and inelasticity y .

The shower reconstruction is performed in two steps. In the first step, the vertex (\vec{x}_{vtx} , t_{vtx}) is reconstructed based on the recorded time of the hits, and in the second step, the direction \hat{e}_s , energy E and inelasticity y are reconstructed based on the number of hits and their distribution in the detector. In both steps, a maximum likelihood fit (see Sec. 4.7) is performed for many different initial shower hypotheses and the solution with the best likelihood is chosen. This factorisation of the fitting procedure works well due to the homogeneity of seawater and its large scattering length, which allows for a precise vertex reconstruction independent of the shower direction⁶⁸ (see Fig. 7.20).

The workflow of the shower reconstruction is illustrated in Fig. 12.1. Each step is explained in the following.

Implementation

The shower reconstruction is implemented as part of the software framework *SeaTray* [182], the official framework for data processing and event reconstruction in ANTARES. Time consuming parts are implemented in **C++**, while the majority of the algorithms are implemented in **Python**. The general structure of the algorithms have been adopted from the ‘Dusj’ shower reconstruction project [183]. All maximum likelihood fits are performed with *Gulliver* [184], a software package within SeaTray.

⁶⁸ This is not the case in ice, where shower direction and photon arrival time show a significant correlation (see Fig. 8.9) due to the photon scattering properties of ice (see Sec. 8.1).

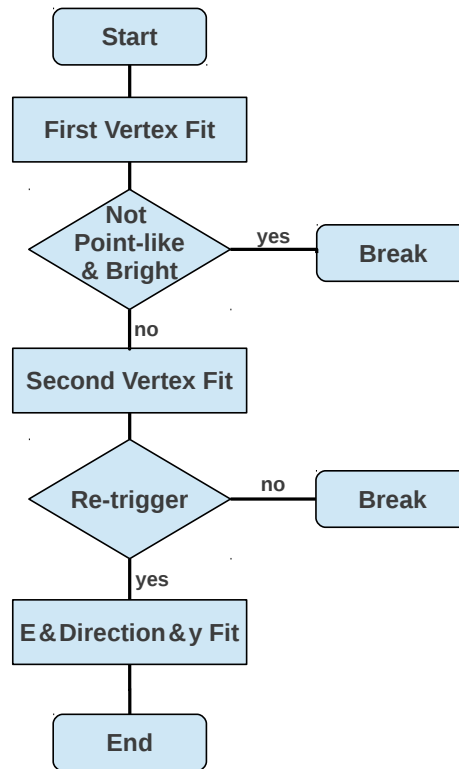


Figure 12.1: Workflow scheme of the shower reconstruction. Each step uses a dedicated hit selection that is based on the results of the previous reconstruction steps.

12.1.1 Vertex reconstruction

The majority of Cherenkov light from electromagnetic and hadronic showers is emitted within a few meters around the neutrino interaction vertex (see Fig. 7.7). Therefore, hits from unscattered photons emitted by a shower are characterised by small time residuals t_{res} (Eq. 7.7) with respect to a point-like emission hypothesis, and can only be detected by PMTs that are oriented towards the vertex, i.e. $\cos(\psi) < 0$, where ψ is the angle between the PMT direction (vector normal to the photocathode plane) and the vector \vec{d} from the vertex to the PMT (see Fig. 7.23).

The vertex reconstruction is performed in two successive maximum likelihood fits. For both fits, the likelihood for the vertex hypothesis $(t_{\text{vtx}}, \vec{x}_{\text{vtx}})$ is given by:

$$L = \sum_{\text{hits}} g(t_{\text{res}}, \psi | t_{\text{vtx}}, \vec{x}_{\text{vtx}}), \quad (12.1)$$

where $g(t_{\text{res}}, \psi | t_{\text{vtx}}, \vec{x}_{\text{vtx}})$ is a function of the hit time residuals t_{res} and angle ψ for a given shower hypothesis $(t_{\text{vtx}}, \vec{x}_{\text{vtx}})$.

While the first vertex fit (prefit) is designed to be very robust against noise hits and an imprecise initial vertex hypothesis, the second vertex fit is more precise but needs a hit selection with higher signal purity and a good initial vertex hypothesis. These requirements for the second vertex fit can easily be achieved by using the result of the prefit. The crucial parts for reconstructing few-GeV $\bar{\nu}$ CC events with only a few signal hits are the initial hit selection and the first vertex fit.

Initial hit selection for first vertex fit

The following hit patterns are defined for the initial hit selection:

L1, L2 as defined for triggers in Sec. 11.1.2,

L3 coincidence between hits on 3 PMTs on the same DOM in a time window $\Delta t \leq 10$ ns,

V2L2 coincidence between two L2 hits on different DOMs, which are closer than 35 m and within a time window $\Delta t \leq 10$ ns + t_D , where $t_D = D/c_{\text{water}}$ is the time required by the light to travel the distance D between the two DOMs,

T0L0 coincidence between two hits on adjacent or next-to-adjacent DOMs on the same string in a time window $\Delta t \leq 10$, ns + t_D .

The general strategy is to find first a *reference hit* that is very likely a signal hit and close to the neutrino interaction vertex. The position/time of this reference hit is then used as an initial vertex hypothesis to select additional hits based on their time residual and further requirements to suppress noise hits.

First, the largest cluster of causally connected L2 hits is selected by requiring $\Delta t \leq D/c_{\text{water}} + 10$ ns for all L2 hits within the cluster (similar to clustering in the shower trigger described in Sec. 11.1.3, but with $D_{\text{max}} = \infty$). From these causally connected L2 hits, the subset of hits that additionally satisfy the L3 or V2L2 criteria is selected. These L3 or V2L2 hits are ranked according to their hit multiplicity (number of coincidences on the same DOM) and the number and multiplicity of causally connected hits in the vicinity. The hit scoring procedure is explained in Appendix C. The hit with the highest score is most signal-like and is expected to be rather close to the neutrino interaction vertex. This most signal-like hit is chosen as reference hit.

Second, all hits around the reference hit are selected that are closer than 100 m, within a time window of -250 ns < $t_{\text{res}} < 10$ ns and causally connected with most L3 or V2L2 hits ('most' means connected with minimal 80% of them and not connected with maximal 2 of them). The lower t_{res} cut allows for distances up to about 50 m between the true neutrino interaction vertex and the reference hit, e.g. because the neutrino interaction is outside the detector volume. The drawback of this relatively large time window is a contamination with noise hits. Therefore, hits are discarded that do not satisfy at least one of the following three requirements: (i) L1 criterion, (ii) causally connected with an adjacent L3 or V2L2 hit on the same string or (iii) T0L0 criterion in addition to being causally connected with a L3 or V2L2 hit in the vicinity of 25 m (this distance allows for similar stores on neighbouring strings).

The hits selected by this procedure are used in the first vertex fit and position/time of the 15 most signal-like hits (see Appendix C) are used as initial vertex hypotheses.

First vertex fit (prefit)

The vertex prefit is performed using the initial hit selection for the 15 different initial vertex hypotheses and the solution with the best likelihood is chosen.

In the vertex prefit, the following function g for the likelihood (Eq. 12.1) is used:

$$g(t_{\text{res}}, \psi) = 1 / \left(\sqrt{a^2 + (t_{\text{res}}/\text{ns})^2} + p(\psi) \right), \quad (12.2)$$

where the parameter $a \neq 0$ avoids the singularity for vanishing t_{res} . The function $p(\psi)$ is ψ -dependent and penalises hits on PMTs that are not oriented towards the assumed vertex position. The penalty is given by:

$$p(\psi) = \begin{cases} 0 & \text{if } \cos(\psi) < 0, \\ p_{\text{max}} & \text{if } \cos(\psi) > \cos(\psi_{\text{th}}), \\ p_{\text{max}} \times \cos(\psi) / \cos(\psi_{\text{th}}) & \text{else,} \end{cases} \quad (12.3)$$

where ψ_{th} is a threshold defining at which angle the maximal penalty p_{max} is reached. For PMTs close to the vertex, a larger value for ψ_{th} is desirable in order to avoid rapid changes in the penalty for minor changes in the vertex position hypothesis. Therefore, a distance-dependent ψ_{th} is used:

$$\cos(\psi_{\text{th}}) = \frac{d_{\text{ref}}}{\sqrt{d_{\text{ref}}^2 + d^2}}, \quad (12.4)$$

where d is the vertex-PMT distance and d_{ref} is a reference distance. In the following, $a = 2 \text{ ns}$, $p_{\text{max}} = 100$ and $d_{\text{ref}} = 10 \text{ m}$ are used.

Hit selection for second vertex fit

Based on the result of the vertex prefit, a rather pure signal hit selection is achieved by selecting hits according to the following criteria:

- $10 \text{ m} < d < 80 \text{ m}$,
- $-50 \text{ ns} < t_{\text{res}} < 50 \text{ ns}$,
- $-1 < \cos(\psi) < 0.1$.

Second vertex fit

In total, 10 initial vertex hypotheses are generated from the result of the prefit (result of the prefit and 9 vertex hypotheses around it with time shifts of $\pm 25 \text{ ns}$ and position shifts of 5 m in a random direction).

For function g in Eq. 12.1, a distance-dependent t_{res} distribution, obtained from simulated $\bar{\nu}_e$ CC events, is used and is shown for three distances in Fig. 12.2. With increasing vertex-PMT distance the t_{res} distribution becomes slightly broader due to scattering and dispersion (see Fig. 8.5 left), and the hit probability decreases due to absorption leading to a relative increase of the noise level.

The fitted vertex with the best likelihood and within 10 m and 50 ns around the result of the prefit is chosen as final vertex.

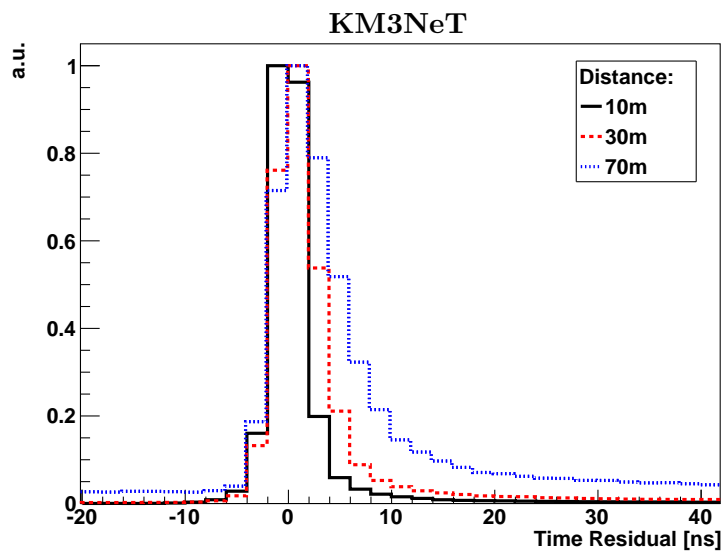


Figure 12.2: Distributions of time residuals t_{res} for three different vertex-PMT distances, obtained from simulations of fully contained $\bar{\nu}_e$ CC events with 5 kHz single noise rate. The time residual is defined with respect to the brightest point of the shower. The distributions are normalised so that the maximum is unity.

12.1.2 Reconstruction of energy, direction and inelasticity

Once the shower vertex is fixed, the remaining parameters (shower energy, direction and the interaction inelasticity) can be fitted. In principle, all of these parameters can be inferred from the angular light distribution (see Fig. 7.21): the shape is sensitive to the inelasticity y , the integral is to first order proportional to the energy (as the light yield is to first order proportional to the shower energy) and the direction in which this angular light emission profile is present gives the shower direction.

The shower energy E , direction \hat{e}_s and inelasticity y are reconstructed using a maximum likelihood fit based on the probability that the hit pattern is created by a trial shower hypothesis $\vec{\alpha} = (t_{\text{vtx}}, \vec{x}_{\text{vtx}}, E, y, \hat{e}_s)$. As discussed in Sec. 7.3.1, the electron mostly is the dominant particle in $\bar{\nu}_e$ CC events and produces the brightest Cherenkov cone. Therefore, the reconstruction is designed to find the electron direction \hat{e}_e and not the neutrino direction⁶⁹.

Final hit selection

Based on the vertex fit result, hits are selected according to the following criteria:

- $10 \text{ m} < d < 80 \text{ m}$
- $-25 \text{ ns} < t_{\text{res}} < 25 \text{ ns}$
- $-1 < \psi < 0.1$

For simplification⁷⁰, all PMT-hits on the same DOM are merged and the times of the individual hits are not taken into account, so that the event is quantified by the number $N_{\text{hits}}^{\text{DOM}}$ of hit PMTs for each DOM. For the fit, all DOMs with $10 \text{ m} < d < 80 \text{ m}$ are considered, that includes also the DOMs without any selected hit.

Likelihood

Ignoring shower-to-shower fluctuations, the probability $P(N_{\text{hits}}^{\text{DOM}})$ to detect $N_{\text{hits}}^{\text{DOM}}$ on a given DOM depends on: E , y , distance d between the vertex and the DOM, angle θ between shower direction \hat{e}_s and the vector \vec{d} from the vertex to the DOM, and the DOM orientation. The DOM orientation can be described by a single angle β between \vec{d} and the DOM direction, because the angular acceptance of the entire DOM (sum of all PMT angular acceptances) shows to first order a rotational symmetry due to the multi-PMT structure (see Fig. 5.3). All of these quantities are illustrated in Fig. 12.3.

The likelihood is computed as follows:

$$L = \prod_{\text{selected DOMs}} P(N_{\text{hits}}^{\text{DOM}}(E, y, d, \theta, \beta) | \vec{\alpha}). \quad (12.5)$$

In order to define the probability $P(N_{\text{hits}}^{\text{DOM}})$, two auxiliary quantities are introduced: the mean number of expected photons $\langle N_\gamma \rangle$ detected by all PMTs in the entire DOM and the

⁶⁹ Using the neutrino direction instead of the electron direction for defining the shower direction has also been tested, but showed overall a slightly worse performance. However, for events with $y \rightarrow 1$, the direction resolution was better when using the neutrino direction, as expected from the interaction kinematics (see Sec. 7.1.2). This suggests that there is room for improvement by combining both approaches. This possibility has not been investigated yet.

⁷⁰ Besides reducing the computation time for the fit, this simplification is justified by the fact that each DOM in principle measures the intensity of the shower event at a given spatial position. As the PMTs on the same DOM are nearly at the same position and unscattered light from a shower arrives at the DOM nearly at the same time, the information of individual PMTs – which PMT is hit at which time – is not indispensable. Of course, the multi-PMT structure is needed to estimate the shower intensity from the number $N_{\text{hits}}^{\text{DOM}}$ of hit PMTs.

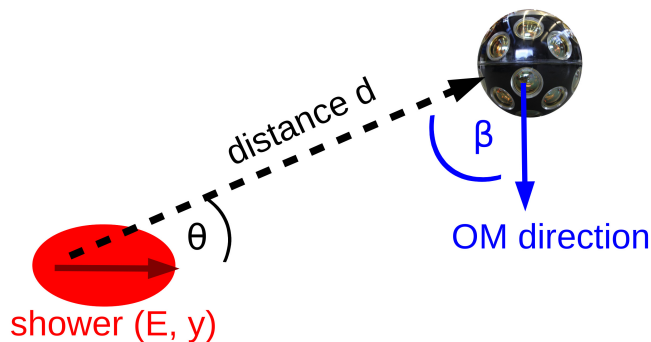


Figure 12.3: Illustration of the quantities relevant for the probability $P(N_{\text{hits}}^{\text{DOM}})$.

variance $\text{var}(N_\gamma)$ of the N_γ distribution. The latter is introduced to take fluctuations in the hadronic shower into account.

The dependency on the DOM orientation and the distance are parameterised. For the dependency on the DOM orientation, $\langle N_\gamma \rangle$ is assumed to follow the angular acceptance of the entire DOM (see Fig. 5.3). For the final hit selection, the attenuation of $\langle N_\gamma \rangle$ with distance d is well described by

$$\langle N_\gamma \rangle(d) \propto \exp(-d/\lambda_{\text{att}}(d)) \cdot d^{-2}, \quad (12.6)$$

where the exponential term describes the effective attenuation due to absorption and scattering (in conjunction with the hit time residual cut) and the latter term describes the geometrical reduction of solid angle coverage of a DOM at a distance d . The effective attenuation length λ_{att} has been derived from a fit to simulations and can be parameterised as $\lambda_{\text{att}}(d) = a + b \cdot d$, with $a = 32.2$ m and $b = 0.034$. The distance dependence of λ_{att} is a consequence of the wavelength dependence of the absorption and scattering lengths (see Fig. 8.1).

Taking these parameterisations into account, $\langle N_\gamma \rangle$ and $\text{var}(N_\gamma)$ depend on E , y , θ and d . Although the d -dependency is already accounted for via the parameterisation, the shape of the θ distribution might slightly change with distance, so that a coarse binning in d is included. The probability density function $P(N_{\text{hits}}^{\text{DOM}})$ depends on $N_{\text{hits}}^{\text{DOM}}$, $\langle N_\gamma \rangle$, $\text{var}(N_\gamma)$, and β . The quantities $\langle N_\gamma \rangle$, $\text{var}(N_\gamma)$ and the probability $P(N_{\text{hits}}^{\text{DOM}})$ are obtained from simulations of $\vec{\nu}_e$ CC events.

Further details on the likelihood were presented in [185].

Example distributions of the expected number of photons $\langle N_\gamma \rangle$ as a function of the angle θ for different inelasticity and energy intervals are shown in Fig. 12.4. As the angle θ is defined with respect to the electron direction, a clear Cherenkov peak of the electron at 42° is visible. With higher inelasticity y (Fig. 12.4 left), this peak becomes fainter due to less energetic electrons, while the number of expected photons in the ‘off-peak region’ ($\theta \gtrsim 60^\circ$) increases due to the more energetic hadronic showers. Therefore, these PDF tables gain sensitivity to the interaction inelasticity y from the ratio of the peak to the off-peak region. With increasing energy (Fig. 12.4 right), the peak becomes brighter, i.e. $\langle N_\gamma \rangle$ increases. The shape of the distribution changes slightly with energy due to the change in the typical scattering angles $\phi_{l,h}$ between the lepton and the hadronic shower (see Sec. 7.1.2).

An example probability density distribution for $P(N_{\text{hits}}^{\text{DOM}})$ as a function of $\langle N_\gamma \rangle$ is shown in Fig. 12.5. With increasing $\langle N_\gamma \rangle$, the number $N_{\text{hits}}^{\text{DOM}}$ of hit PMTs on a DOM also increase. The slope is smaller than unity and decreases with $\langle N_\gamma \rangle$, as more than one

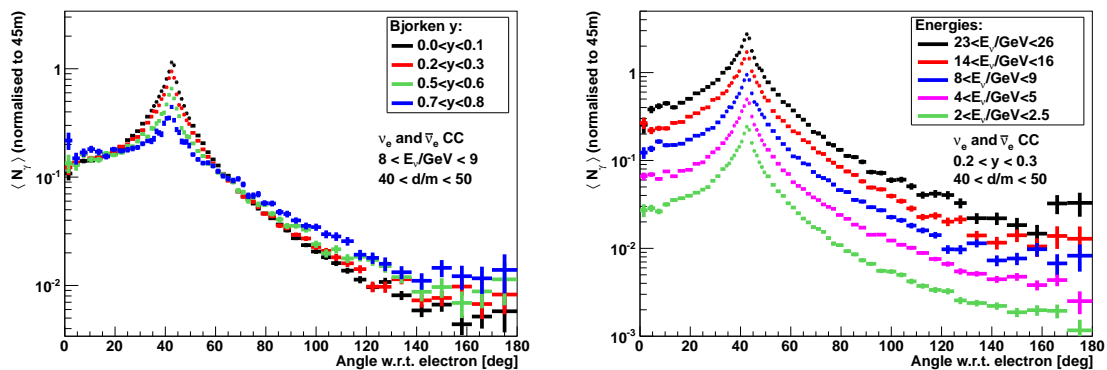


Figure 12.4: Number of expected photons $\langle N_\gamma \rangle$ detected by all PMTs in the entire DOM as a function of angle θ between shower direction, which is the electron direction, and the vector from the vertex to the DOM for different inelasticity y intervals (left) and for different energy intervals (right). Reference distance, shower energy, inelasticity are: $d = 45$ m, $E = 8.5$ GeV, $0.2 < y < 0.3$.

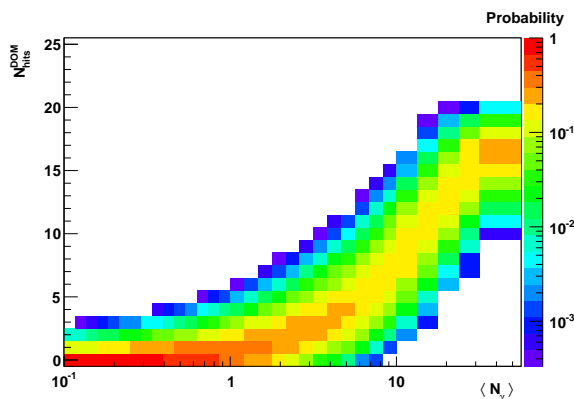


Figure 12.5: Probability to detect $N_{\text{hits}}^{\text{DOM}}$ hits on a DOM as a function of number of expected photons $\langle N_\gamma \rangle$ for $150^\circ < \beta < 180^\circ$, i.e. light reaching the DOM from below.

photon can hit the same PMT. For $\langle N_\gamma \rangle \gtrsim 40$, $N_{\text{hits}}^{\text{DOM}}$ saturate to the number of PMTs oriented to the vertex.

Also more smoothed tables for $\langle N_\gamma \rangle$ have been studied. The smoothed counterpart of Fig. 12.4 (left) is shown in Fig. D.2 (Appendix). It turned out that the unsmoothed tables work better for energy and particularly for inelasticity reconstruction. Therefore, the unsmoothed tables are used for all results shown here.

Fitting procedure

For technical reasons, each event is fitted with 9 different fixed inelasticity y assumptions⁷¹ ($y = [0 - 0.1, 0.1 - 0.2, \dots, 0.7 - 0.8, 0.8 - 1]$). For each fixed y , the likelihood maximisation is performed for 5 different initial shower hypotheses. The initial shower hypothesis is calculated from the selected hits. The initial direction is estimated by the sum of all vectors from the vertex to the DOM weighted by $N_{\text{hits}}^{\text{DOM}}$ and the initial energy is estimated empirically by $(\sum N_{\text{hits}}^{\text{DOM}} - 20)/4$. The other four seeds are randomly chosen perpendicular to the first shower hypotheses with the same energy.

⁷¹ The last inelasticity y bin (0.8-1) is chosen larger than the other bins, as the MC statistics decreases for $y \rightarrow 1$ and $y > 0.8$ is anyway hardly reconstructable (see Sec. 7.3.1).

Finally, the result with the best likelihood of all 45 fits is selected. Thus, the final result has a discrete value for the reconstructed inelasticity y .

Due to this multiple fitting procedure and large number of DOMs in the likelihood calculation this step is the most time-consuming part in the reconstruction algorithm and takes ~ 5 seconds per event on the ‘standard’ computer at the computing centre in Lyon [186]. The time consumption is mainly independent of the number of selected hits and therefore the neutrino energy, because the likelihood in Eq. 12.5 takes all DOMs and not only hit DOMs into account. For very large number of signal hits (few tens of L1 hits or more), the hit selection and especially the clustering, which both scale with $\mathcal{O}(N_{\text{hits}}^2)$, can add additional run time.

12.1.3 Decisions in reconstruction flow

In the flow of the reconstruction (see Fig. 12.1), two decisions are made, which can lead to a break of the algorithm, i.e. the event is discarded.

Atmospheric muon suppression

After the first vertex fit, events that are bright and do not look point-like are discarded. This requirement is intended to work as an ‘anti bright muon cut’ that leads to a significant speed-up in run time of the reconstruction algorithm on atmospheric muon events (dominating the trigger rate, see Sec. 11) and has only a negligible effect on the efficiency for signal shower-like events.

The general idea is that an atmospheric muon traversing the detector produces a large amount of hits, i.e. is bright, and these hits do not fit to a point-like light emission hypothesis. Therefore, for all events with more than 15 causally connected L3 or V2L2 hits in the initial hit selection, the time residuals for these hits are calculated and time ordered. If the difference between the 80% and 20% quantiles of these time residuals is larger than 15 ns (dictated by the longitudinal shower elongation, see Fig. 7.7) the event is defined as not point-like and the reconstruction algorithm for this event is stopped. In this case, the time-consuming part of the reconstruction (energy, direction and inelasticity reconstruction, see Sec. 12.1.2) is not performed. This procedure works well due to the good vertex resolution (see Sec. 12.3.1).

About $\sim 2/3$ of all triggered atmospheric muon events are discarded by this requirement, while the loss in efficiency is $\sim 1\%$ for $\vec{\nu}_e$ CC events with more than 15 causally connected L3 or V2L2 hits. This magnitude of efficiency loss is expected from the amount of muons with sufficient energy coming from π^\pm/K^\pm decays in hadronic showers (cf. Sec. 7.2.3). For $\vec{\nu}_\mu$ CC events, the efficiency loss is of course larger due to the outgoing muon. Further details are given in Sec. 12.3.6. Note that the minimum number of hits corresponds to a minimum neutrino energy of about ~ 20 GeV for $\vec{\nu}_e$ CC events. Hence, this requirement does not have any effect on $\vec{\nu}_e$ CC events in the energy range relevant for the NMH measurement.

Re-triggering

Before the energy, direction and inelasticity reconstruction (time-consuming part) is performed, it is checked if the final hit selection (including also hits with $d < 10$ m) fulfills the shower trigger conditions (see Sec. 11). Events missing this condition are discarded. This requirement ensures a reconstruction efficiency nearly independent of the trigger and noise conditions, because the hits on which the event reconstruction is based are able to fire the trigger independent of the other hits in this event.

Discarded events have either misreconstructed interaction vertices or passed the trigger solely due to matching noise-like hits. Both classes of events are not usable. A positive side

effect is that about 50% of the remaining atmospheric muons do not pass this condition, leading to an additional speed-up in run time.

12.2 Event selection

The final event selection criteria are:

- fully performed shower reconstruction, i.e. passing ‘anti atmospheric muon suppression’ and ‘re-triggering’ requirements (see Sec. 12.1.3),
- $E_{\text{reco}} > 1 \text{ GeV}$,
- results of both vertex fits are similar in space and time: distance $< 4 \text{ m}$ and time difference $< 20 \text{ ns}$,
- a minimum of 7 (3) out of the 15 (10) reconstructed vertices from different seeds in the first (second) vertex fit are similar to the selected vertex of this fit: distance $< 2 \text{ m}$ and time difference $< 10 \text{ ns}$,
- $\text{cov}_{20^\circ} \geq 0.4$, $\text{cov}_{45^\circ} \geq 0.4$, $\text{cov}_{60^\circ} \geq 0.4$ and $\text{cov}_{75^\circ} \geq 0.4$.

The *coverage* cov_α is defined as the fraction of directions on a cone with an opening angle α around the reconstructed direction at the reconstructed vertex position that satisfy the following containment condition: $L_{\text{inVol}} > 20 \text{ m}$, where L_{inVol} is the path length inside the instrumented volume for distances between 10 m and 70 m away from the vertex.

This coverage cut is introduced to ensure that a reasonable fraction of the expected hit pattern from the reconstructed shower is contained in the instrumented volume. Therefore, the coverage cut is in principle a containment cut for the reconstructed vertex that depends on the reconstructed shower direction.

12.3 Reconstruction performance

The performance of the shower reconstruction is studied based on the simulations described in Sec. 6.5 and events are selected according to the criteria described in Sec. 12.2. The ORCA benchmark detector with 6 m vertical spacing between the DOMs is assumed, if not stated otherwise. For all following results, the neutrino events are weighted to reproduce the conventional atmospheric neutrino flux following the Bartol model [84].

12.3.1 Performance for charged-current electron neutrino events

Effective volume

The effective volume V_{eff} (Eq. 11.5) for upgoing $\bar{\nu}_e$ CC events is shown in Fig. 12.6 as a function of neutrino energy for different neutrino zenith angle ranges. Depending on the zenith angle, the plateau reaches 3.8 Mm^3 (horizontal, $\cos(\theta_\nu) \approx 0$), 3.6 Mm^3 (vertical upgoing, $\cos(\theta_\nu) \approx -1$) and around 3.7 Mm^3 for all upgoing events (atmospheric neutrino flux, $-1 \leq \cos(\theta_\nu) \leq 0$). The turn-on is slightly steeper for vertical upgoing than for horizontal events, since more PMTs are oriented downward than upward in a DOM (see Sec. 5.1). 90% of the plateau value is reached at $E_\nu \approx 8 \text{ GeV}$ ($E_\nu \approx 7 \text{ GeV}$) for ν_e CC ($\bar{\nu}_e$ CC). The turn-on is slightly steeper for $\bar{\nu}_e$ CC than for ν_e CC due to the lower average inelasticity and the resulting larger average light yield (see Sec. 7.2.2).

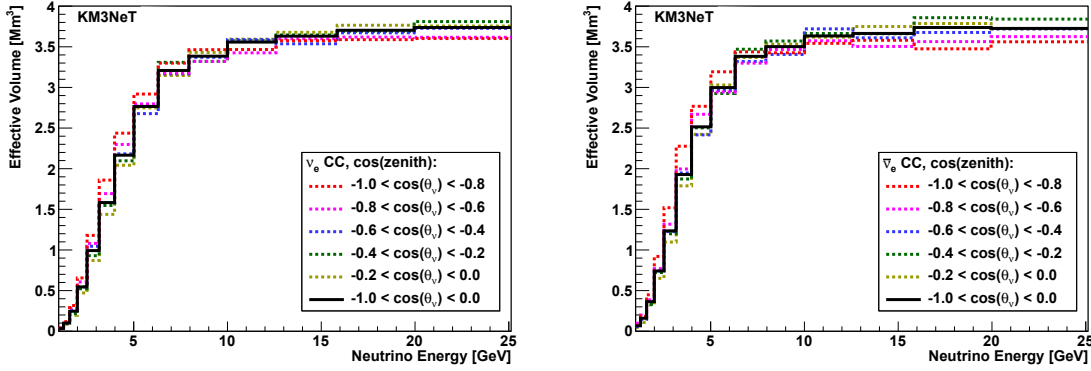


Figure 12.6: Effective volumes in Mm^3 (10^6 m^3) as a function of neutrino energy for ν_e CC (left) and $\bar{\nu}_e$ CC (right) events in different ranges of true neutrino zenith angle θ_ν . The solid black line corresponds to upgoing neutrinos weighted according to the Bartol flux model.

Vertex resolution

The distance between neutrino interaction position and reconstructed vertex position is shown in Fig. 12.7 for all selected events in the energy range of $E_\nu = 2 - 30 \text{ GeV}$. The distance is split into a component longitudinal and perpendicular to the neutrino direction. An offset in neutrino direction is clearly visible and expected, since the brightest point of the shower is reconstructed and not the interaction vertex position. As discussed in Sec. 7.2.2, the brightest point of the shower is offset by $0.5 - 2 \text{ m}$ in the relevant energy range (see Fig. 7.7). The longitudinal and perpendicular distances are fitted with Gaussian functions for different neutrino energy and inelasticity bins. Exemplary, the distributions and Gaussian fits are shown for $6 \text{ GeV} < E_\nu < 7 \text{ GeV}$ and $0.2 < y < 0.4$ in Fig. 12.8.

The mean of the Gaussian fit to the distribution of the longitudinal distances corresponds to the shift between the brightest point and the neutrino interaction. The vertex resolution corresponds to the resolution of the brightest point and is given by the fitted widths. The longitudinal and perpendicular width are combined to a three-dimensional resolution of the vertex by: $\sigma_{3D} = \sqrt{\sigma_{\text{long}}^2 + \sigma_{\text{perp}}^2}$. The longitudinal vertex shift, the longitudinal vertex resolution, the perpendicular vertex resolution, and the three-dimensional

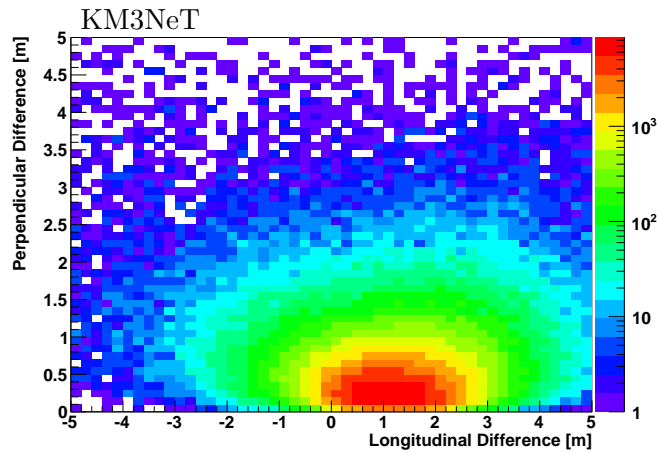


Figure 12.7: Longitudinal and perpendicular distance between neutrino interaction position and reconstructed vertex position for $\bar{\nu}_e$ CC events with $E_\nu = 2 - 30 \text{ GeV}$.

vertex resolution are shown in Fig. 12.9 in the E_ν - y plane. With increasing E_ν , the distance of the reconstructed brightest point from the interaction vertex increases. The three-dimensional vertex resolution is about $\sigma_{3D} \approx 0.5 - 1$ m and is dominated by the longitudinal vertex resolution. This precise vertex reconstruction justifies the factorisation of the shower reconstruction into a vertex reconstruction and a shower energy, direction and inelasticity reconstruction.

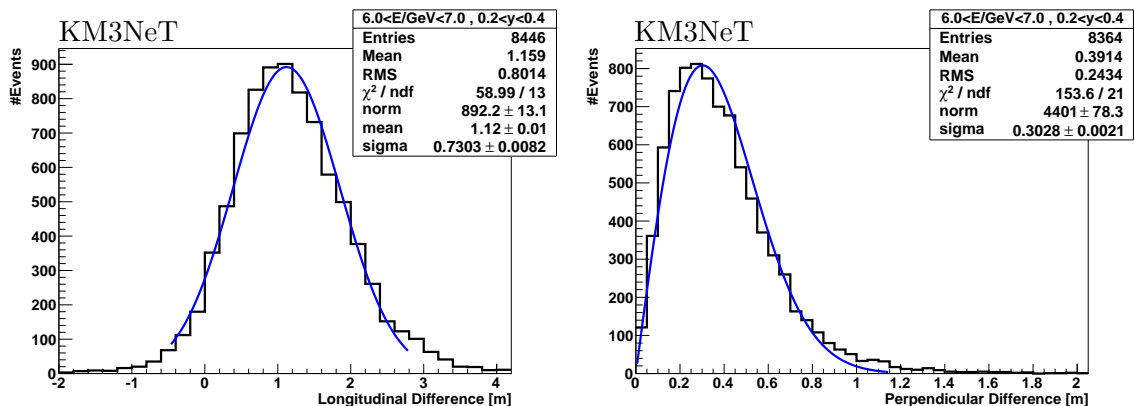


Figure 12.8: Longitudinal (left) and perpendicular (right) distance between neutrino interaction position and reconstructed vertex position for $\bar{\nu}_e$ CC events with $6 < E_\nu/\text{GeV} < 7$ and $0.2 < y < 0.4$. Distributions are fitted with a Gaussian (left) and ‘distance \times Gaussian’ (right).

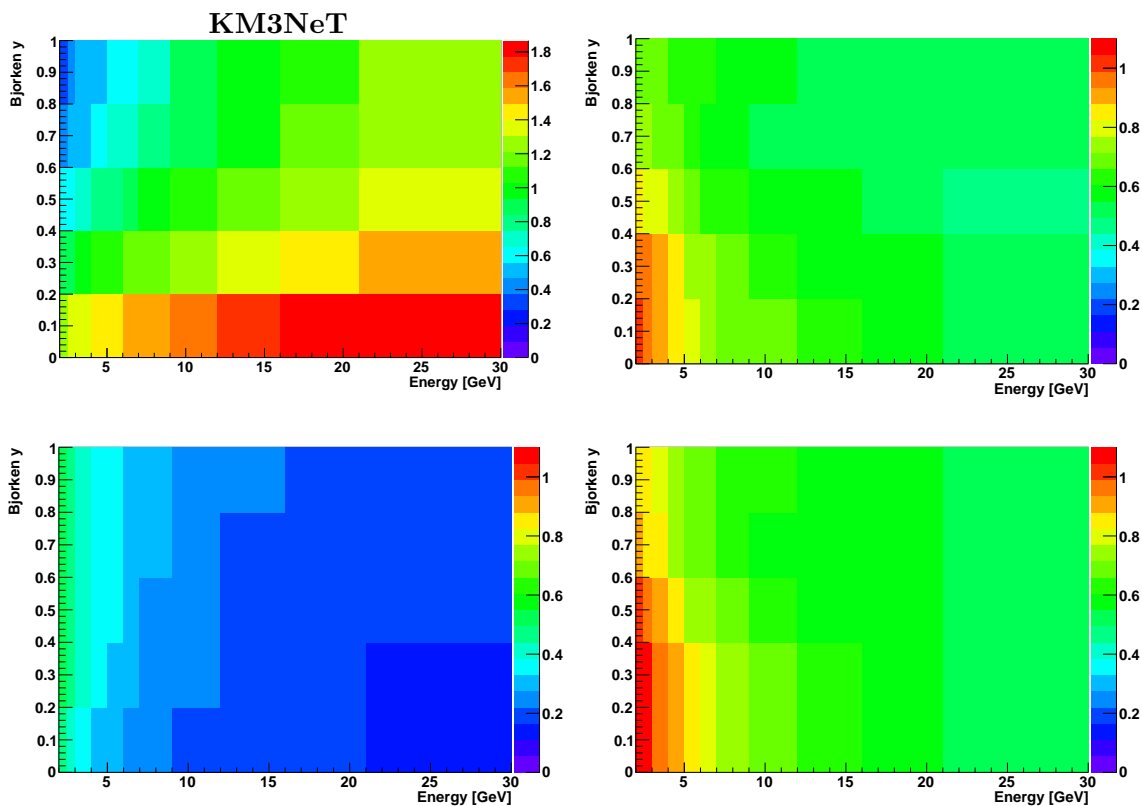


Figure 12.9: Vertex resolution for $\bar{\nu}_e$ CC events in E_ν - y plane. Colour code represents distance between neutrino interaction vertex and reconstructed brightest point. Mean value (top left) and width (top right) from Gaussian fits to longitudinal distances, width from perpendicular distances (bottom left) and three-dimensional resolution σ_{3D} (bottom right).

Direction resolution

The median neutrino direction resolution (angle between reconstructed direction and neutrino direction) is shown in Fig. 12.10 as a function of neutrino energy for different neutrino zenith angle ranges and for ν_e CC and $\bar{\nu}_e$ CC events separately. The median direction resolution is better than 10° for upgoing ν_e ($\bar{\nu}_e$) CC events with energies above 8.5 GeV (5.5 GeV). Resolutions are slightly better for vertical upgoing than for horizontal neutrinos.

As the reconstruction is designed to find the electron direction, the resolution is better for $\bar{\nu}_e$ than for ν_e due to the smaller average inelasticity for $\bar{\nu}_e$ leading on average to a smaller intrinsic scattering angle $\phi_{\nu,e}$ between the neutrino and the electron (see Fig. 7.4). The median intrinsic scattering angle, the median resolution with respect to the electron direction and the neutrino direction are shown in Fig. 12.11 as a function of neutrino energy. For the relevant energy range, the median electron direction resolution is smaller than the intrinsic scattering angle and the median neutrino direction resolution, verifying that the reconstruction actually has the ability to find the electron in $\bar{\nu}_e$ CC events.

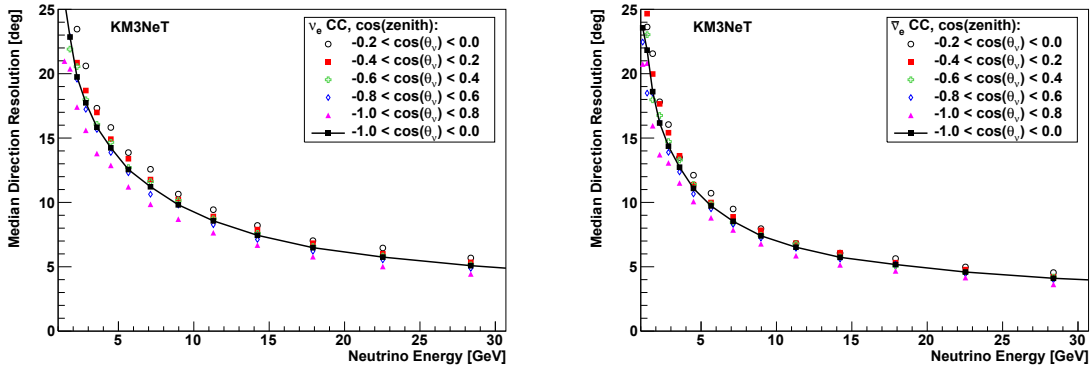


Figure 12.10: Median neutrino direction resolution (angle between reconstructed direction and neutrino direction) as a function of neutrino energy for different true neutrino zenith ranges and for ν_e CC (left) and $\bar{\nu}_e$ CC (right). The black line corresponds to upgoing neutrinos weighted according to the Bartol flux model.

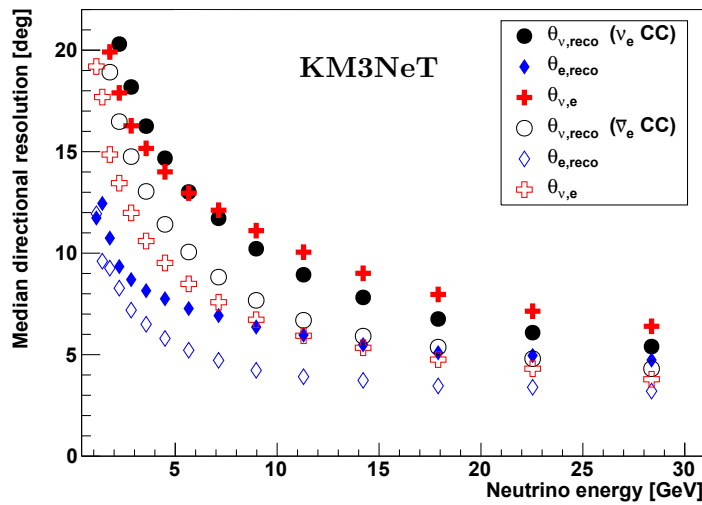


Figure 12.11: Median intrinsic scattering angle ($\phi_{\nu,e}$, red crosses), median electron direction resolution ($\phi_{e,reco}$, blue diamonds) and the median neutrino direction resolution ($\phi_{\nu,reco}$, black circles) as a function of neutrino energy for upgoing ν_e CC (solid marker) and $\bar{\nu}_e$ CC (hollow marker) events.

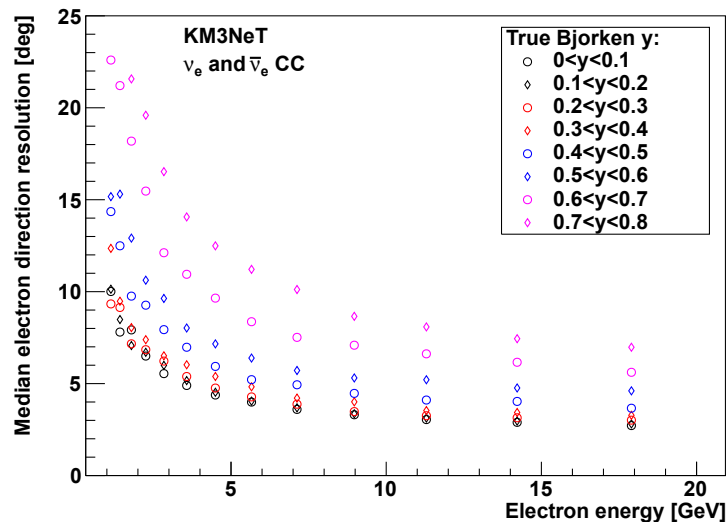


Figure 12.12: Median electron direction resolution (angle between reconstructed direction and electron direction) as a function of electron energy for upgoing $\bar{\nu}_e$ CC events. Different marker colors and styles represent different true inelasticity y ranges.

Fig. 12.12 shows the median electron direction resolution as a function of electron energy for different true inelasticity y ranges. The reconstruction of the electron direction is only slightly affected by the additional light from the hadronic shower up to $y \lesssim 0.5$. For $y \gtrsim 0.5$, the reconstruction can additionally be confused by high energetic particles in the hadronic shower producing a brighter Cherenkov cone than that from the electron. Due to momentum conservation, the most energetic particles produced in neutrino interactions tend to have smaller scattering angles with respect to the neutrino direction. Therefore, by reconstructing sometimes the leading particle from the hadronic shower the median neutrino direction for ν_e CC events is slightly better than the neutrino-electron intrinsic scattering angle for $E_\nu \gtrsim 5$ GeV, as can be seen from Fig. 12.11.

Inelasticity resolution

The resolutions of the inelasticity y for a low, medium and high y range are shown in Fig.12.13 (left) for $6 \text{ GeV} < E_\nu < 12 \text{ GeV}$. The distributions of the reconstructed inelasticity y_{reco} and true inelasticity y_{true} for ν_e CC and $\bar{\nu}_e$ CC events are shown in Fig. 12.13 (right) for $6 \text{ GeV} < E_\nu < 12 \text{ GeV}$.

The absence of $y_{\text{reco}} > 0.8$ can be explained by dominant particles in the hadronic shower mimicking a lower inelasticity, as discussed in Sec. 7.3.1. The accumulation of events at low y_{reco} is larger than expected from the true inelasticity y_{true} distributions and visible for ν_e CC as well as $\bar{\nu}_e$ CC events. This is a feature of the reconstruction algorithm.

Due to the sensitivity to y , the y_{reco} distributions are different for ν_e and $\bar{\nu}_e$ CC events leading to a separation power between both channels. This sensitivity to y can also be used to separate $\bar{\nu}_e$ CC events from $\bar{\nu}$ NC and $\bar{\nu}_\tau$ CC events. The separation power is discussed in Sec. 12.4.1.

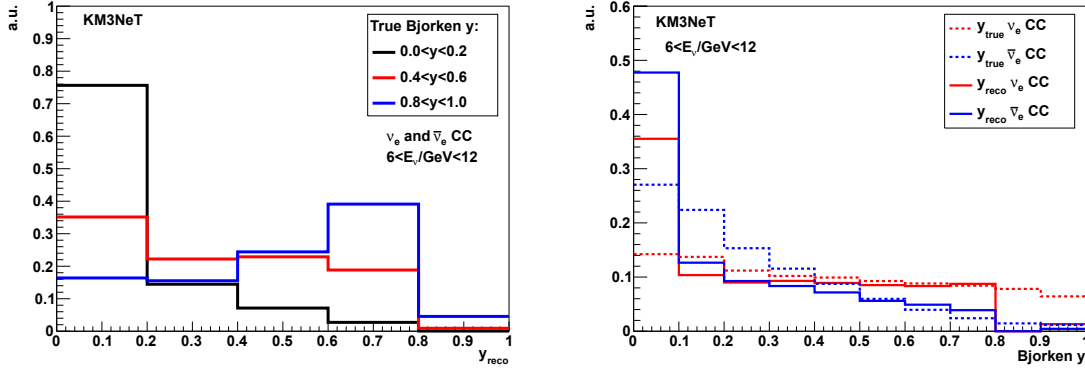


Figure 12.13: Distributions of reconstructed inelasticity y_{reco} for three different true y ranges ($y = [0 - 0.2, 0.4 - 0.6, 0.8 - 1]$) for upgoing $\bar{\nu}_e$ CC events with $6 \text{ GeV} < E_\nu < 12 \text{ GeV}$ (left). Distributions of inelasticity y_{reco} (solid lines) and true inelasticity y_{true} (dashed lines) for ν_e CC and $\bar{\nu}_e$ CC events (right).

Energy resolution

In Fig. 12.14 (left), the reconstructed energy is shown as a function of the neutrino energy for $\bar{\nu}_e$ CC events. The reconstructed energy is systematically higher than the neutrino energy. Therefore, an energy correction depending on the reconstructed zenith angle θ_{reco} , reconstructed inelasticity y_{reco} and reconstructed energy E_{reco} is applied. The corrected reconstructed energy $E_{\text{reco}}^{\text{corr}}$ is given by

$$E_{\text{reco}}^{\text{corr}} = f(y_{\text{reco}}, \cos(\theta_{\text{reco}}), E_{\text{reco}}) \cdot E_{\text{reco}}, \quad (12.7)$$

where the three-dimensional correction function $f(y_{\text{reco}}, \cos(\theta_{\text{reco}}), E_{\text{reco}})$ has been calculated from the simulations such that the median corrected reconstructed energy is equal to the neutrino energy assuming the Bartol flux model. Further details on the energy correction procedure are given in Appendix D.1. The corrected reconstructed energy as a function of the neutrino energy is shown in Fig. 12.14 (right).

In the following, the term ‘reconstructed energy’ and E_{reco} represent the reconstructed energy after the energy correction.

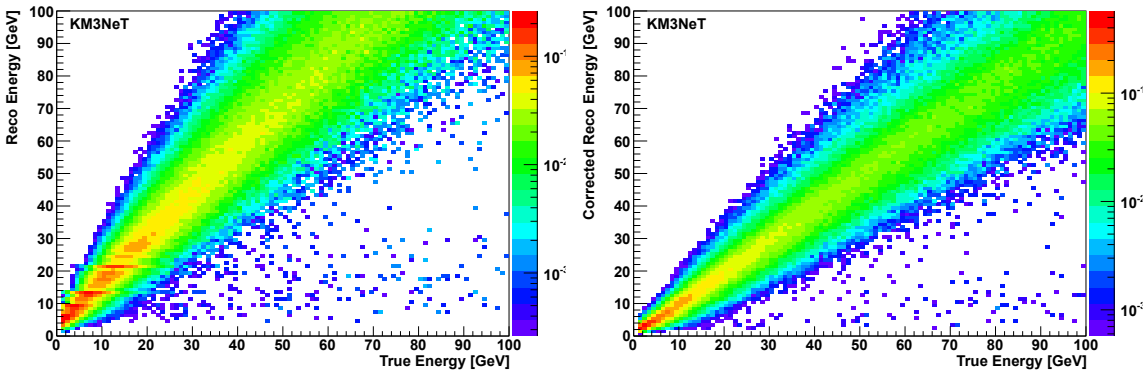


Figure 12.14: Reconstructed energy (without correction in Eq. 12.7) as a function of true neutrino energy for $\bar{\nu}_e$ CC (left). Corrected reconstructed energy for the same events (right). Each energy bin is normalised to unity.

The difference between reconstructed and neutrino energy in different neutrino energy bins is shown in Fig. 12.15 for ν_e CC and $\bar{\nu}_e$ CC events separately. These distributions are very well described by Gaussians.

The median fractional energy resolution – given as $|E_{\text{reco}} - E_\nu|/E_\nu$ – is better than 18% for neutrino energies above 5 GeV for upgoing ν_e CC and $\bar{\nu}_e$ CC events and is shown in Fig. 12.16. The relative energy resolution – given as the RMS of $(E_{\text{reco}} - E_\nu)$ distributions (see Fig. 12.15) over neutrino energy – is better than 26% (24%) for neutrino energies above 7 GeV for upgoing ν_e ($\bar{\nu}_e$) CC events and is shown as a function of visible energy E_{vis} (Eq. 7.10) in Fig. 12.18 (left), together with the resolution for the other shower-like neutrino interaction channels. For $\bar{\nu}_e$ CC events, E_{vis} is equal to E_ν . The resolution is better for $\bar{\nu}_e$ CC events than for ν_e CC events due to the lower average contribution from the hadronic shower, which shows larger fluctuations than electromagnetic showers (see Sec. 9). Fig. 12.18 (right) shows the mean relative offset between the mean reconstructed energy and the visible energy. At energies corresponding to the effective volume turn-on region the reconstructed energy is overestimated for $\bar{\nu}_e$ CC events, because only events are well reconstructed that appear more energetic than they actually are. Above ~ 9 GeV, the reconstructed energies are slightly overestimated (underestimated) for $\bar{\nu}_e$ (ν_e) CC due to the smaller light yield of hadronic showers compared to electromagnetic showers. The magnitude of over-/underestimated is compatible with the expectation from the average light yield (cf. Fig. 9.22).

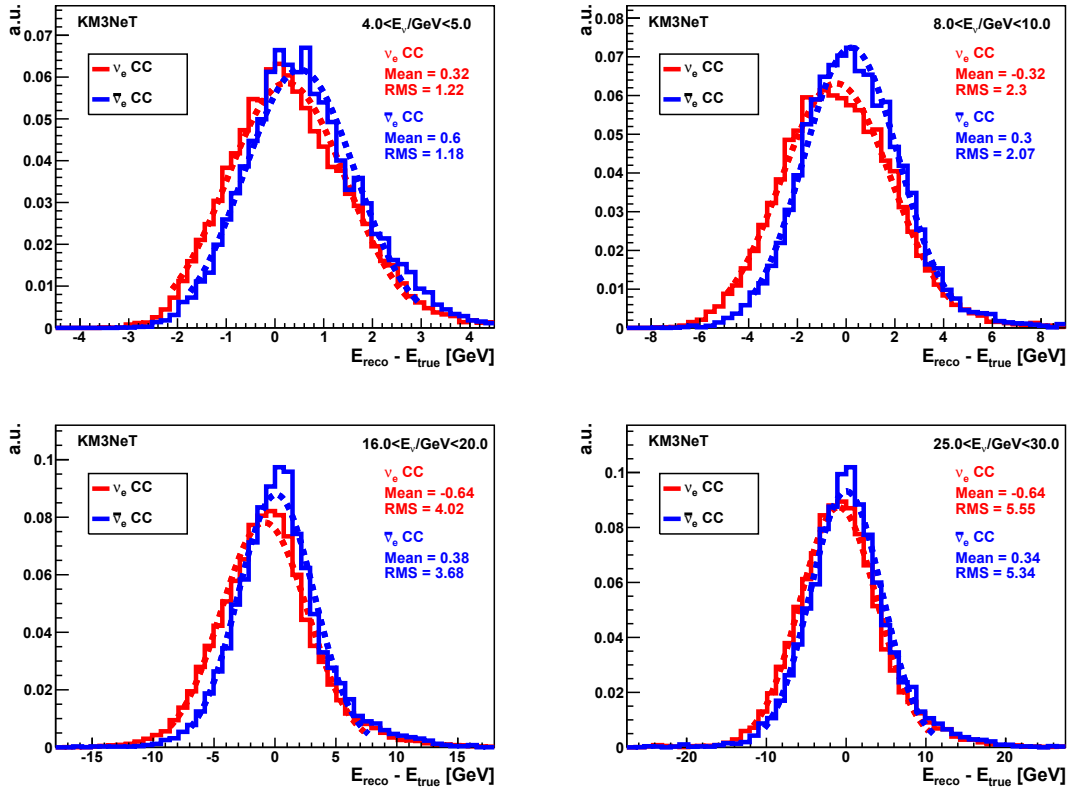


Figure 12.15: Difference between reconstructed energy E_{reco} and neutrino energy E_{true} in different neutrino energy bins for ν_e CC (red) and $\bar{\nu}_e$ CC (blue) events. Dashed lines show Gaussian fits.

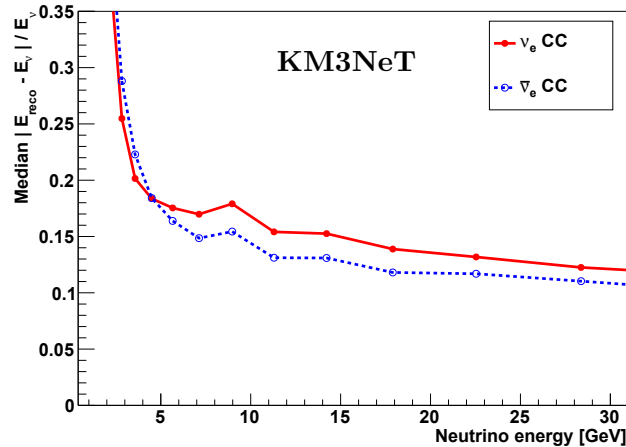


Figure 12.16: Median fractional energy resolution ($|E_{\text{reco}} - E_{\nu}|/E_{\nu}$) as a function of neutrino energy for ν_e CC (red solid) and $\bar{\nu}_e$ CC (blue dashed) events.

12.3.2 Performance for other shower-like neutrino events

The performance of the shower reconstruction is evaluated separately on different shower-like neutrino interaction event samples: ν_e and $\bar{\nu}_e$ CC events, $\nu_{e/\mu}$ and $\bar{\nu}_{e/\mu}$ NC events, ν_{τ} and $\bar{\nu}_{\tau}$ CC events where the τ lepton decays in an electron or hadrons and neutrino(s).

Effective volumes for upgoing shower-like neutrino events are shown in Fig. 12.17 (left) as a function of neutrino energy. The turn-on is much steeper for $\bar{\nu}_e$ CC events than for $\bar{\nu}$ NC and $\bar{\nu}_{\tau}$ CC events, since the outgoing neutrinos are invisible to the detector.

The median direction resolution is shown in Fig. 12.17 (right) as a function of neutrino energy. The direction resolution for $\bar{\nu}$ NC and $\bar{\nu}_{\tau}$ CC events is clearly worse than for $\bar{\nu}_e$ CC events, since the information of the outgoing neutrinos is unavailable.

The relative energy resolution – given as RMS over visible energy E_{vis} – for upgoing shower-like neutrino events is shown as a function of E_{vis} (Eq. 7.10) in Fig. 12.18 (left). As expected, the resolution is worse for events with higher average contribution from hadronic showers, which show larger fluctuations (see Sec. 9).

Due to the smaller light yield of hadronic showers compared to electromagnetic showers, the ratio $\langle E_{\text{reco}} \rangle / E_{\text{vis}}$ is different for each neutrino interaction channel and energy-dependent. This can be seen in Fig. 12.18 (right). The higher the fraction of electromagnetic shower component in the event the higher is the mean reconstructed energy. This leads also to different turn-on behaviours in the effective volume for both shower types, and consequently to different compositions (in terms of electromagnetic and hadronic shower components) of well reconstructed neutrino events. The latter explains the behaviour below $E_{\text{vis}} \lesssim 10$ GeV.

The distribution of the reconstructed inelasticity y_{reco} for $\bar{\nu}$ NC events with hadronic shower energies of $6 \text{ GeV} < E_h < 12 \text{ GeV}$ is shown in Fig. 12.19. As expected, the y_{reco} distribution for $\bar{\nu}$ NC events looks similar to the distribution for $\bar{\nu}_e$ CC events with $0.8 < y < 1$ (see Fig. 12.13), but different to other y ranges.

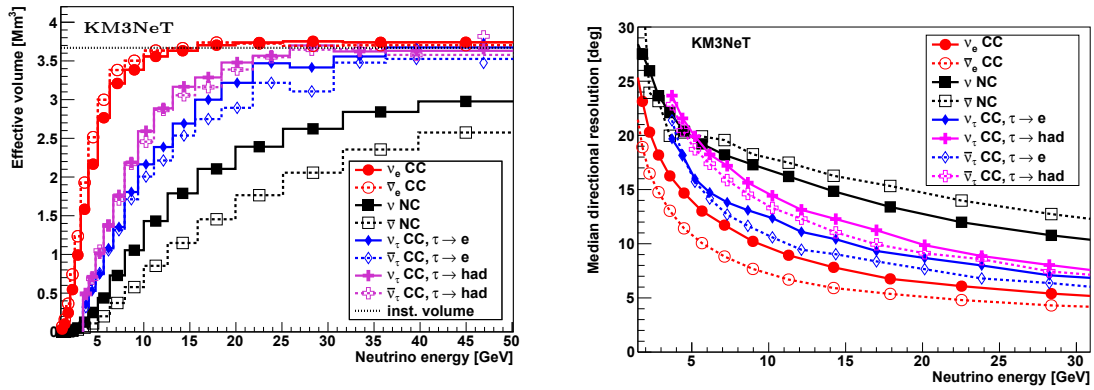


Figure 12.17: Effective volume (left) and median neutrino direction resolution (right) as a function of neutrino energy for different upcoming shower-like neutrino event types.

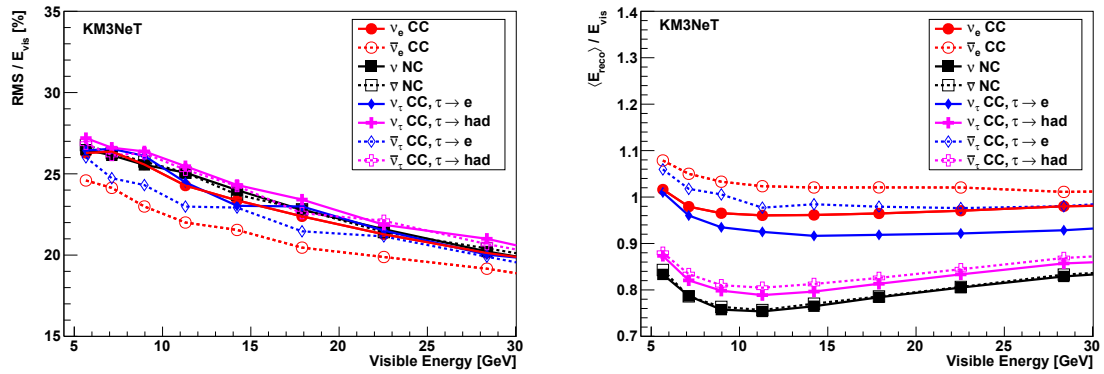


Figure 12.18: Relative energy resolution $\text{RMS}/E_{\text{vis}}$ as a function of the visible energy E_{vis} (Eq. 7.10) for shower-like neutrino interaction channels (left) and mean relative offset in reconstructed energy – given as $\langle E_{\text{reco}} \rangle / E_{\text{vis}}$ – as a function of E_{vis} (right).

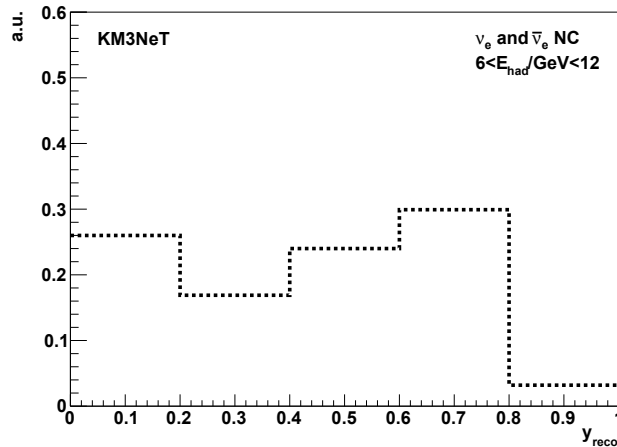


Figure 12.19: Distribution of reconstructed inelasticity y_{reco} for $\bar{\nu}$ NC events with hadronic shower energies of $6 \text{ GeV} < E_h < 12 \text{ GeV}$ and arbitrary true inelasticity.

12.3.3 Correlations between energy and direction resolutions

Energy and direction resolutions are intrinsically strongly correlated via the inelasticity y . In $\bar{\nu}_e$ CC events with small y , the shower reconstruction will in most cases find the electron, which shows a small opening angle to the incoming neutrino (see Fig. 7.4). These events show only small fluctuations in the number of emitted photons (see Sec. 9.3.1), and will consequently often be reconstructed with a rather precise energy estimate. For large- y events, the situation is the other way around: large intrinsic fluctuations in number of emitted photons and mean photon direction (see Sec. 9.4).

Fig. 12.20 shows the median neutrino direction (left) and relative energy resolution (right) as a function of neutrino energy and true inelasticity y for upgoing $\bar{\nu}_e$ CC events. The same figures but using instead the reconstructed energy E_{reco} and inelasticity y_{reco} are shown in Fig. 12.21. The discussed correlations are clearly visible for true as well as reconstructed quantities. The mean reconstructed energy $\langle E_{\text{reco}} \rangle$ of course also depends on E_ν and y and is shown in Fig. 12.22.

In some regions in the E - y plane (high energy and low inelasticity), the energy resolution is better when plotted for reconstructed quantities than for true quantities. This is mainly caused by the fact that for low y the mean reconstructed energy $\langle E_{\text{reco}} \rangle$ is slightly (up to $\sim 10\%$) larger than E_ν (see Fig. 12.22).

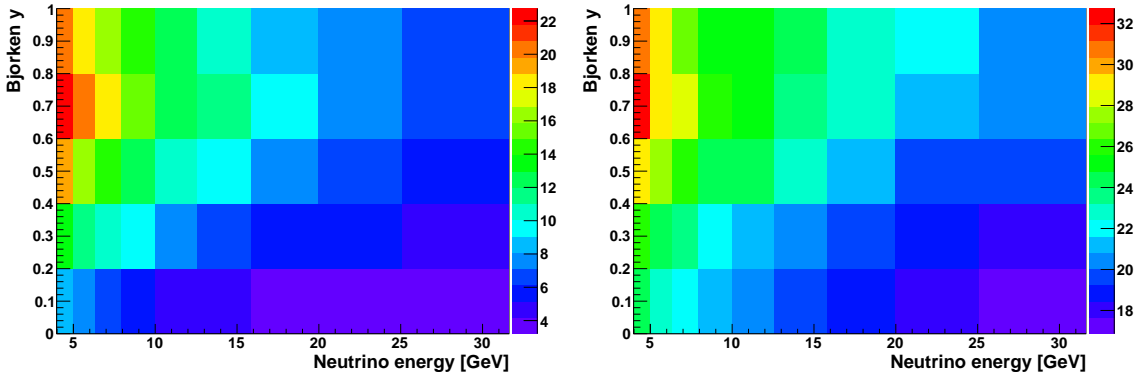


Figure 12.20: Median neutrino direction (left) and relative energy resolution RMS/E_ν (right) as a function of neutrino energy E_ν and true inelasticity y for upgoing $\bar{\nu}_e$ CC events. The color code represents the direction (relative energy) resolution in degree (percent).

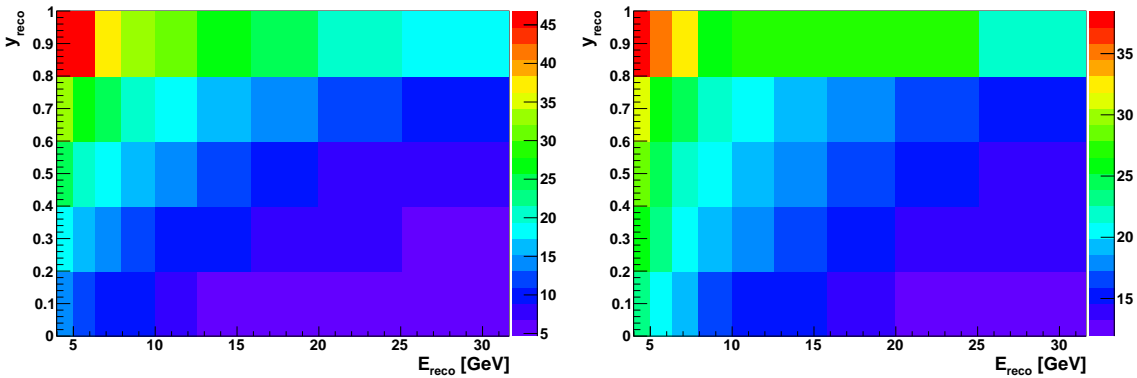


Figure 12.21: Same as Fig. 12.20, but as a function of reconstructed energy E_{reco} and inelasticity y_{reco} . Relative energy resolution is measured as $\text{RMS}/E_{\text{reco}}$.

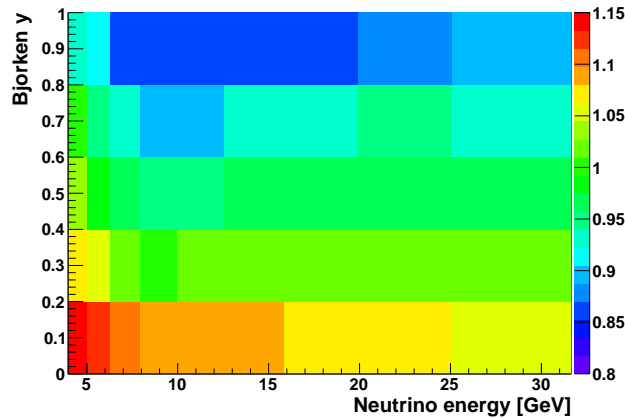


Figure 12.22: Ratio of mean reconstructed energy and neutrino energy $\langle E_{\text{reco}} \rangle / E_\nu$ as a function of neutrino energy and true inelasticity y for upgoing $\bar{\nu}_e$ CC events.

12.3.4 Performance for different vertical spacings between DOMs

The different detector configurations studied in this section are described in Sec. 6.4. The performance for different vertical spacings between DOMs is studied for upgoing $\bar{\nu}_e$ CC events weighted according to the Bartol flux model. For all detector configurations, events are selected according to the same criteria as described in Sec. 12.2. A dedicated energy correction is applied (see Eq. 12.7) for each detector configuration.

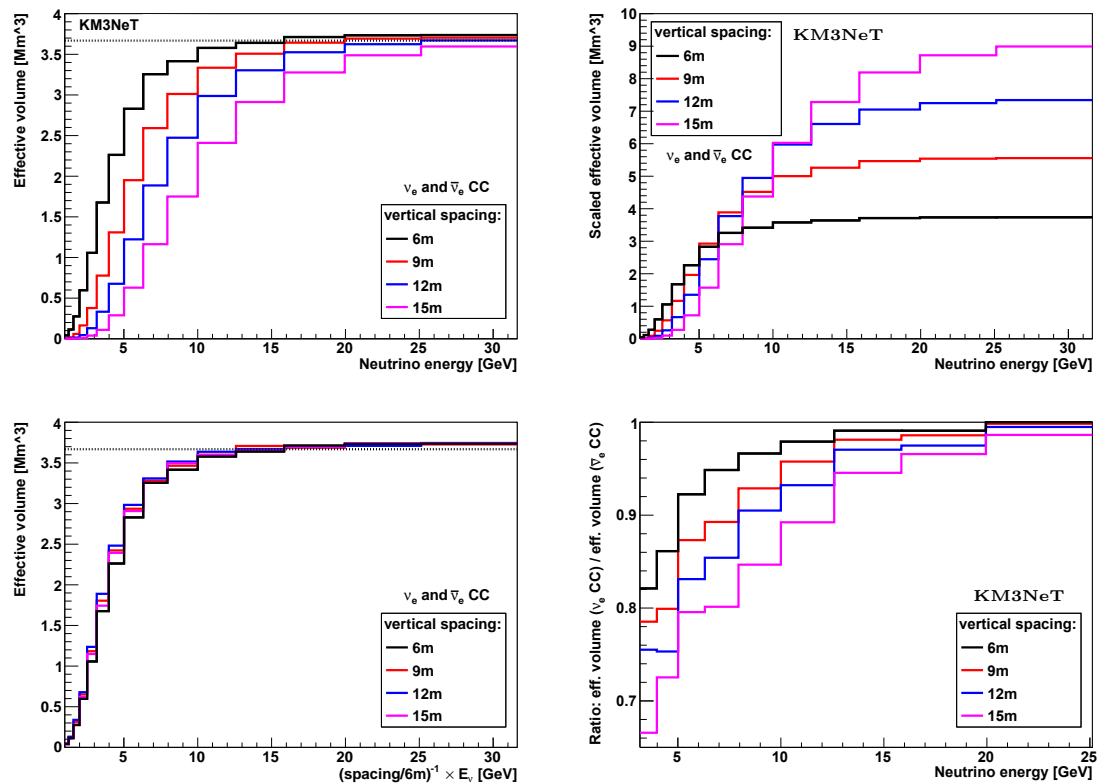


Figure 12.23: Effective volumes for different vertical spacings as a function of neutrino energy for upgoing $\bar{\nu}_e$ CC events (top left). Effective volumes with y-axis scaled by a factor 1/1.5/2/2.5 (top right) and x-axis shrunk by 1/1.5/2/2.5 (bottom left) for 6m/9m/12m/15m. Ratio of effective volumes for ν_e CC and $\bar{\nu}_e$ CC events (bottom right).

The effective volumes for the masked detector configurations with different vertical spacings are shown as a function of neutrino energy in Fig. 12.23 (top left). For all detector configurations, a similar plateau value is reached, but the turn-on is less steep for smaller DOM density (larger vertical spacing). Assuming the same number of DOMs for each vertical spacing, these effective volumes are scaled accordingly in Fig. 12.23 (top right). The turn-on of effective volumes for different detector configurations scales to first order⁷² with the neutrino energy, as can be seen from Fig. 12.23 (bottom left). The ratio of effective volumes for ν_e CC and $\bar{\nu}_e$ CC is shown in Fig. 12.23 (bottom right).

In Fig. 12.24, the resolutions for $\bar{\nu}_e$ CC events for the different vertical spacings between DOMs are summarised. The performance for other shower-like neutrino events for different vertical spacings is similar as described above.

The energy and direction resolution deteriorates only slightly for larger vertical spacings, as the energy resolution is dominated by intrinsic fluctuations in the number of emitted photons and the direction resolution is dominated by the neutrino interaction kinematics, as discussed in Sec. 12.5.2.

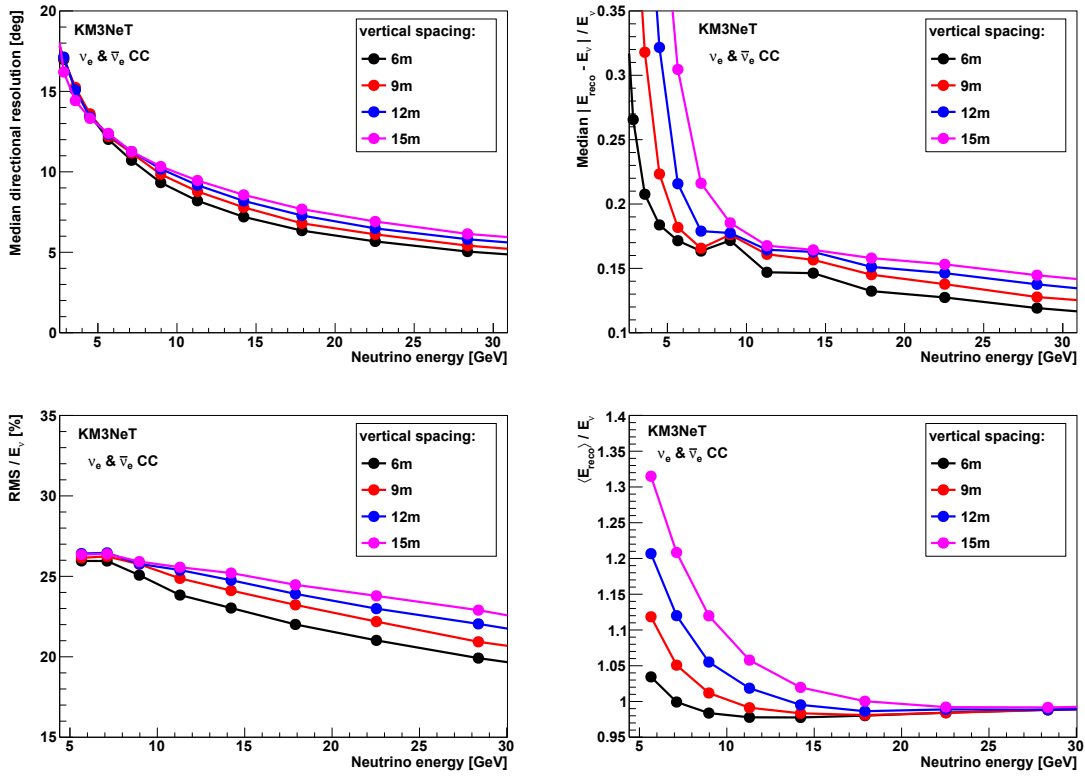


Figure 12.24: Resolution of the shower reconstruction for different vertical spacings for upgoing $\bar{\nu}_e$ CC events as a function of neutrino energy E_ν . Top left: median neutrino direction. Top right: median fractional energy resolution $|E_{\text{reco}} - E_\nu|/E_\nu$. Bottom left: relative energy resolution RMS/E_ν . Bottom right: mean relative offset in reconstructed energy $\langle E_{\text{reco}} \rangle / E_\nu$.

⁷² Here, two opposing effects nearly cancel, establishing this first order proportionality. Due to absorption, the number of photons reaching a photosensor decreases faster than linear with photocathode density, while the light yield of hadronic showers increases faster than linear with energy (see Fig. 7.10). This also explains the unclear tendency if sparser- or more-densely instrumented detectors show a steeper turn-on in Fig. 12.23 (bottom left).

12.3.5 Effect of variation in seawater/PMT properties and noise level

The reconstruction performances have been studied for variations in seawater properties, PMT quantum efficiencies (QE) and optical background noise. For this purpose, the absorption and scattering lengths λ_{abs} and λ_{scat} have been changed by $\pm 10\%$, while the QE has been changed by -10% . These parameters are discussed in Sec. 4.5 and Sec. 4.6, respectively. In order to test the influence of the optical background, the single noise rate is increased from an already conservative rate of 10 kHz to 20 kHz in the whole detector. Bioluminescence does not produce correlated noise apart from random coincidences and can be simulated by increasing single noise rates. This hypothesis is verified using ANTARES data in Sec. 10.6.

It is expected that the seawater properties (λ_{abs} and λ_{scat}) will be determined using the KM3NeT calibration system [187] with a smaller uncertainty than the variation assumed here. The QE of each individual PMT is expected to be measured using ^{40}K coincidences with a precision of $\sim 1\%$ [140].

Changing the seawater properties requires a re-simulation of photon propagation, i.e. KM3Sim (see Sec. 6.1), while reducing the QE was performed by removing 10% of the detected photons from the standard simulation. In all cases, the trigger conditions are unchanged compared to the nominal values⁷³ and events are selected according to the same criteria as for the nominal values. These studies have been performed for the benchmark detector with 6 m vertical spacing between the DOMs – similar effects are expected for larger spacings.

Effect of known parameter variations

In the following, it is assumed that the true seawater, PMT and noise properties are known so that they can be accounted for in the reconstruction. The adjustment for the energy, direction and inelasticity reconstruction (see Sec. 12.1.2) are the following: for a change in absorption length λ_{abs} , the effective attenuation length λ_{att} (Eq. 12.6) used to calculate the number of expected photons $\langle N_\gamma \rangle$ is scaled by the same amount as λ_{abs} ; for a change in scattering length λ_{scat} , nothing has to be adjusted; for a change in QE, the number of expected photons $\langle N_\gamma \rangle$ is scaled accordingly; for a change in single noise rates, the constant noise level in the probability density function $P(N_{\text{hits}}^{\text{DOM}})$ for the number of hit PMTs is adjusted by adding the Poissonian expectation from uncorrelated noise hits.

The energy and direction resolution is shown in Fig. 12.25 and Fig. 12.26 together with the performance for the nominal values. For all studied variations, the energy and direction resolutions are very similar, as the resolutions are not dominated by detector effects (see Sec. 12.5.2). For 20 kHz single noise rates, the resolutions are as good as for 10 kHz confirming the good signal-to-noise ratio due to small time windows in the hit selections (see Sec. 12.1.2) allowed by the large scattering length in seawater.

The effective volumes are shown in Fig. 12.27. For all studied variations, a similar plateau value is reached, but the turn-on is less steep for less detected photons, i.e. reduced λ_{abs} or QE. For 20 kHz single noise rates, the turn-on is also less steep compared to a 10 kHz noise rate.

The negligible deterioration in direction and energy resolution in conjunction with the relatively modest loss in effective volume for an increase in single noise rates by a factor of two⁷⁴ compared to the nominal assumed rate of 10 kHz demonstrates the robustness of the reconstruction against higher noise rates.

⁷³ For 20 kHz single noise rate, the trigger rate from pure noise would be too high, so that the trigger conditions would have to be tightened. However, the purpose of this study is to demonstrate the robustness of the reconstruction with respect to an increased noise rate.

⁷⁴ This is even a factor of 2.5 compared to the measured 8 kHz [139].

Note that PMTs or complete DOMs that are temporarily switched off (see Sec. 10) due to bioluminescence bursts change on average just the DOM density of the detector and this is equivalent to changing the vertical spacing between DOMs, which is studied in Sec. 12.3.4.

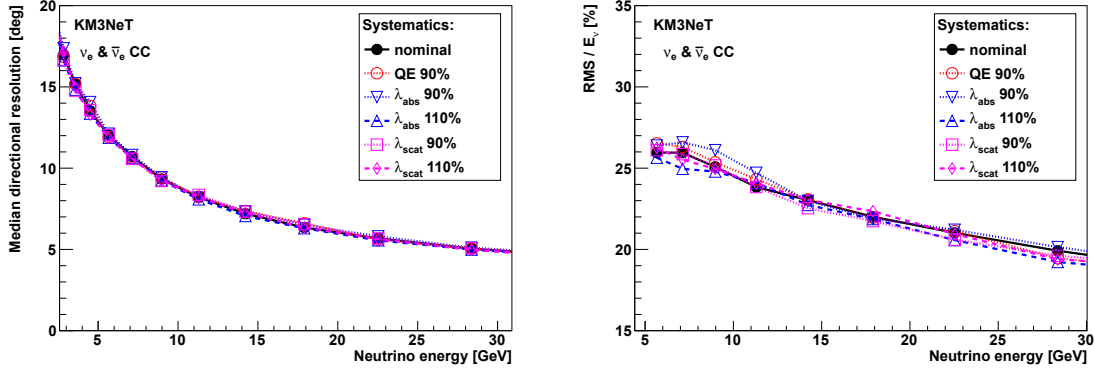


Figure 12.25: Resolution of the shower reconstruction for different optical properties (λ_{abs} and λ_{scat}) and quantum efficiencies (QE) for upgoing $\bar{\nu}_e$ CC events. Median neutrino direction (left) and relative energy resolution RMS/E_ν (right).

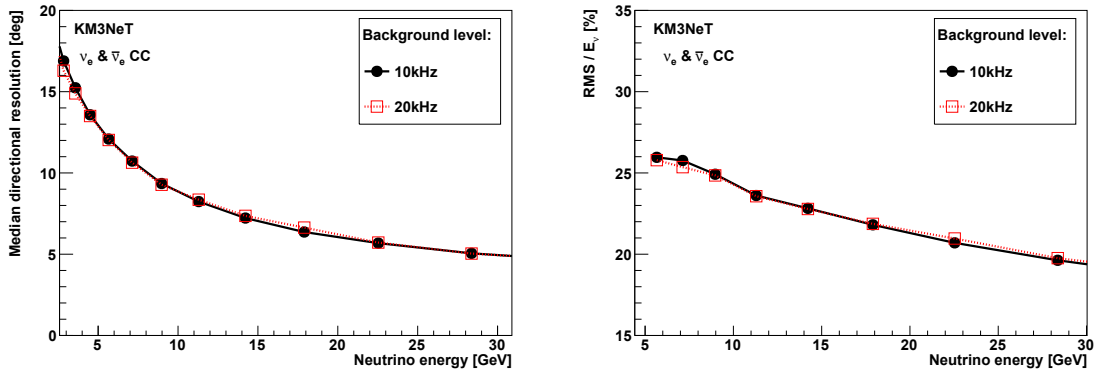


Figure 12.26: Shower reconstruction resolution for 10 kHz and 20 kHz single noise rates for upgoing $\bar{\nu}_e$ CC events. Median neutrino direction (left) and relative energy resolution RMS/E_ν (right).

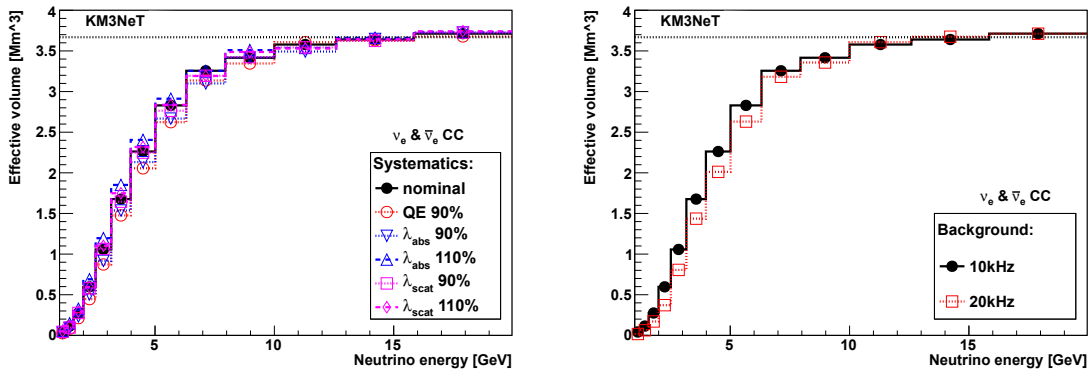


Figure 12.27: Effective volumes for upgoing $\bar{\nu}_e$ CC events. Different optical properties as well as quantum efficiencies (left), and noise rates (right).

Effect of undetected parameter variations

In the following, it is assumed that the variation relative to the nominal seawater and PMT properties are unknown so that they cannot be accounted for in the reconstruction. In addition, the effect of an undetected⁷⁵ increase in noise level is investigated.

While the direction resolution is unaffected, Fig. 12.28 depicts the ratio of mean and RMS of the reconstructed energy for the nominal and varied parameters. A $\pm 10\%$ variation in λ_{scat} has a negligible effect on the mean reconstructed energy, while the same variation in λ_{abs} induces a corresponding shift in reconstructed energy of $\pm 8\%$. As expected, a decrease in QE of 10% results in a corresponding downward shift in energy of 10%. For each varied parameter, the RMS of the reconstructed energy changes by similar amount as the mean reconstructed energy, i.e. the distributions of reconstructed energy are just scaled by a constant factor so that the relative RMS energy resolution is unaffected. Therefore, all of these uncertainties together can safely be described by a single ‘energy scale’ factor, as applied in the ‘Letter of Intent’ [3].

An undetected increase in single noise of 10 kHz per PMT in the entire detector leads to a constant shift in energy by about ~ 0.7 GeV.

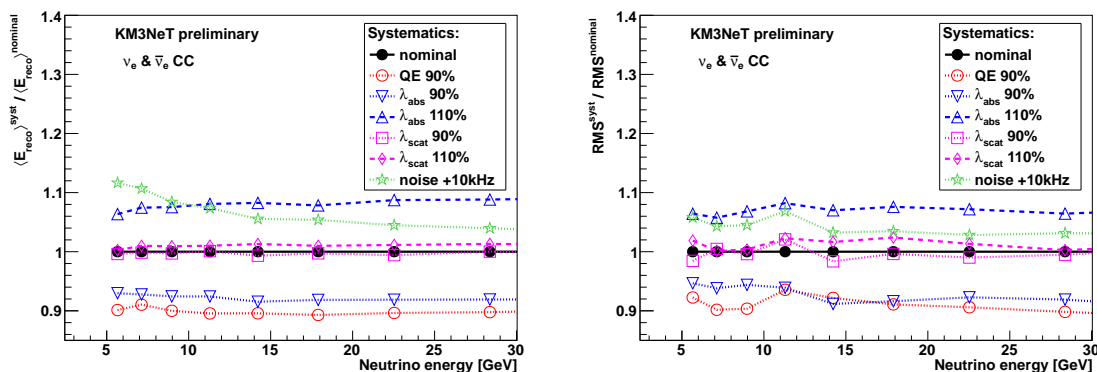


Figure 12.28: Ratio of mean (left) and RMS (right) of reconstructed energy for nominal and varied optical properties (λ_{abs} and λ_{scat}), quantum efficiencies (QE), and extra noise rates for upgoing $\bar{\nu}_e$ CC events. Parameter variations are assumed to be undetected.

12.3.6 Performance for track-like events

Although the shower reconstruction is not designed to reconstruct track-like event signatures (see Sec. 3.2.4), it is important to study the reconstruction performance on $\bar{\nu}_\mu$ CC and atmospheric muon events, in particular with a focus on the energy and direction regimes relevant for the NMH measurement. Nevertheless, it should be kept in mind that no dedicated algorithm to separate track-like and shower-like event signatures is applied here. In the ORCA sensitivity study performed in the ‘Letter of Intent’ [3], this event classification is applied after the shower and track reconstruction using the output of these reconstructions.

Muon neutrino charged-current events

Depending on the inelasticity y , a $\bar{\nu}_\mu$ CC event can look more or less track-like. For $y \rightarrow 1$, the outgoing muon does not result in a visible track sticking out of the accompanying hadronic shower and the event signature appears more shower-like. Therefore, all performances are shown separately for different y -ranges.

Fig. 12.29 shows the effective volume for $\bar{\nu}_\mu$ CC events. For $y > 0.8$, the shape of the effective volume resembles that of $\bar{\nu}_e$ CC events (cf. Fig. 12.6), but with a less steep turn-

⁷⁵ Hit rates on every PMT are permanently monitored, i.e. the actual noise level is in principle known.

on due to the lower average light yield of hadronic compared to electromagnetic showers (see Fig. 7.10). For $y \rightarrow 0$, the turn-on becomes steeper and the effect of the ‘anti bright muon cut’ (see Sec. 12.1.3) is clearly visible as a drop in effective volume for events with muon energies above $\gtrsim 5$ GeV.

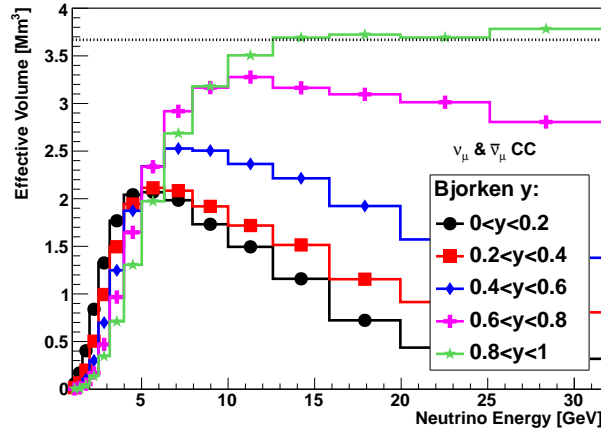


Figure 12.29: Effective volumes as a function of neutrino energy for upgoing $\bar{\nu}_\mu$ CC events in different ranges of inelasticity y .

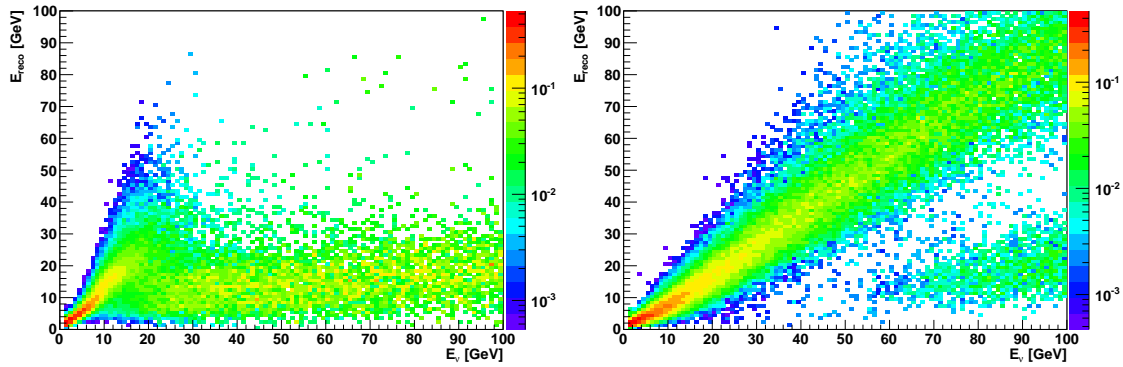


Figure 12.30: Reconstructed energy E_{Teco} as a function of neutrino energy E_ν for upgoing $\bar{\nu}_\mu$ CC events and inelasticity $y < 0.2$ (left) and $y > 0.8$ (right).

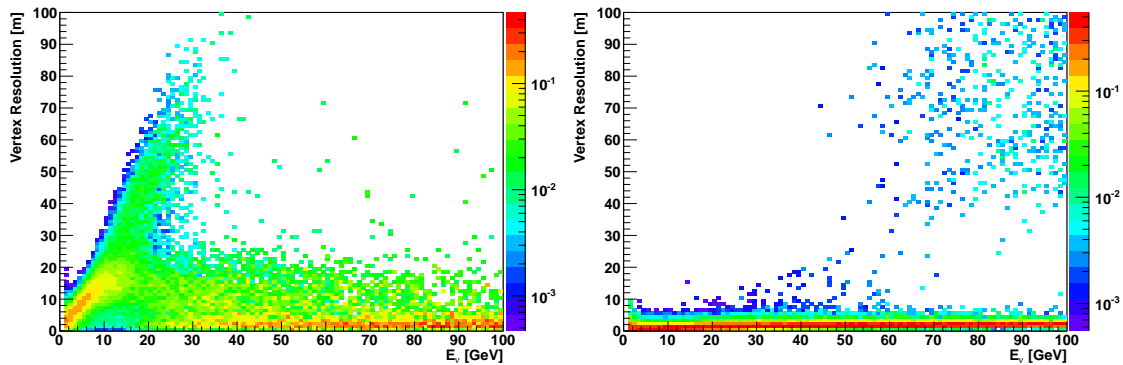


Figure 12.31: Resolution of neutrino interaction vertex as a function of neutrino energy E_ν for upgoing $\bar{\nu}_\mu$ CC events and inelasticity $y < 0.2$ (left) and $y > 0.8$ (right).

The reconstructed energy E_{reco} and the vertex resolution as a function of the neutrino energy E_ν are shown in Fig. 12.30 and Fig. 12.31, respectively. For $y > 0.8$ (right plots), E_{reco} scales roughly linear with E_ν and the reconstructed vertex is within a few metres of the neutrino interaction vertex. The few events with $E_\nu \gtrsim 60$ GeV and $E_{\text{reco}} \lesssim 30$ GeV are caused by neutrinos interacting far outside the detector and the muon is entering the detector, so that only the muon is visible and the reconstructed vertex position far away from the true neutrino interaction vertex ($\gtrsim 40$ m). As these events appear as track-like, they would likely be identified as not shower-like by dedicated event classification algorithms, as applied in the ‘Letter of Intent’ [3], and could therefore be removed from the final shower-like event sample used for the NMH determination. For $y < 0.2$ (left plots) and $E_\nu \lesssim 15$ GeV, E_{reco} is on average slightly overestimated and the reconstructed vertex is often roughly at the middle of the muon track (offset ~ 15 m for $E_\nu = 10$ GeV producing a muon with track length ~ 40 m). For $y < 0.2$ and $E_\nu \gtrsim 15$ GeV, all selected events have always $E_{\text{reco}} \lesssim 20$ GeV independent of E_ν and a vertex position close to interaction vertex. These are events where the interaction vertex is close to the surface of the instrumented volume and the muon is leaving the detector undetected. Only the first track segment and the hadronic shower are visible to the detector. These events could have been removed by tightening the event selection criteria (see Sec. 12.2), particularly the containment criteria, or by dedicated event classification algorithms, as applied in the ‘Letter of Intent’ [3]. All events where a sufficiently long muon track is visible are discarded by the ‘anti bright muon cut’.

The median direction resolution is shown in Fig. 12.32 for $\bar{\nu}_\mu$ CC events. For small energies ($E_\nu \lesssim 5$ GeV and $y < 0.2$ – slightly higher energies for larger y), the direction resolution is very similar to that of $\bar{\nu}_e$ CC events (cf. Fig. 12.20 left). The deterioration at higher energies (and not $y \rightarrow 1$) is again caused by the fact that only events with a muon leaving the detector mostly undetected are selected. As expected, for events with an insignificant muon track length ($y > 0.8$ for considered E_ν range), the direction resolution is very similar to that of $\bar{\nu}_e$ CC events with the same inelasticity (cf. Fig. 12.20 left).

It can be concluded that the shower reconstruction works as expected for $\bar{\nu}_\mu$ CC events that appear as nearly shower-like, i.e. large inelasticity y . These events will naturally also be classified as shower-like by any event signature classification algorithm.

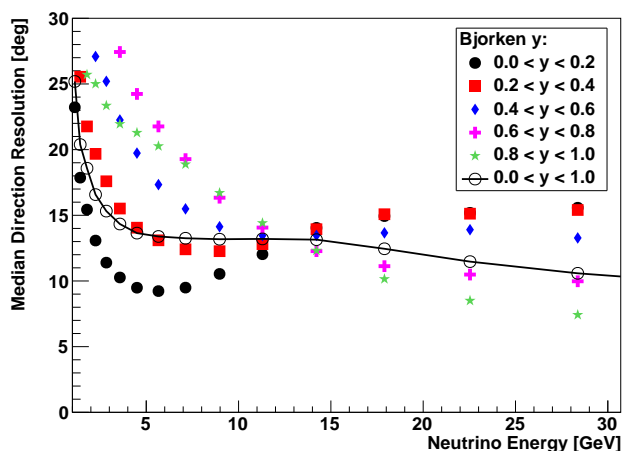


Figure 12.32: Median neutrino direction resolution as a function of neutrino energy for upgoing $\bar{\nu}_\mu$ CC events in different ranges of inelasticity y . The black line corresponds to all selected events.

Atmospheric muons

Fig. 12.33 shows the selected atmospheric muon events in the $E_{\text{reco}}-\theta_{\text{reco}}$ plane. As expected, most atmospheric muons are reconstructed as downgoing. The effect of the ‘anti bright muon cut’ (see Sec. 12.1.3) is clearly visible for $E_{\text{reco}} \gtrsim 20$ GeV. Within the simulated lifetime of about 15.5 days, only a few tens of atmospheric muon events end up in the relevant phase space region for the NMH sensitivity, namely $\cos(\theta_{\text{reco}}) < 0.5$ and $E_{\text{reco}} < 15$ GeV (see Sec. 3.2.3). This corresponds to about thousand events per year. Without any dedicated algorithms for (atmospheric) muon rejection, the event rate in this phase space region is dominated by neutrino-induced and not by atmospheric muon events (for comparison, trigger rates are $\sim 10^5$ times larger for atmospheric muons than for neutrinos).

In the ‘Letter of Intent’ [3], a few percent contamination of atmospheric muons is achieved by a further event classification that uses many of the output parameters of the shower reconstruction algorithm presented here.

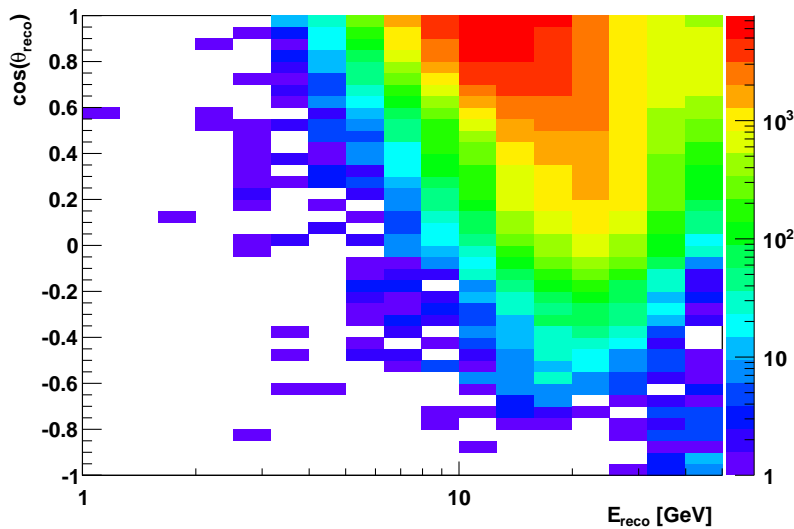


Figure 12.33: Atmospheric muon events reconstructed with the shower reconstruction and passing the event selection criteria as a function of reconstructed energy E_{reco} and cosine of the zenith angle $\cos(\theta_{\text{reco}})$ for a simulated lifetime of about 15.5 days.

12.3.7 Suppression of pure-noise events

Pure-noise events could in principle fake signal events, because the events relevant for the NMH measurement are close to the energy threshold of trigger and reconstruction. This has been studied by generating pure-noise events. A difficulty is that 10 kHz/PMT single rates result in about 4 GB of simulated noise data per simulated second of noise. Therefore, only a small lifetime of pure noise is generated.

Two different samples of pure-noise events are studied: (i) triggered with the normal trigger conditions (see Eq. 11.4) and reconstructed with the nominal reconstruction procedure described in Sec. 12.1, and (ii) triggered with a looser trigger configuration and reconstructed without the re-triggering criterion (see Sec. 12.1.3) in order to enhance statistics. The simulated lifetime is about ~ 130 seconds for both samples.

About a fraction of $\sim 1/40$ of the ~ 2500 pure-noise events in the first sample pass the re-triggering criterion. The number $N_{\text{vtx}}^{1,\text{Fit}}$ of reconstructed vertices in the first vertex fit that are similar to the selected vertex (see Sec. 12.2) is the most effective parameter

for rejecting pure-noise events. As noise on different DOMs is not correlated (a single ^{40}K decay is not bright enough and all other optical noise sources do not emit correlated light), different seeds (PMT positions and hit times) in the vertex fit will most probably result in sufficiently different vertex fit results.

Fig. 12.34 shows the distributions of $N_{\text{vtx}}^{1.\text{Fit}}$ for pure-noise events. For comparison, the direction error versus $N_{\text{vtx}}^{1.\text{Fit}}$ for upgoing $\bar{\nu}_e$ CC events with $6\text{ GeV} < E_\nu < 8\text{ GeV}$ is shown in Fig. 12.35. While most vertex fits convert to similar vertices in $\bar{\nu}_e$ CC events, pure-noise events show a steeply falling $N_{\text{vtx}}^{1.\text{Fit}}$ distribution resembling an exponential decay. The exponential decay constant is larger for the first noise sample (black in Fig. 12.34) than for the second noise sample (purple), indicating that re-triggering and $N_{\text{vtx}}^{1.\text{Fit}}$ are slightly correlated. Extrapolating the black histogram to the chosen event selection criterion of $N_{\text{vtx}}^{1.\text{Fit}} = 7$ ($\sim 1/500$), combining with the re-triggering reduction factor ($\sim 1/40$) and including the reduction due to the other event selection criteria ($\sim 1/4$) would yield about

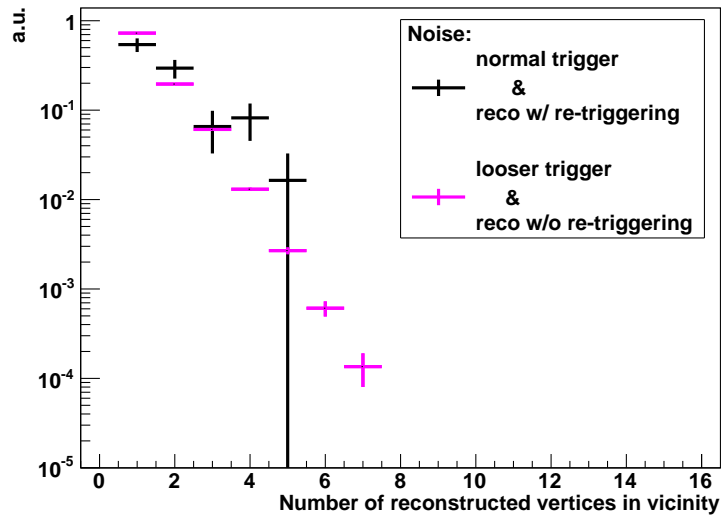


Figure 12.34: Distributions of $N_{\text{vtx}}^{1.\text{Fit}}$ for pure-noise events triggered and reconstructed with the nominal procedure described in Sec. 12.1 (black), and triggered with a looser trigger configuration and reconstructed without the re-triggering criterion (purple). No further event selection criteria are applied. Distributions are normalised to unity.

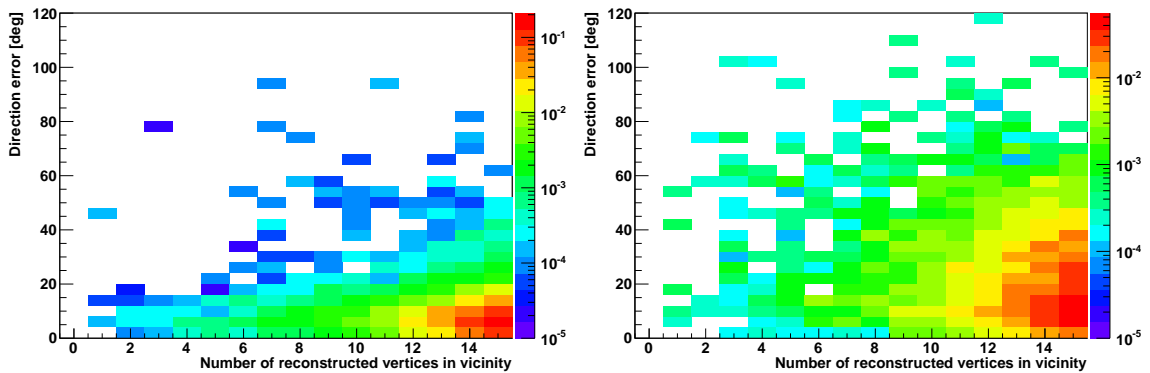


Figure 12.35: Direction reconstruction error versus $N_{\text{vtx}}^{1.\text{Fit}}$ for upgoing $\bar{\nu}_e$ CC events with $6\text{ GeV} < E_\nu < 8\text{ GeV}$ and either $y < 0.2$ (left) or $y > 0.8$ (right). Events are selected according to the criteria outlined in Sec. 12.2 apart from the $N_{\text{vtx}}^{1.\text{Fit}}$ criterion.

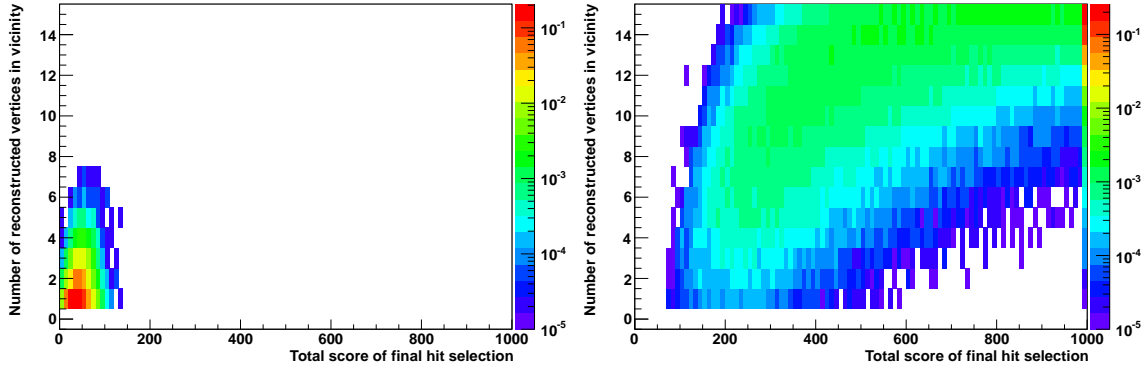


Figure 12.36: $N_{\text{vtx}}^{1,\text{Fit}}$ versus total hit score for pure-noise events (left) and upgoing $\bar{\nu}_e$ CC events (right). Pure-noise events are triggered with the looser trigger configuration as well as reconstructed without the re-triggering criterion, and no further event selection criteria are applied. The $\bar{\nu}_e$ CC events are triggered and reconstructed with the nominal procedure, and events are selected as described in Sec. 12.2 apart from the $N_{\text{vtx}}^{1,\text{Fit}}$ criterion.

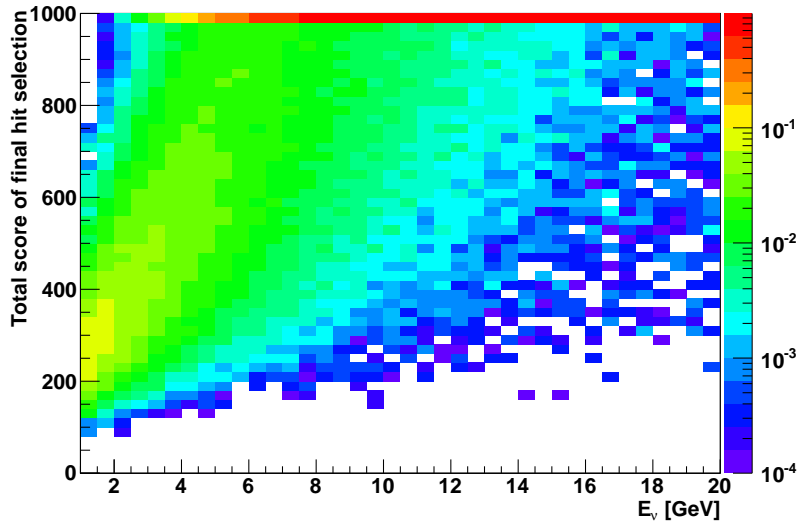


Figure 12.37: Total hit score for upgoing $\bar{\nu}_e$ CC events as a function of E_ν . Events are triggered and reconstructed with the nominal procedure. All selection criteria outlined in Sec. 12.2 are applied.

~ 20 pure-noise events per day. Of course, this contamination ($\sim 1:1$) is too high for the precision needed for a measurement such as the NMH determination. However, only vertex fit quality parameters are utilised so far and many other quality parameters provide further noise suppression power.

A very promising quality parameter that characterises the spatial distribution of the hits is the sum of scores of all hits (see Appendix C for hit scoring procedure) in the final hit selection for the energy, direction and inelasticity fit (see Sec. 12.1.2). Fig. 12.36 shows $N_{\text{vtx}}^{1,\text{Fit}}$ against this total hit score for pure-noise events and upgoing $\bar{\nu}_e$ CC events. Although both parameters seem to be loosely correlated for pure-noise events, the total hit score can be used to reduce significantly the contamination of pure-noise events. Fig. 12.37 shows the total hit score as a function of neutrino energy for upgoing $\bar{\nu}_e$ CC events. The total hit score increases rapidly with light yield and consequently with energy. For example, an additional requirement with at least a total hit score larger ≥ 200 would reject $\lesssim 1\%$

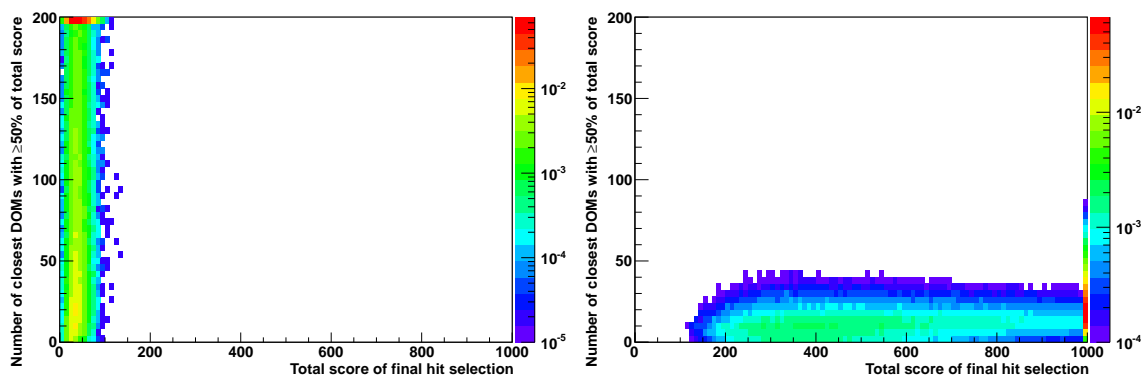


Figure 12.38: Total hit score versus minimum number of closest DOMs around the reconstructed vertex that contain together at least 50% of the total hit score for pure-noise events (left) and upgoing $\bar{\nu}_e$ CC events (right). Pure-noise events are triggered with the looser trigger configuration and reconstructed without the re-triggering criterion, and no further event selection criterion is applied. The $\bar{\nu}_e$ CC events are triggered, reconstructed and selected following the nominal procedure.

of the upgoing $\bar{\nu}_e$ CC events with $E_\nu \approx 4$ GeV (compared to the nominal event selection in Sec. 12.2).

In a similar fashion, many other quality parameters based on time residuals and spatial hit distributions with respect to the reconstructed event hypothesis can be devised, allowing a further noise suppression. One final example of such a parameter is the minimum number of closest DOMs around the reconstructed vertex position that contain together at least 50% of the total hit score. This parameter is shown in Fig. 12.38 versus the total hit score. While hits with a high score are located close to the vertex in neutrino-induced events, this is not the case for pure-noise events, where the reconstructed vertex position is uncorrelated from the spatial hit distribution, as only time residuals are used in the vertex reconstruction.

From these studies, it can be expected that a pure event sample of only neutrino-induced events can be achieved without any significant reduction in effective volume compared to that presented above.

12.4 Advantages due to reconstructing interaction inelasticity

Reconstructing the interaction inelasticity y (Eq. 2.6) has two advantages, as it allows: (i) a statistical separation between ν_e CC, $\bar{\nu}_e$ CC, $\bar{\nu}$ NC and $\bar{\nu}_\tau$ CC events, and (ii) to account for the different light yields of hadronic and electromagnetic showers (see Fig. 7.10), which otherwise intrinsically deteriorates the energy resolution. Both advantages are quantitatively studied in the following for the ORCA benchmark detector.

12.4.1 Separation between different shower-like neutrino event classes

Distributions of reconstructed inelasticity y_{reco} for $\bar{\nu}_e$ CC and $\bar{\nu}$ NC are shown in Fig. 12.13 and Fig. 12.19, respectively. The degree to which they differ from each other can be quantified by separation power introduced in Eq. 9.7. The statistical separation power between ν_e CC \leftrightarrow $\bar{\nu}_e$ CC, ν_e CC \leftrightarrow $\bar{\nu}$ NC, and $\bar{\nu}_e$ CC \leftrightarrow $\bar{\nu}$ NC is shown in Fig. 12.39 for the two cases of using the reconstructed inelasticity y_{reco} as well as the inelasticity y_{lead} from the most energetic particle producing the brightest Cherenkov cone in the event (see Eq. 7.9). Fig. 12.40 shows the separation power between ν_τ CC \leftrightarrow ν_e CC and ν_τ CC \leftrightarrow $\bar{\nu}$ NC. The statistical identification of $\bar{\nu}_\tau$ CC events is particularly interesting for measuring $\bar{\nu}_\tau$ appearance, another scientific goal of ORCA (see Sec. 5.6).

For separation of ν_e CC \leftrightarrow $\bar{\nu}_e$ CC events (ν_e CC \leftrightarrow $\bar{\nu}$ NC / $\bar{\nu}_e$ CC \leftrightarrow $\bar{\nu}$ NC / ν_τ CC \leftrightarrow ν_e CC / ν_τ CC \leftrightarrow $\bar{\nu}$ NC) using y_{reco} , values around 0.04 (0.17/0.33/0.10/0.01) are achieved for $E_{\text{reco}} = 10$ GeV. The theoretically achievable separation power using y_{lead} gives values around 0.10 (0.22/0.58/0.18/0.03) for $E_{\text{vis}} = 10$ GeV, respectively.

It should be mentioned that apart from the difference in y_{reco} distributions the mean reconstructed energy is different for ν_e CC, $\bar{\nu}_e$ CC, $\bar{\nu}_\tau$ CC and $\bar{\nu}$ NC events giving additional separation power in conjunction with the steeply falling neutrino flux.

The gain in NMH sensitivity due to reconstructing the inelasticity is studied in Sec. 13.2.2.

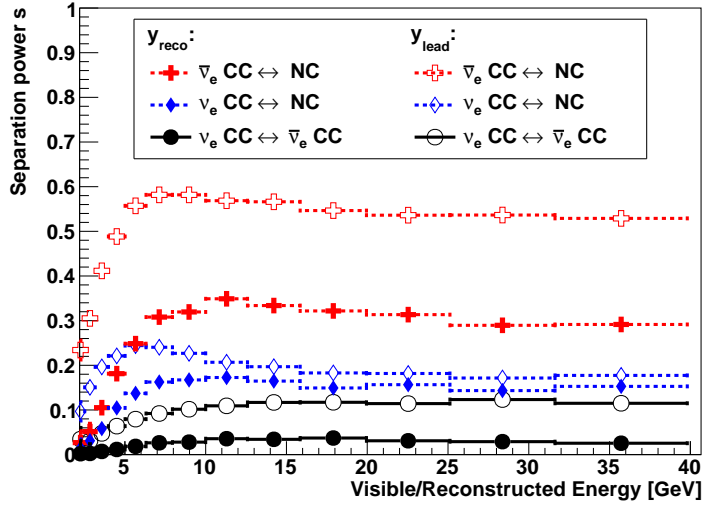


Figure 12.39: Statistical separation power s (see Eq. 9.7) between ν_e CC \leftrightarrow $\bar{\nu}_e$ CC (black circles), ν_e CC \leftrightarrow $\bar{\nu}$ NC (blue diamonds), and $\bar{\nu}_e$ CC \leftrightarrow $\bar{\nu}$ NC (red crosses) as a function of energy when using the reconstructed inelasticity y_{reco} (filled marker) and y_{lead} from the leading particle (hollow marker). For both cases, only selected events (see Sec. 12.2) are considered.

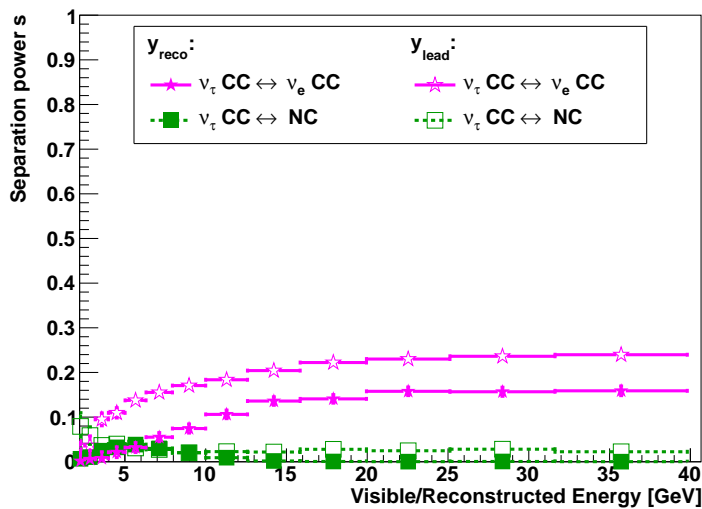


Figure 12.40: Statistical separation power s (see Eq. 9.7) between ν_τ CC \leftrightarrow ν_e CC (purple stars) and ν_τ CC \leftrightarrow $\bar{\nu}$ NC (green squares) as a function of energy when using the reconstructed inelasticity y_{reco} (filled marker) and y_{lead} from the leading particle (hollow marker). For both cases, only selected events (see Sec. 12.2) are considered.

12.4.2 Improvement of energy resolution

In order to quantify the improvement due to fitting the inelasticity y in addition to the shower energy and direction, the energy resolution is compared between two cases: allowing the reconstruction to fit y and assuming a fixed y . As the reconstruction algorithm anyway performs the likelihood maximisation with different fixed y assumptions (see Sec. 12.1.2), this comparison can easily be extracted from the individual fit results. The only step that is missing compared to the normal reconstruction procedure is the selection of the fit result with the best likelihood. For the case of not selecting the best likelihood, a similar energy correction as described in Eq. 12.7 and Appendix D.1 is applied.

Fig. 12.41 shows the comparison of the relative energy resolution for upgoing $\bar{\nu}_e$ CC events that are very well contained in the detector. Here, events are selected based on MC truth information such that the vertex position shifted by 30 m in the neutrino direction is within a cylinder with radius $R = 60$ m and height $|z| < 25$ m around the detector centre. Some example $(E_{\text{reco}} - E_\nu)$ distributions are shown in Fig. D.3 (Appendix). The relative improvement due to including the inelasticity y in the shower reconstruction is about $\sim 8\%$ for $E_\nu = 10$ GeV and increases with energy, while it is negligible for $E_\nu \lesssim 5$ GeV.

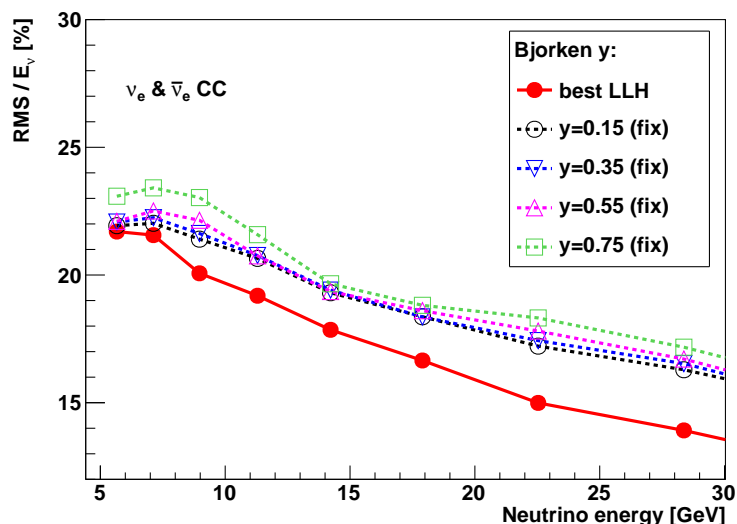


Figure 12.41: Relative energy resolution RMS/E_ν as a function of neutrino energy for upgoing MC truth contained $\bar{\nu}_e$ CC events. Resolutions for the normal reconstruction procedure (red) and four different fixed inelasticity y assumptions (other colours) are shown separately.

12.5 Comparisons of reconstruction performance

The effective volume of the shower reconstruction is compared with that at trigger level in Sec. 12.5.1 and the achieved resolutions are compared with the intrinsic limitations on neutrino energy, direction and inelasticity resolutions in Sec. 12.5.2. In Sec. 12.5.3, the achieved reconstruction performance is compared with that of the PINGU experiment [77], the main competitor of the ORCA experiment with a very similar detector concept and scientific goals.

For all comparisons, the ORCA benchmark detector with 6 m vertical spacing between the DOMs is assumed and events are weighted according to the Bartol atmospheric neutrino flux model [84].

12.5.1 Comparison of effective volume with respect to trigger level

The effective volume of $\bar{\nu}_e$ CC events after trigger and after the shower reconstruction with nominal event selection are compared in Fig. 12.42. Many triggered events do not pass the event selection of the shower reconstructing. However, most of the not selected events are not fully contained in the detector. These events are discarded on purpose due to the coverage cut in the event selection (see Sec. 12.2). Fig. 12.42 shows in addition the effective volumes for an event selection with a strict containment criterion on MC truth information (same as in Sec. 12.4.2). For those very well contained events, nearly all triggered events are reconstructed.

This emphasises again that triggering is a key ingredient for the NMH determination with the ORCA detector. Suggestions for improvements of the existing trigger procedure are given in Sec. 11.4.

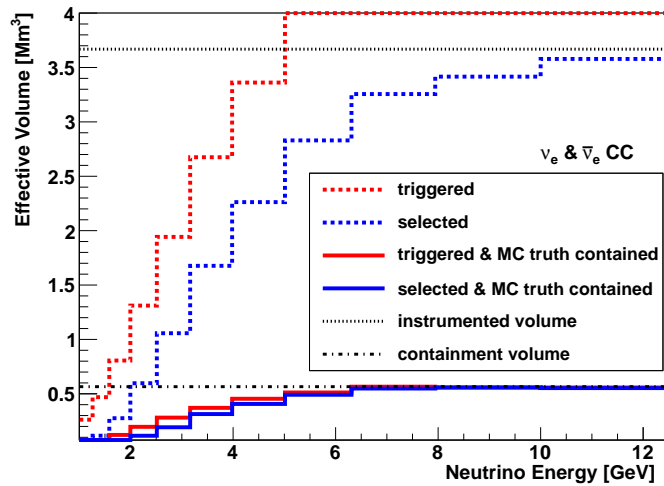


Figure 12.42: Effective volumes after trigger (red) and after shower reconstruction with corresponding event selection (blue) for two different input event samples: all events (dashed) and MC truth contained events as defined in the text (solid). Instrumented volume and containment volume are also indicated (black).

12.5.2 Comparison of resolutions with intrinsic limitations

Energy resolution comparison

A comparison of the achieved energy resolution and the intrinsic limitations derived in Sec. 9.5 is shown in Fig. 12.43 for $\bar{\nu}_e$ CC events. In order to eliminate the influence of poorly contained events, which are excluded in the intrinsic limits, the shower reconstruction resolution for an event selection with a strict containment criterion on MC truth information (same as in Sec. 12.4.2) is additionally shown. The resolution for these fully contained events is significantly better ($\Delta E/E = 20.1\%$ compared to 23.9% at $E_\nu = 10$ GeV) than the nominal energy resolution and is comparable to the limiting accuracy in the ‘ e^\pm unresolved’ case ($\Delta E/E = 19.3\%$) and above the ‘ e^\pm resolved’ case ($\Delta E/E = 16.8\%$). This is not unexpected, since the reconstruction is unable to perfectly differentiate between photons from the electron and hadronic shower. Remarkably, the relative improvement in energy resolution due to including the inelasticity y in the shower reconstruction in Fig. 12.41 is qualitatively similar (quantitatively about half as much: $\sim 8\%$ vs $\sim 14\%$ for $E_\nu = 10$ GeV) to the theoretical expectation from the intrinsic limits, namely the relative difference between the ‘ e^\pm unresolved’ and ‘ e^\pm resolved’ case.

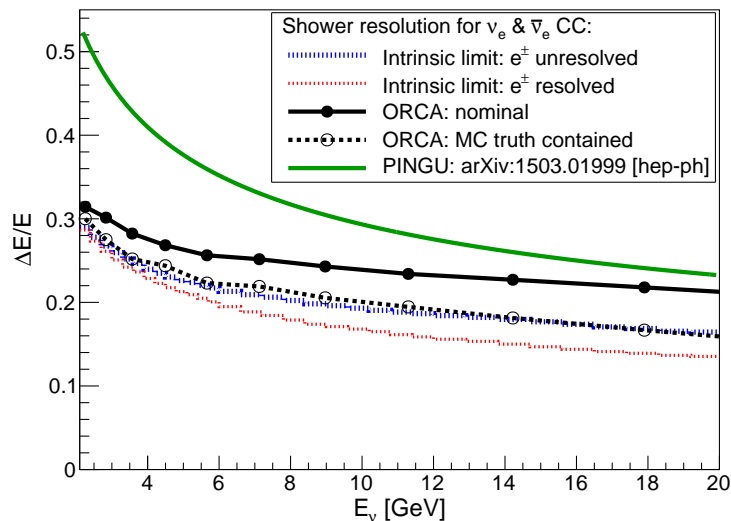


Figure 12.43: Relative energy resolution RMS/E_ν as a function of neutrino energy E_ν for upgoing $\bar{\nu}_e$ CC events. Resolutions achieved by the shower reconstruction for nominal event selection (black solid) and for a strict containment criterion on MC truth information (black dashed) are compared with the intrinsic limits in the ‘ e^\pm unresolved’ (blue dotted) and ‘ e^\pm resolved’ case (red dotted) for assuming a 2.5 : 1 mixture of ν_e and $\bar{\nu}_e$ CC events. The two intrinsic limit cases differ in the assumption about the ability to differentiate between photons from the electron and hadronic shower and are discussed in Sec. 9.5.2 and Sec. 9.5.4, respectively. A Gaussian approximation [188] of the PINGU energy resolution is also shown (green): $\sigma_E/E = 0.369/(E^{0.246} - 0.508)$.

This comparison reveals that the energy resolution achieved by the shower reconstruction is dominated by intrinsic fluctuations in the number of emitted photons (see Sec. 9.6). In particular, detector-geometry-related properties, such as detection element design (clumpiness, see Sec. 9.1.1) and calibration uncertainties, have only a small impact, justifying the assumptions made for deriving the intrinsic reconstruction accuracy limits in Sec. 9. In addition, this also explains the only minor deterioration for larger vertical spacings between DOMs in Fig. 12.24.

The influence of events which are not fully contained indicates that a significantly larger detector with a better surface-to-volume will be able to achieve better energy resolutions than the assumed detector with 115 detection strings (see Sec. 5.2). Hence, the expected statistical NMH sensitivity will scale faster than $\sqrt{V_{\text{eff}}}$ with the effective volume V_{eff} due to a better performance of a larger detector.

Direction resolution comparison

Fig. 12.44 compares the achieved neutrino direction resolution for $\bar{\nu}_e$ CC events and the intrinsic limitations for the two scenarios that the hadronic shower is reconstructed as a whole (with and without the ability to differentiate between photons from the electron and hadronic shower – ‘ e^\pm resolved’ and ‘ e^\pm unresolved’, respectively) and the direction of the leading particle in the entire neutrino-induced event is identified (see Sec. 7.3.2). The achieved direction resolution is comparable to the limiting accuracy in the ‘ e^\pm unresolved’ case and slightly above the ‘ e^\pm resolved’ case as well as the ‘leading particle’ limitation. This is not unexpected, as the shower reconstruction is designed to identify the brightest Cherenkov cone, which is mostly the outgoing electron. This capability of the shower reconstruction becomes obvious from Fig. 12.11 and Fig. 12.12. Indeed, the achieved

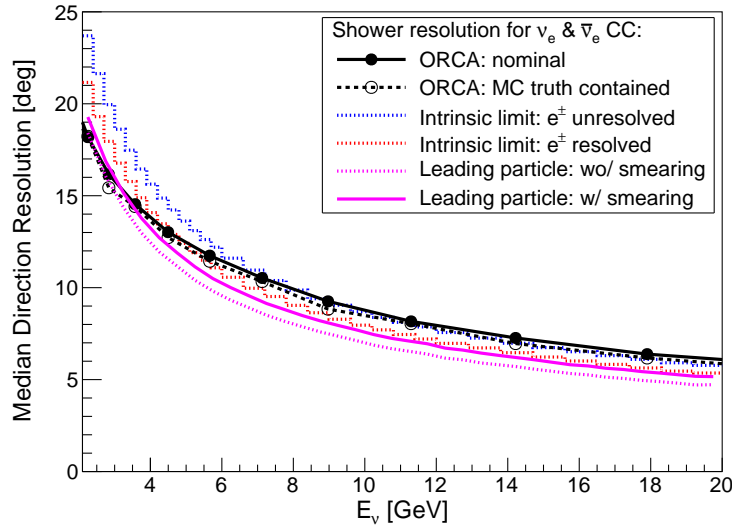


Figure 12.44: Median neutrino direction resolution as a function of neutrino energy E_ν for upgoing $\bar{\nu}_e$ CC events. The black, blue and red lines are for the same scenarios as discussed in Fig. 12.43 and the purple lines are for the ‘leading particle’ case (see Sec. 7.3.2) with true (dotted) and with smeared (solid) particle direction. For smearing in the later case, the intrinsic ‘1D’ limit for electrons (see Sec. 9.3.2) is applied for all particle species.

electron direction resolution in Fig. 12.12 for $\bar{\nu}_e$ CC events with $y \lesssim 0.5$ is close⁷⁶ to the intrinsic ‘1D’ limit for electrons and significantly better than the ‘2D’ limit in Fig. 9.8.

The ‘event selection effect’ discussed in Sec. 9.1.4 is clearly visible for low energies and leads to achieved resolutions better than the limits due to preferentially selecting (and triggering, see Fig. 11.3) low-inelasticity events with intrinsically better properties.

Inelasticity resolution comparison

The distributions of the reconstructed inelasticity y_{reco} from the shower reconstruction (see Fig. 12.13 right) and from the intrinsic energy resolution limits on electrons and hadronic showers (see Fig. 9.25) differ mainly at large y . This difference is caused by the fact that the intrinsic limits assume that photons from the outgoing electron can unambiguously be identified, however, the reconstruction cannot distinguish the light signature (single Cherenkov cone) produced by a single electron and a single hadron, as discussed in Sec. 7.3.1. Only the relative light intensity (\sim particle energy) of the brightest Cherenkov cone to the entire event allows a statistical electron identification.

As the difference between ν and $\bar{\nu}$ is largest at $y \rightarrow 1$, the separation power for separating ν_e CC \leftrightarrow $\bar{\nu}_e$ CC events using the intrinsic energy resolutions in Fig. 9.26 is significantly better than that achieved using the reconstructed inelasticity y_{reco} or the inelasticity y_{lead} from the leading particle (see Eq. 7.9) in Fig. 12.39.

Note that in Fig. 12.39 only selected events are used, while in Fig. 9.26 all events are used. This explains the significantly steeper increase of separation power in Fig. 9.26.

⁷⁶ Different direction error representation methods are used in Fig. 12.12 (median) and Fig. 9.8 (68.27% quantile). For a two-dimensional Gaussian, the difference between both is a scale factor of ~ 1.3 .

12.5.3 Comparison with PINGU

The achieved performance of the shower reconstruction for ORCA presented here can be compared to the shower reconstruction performance of the PINGU experiment [77]. Such a comparison was already performed in [63], which uses the ORCA shower resolutions presented in [181]. These resolutions are based on a preliminary version of the shower reconstruction presented in Sec. 12.1, however, are very similar to the resolutions presented in Sec. 12.3.

The relevant differences between the ORCA and PINGU detector are the detection medium (seawater vs. deep glacial ice) with its different optical properties (see Sec. 8.1) and a different DOM design (multiple small PMTs vs. single large PMTs).

Effective volume comparison

Fig. 12.45 compares the effective volume for $\bar{\nu}_e$ CC events. Besides a slightly larger plateau value and a slightly larger threshold energy for ORCA, the effective volumes are very similar for both experiments. This is not unexpected, since both detectors have a similar instrumented volume (\sim plateau value) with a similar photocathode area density (\sim energy range of turn-on) and the number of emitted Cherenkov photons is nearly identical in both detector media. The slightly faster turn-on for PINGU might be a consequence of the absence of ^{40}K in ice as well as the larger absorption length (i.e. more detected photons) in ice compared to seawater.

Energy resolution comparison

Fig. 12.46 (left) compares the median fractional energy resolutions. The ORCA shower resolution for $\bar{\nu}_e$ CC events is significantly better than that of PINGU with 15% compared to 21% at $E_\nu = 10$ GeV. Although the PINGU collaboration has not published a Gaussian approximation of their energy resolution, a parameterisation that captures the main features described in [77] is given in [188]. This parameterisation is compared to the achieved energy resolution for ORCA in Fig. 12.43. The relative difference between the resolutions for ORCA and PINGU is similar to that in Fig. 12.46 (left).

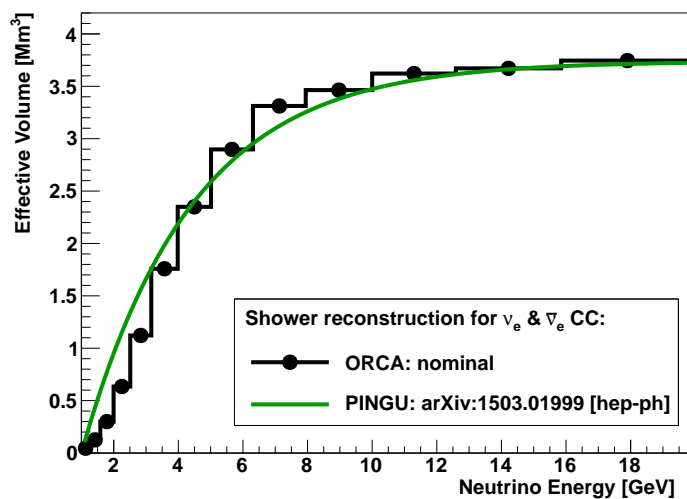


Figure 12.45: Effective volume for upgoing $\bar{\nu}_e$ CC events of the ORCA shower reconstruction (blue) and PINGU (green). For PINGU, the parameterisation given in [188] is shown: $V_{\text{eff}}(E_\nu) = 3.44/\rho_{\text{ice}}[1 - \exp(-0.294(E_\nu - 1 \text{ GeV}))]$.

Interestingly, the PINGU energy resolution is significantly worse than that of ORCA and the intrinsic limits (which are nearly identical for both experiments, as discussed in Sec. 9.6), indicating that the PINGU energy resolution is significantly deteriorated either by events that are insufficiently contained inside the instrumented volume or by the worse vertex resolution (due to more light scattering leading to broader time residual distributions, see Sec. 8.2) in conjunction with the photon-absorption dependency in the energy reconstruction. The former would require a larger detector, and the latter might be improved by using multi-PMT DOMs (cf. Fig. 8.9) or by a denser instrumentation increasing the number of detected unscattered photons. All of these options require either technological development or more detection strings and DOMs, which both delays the detector deployment and hence the NMH measurement.

Zenith angle resolution comparison

As the PINGU collaboration has only published median neutrino zenith angle resolutions (instead of median space angle resolutions), only these can be compared and are shown in Fig. 12.46 (right). The resolutions for $\vec{\nu}_e$ CC events achieved by the ORCA shower reconstruction are much better than that of PINGU, indicating that PINGU is not capable of identifying the direction of the particle producing the brightest Cherenkov cone, otherwise the direction resolution would be similar to that of ORCA. This difference is caused by larger scattering in ice than in seawater, as discussed in Sec. 8.

Inelasticity resolution comparison

The PINGU collaboration has not published any resolution of the inelasticity for $\vec{\nu}_e$ CC events, so that a comparison is not possible. As the identification of individual Cherenkov cones from energetic particles in few-GeV $\vec{\nu}_e$ CC events is an essential capability for reconstructing the interaction inelasticity, the inelasticity reconstruction is much more challenging in ice than in seawater due to the optical properties of both media, as discussed in Sec. 8.

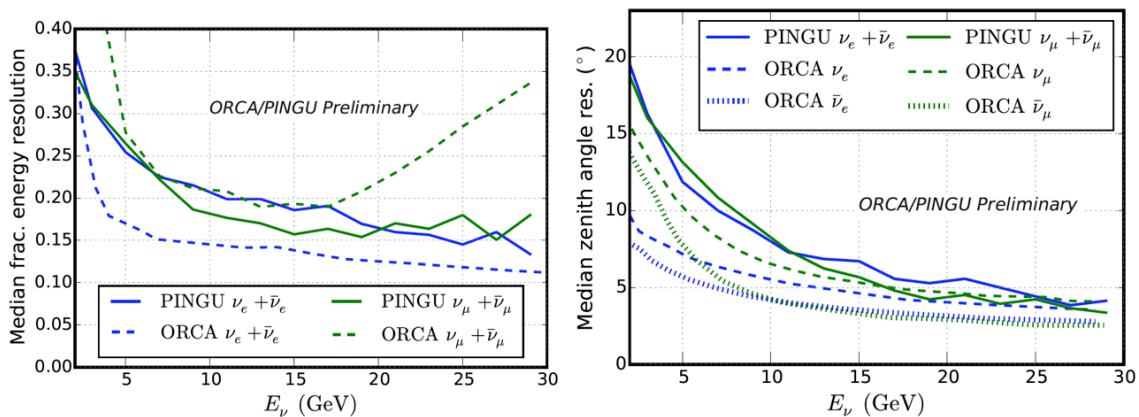


Figure 12.46: Median fractional energy $|E_{\text{reco}} - E_\nu|/E_\nu$ resolution (left) and median neutrino zenith angle resolution (right) for upgoing $\vec{\nu}_e$ CC events achieved by PINGU (blue solid) and ORCA (blue dashed for ν_e CC and blue dotted for $\bar{\nu}_e$ CC). Taken from [63], which is based on the resolutions from a preliminary version [181] of the ORCA shower reconstruction presented in this section. In addition, resolutions for $\vec{\nu}_\mu$ CC events are shown (green).

12.6 Conclusions

The reconstruction algorithm developed for shower-like events in the ORCA detector achieves excellent vertex, direction and energy reconstruction resolutions, while the effective volume in saturation is close to the instrumented volume. As the reconstruction strategy exploits the different phenomenology of few-GeV hadronic showers compared to electromagnetic showers induced by single electrons (see Sec. 7), the reconstruction can find the electron direction in $\bar{\nu}_e$ CC events, and is therefore able to gain access to the interaction inelasticity y .

The y -sensitivity allows partly a separation of ν_e CC, $\bar{\nu}_e$ CC, $\bar{\nu}_\tau$ CC and $\bar{\nu}$ NC events on a statistical basis (see Sec. 12.4.1). In addition, it allows to compensate for different light yields of electromagnetic and hadronic showers in the neutrino energy reconstruction. The relative improvement of the neutrino energy resolution due to including the inelasticity y in the reconstruction is about $\sim 8\%$ for $\bar{\nu}_e$ CC events (see Sec. 12.4.2).

For the ORCA benchmark detector, the neutrino energy resolution is Gaussian-like with a relative resolution RMS/E_ν better than 26% (24%) and the median neutrino direction resolution is better than 11° (9°) for upgoing ν_e ($\bar{\nu}_e$) CC events with $E_\nu \gtrsim 7$ GeV (see Sec. 12.3.1). Reconstruction errors are only slightly larger for sparser detector layouts (see Sec. 12.3.4).

Achieved neutrino energy and direction resolutions are close to the limits imposed by the intrinsic fluctuations in Cherenkov light signatures, as discussed in Sec. 12.5.2. Due to the nature of these intrinsic limits, detector configurations with larger vertical spacings between the DOMs, and consequently larger instrumented volumes, show only a minor degradation in energy and direction resolutions, while the corresponding effective volumes saturate at higher values, however, with less steep turn-on. The possible gain in NMH sensitivity due to a detector configuration optimisation is investigated in Sec. 13.2.3.

Undetected variations in water/PMT properties of the order of a few percent do not deteriorate the energy and direction resolution. They only shift the mean reconstructed energy (see Sec. 12.3.5). Thus, such uncertainties can safely be described by a single ‘energy scale’ uncertainty, as done in the ‘Letter of Intent’ [3]. The performance of the shower reconstruction is robust against an increase of noise level by a factor two (see Sec. 12.3.5). Consequently, it is expected that the assumed reconstruction performance can be achieved for most of the data taking time. It is feasible to select a pure shower-like neutrino event sample without pure-noise events, i.e. events with only optical background hits, based on quality parameters of the shower reconstruction without any significant reduction in effective volume (see Sec. 12.3.7). Therefore, neglecting pure-noise events in the NMH sensitivity in Sec. 13 and in the ‘Letter of Intent’ [3] is justified.

The comparison of the effective volume with respect to the trigger level (see Sec. 12.5.1) reveals that nearly all fully contained events that are triggered are also well reconstructed. Hence, lowering the trigger threshold will also increase the available statistics of well reconstructed few-GeV neutrinos, and therefore increase the NMH sensitivity. This emphasises again the importance of triggering for the NMH determination with ORCA.

Compared to the PINGU – the main competitor of the ORCA experiment – the developed ORCA shower reconstruction achieves significantly better direction and energy resolutions, while the effective volumes are comparable (see Sec. 12.5.3).

13 Neutrino mass hierarchy sensitivity in shower channel

The sensitivity to the neutrino mass hierarchy (NMH) is studied in this section with regard to the performance of the developed shower reconstruction for KM3NeT/ORCA (see Sec. 12).

In particular, the gain in sensitivity due to the reconstructed inelasticity y , which adds a statistical separation power between ν_e CC, $\bar{\nu}_e$ CC, $\bar{\nu}$ NC and $\bar{\nu}_\tau$ CC events, is estimated. In addition, a detector layout optimisation is performed and the influence of correlations in the reconstructed quantities are investigated.

13.1 Simplified sensitivity calculation

The NMH sensitivity calculation in this section follows a significantly different approach than that followed in the ‘Letter of Intent’ [3], which is briefly described in Sec. 3.3.2.

First of all, only true shower-like events (based on MC truth), i.e. $\bar{\nu}_e$ CC, $\bar{\nu}$ NC and $\bar{\nu}_\tau$ CC with non-muonic τ decays, are considered. Track-like events are not taken into account. Pure-noise events are neglected, as justified in Sec. 13. This MC truth based event selection is equivalent to assuming a perfect event classification with 100% purity. This treatment allows to concentrate on the influence of the shower reconstruction performance on ORCA’s sensitivity to the NMH. All events are reconstructed with the shower reconstruction for ORCA described in Sec. 12.

For simplification, the oscillation parameters for either mass hierarchy are fixed to the values given in Tab. 2.2. Note that they are slightly different for the two NMH assumptions. Systematic uncertainties in the neutrino flux, interaction cross sections and detector response are not considered. As all parameters are fixed except the binary decision between the two NMH possibilities, no fit with the oscillation parameters and systematics as free parameters is needed.

Under these assumptions, the expected significance of the NMH determination can be estimated using the asymmetry variable \mathcal{A} introduced in Eq. 3.7. The absolute value of this asymmetry is a measure of statistical significance of the difference between the expected number of events for NH and IH. The total significance \mathcal{S} is given by

$$\mathcal{S} = \sqrt{\sum_i \mathcal{A}_i^2} = \sqrt{\sum_i \frac{(N_{\text{IH}}^i - N_{\text{NH}}^i)^2}{N_{\text{NH}}^i}}, \quad (13.1)$$

where the summation is over all bins i of reconstructed quantities, e.g. E_{reco} , θ_{reco} and y_{reco} . This is same significance metric as used in [2].

The expected number of events N_{NH} and N_{IH} are obtained by assigning two weights to each simulated event: assuming either NH or IH (and the correlation neutrino oscillation parameter, see Tab. 2.2). These weights take into account all detector-independent ingredients, i.e. the atmospheric neutrino flux, the neutrino oscillation and the neutrino interaction cross sections⁷⁷, and depend on the true neutrino parameters: E_ν , θ_ν , $\nu/\bar{\nu}$ and flavour. The assumed neutrino interaction rates are the same as calculated in the first part of the event rate calculation for the ‘Letter of Intent’ [3], described in Sec. 3.3.1.

The total significance \mathcal{S} determined with this approach will overestimate the NMH sensitivity due to the optimistic assumptions (only shower-like channel, perfect event classification, no systematics, known oscillation parameters). However, relative differences in

⁷⁷ As using **gSeaGen** (see Sec. 6.1), the neutrino interaction cross sections implemented in GENIE are employed already in the event generation simulation.

significance can be used to estimate to first order the possible gain due to different assumed ORCA detector performances.

Note that this event-by-event weighting procedure preserves all correlations between reconstructed quantities, e.g. between energy and direction resolution (see Fig. 12.20 and Fig. 12.21).

13.2 Sensitivity studies

The NMH asymmetry \mathcal{A} in the $E_{\text{reco}}-\theta_{\text{reco}}$ plane is shown in Fig. 13.1 for the ORCA benchmark detector with 6 m vertical spacing between DOMs (see Sec. 6.3). The resulting total significance is about $\mathcal{S} \approx 3.17\sigma$ for one year of operation time.

The number of events as well as the significance for each of the three shower-like neutrino event classes ($\bar{\nu}_e$ CC, $\bar{\nu}$ NC and $\bar{\nu}_\tau$ CC with non-muonic τ decays) is shown separately in Fig. 13.2. As already mention in Sec. 3.2.3, the number of detected neutrino-induced events is dominated by $\bar{\nu}_e$ CC interactions, which also contribute dominantly to the NMH sensitivity.

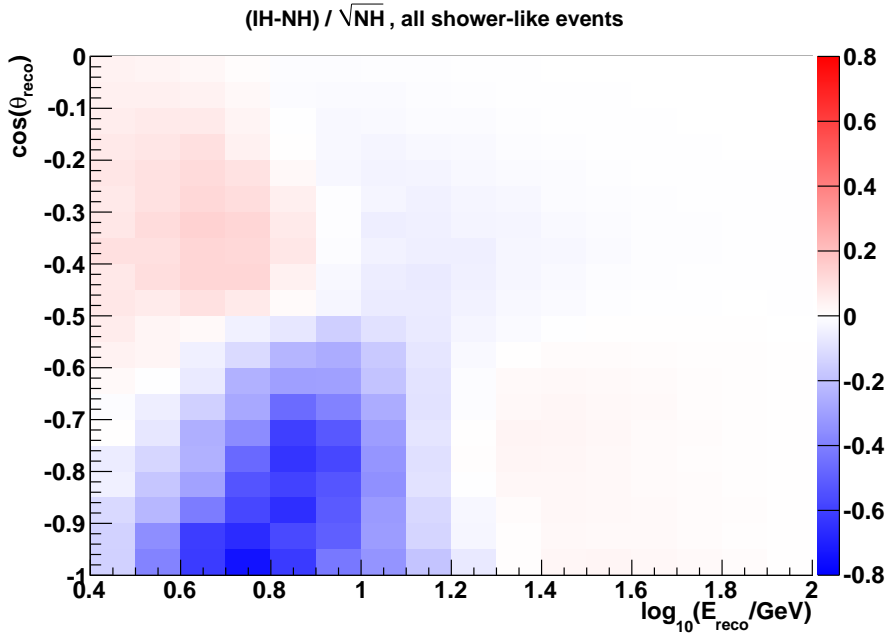


Figure 13.1: Asymmetry \mathcal{A} (Eq. 3.7) for shower-like events as a function of reconstructed energy $\log_{10}(E_{\text{reco}})$ and cosine of the zenith angle $\cos(\theta_{\text{reco}})$. Color code represents the significance in Gaussian- σ per bin for one year of operation time.

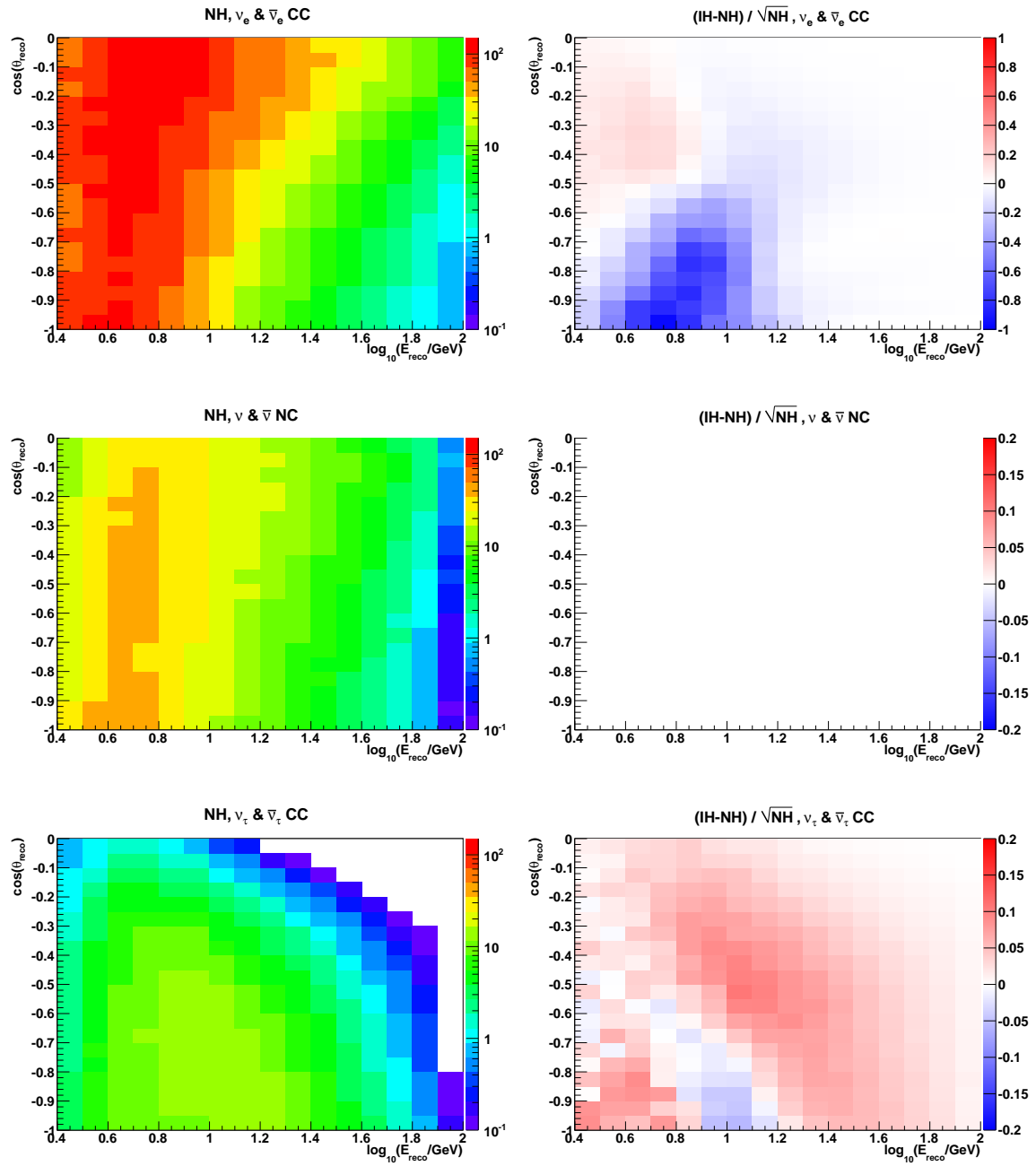


Figure 13.2: Number of events assuming NH (left) and NMH asymmetry \mathcal{A} (right) in the $E_{\text{reco}}-\theta_{\text{reco}}$ plane for the three shower-like neutrino event classes: $\bar{\nu}_e$ CC (top), $\bar{\nu}$ NC (middle) and $\bar{\nu}_\tau$ CC with not-muonic τ decays (bottom). The NMH asymmetry \mathcal{A} is defined in Eq. 3.7. One year operation time of the ORCA benchmark detector is assumed. The NC channel contains no NMH information, so that no asymmetry \mathcal{A} is visible.

13.2.1 Effect of finite Monte Carlo statistics

Limited statistics of MC events introduces a bias towards too high significances \mathcal{S} . This effect is shown in Fig. 13.3. The bias increases with decreasing event statistics. For smaller event statistics, the relative fluctuations of the asymmetry \mathcal{A}_i in each bin increase. As the total significance \mathcal{S} is given by quadratically summing the asymmetries \mathcal{A}_i of all bins (see Eq. 13.1), fluctuations that lead to a change of sign of \mathcal{A}_i result on average in an increase in significance. The same effect was also observed in [35].

From Fig. 13.3, a relatively stable result for the full amount of MC statistics is expected, which will be also close to the limit of infinite MC statistics. For comparison, the significance for smaller and larger $\log_{10}(E_{\text{reco}})-\cos(\theta_{\text{reco}})$ bins is also shown in Fig. 13.3. The increase in significance for more bins (black and blue star) mainly originates from the fact that the event statistics per bin decreases. For less bins (purple star), the significance decreases considerably below the value of reference binning. This shows that the chosen reference binning (used in all figures in this section) is sufficient to resolve the NMH asymmetry pattern, while maximising the event statistics in each bin.

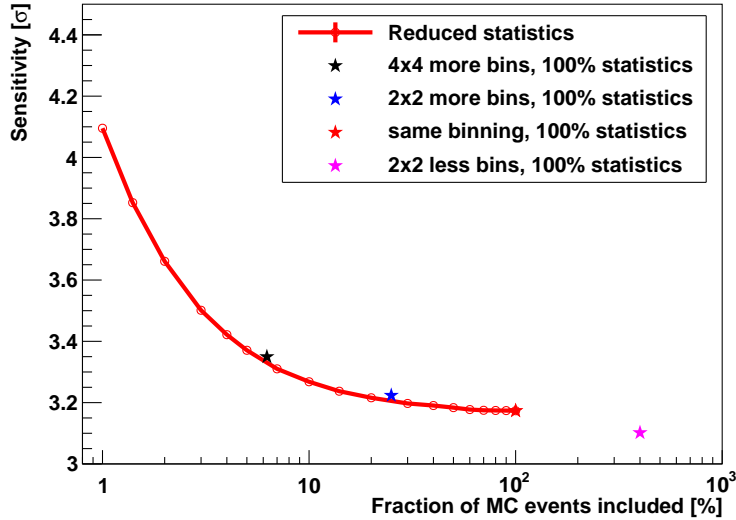


Figure 13.3: Total significance \mathcal{S} as a function of the fraction of MC events used to calculate \mathcal{S} (red line) for one year of operation time of the ORCA benchmark detector. Same $\log_{10}(E_{\text{reco}})-\cos(\theta_{\text{reco}})$ binning as in Fig. 13.1 is used. Colored stars show \mathcal{S} for 4 times more (black), 2 times more (blue) and 2 times less bins (purple) in $\log_{10}(E_{\text{reco}})$ as well as $\cos(\theta_{\text{reco}})$ than the binning (red) used in Fig. 13.1 using 100% of MC statistics.

13.2.2 Improvement due to interaction inelasticity

The NMH significance \mathcal{S} (Eq. 13.1) can be increased by adding a third binning dimension (other two: reconstructed energy E_{reco} and direction θ_{reco}). A variable that contains information on the NMH is the reconstructed inelasticity y_{reco} , as it allows a statistical separation between ν_e CC, $\bar{\nu}_e$ CC, $\bar{\nu}_\tau$ NC and $\bar{\nu}_\tau$ CC events. The separation power between these event classes is estimated in Sec. 12.4.1. In the following, the improvement in NMH significance due to adding y_{reco} is determined. Five equidistant y_{reco} bins (0–0.2, 0.2–0.4, 0.4–0.6, 0.6–0.8, 0.8–1) are assumed.

The NMH asymmetry \mathcal{A} in the $E_{\text{reco}}-\theta_{\text{reco}}$ plane for the five different y_{reco} bins is shown in Fig. 13.4. The total significance is about $\mathcal{S}_5^{y_{\text{reco}}} \approx 3.28 \sigma$ for one year of operation time of the ORCA benchmark detector. Of course, the effect of less event statistics per bin

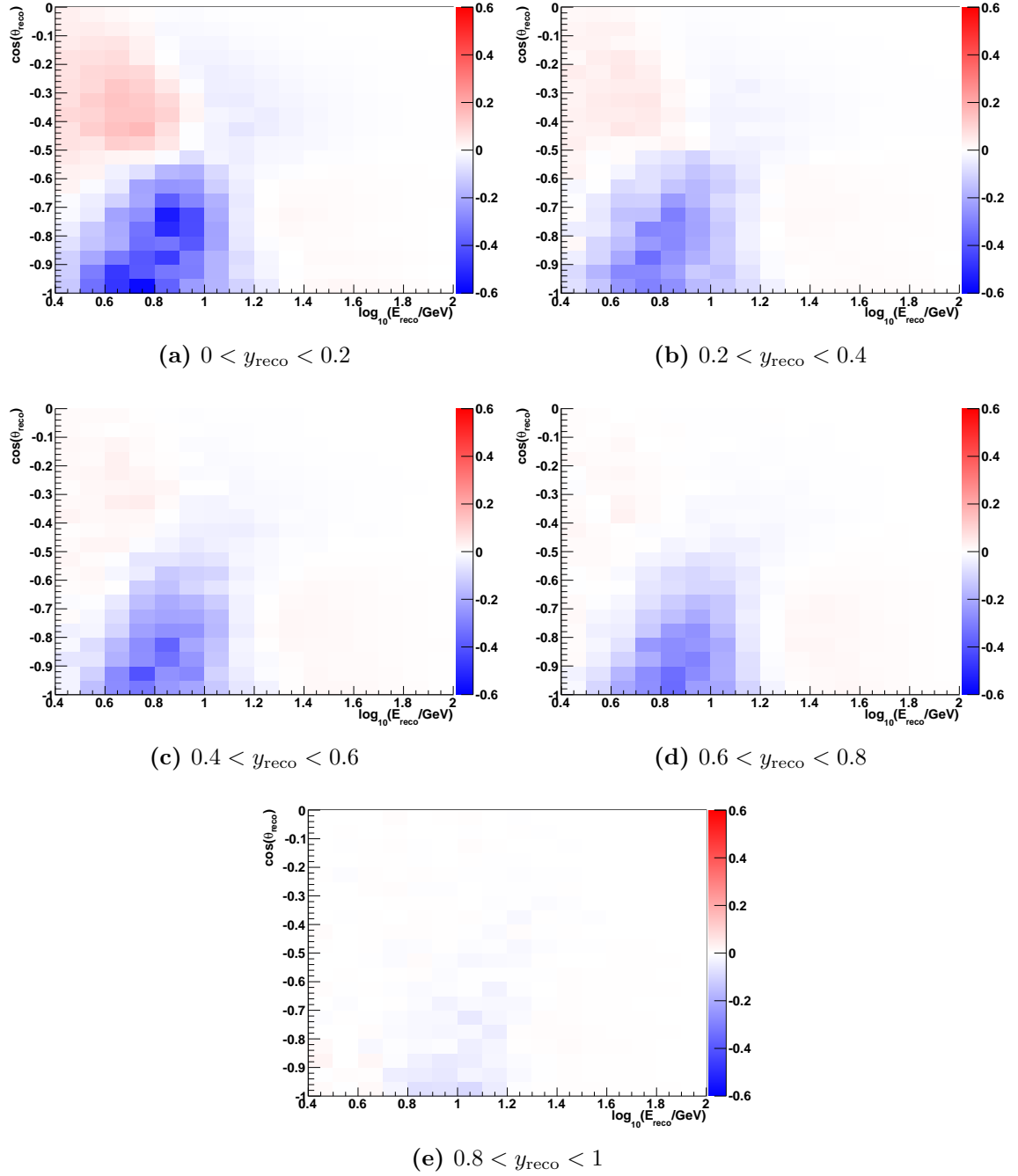


Figure 13.4: NMH asymmetry \mathcal{A} (Eq. 3.7) in the $E_{\text{reco}}-\theta_{\text{reco}}$ plane for 5 different y_{reco} bins. All shower-like events are used and one year operation time of the ORCA benchmark detector is assumed.

has to be taken into account when increasing the number of bins. Fig. 13.5 shows the distribution of significance $\mathcal{S}_5^{y_{\text{rand}}}$ for the case that the events are randomly distributed among 5 bins in a third dimension called y_{rand} . The size of the y_{rand} bins are chosen such that the bins contain the same average⁷⁸ fraction of events as in the case of y_{reco} . Then, the total significance is about $\mathcal{S}_5^{y_{\text{rand}}} \approx 3.22 \sigma$.

Thus, the resulting improvement due to adding the reconstructed inelasticity y_{reco} as a

⁷⁸ For the averaging, the y fraction in each $\log_{10}(E_{\text{reco}})-\cos(\theta_{\text{reco}})$ bin is weighted with significance squared \mathcal{A}^2 in that bin. This procedure gives the following y_{rand} bin sizes: 0.50, 0.20, 0.17, 0.12, 0.01.

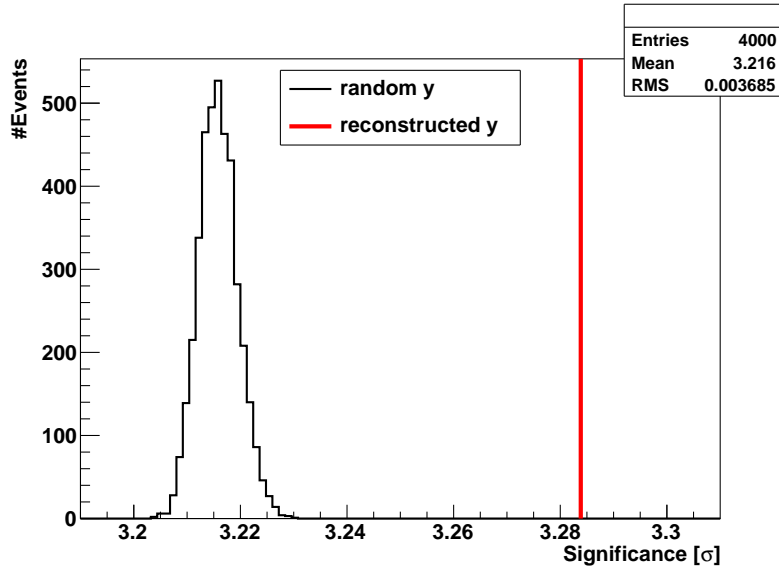


Figure 13.5: Distribution of significance $\mathcal{S}_5^{y_{\text{rand}}}$ for 4000 iterations of randomly assigned y_{rand} values used as third binning dimension (black histogram). The full available MC statistics is used. For comparison, the significance $\mathcal{S}_5^{y_{\text{reco}}}$ for the case of using the reconstructed y_{reco} is also indicated (red line).

third dimension in the NMH significance calculation corresponds to a reduction in needed operation time for a given significance level of about $\sim 4\%$.

When using the resolution limit on the inelasticity y_{lead} from the leading particle (see Sec. 7.3.1) instead of the reconstructed inelasticity y_{reco} , the total significance is about $\mathcal{S}_5^{y_{\text{lead}}} \approx 3.52\sigma$. This corresponds to a reduction in needed operation time of about $\sim 20\%$. For 10 instead of 5 bins in y_{lead} , the reduction factor increases to $\sim 30\%$. Note that only events selected by the shower reconstruction are considered for this study, which introduces a bias towards $\bar{\nu}_e$ CC compared to ν_e CC events (see Fig. 12.23).

The amount of improvement decreases with increasing vertical spacing between the DOMs, as can be seen from Tab. 13.1. This can be explained due to the fact that with a sparser detector less information on the inelasticity y is contained in the observed hit signature. In addition, the ratio of effective volumes of ν_e CC and $\bar{\nu}_e$ CC events is unfavourable for larger vertical spacings (see Fig. 12.23) in the energy range relevant for the NMH measurement. This reduces the possible improvement due to including the inelasticity. This is the case for y_{reco} as well as for y_{lead} .

Note that this simplified sensitivity study does not consider the fact that the reconstructed inelasticity y_{reco} may also help to constrain the systematic uncertainty on the $\bar{\nu}/\nu$ ratio in regions of the $E_{\text{reco}}-\theta_{\text{reco}}$ parameter space that are not sensitive to the NMH.

13.2.3 Detector layout optimisation

Using the simulations for the ORCA detector configurations with different vertical spacings between the DOMs described in Sec. 6.4, the NMH sensitivity can be calculated for each of the detector configurations. The results are summarised in Tab. 13.1.

The detector configuration with 9 m vertical spacing between the DOMs shows the largest NMH sensitivity. This is the same outcome as in the full NMH sensitivity study performed in the ‘Letter of Intent’ [3], which includes also the track-like channel, event classification and systematic uncertainties. This result is not surprising, as the NMH sensitivity is dominated by the sensitivity in the shower channel (see Fig. 3.7).

detector configuration vertical spacing [m]	$\mathcal{S}_{\text{no } y\text{-bins}} [\sigma]$	$\mathcal{S}_5^{y_{\text{rand}}} y\text{-bins} [\sigma]$	$\mathcal{S}_5^{y_{\text{reco}}} y\text{-bins} [\sigma]$	$\mathcal{S}_5^{y_{\text{lead}}} y\text{-bins} [\sigma]$
6	3.17	3.22	3.28	3.52
9	3.39	3.45	3.49	3.77
12	3.26	3.35	3.36	3.61
15	2.92	3.02	3.02	3.20

Table 13.1: Significances for different ORCA detector configurations with 6 m, 9 m, 12 m and 15 m vertical spacing between the DOMs calculated with four different treatments of the inelasticity. $\mathcal{S}_{\text{no } y\text{-bins}}$: only two dimensions (E_{reco} and θ_{reco}). $\mathcal{S}_5^{y_{\text{rand}}} y\text{-bins}$: third dimension with a random variable y_{rand} . $\mathcal{S}_5^{y_{\text{reco}}} y\text{-bins}$: third dimension using reconstructed inelasticity y_{reco} . $\mathcal{S}_5^{y_{\text{lead}}} y\text{-bins}$: third dimension using y_{lead} from the leading particle (Eq. 7.9).

13.2.4 Comparison of uncorrelated and correlated resolutions

The event-by-event weighting procedure described in Sec. 13.1 preserves all correlations between reconstructed quantities. In the ‘Letter of Intent’ [3], these correlations are neglected, i.e. neutrino energy and direction are smeared independently. The procedure followed here gives also the opportunity to study the difference between the two cases: correlated and uncorrelated reconstructed quantities.

For the case of uncorrelated reconstructed quantities, the reconstructed energies E_{reco} of events with similar true neutrino energies E_ν are randomly interchanged among each other and the reconstructed directions θ_{reco} are randomly interchanged among events with similar E_ν and θ_ν . This corresponds approximately to the procedure followed in the ‘Letter of Intent’ [3].

The NMH sensitivities calculated following the procedure with uncorrelated reconstruction resolutions is always smaller than that with correlated reconstruction resolutions. For the ORCA benchmark detector with 6 m vertical spacing between the DOMs, the difference is about $\sim 4.5\%$ in needed operation time for a given significance level. For larger vertical spacings, the effect is even smaller ($\sim 1.5\%$ for 9 m, and negligible for 12 m/15 m).

The reason for this dependence on the vertical spacings between the DOMs comes from the energy threshold of the reconstruction. For larger spacings, the effective volumes are not in the plateau for energies relevant for the NMH measurement (see Fig. 12.23). This effectively acts as a preselection of events. Only comparatively bright events with a small hadronic shower component (small inelasticity y) are reconstructed. Hence, the reconstructed quantities are only randomly interchanged between events with similar properties, i.e. inelasticity y . This leads for larger vertical spacings between the DOMs to the same NMH sensitivities independent of the followed procedure.

As the correlation between energy and direction have only a minor effect on the NMH sensitivity in the shower channel, the NMH sensitivity calculated in the ‘Letter of Intent’ [3] – neglecting these correlations and apply an independent smearing – is not significantly affected.

13.3 Conclusions

The NMH sensitivity study performed in this section emphasises the importance of the developed shower reconstruction for KM3NeT/ORCA’s results presented in the ‘Letter of Intent’ [3] and in particular for the detector optimisation.

Using a simplified NMH sensitivity calculation and considering only shower-like neutrino events, the same optimal detector configuration of the ORCA detector (9 m vertical

spacing between DOMs) is found as in the ‘Letter of Intent’ [3]. The sensitivity gain in the shower channel due to reconstructed inelasticity y_{reco} is rather moderate ($\sim 4\%$ in needed operation time), but there is room for improvement if the inelasticity reconstruction improves (up to $\sim 30\%$ when using the resolution limit y_{lead} from the leading particle, see Eq. 7.9). The influence of correlations in the reconstructed quantities on the NMH sensitivity is moderate, because the event selection effect takes already accounts for most correlations in the relevant energy range. Hence, the NMH sensitivity calculated in the ‘Letter of Intent’ [3], where these correlations are neglected, are not significantly affected.

14 Summary and outlook

One of the most important open questions in neutrino physics is the determination of the mass hierarchy of the three Standard Model neutrinos. The neutrino mass hierarchy can be determined by measuring the energy- and zenith-angle-dependent oscillation probabilities of atmospheric neutrinos that have traversed the Earth. This is the main science goal pursued by KM3NeT/ORCA, a future multi-megaton underwater Cherenkov detector in the deep Mediterranean Sea. The degree to which ORCA can contribute to the neutrino mass hierarchy determination depends significantly on the attainable reconstruction accuracy and detection efficiency for neutrinos in the few-GeV energy regime. The subject of this thesis was to evaluate these key detector performance indicators for the ORCA benchmark detector and to optimise the detector layout for the neutrino mass hierarchy measurement. A focus was put on shower-like neutrino events, in particular $\bar{\nu}_e$ CC interactions, which contribute most to the neutrino mass hierarchy sensitivity.

Two main developments have been achieved: First, a new reconstruction method for shower-like neutrino events has been developed. Its excellent performance is a key ingredient for ORCA's sensitivity to the neutrino mass hierarchy. The reconstruction method was published in the 'Letter of Intent' [3] of the KM3NeT collaboration. Second, from a more fundamental perspective, neutrino reconstruction accuracy limits imposed by intrinsic fluctuations in Cherenkov light signatures have been derived. These results are currently prepared for publication [158].

As part of this thesis, the Cherenkov light signatures of few-GeV neutrinos interacting in seawater were extensively investigated. In particular, the differences between hadronic and electromagnetic showers were elaborated upon. Based on this important groundwork for neutrino event reconstruction with underwater Cherenkov detectors in general, a new shower reconstruction algorithm tailored for the needs of the ORCA detector has been developed. Shower energy, direction and the interaction inelasticity y are reconstructed via a maximum likelihood fit. As the reconstruction exploits the different characteristics of few-GeV hadronic showers compared to electromagnetic showers induced by single electrons, the reconstruction can find the electron direction in $\bar{\nu}_e$ CC events, and is therefore able to gain access to the interaction inelasticity y .

Detailed simulations of the ORCA benchmark detector showed that the reconstruction achieves excellent accuracy on the neutrino, with a interaction vertex resolution better than 1 m, a median direction resolution better than $11^\circ/9^\circ$ and a energy resolution better than 26%/24% for $\nu_e/\bar{\nu}_e$ CC events with neutrino energies above 7 GeV. At the same time, the effective volume in saturation (at high energies) is close to the instrumented volume, and its turn-on (at low energies) is mainly driven by the efficiency of the trigger system. The neutrino direction resolution is dictated by the intrinsic neutrino-electron scattering angle, and the neutrino energy resolution is dominated by intrinsic fluctuations in the Cherenkov light yield of hadronic showers. The ability for reconstructing the inelasticity y in shower-like events allows the different light yields of electromagnetic and hadronic showers to be accounted for, improving the energy resolution (relative improvement $\sim 8\%$). Furthermore, the reconstructed y provides a statistical separation power between ν_e CC, $\bar{\nu}_e$ CC, $\bar{\nu}_\tau$ CC and $\bar{\nu}$ NC events, leading to an increase in neutrino mass hierarchy sensitivity. This sensitivity gain has been estimated for the developed shower reconstruction to be rather moderate ($\sim 4\%$ reduction in needed operation time), but with further improvements it could be significant larger (up to $\sim 30\%$).

The photosensor density of the ORCA detector has been optimised based on the shower reconstruction performance and using the neutrino mass hierarchy sensitivity as figure of merit. A more-sparsely instrumented but correspondingly larger detector layout than that

of the ORCA benchmark detector, with 9 m instead of 6 m vertical distance between adjacent optical modules, was found to be optimal. The same optimum was also found in the more-detailed study in the ‘Letter of Intent’ [3], which includes also track-like events, event classification and systematic uncertainties. This emphasises the importance of the developed shower reconstruction for ORCA’s results. The optimisation of the trigger configuration was also performed as part of this thesis, and has been applied in the ‘Letter of Intent’ [3].

Compared to PINGU – the main competitor of ORCA with very similar detector concepts and scientific goals – the developed ORCA shower reconstruction achieves significantly better direction and energy resolutions, while the effective volume is comparable. In order to investigate if a Cherenkov detector in the deep glacial ice can reconstruct the electron in $\bar{\nu}_e$ CC events, simulations with the optical properties of average PINGU ice were performed. These simulations suggested that such an ice-based detector is hardly able to distinguish the Cherenkov light signatures from the outgoing electron and the hadronic shower due to the worse light scattering properties of deep glacial ice. Hence, estimating the inelasticity y in $\bar{\nu}_e$ CC events is much more difficult for Cherenkov detectors in deep glacial ice than in deep-sea water.

The intrinsic fluctuations in Cherenkov light signatures of few-GeV electrons, muons and hadronic showers have been investigated in order to derive intrinsic limits imposed on the attainable neutrino reconstruction accuracy. This study revealed that the neutrino reconstruction accuracy is dominated by the large fluctuations in number and direction of emitted Cherenkov photons from hadronic showers. The main energy error contribution comes from the large variety of possible compositions of final-state hadrons, while the uncertainty due to detecting only a small fraction of the emitted Cherenkov photons plays only a minor role assuming the photosensor density of the ORCA benchmark detector. This suggests that a sparser but correspondingly larger detector layout would be more optimal, and therefore explains the underlying reason for the outcome of the ORCA detector layout optimisation. Another important conclusion is that in-ice Cherenkov detectors do not profit significantly in energy resolution from the large photon statistics due to less photon absorption. The study of intrinsic resolution limits was performed in collaboration with C. W. James and is currently being prepared for publication [158].

Remarkably, it turned out that neutrino energy and direction resolutions achieved by the developed shower reconstruction are close to the intrinsic resolution limits. This result justified on the one hand the optimistic assumptions made for deducing these limits, and on the other hand revealed that the achieved resolutions are close to the optimum that could be achieved with such a detector. It also suggests that the influence of the instrumental effects is small.

Besides the detector performance for neutrino-induced signal events, also the expected ORCA detector response to the optical background noise from radioactive Potassium-40 decays, and particularly from bioluminescent organisms in the deep Mediterranean Sea, has been investigated. Using data recorded with ANTARES, an underwater Cherenkov detector that is located only 10 km from the ORCA site and has been in operation for about ten years, it was shown that bioluminescence bursts from macroscopic organisms are not expected to significantly impact either the ORCA detector performance or the detector layout optimisation. For this, a more comprehensive insight into the characteristics of bioluminescence bursts had to be gained. In addition, it was shown that the shower reconstruction performance is robust against an increase of the background noise level by a factor of two above the usually assumed level. Consequently, it is expected that the evaluated performance can be achieved for most of the data-taking time. The feasibility of the neutrino mass hierarchy measurement with ORCA is therefore not compromised by the optical background noise in the deep Mediterranean Sea.

Outlook

In the near future, the full simulation of the optimised detector layout will be finished, allowing the exact performance for this new detector geometry to be evaluated. In the detector layout optimisation performed in this thesis and in the ‘Letter of Intent’ [3], the performance for sparser configurations than the ORCA benchmark detector was evaluated by masking parts of the benchmark detector. This masking procedure overestimates the negative effect of events which are not fully contained, because the surface-to-volume ratio for the masked detector configuration is larger than it would be for a full detector with the same number of photosensors. Hence, the full simulation is expected to result in a better detector performance and consequently an increased neutrino mass hierarchy sensitivity.

Although the trigger configuration optimisation performed in this thesis maximised the trigger efficiency of the available trigger algorithms, the trigger efficiency is currently limiting the effective volume for low-energy neutrinos. Several promising ideas for improving the strategies of the trigger algorithms themselves have been suggested. Once implemented in the trigger software, a significant gain in the number of detected neutrino events with energies relevant for the neutrino mass hierarchy measurement (up to $\sim 40\%$ more reconstructable neutrino events for $E_\nu = 4 \text{ GeV}$) and therefore an increase in neutrino mass hierarchy sensitivity are expected.

Despite the fact that the developed shower reconstruction is close to its intrinsic resolution limits, the reconstruction can be improved by resolving the substructure in hadronic showers. Cherenkov cones from individual hadronic particles were assumed to be not reconstructable for deriving the intrinsic resolution limits. Therefore, a multi-particle reconstruction strategy that tries to fit multiple Cherenkov cones to the event signature should be investigated. Further potential methodological improvements for neutrino direction reconstruction have been identified in the course of the intrinsic resolution limit study. This points the way for future reconstruction efforts in ORCA.

After the first ORCA detection string is deployed (foreseen for early 2017), the estimate of the impact of bioluminescence on the neutrino mass hierarchy measurement with ORCA can be refined, and the biological understanding of the bioluminescent organisms can be advanced.

After resolving the neutrino mass hierarchy, the next open questions in neutrino physics can be targeted, namely whether neutrinos violate CP symmetry and, if so, what is the value of the CP-violating phase δ_{CP} . CP violation is one of the possible mechanisms explaining the observed imbalance of matter and antimatter in the universe. Several next-generation neutrino experiments are currently proposed for discovering CP violation in the lepton sector. For this important measurement, also an ORCA-like detector should be considered. A five to ten times denser instrumentation than the ORCA benchmark detector would be needed to reduce the neutrino energy threshold to about 0.5 GeV. First studies for such a densely-instrumented ice-based Cherenkov detector have already been performed [177]. However, the favourable light scattering properties of seawater suggest that a deep-sea Cherenkov detector might be more suited.

Zusammenfassung und Ausblick

Eine der wichtigsten offen Fragen der Neutrinophysik ist die Bestimmung der Massenhierarchie der drei Neutrinos des Standardmodells. Die Neutrinomassenhierarchie lässt sich durch die Präzisionsmessung der energie- und zenitwinkelabhängigen Oszillationswahrscheinlichkeiten von atmosphärischen Neutrinos, die die Erde durchquert haben, aufklären. Diese Messung ist das Hauptziel von KM3NeT/ORCA, einem zukünftigen, mehrere Megatonnen instrumentierenden Wasser-Tscherenkow-Detektor im Mittelmeer. Die Sensitivität von ORCA auf die Neutrinomassenhierarchie hängt maßgeblich von der erreichbaren Rekonstruktionsgenauigkeit und Nachweiseffizienz für Neutrinos im Energiebereich von einigen GeV ab. Das Ziel dieser Arbeit war die Bestimmung dieser Leistungsindikatoren für den ORCA-Referenzdetektor und die Optimierung des Detektorlayouts für die Messung der Neutrinomassenhierarchie. Hierbei lag das Hauptaugenmerk auf schauerartigen Neutrinoereignissen, insbesondere von $\bar{\nu}_e$ CC Wechselwirkungen, welche die Sensitivität auf die Neutrinomassenhierarchie maßgeblich beeinflussen.

Die zwei zentralen Ergebnisse dieser Arbeit waren: Zum Einen wurde eine neue Rekonstruktionsstrategie für schauerartige Neutrinoereignisse entwickelt. Mit ihrer exzellenten Leistungsfähigkeit trägt diese Rekonstruktion wesentlich zur Sensitivität von ORCA auf die Neutrinomassenhierarchie bei. Die Rekonstruktionsmethode wurde im Rahmen des ‘Letter of Intent’ [3] der KM3NeT Kollaboration veröffentlicht. Zum Anderen konnten untere Grenzen des Auflösungsvermögen von Neutrinoereignissen aus den intrinsischen Fluktuationen der Tscherenkow-Licht-Signaturen abgeleitet werden. Diese Resultate werden momentan zur Veröffentlichung vorbereitet [158].

Im Rahmen dieser Arbeit wurden die Tscherenkow-Licht-Signaturen von neutrinoinduzierten Ereignissen im Energiebereich von einigen GeV umfassend untersucht. Hierbei wurden insbesondere Unterschiede zwischen hadronischen und elektromagnetischen Schauern herausgearbeitet. Basierend auf diesen grundlegenden Vorarbeiten für die Rekonstruktion von Neutrinoereignissen im Allgemeinen wurde ein neuer, auf die Bedürfnisse des ORCA-Detektors maßgeschneiderter Rekonstruktionsalgorithmus für schauerartige Neutrinoereignisse entwickelt. Schauerenergie, -richtung und Inelastizität y der Neutrinowechselwirkung werden mittels einer Maximum-Likelihood-Methode rekonstruiert. Die Rekonstruktion nutzt die unterschiedlichen Charakteristika hadronischer Schauer und von einzelnen Elektronen induzierter elektromagnetischer Schauern aus. Somit lässt sich die Richtung des auslaufenden Elektrons in $\bar{\nu}_e$ CC Ereignissen rekonstruieren, wodurch auch die Inelastizität y der Neutrinowechselwirkung zugänglich ist.

Detaillierte Simulationen des ORCA-Referenzdetektors zeigten das exzellente Auflösungsvermögen der Rekonstruktion: Wechselwirkungsvertex besser als 1 m, Neutrinorichtung im Median besser als $11^\circ/9^\circ$ und Neutrinoenergie besser als 26%/24% für $\nu_e/\bar{\nu}_e$ CC Ereignisse mit Neutrinoenergien über 7 GeV. Das effektive Volumen erreicht hierbei in Sättigung (bei hohen Energien) das instrumentierte Volumen und sein Anstiegsverhalten (bei niedrigen Energien) ist im Wesentlichen durch die Effizienz des Triggersystems gegeben. Die Auflösung für die Neutrinorichtung wird durch den intrinsischen Neutrino-Elektron-Streuwinkel und die Auflösung für die Neutrinoenergie durch die intrinsischen Fluktuationen der Anzahl der vom hadronischen Schauer emittierten Photonen dominiert. Die Sensitivität der entwickelten Rekonstruktion auf die Inelastizität y in schauerartigen Neutrinoereignissen erlaubt eine Berücksichtigung der unterschiedlichen Lichtausbeuten von elektromagnetischen und hadronischen Schauern und so eine Verbesserung der Energieauflösung (relative Verbesserung $\sim 8\%$).

Die Rekonstruktion von y bietet zusätzlich eine statistische Trennkraft zwischen ν_e CC, $\bar{\nu}_e$ CC, $\bar{\nu}_\tau$ CC und $\bar{\nu}$ NC Ereignissen, was zu einer erhöhten Sensitivität auf die Neutri-

nomassenhierarchie beiträgt. Für die entwickelte Schauerrekonstruktion wurde ein relativ geringer Zuwachs der Sensitivität auf die Neutrinomassenhierarchie bestimmt ($\sim 4\%$ Reduktion der benötigten Messdauer). Mit weiteren Verbesserungen könnte der Zuwachs jedoch signifikant größer sein (bis zu $\sim 30\%$).

Des Weiteren wurde die Photosensordichte des ORCA-Detektors basierend auf der Leistungsfähigkeit der entwickelten Schauerrekonstruktion optimiert. Als Bewertungskriterium diente hierzu die Sensitivität auf die Neutrinomassenhierarchie. Ein weniger dicht instrumentierter, aber dafür entsprechend größerer Detektor als der ORCA-Referenzdetektor mit einem vertikalen Abstand von 9 m anstelle von 6 m zwischen übereinander liegenden optischen Modulen stellte sich als optimal heraus. Dasselbe Optimum ergab sich ebenfalls in der ausführlicheren Studie im ‘Letter of Intent’ [3], welche auch spurartige Ereignisse, Ereignisklassifikation und systematische Unsicherheiten in die Untersuchung mit einschloss. Dies unterstreicht die Relevanz der entwickelten Schauerrekonstruktion für ORCA. Die Optimierung der Triggerkonfiguration wurde ebenfalls im Rahmen dieser Arbeit durchgeführt und ist im ‘Letter of Intent’ [3] verwendet worden.

Verglichen mit PINGU – dem Hauptkonkurrenten von ORCA mit sehr ähnlichen Detektorkonzepten und wissenschaftlichen Zielen – weist die für ORCA entwickelte Schauerrekonstruktion signifikant bessere Richtungs- und Energieauflösungen bei ähnlichem effektiven Volumen auf. Um zu untersuchen, ob mit einem Tscherenkow-Detektor im Gletschereis des Südpols die Rekonstruktion des auslaufenden Elektrons in $\bar{\nu}_e$ CC Ereignissen ebenfalls möglich ist, wurden Simulationen mit den optischen Eigenschaften von durchschnittlichem PINGU-Eis erzeugt. Diese Simulationen zeigen, dass ein solcher eisbasierter Detektor kaum in der Lage sein kann, die Tscherenkow-Licht-Signatur des auslaufenden Elektrons von der des hadronischen Schauers aufgrund der unvoreilhaftigen Streueigenschaften des Lichts im Eis zu unterscheiden. Folglich ist auch die Bestimmung der Inelastizität y in $\bar{\nu}_e$ CC Ereignissen mit Tscherenkow-Detektoren deutlich schwieriger im Gletschereis als im Tiefseewasser.

Zudem wurden die intrinsischen Fluktuationen der Tscherenkow-Licht-Signaturen von Elektronen, Myonen und hadronischen Schauern im Energiebereich von einigen GeV untersucht, um daraus untere Grenzen für das bestmöglich zu erreichende Auflösungsvermögen von Neutrinorekonstruktionen abzuleiten. Diese Studie konnte zeigen, dass die Auflösung der Neutrinorekonstruktion durch die großen Fluktuationen in der Anzahl und Richtung der emittierten Tscherenkow-Photonen im hadronischen Schauer dominiert wird. Der größte Beitrag zum Fehler der Neutrinoenergiekonstruktion resultiert aus den vielen möglichen Zusammensetzungen der hadronischen Endzustände. Der Nachweis einer relativ kleinen Anzahl an emittierten Tscherenkow-Photonen nimmt nur eine untergeordnete Rolle ein, wenn von einer Photosensordichte wie die des ORCA-Referenzdetektors ausgegangen wird. Dies legt einen weniger dicht instrumentierten, aber dafür entsprechend größeren Detektor nahe, womit das Resultat der Optimierungsstudie des ORCA-Detektorlayouts zu erklären ist. Eine weitere wichtige Schlussfolgerung ist, dass eisbasierte Tscherenkow-Detektoren trotz der geringeren Lichtabsorption und somit größeren Anzahl an nachgewiesenen Photonen nicht signifikant in der Energieauflösung gegenüber Wasser-Tscherenkow-Detektoren profitieren. Die Studie zum intrinsischen Auflösungsvermögen wurde in Zusammenarbeit mit C. W. James durchgeführt und wird momentan zur Veröffentlichung vorbereitet [158].

Bemerkenswerterweise hat sich herausgestellt, dass die Auflösungen der entwickelten Schauerrekonstruktion dicht an das intrinsische Auflösungsvermögen heranreichen. Dies rechtfertigt zum Einen die optimistischen Annahmen, die für die Ableitung des intrinsischen Auflösungsvermögens gemacht wurden, zum Anderen zeigt es, dass mit der entwickelten Rekonstruktion nahezu das bestmögliche Auflösungsvermögen eines solchen Detektors erreicht werden kann. Zudem legt dies nahe, dass der Einfluss von instrumentellen Effekten klein ist.

Neben der Leistungsfähigkeit des Detektors für neutrinoinduzierte Signalereignisse wurde auch das zu erwartende Verhalten des ORCA-Detektors auf den optischen Untergrund durch Zerfälle des radioaktiven Isotops Kalium-40 und insbesondere durch die biolumineszenten Organismen in der Tiefsee des Mittelmeeres untersucht. Mit den Daten des ANTARES-Detektors, einem nur 10 km vom ORCA-Standort entfernten und seit etwa zehn Jahren betriebenen Wasser-Tscherenkow-Detektor, konnte abgeschätzt werden, dass Lichtblitze biolumineszenter Organismen nur einen geringen Einfluss auf die Leistungsfähigkeit des ORCA-Detektors und die Detektoroptimierung haben. Hierfür war es zunächst nötig tiefergehende Erkenntnisse über die Eigenschaften dieser Lichtblitze zu erlangen. Des Weiteren konnte gezeigt werden, dass die Leistungsfähigkeit der Schauerrekonstruktion robust gegenüber einem Anstieg des Rauschniveaus um einen Faktor zwei ist. Folglich ist zu erwarten, dass die in dieser Arbeit bestimmte Leistungsfähigkeit für einen Großteil der Datennahmezeit erreicht wird. Die Machbarkeit der Messung der Neutrinomassenhierarchie mit ORCA wird somit durch den optischen Untergrund in der Tiefsee des Mittelmeeres nicht signifikant beeinträchtigt.

Ausblick

In naher Zukunft werden die vollständigen Simulationen des optimierten ORCA-Detektorlayouts abgeschlossen sein, welche die Bestimmung der exakten Leistungsfähigkeit dieser neuen Detektorgeometrie erlauben. In der Studie zur Detektoroptimierung in dieser Arbeit und im ‘Letter of Intent’ [3] wurden weniger dicht instrumentierte Detektorlayouts durch das Maskieren von Teilen des ORCA-Referenzdetektors realisiert. Dieses Vorgehen überschätzt den negativen Effekt nicht vollständig im Detektorvolumen enthaltener Ereignisse, da das Oberfläche-zu-Volumen-Verhältnis der maskierten Detektorkonfiguration größer ist als bei einem vollständigen Detektor mit derselben Anzahl an Photosensoren. Daher wird die vollständige Simulation des optimierten ORCA-Detektorlayouts eine bessere Leistungsfähigkeit und somit eine höhere Sensitivität auf die Neutrinomassenhierarchie ergeben.

Obwohl die in dieser Arbeit durchgeführte Optimierung der Triggerkonfigurationen die Triggereffizienz der vorhandenen Triggeralgorithmen maximiert, ist die Triggereffizienz ein limitierender Faktor des effektiven Volumens für niederenergetische Neutrinos. Einige vielversprechende Ideen zur Verbesserung der Triggerstrategien wurden vorgeschlagen. Wenn diese in der Triggersoftware umgesetzt sind, ist ein signifikanter Zuwachs an detektierten Neutrinoereignissen im für die Neutrinomassenhierarchie relevanten Energiebereich (bis zu $\sim 40\%$ mehr rekonstruierbare Neutrinoereignisse für $E_\nu = 4 \text{ GeV}$) und somit an Sensitivität auf die Neutrinomassenhierarchie zu erwarten.

Entgegen der Tatsache, dass die entwickelte Schauerrekonstruktion nahezu das intrinsische Auflösungsvermögen erreicht, könnte eine Verbesserung der Rekonstruktion durch das Auflösen der Unterstruktur im hadronischen Schauer möglich sein. Die Rekonstruierbarkeit von Tscherenkow-Kegeln einzelner hadronischer Teilchen wurde für das Ableiten der intrinsische Auflösungsvermögen ausgeschlossen. Daher sollte eine Mehr-Teilchen-Rekonstruktionsstrategie erwogen werden, welche die Beschreibung der Detektorsignatur mit mehreren Tscherenkow-Kegeln versucht. Weitere methodische Verbesserungen in der Rekonstruktion der Neutrinorichtung wurden im Zuge der Studien zum intrinsischen Auflösungsvermögen ausgemacht. Diese weisen den Weg für zukünftige Rekonstruktionseentwicklungen in ORCA.

Sobald die erste Trosse des ORCA-Detektors ausgebracht ist (für Anfang 2017 vorgesehen), kann die Auswirkung von Biolumineszenz auf die Messung der Neutrinomassenhierarchie mit ORCA genauer beurteilt und das biologische Verständnis der biolumineszenten Organismen vorangetrieben werden.

Nachdem die Neutrinomassenhierarchie aufgeklärt ist, kann die nächste offene Frage

der Neutrinophysik angegangen werden. Nach wie vor ist unbekannt, ob Neutrinos die CP-Symmetrie verletzen und falls dem so ist, was der Zahlenwert der CP-verletzenden Phase δ_{CP} ist. CP-Verletzung ist einer der möglichen Mechanismen zur Erklärung des Ungleichgewichts zwischen Materie und Antimaterie im Universum. Verschiedene Neutrinoexperimente der nächsten Generation werden momentan zur Entdeckung von CP-Verletzung im Leptonsektor vorgeschlagen. Für diese wichtige Messung sollte auch ein dem ORCA-Detektor ähnlicher Detektor in Betracht gezogen werden. Dieser sollte eine fünf- bis zehnmals dichtere Instrumentierung als der ORCA-Referenzdetektor aufweisen, um die Nachweisschwelle für Neutrinos auf etwa 0.5 GeV zu senken. Erste Untersuchungen zu den Erfolgsaussichten eines derartig instrumentierten Tscherenkow-Detektor im Eis wurden bereits durchgeführt [177]. Die vorteilhafteren Lichtbrechungseigenschaften des Tiefseewassers legen jedoch nahe, dass ein Wasser-Tscherenkow-Detektor wahrscheinlich geeigneter ist.

A Further simulation details

A.1 KM3NeT PMT and DOM characteristics

Wavelength-dependent quantum efficiencies of KM3NeT PMTs are shown in Fig. A.1, and the PMT's angular acceptance is shown in Fig. A.2. PMT orientations and positions within a KM3NeT DOM are summarised in Tab. A.1.

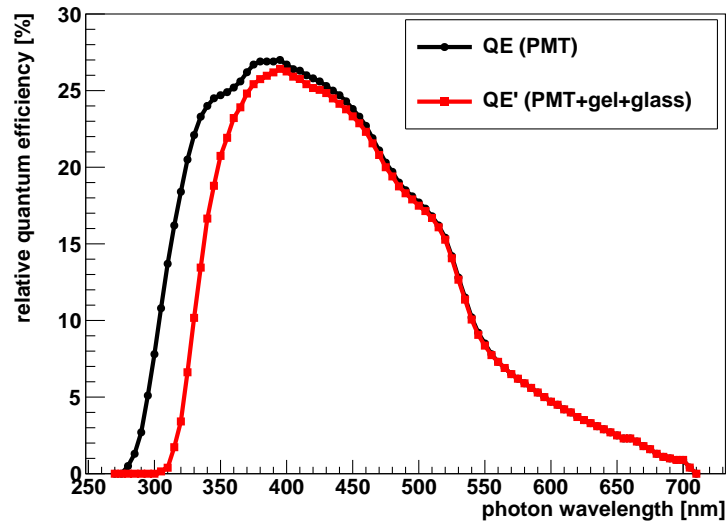


Figure A.1: Quantum efficiency (QE, black) of the KM3NeT PMT and effective quantum efficiency (QE', red) including the PMT QE and the optical transmittivity of glass sphere as well as gel as a function of photon wavelength. Data taken from [156].

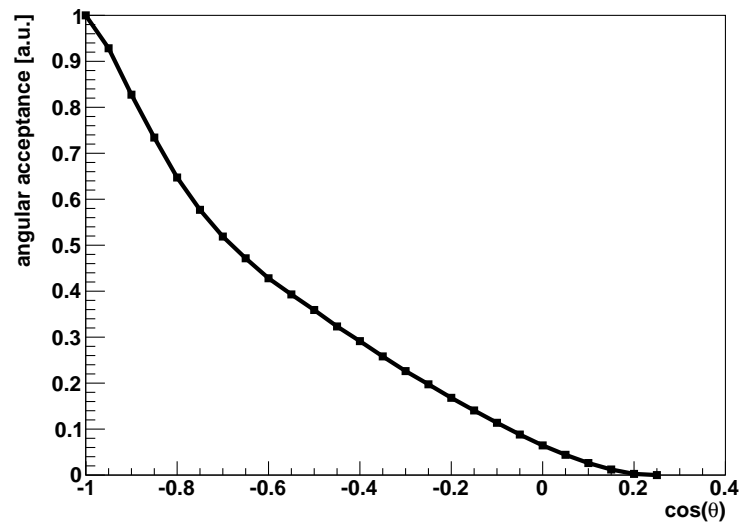


Figure A.2: Angular acceptance of the KM3NeT PMT including the effect of the reflector ring as a function of the angle θ between the incident photon and the axis of the PMT, i.e. vector normal to the photocathode plane. Head-on incidence corresponds to $\cos(\theta) = -1$. Normalised to maximal values equals unity. Data taken from [156].

#	θ [rad]	φ [rad]	x [m]	y [m]	z [m]	dx	dy	dz
1	3.142	0.000	0.000	0.000	-0.200	0.000	0.000	-1.000
2	2.582	0.524	0.092	0.053	-0.169	0.460	0.266	-0.847
3	2.582	1.571	0.000	0.106	-0.169	0.000	0.531	-0.847
4	2.582	2.618	-0.092	0.053	-0.169	-0.460	0.266	-0.847
5	2.582	3.665	-0.092	-0.053	-0.169	-0.460	-0.266	-0.847
6	2.582	4.712	0.000	-0.106	-0.169	0.000	-0.531	-0.847
7	2.582	5.760	0.092	-0.053	-0.169	0.460	-0.266	-0.847
8	2.162	0.000	0.166	0.000	-0.111	0.830	0.000	-0.557
9	2.162	1.047	0.083	0.144	-0.111	0.415	0.719	-0.557
10	2.162	2.094	-0.083	0.144	-0.111	-0.415	0.719	-0.557
11	2.162	3.142	-0.166	0.000	-0.111	-0.830	0.000	-0.557
12	2.162	4.189	-0.083	-0.144	-0.111	-0.415	-0.719	-0.557
13	2.162	5.236	0.083	-0.144	-0.111	0.415	-0.719	-0.557
14	1.872	0.524	0.165	0.096	-0.059	0.827	0.478	-0.296
15	1.872	1.571	0.000	0.191	-0.059	0.000	0.955	-0.296
16	1.872	2.618	-0.165	0.096	-0.059	-0.827	0.478	-0.296
17	1.872	3.665	-0.165	-0.096	-0.059	-0.827	-0.478	-0.296
18	1.872	4.712	0.000	-0.191	-0.059	0.000	-0.955	-0.296
19	1.872	5.760	0.165	-0.096	-0.059	0.827	-0.478	-0.296
20	1.270	0.000	0.191	0.000	0.059	0.955	0.000	0.296
21	1.270	1.047	0.096	0.165	0.059	0.478	0.827	0.296
22	1.270	2.094	-0.096	0.165	0.059	-0.478	0.827	0.296
23	1.270	3.142	-0.191	0.000	0.059	-0.955	0.000	0.296
24	1.270	4.189	-0.096	-0.165	0.059	-0.478	-0.827	0.296
25	1.270	5.236	0.096	-0.165	0.059	0.478	-0.827	0.296
26	0.980	0.524	0.144	0.083	0.111	0.719	0.415	0.557
27	0.980	1.571	0.000	0.166	0.111	0.000	0.830	0.557
28	0.980	2.618	-0.144	0.083	0.111	-0.719	0.415	0.557
29	0.980	3.665	-0.144	-0.083	0.111	-0.719	-0.415	0.557
30	0.980	4.712	0.000	-0.166	0.111	0.000	-0.830	0.557
31	0.980	5.760	0.144	-0.083	0.111	0.719	-0.415	0.557

Table A.1: PMT positions (x, y, z) and orientations ($\theta, \varphi, dx, dy, dz$) within a KM3NeT DOM. Positions are relative to DOM centre. The angle θ is measured with respect to z -axis ($\theta = \pi$ correspond to a PMT pointing downward) and the azimuth angle φ describes the rotation in the x - y plane. In the shower reconstruction (see Sec. 12), the angle $\beta = \pi - \theta$ is used. Data taken from [156].

A.2 GEANT settings for GENSHWR simulations

For the GENSHWR simulations, GEANT 3.21 is set to track electrons down to their Cherenkov threshold of 0.25 MeV and photons down to 0.4 MeV, at which the maximum energy of Compton knock-on electrons is 0.25 MeV. The simulation also allows the explicit production and tracking of δ -electrons above 0.25 MeV. To ensure the necessary accuracy of electron-tracking at low energies, the standard GEANT 3.21 routine ‘`gtelec.f`’ is modified (setting IABAN to 0) to avoid the premature stopping of electrons. Additionally, slow neutrons (below ~ 100 MeV kinetic energy) are artificially removed from the simulation to avoid an unphysical number of induced decays of nuclei in the seawater.

B Further material for bioluminescence studies

B.1 Trident bursts

In one of the GRB-triggered data sets (grb_110_298695091) a peculiar series of very bright light bursts occurred.

The hit rates observed by one OM are shown in Fig. B.1 and Fig. B.2. A series of five ‘trident bursts’ is observed. Each trident burst consists of three individual light bursts. Each individual burst has a duration of ~ 50 ms and its time profile is roughly rectangle-like or Gaussian-like with a similar steep rising and falling edge. The time between the first and second as well as the second and third burst is ~ 300 ms (see Fig. B.2). The time between consecutive trident bursts is ~ 10 s. All OMs in the detector that were close enough to the light source observed the same time profile, as can be seen in Fig. B.3. Each burst was bright enough to illuminate a volume of about $100\text{ m} \times 100\text{ m} \times 100\text{ m}$, as can be seen from Fig. B.4. This is about 1000 times brighter than the typical burst from the dominant class of bioluminescence bursts studied in Sec. 10.4.

An additional series of such trident bursts was observed about 20 minutes before the series of bursts in the GRB-triggered data set. The centre-of-gravity of the hit rates was shifted by several tens of metres with respect to that observed in Fig. B.4, indicating a movement of the light source.

Each of these bursts lead to ~ 100 triggered events per TS (usual trigger rates are of order $\mathcal{O}(1)$ per TS). Based on this feature, a brief investigation on the normal ‘physics’ ANTARES data, i.e. events triggered by one of the ‘physics triggers’, showed that such series of trident bursts occur about once per month, but irregularly.

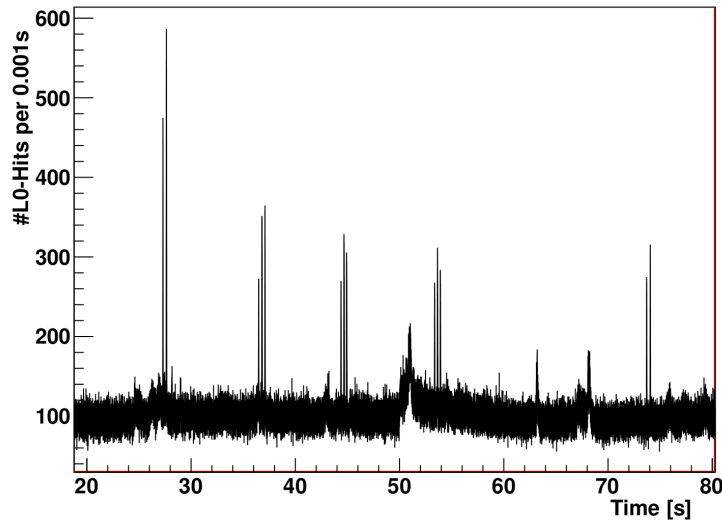


Figure B.1: Hit rates for one OM (line 2, OM 67) in the GRB-triggered data set with grb_110_298695091 (see Tab. 10.1). About 1 minute of data is shown.

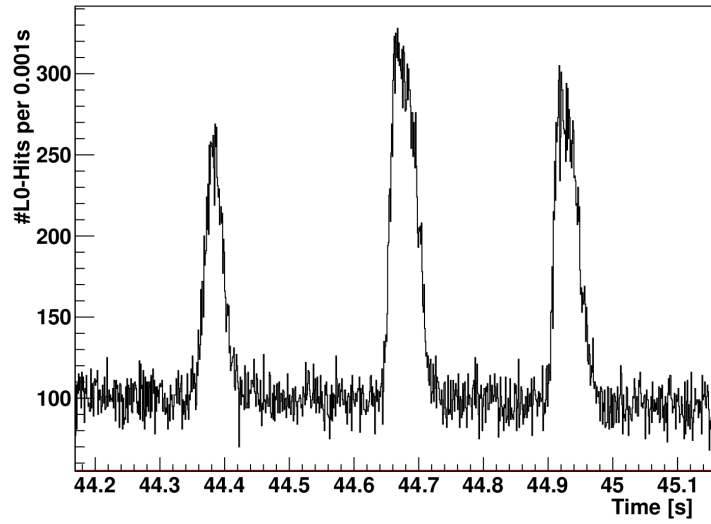


Figure B.2: A zoom into the hit rates shown in Fig. B.1. About 1 second of data is shown.

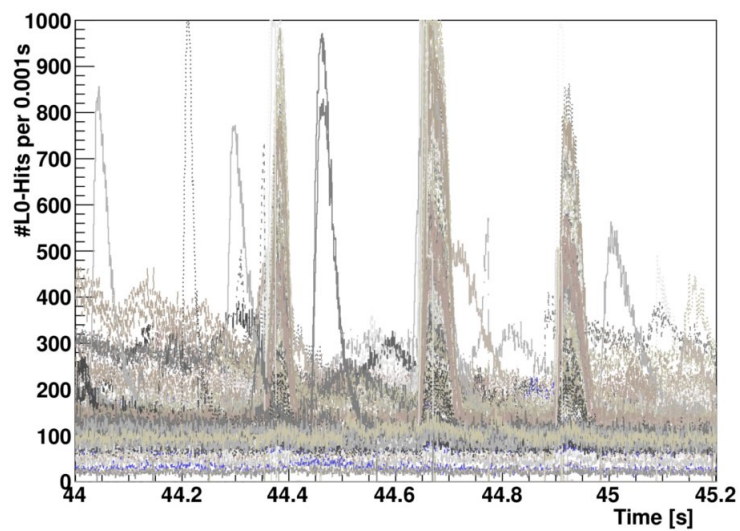


Figure B.3: Hit rates from all OMs in the GRB-triggered data set with grb_110_298695091 (see Tab. 10.1). A similar time range as in Fig. B.2 is shown.

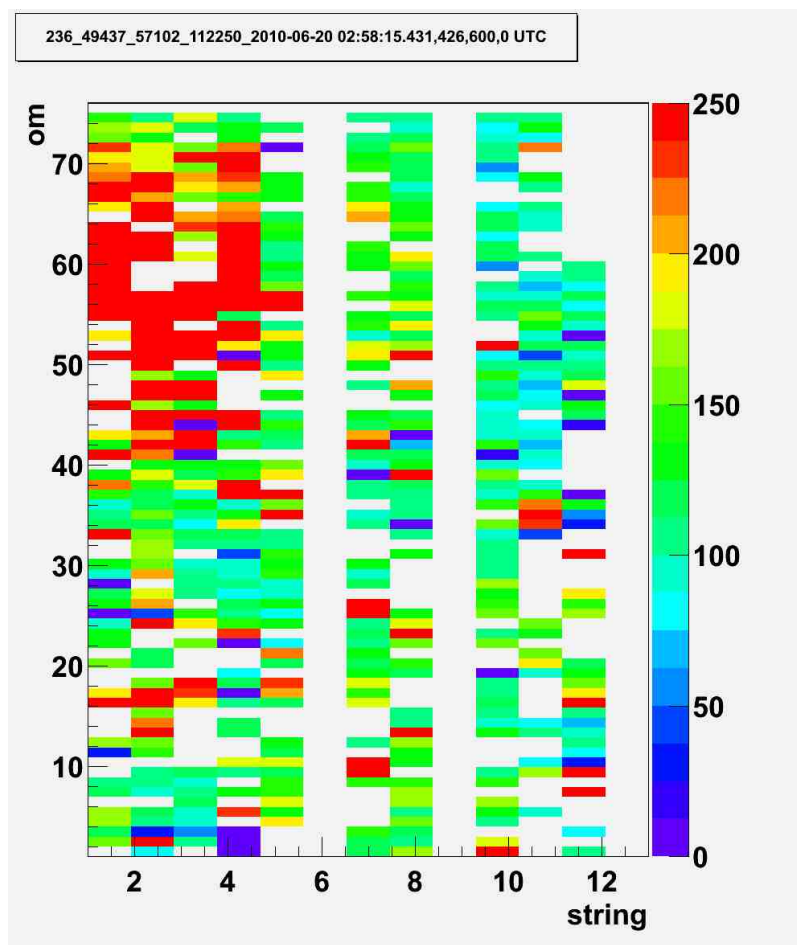


Figure B.4: Hit rates for all OMs in the detector are shown as colour code as a function of 'string' number and 'om' number. Figure provided by Thomas Eberl.

B.2 Additional plots

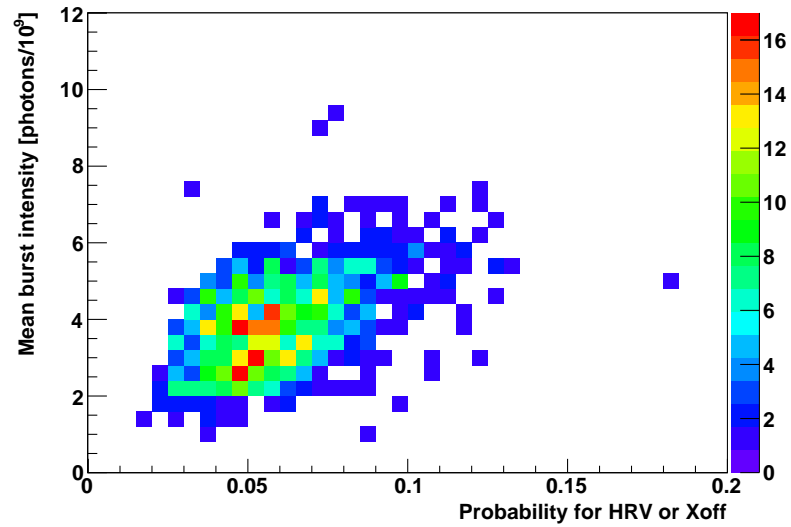


Figure B.5: Probability $P_{\text{HRV},\text{Xoff}}$ that an OM is in HRV or Xoff (see Sec. 10.2) versus mean intensity of bioluminescence burst calculated from inter-storey correlations (see Sec. 10.4.4) for all selected runs (see Sec. 10.4.1) with $6 \text{ cm/s} < v < 7 \text{ cm/s}$.

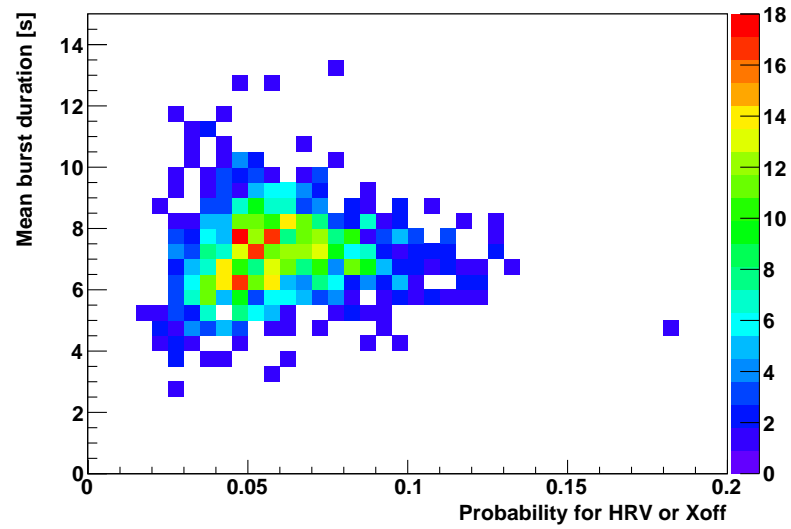


Figure B.6: Probability $P_{\text{HRV},\text{Xoff}}$ that an OM is in HRV or Xoff (see Sec. 10.2) versus duration of bioluminescence burst calculated from in-time correlations (see Sec. 10.4.3) for all selected runs (see Sec. 10.4.1) with $6 \text{ cm/s} < v < 7 \text{ cm/s}$.

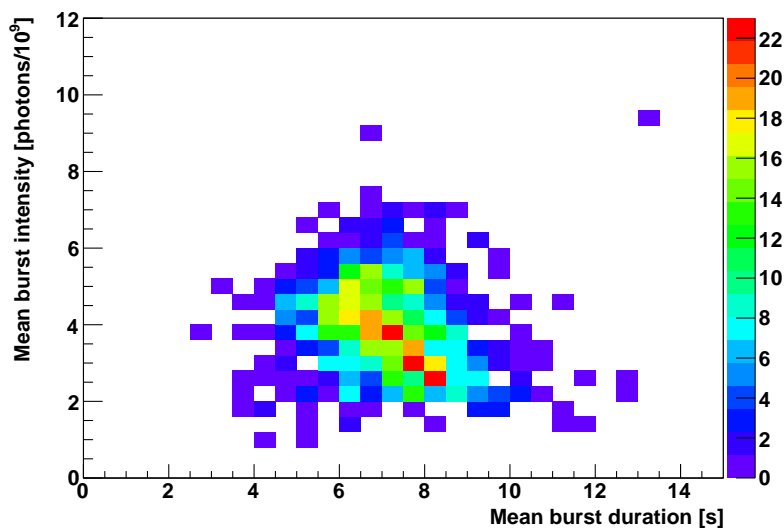


Figure B.7: Duration of bioluminescence burst calculated from in-time correlations (see Sec. 10.4.3) versus mean burst intensity calculated from inter-storey correlations (see Sec. 10.4.4) for all selected runs (see Sec. 10.4.1) with $6 \text{ cm/s} < v < 7 \text{ cm/s}$.

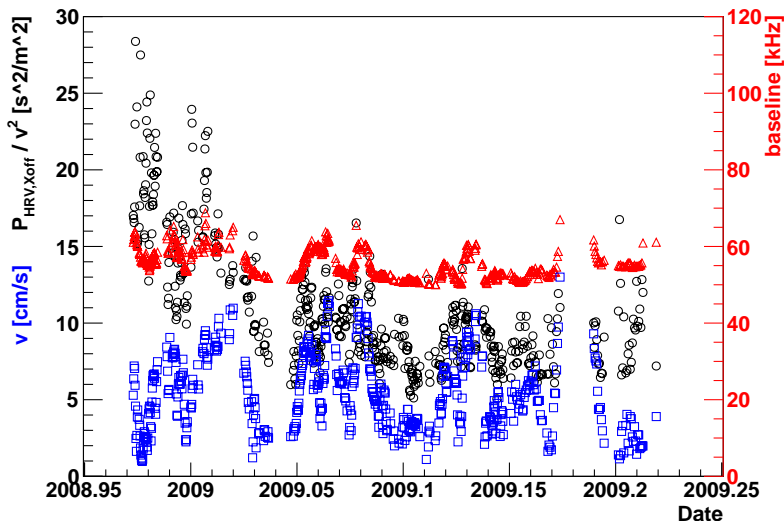


Figure B.8: Probability $P_{\text{HRV},\text{Xoff}}$ that an OM is in HRV or Xoff (see Sec. 10.2) divided by sea current velocity squared v^2 (black circles, left axis), sea current velocity v (blue squares, left axis), and baseline rate (red triangles, right axis) as a function of date in winter 2008/2009 for all selected runs (see Sec. 10.4.1). Sea current velocity and baseline rate are taken from the ANTARES database.

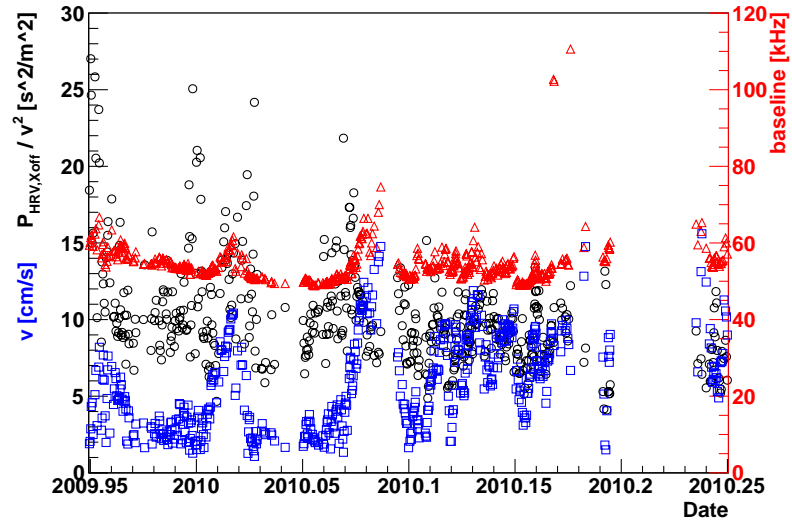


Figure B.9: Same as Fig. B.8 but for winter 2009/2010.

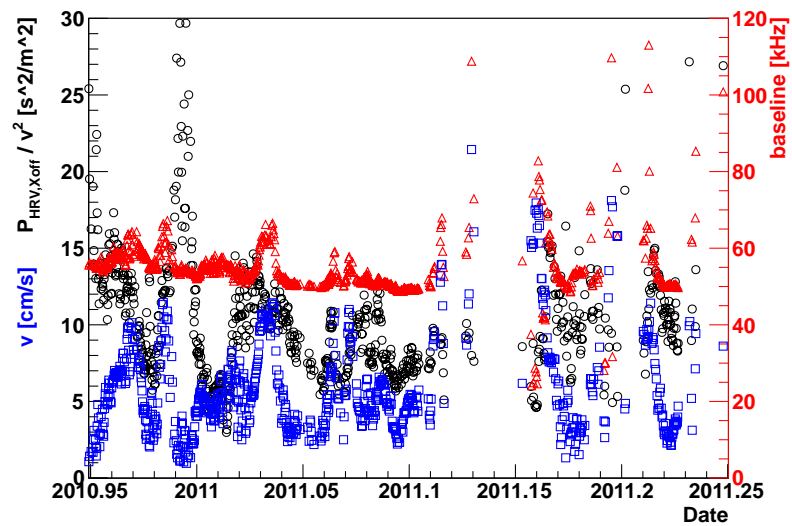


Figure B.10: Same as Fig. B.8 but for winter 2010/2011.

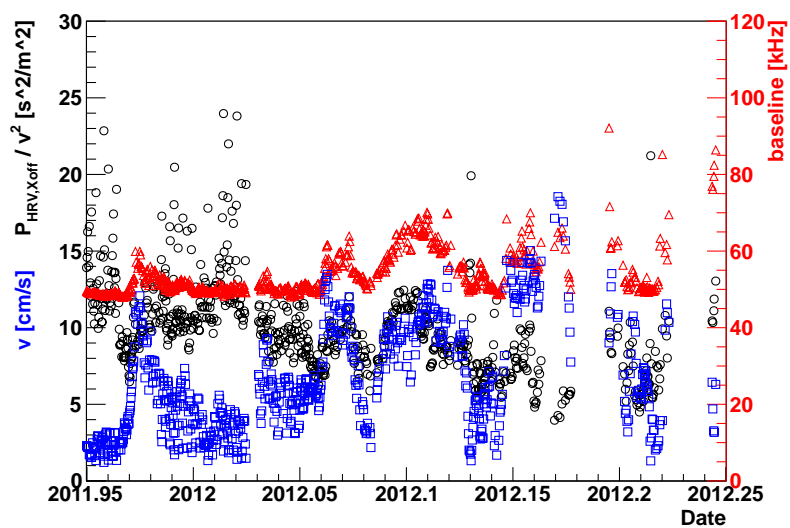


Figure B.11: Same as Fig. B.8 but for winter 2011/2012.

C Hit scoring

In order to identify signal-like hits, a hit scoring scheme has been invented. Each hit DOM is assigned a score that takes into account the hit multiplicity (number of coincidences on the same DOM) as well as the number and multiplicity of causally connected hits in the vicinity. The general idea is that neutrino-induced events have a high hit density around the interaction vertex (or muon track), and therefore hits with a lot of other hits in their vicinity are rewarded.

The whole hit scoring scheme has not been optimised, but is based on educated guesses. Nevertheless, a very satisfying performance is obtained, such that the general idea should also be investigated for triggering, as suggested in Sec. 11.4.

Hit scoring scheme

The score W of a hit DOM is calculated as:

$$W = w_{\text{self}} N_{\text{self}} + w_m(N_{\text{self}}) [w_{\text{adj}} w_m(N_{\text{adj}}) + w_{\text{nadj}} w_m(N_{\text{nadj}}) + w_{\text{vic}} w_m(N_{\text{vic}})], \quad (\text{C.1})$$

where N_{self} is the hit multiplicity on the considered DOM, $N_{\text{adj}}/N_{\text{nadj}}$ are the hit multiplicities on the adjacent/next-to-adjacent DOMs on the same string, and N_{vic} is the hit multiplicity on DOMs in the vicinity of $d = 25$ m around the considered DOM (this distance allows for DOMs on similar storeys but neighbouring strings). Only causally connected hits (see Eq. 11.1) are considered. From the hit multiplicity N , a weight $w_m(N)$ is calculated as:

$$w_m(N) = 1 + \sqrt{N - 1}. \quad (\text{C.2})$$

For the other weights, the following first-guess values are used:

$$w_{\text{self}} = 3, \quad w_{\text{adj}} = 3, \quad w_{\text{nadj}} = 2, \quad w_{\text{vic}} = 1. \quad (\text{C.3})$$

Performance

The performance of the hit scoring scheme is evaluated on pure-noise events as well as on signal $\bar{\nu}_e$ CC events that are ‘around’ the trigger threshold. For the selection of signal events, it is required that they have produced exactly 3 L1 hits, i.e. DOMs with a minimum of $N_{\text{hits}}^{\text{DOM}} = 2$ coincidence hits (within 10 ns, but no cut on neither the angle $\theta_{\text{L}2}$ between hit PMTs nor the distances D_{max} between hit DOMs, see Sec. 11.1) taking into account only signal hits and no noise hits. For calculating the hit scores, the noise hits are of course considered in order to have the same situation as for pure-noise events.

Fig. C.1 shows the resulting hit score distributions separately for different hit multiplicities $N_{\text{hits}}^{\text{DOM}}$ on a DOM. Significantly higher scores are reached for signal hits produced by signal events than for noise hits in pure-noise events. This is in particular the case for DOMs with $N_{\text{hits}}^{\text{DOM}} = 2$ or $N_{\text{hits}}^{\text{DOM}} \geq 3$.

In pure-noise events that fire the shower trigger (see Sec. 11.1.3), at least ≥ 3 L1 hits with a maximal distance of $D_{\text{max}} \leq 40$ m are present, i.e. these L1 hits will have on average higher scores than ‘normal’ (isolated) noise L1 hits. For improving the trigger, it is therefore interesting to study the hit scores of these 3 L1 hits in pure-noise events and compare these with hit scores in signal events. Here, the signal events are also required to have exactly 3 signal L1 hits within $D_{\text{max}} \leq 40$ m and no additional L1 signal hit, i.e. the selected signal events just managed to fire the shower trigger. For noise and signal events, only the hit scores of the 3 L1 hits that are within $D_{\text{max}} \leq 40$ m are considered. Fig. C.2 shows the resulting hit score distributions for L1 hits in pure-noise and signal events. Also in these triggered pure-noise events, the noise L1 hits that fired the shower trigger show significantly lower hit scores than signal L1 hits.

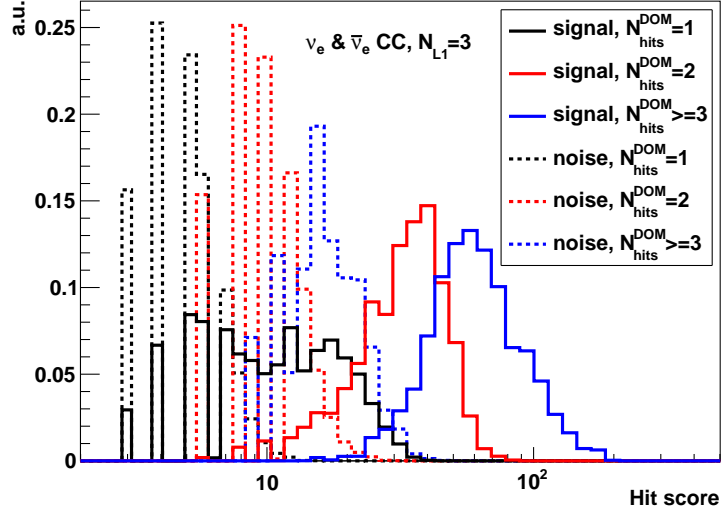


Figure C.1: Distributions of hit scores for signal hits in $\bar{\nu}_e$ CC events with exactly 3 signal L1 hits weighted according to the Bartol flux model (solid) and noise hits in pure-noise events without any requirements (dashed). Distributions for DOMs with a different number of hit multiplicities $N_{\text{hits}}^{\text{DOM}}$ are shown separately in different colours. All distributions are normalised to unity.

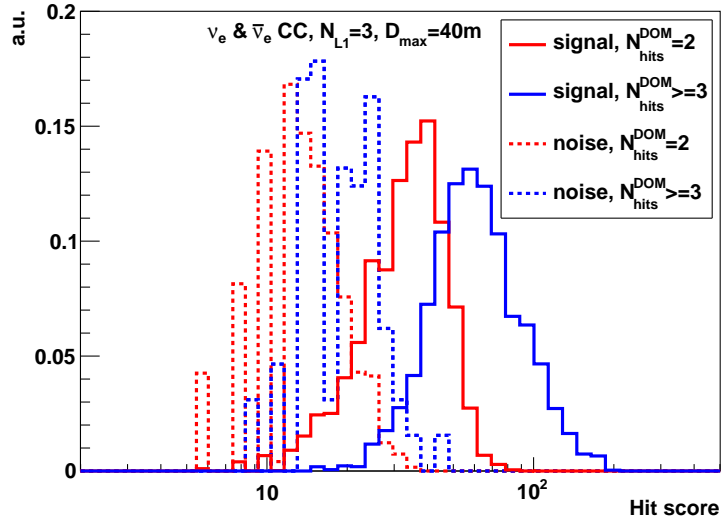


Figure C.2: Same as Fig. C.1, but for signal and noise events that just managed to fire the shower trigger, i.e. 3 L1 hits within $D_{\text{max}} \leq 40$ m (and no additional signal L1 hit in case of signal events).

D Further shower reconstruction details

D.1 Energy correction procedure

The three-dimensional correction function $f(y_{\text{reco}}, \cos(\theta_{\text{reco}}), E_{\text{reco}})$ used in Eq. 12.7 to correct the actually reconstructed energy E_{reco} taking into account the reconstructed zenith angle θ_{reco} and inelasticity y_{reco} is realised by interpolating in a relatively sparse three-dimensional array of correction factors. These correction factors have been calculated from MC such that in each bin the median relative energy offset $(E_{\text{reco}} - E_{\text{true}})/E_{\text{reco}}$ in $\bar{\nu}_e$ CC events is corrected to zero, i.e. one event per bin is set to exactly the correct energy. The correction factors $a(y_{\text{reco}}, \cos(\theta_{\text{reco}}), E_{\text{reco}})$ are applied to the reconstructed energy by:

$$E_{\text{reco}}^{\text{corr}} = E_{\text{reco}} \times (1 - a). \quad (\text{D.1})$$

The binning of the correction-factor array in each dimension is the following:

- E_{reco} : 8 bins with [4, 7, 10, 14, 20, 30, 50, 70, 100] GeV as bin edges. For energies below the first and above the last bin edge, the correction factor of the first and last bin is used, respectively.
- y_{reco} : same 9 bins that are used in the reconstruction, i.e. [0, 0.1, 0.2, ..., 0.8, 1].
- $\cos(\theta_{\text{reco}})$: 20 equidistant bins, i.e. [-1, -0.9, -0.8, ..., 0.8, 0.9, 1].

In total, this are $8 \times 9 \times 20 = 1440$ bins.

As in total $\sim 1.25 \times 10^6$ $\bar{\nu}_e$ CC events are used to calculate the correction factors, about a fraction of $\sim 0.1\%$ events (one event per bin) is set to exactly the correct value (using MC truth information). Hence, this energy correction procedure does not overestimate the energy resolution quoted in Sec. 12.3.

An example two-dimensional slice of the correction-factor array for the E_{reco} -bin centred around 8.5 GeV is shown in Fig. D.1.

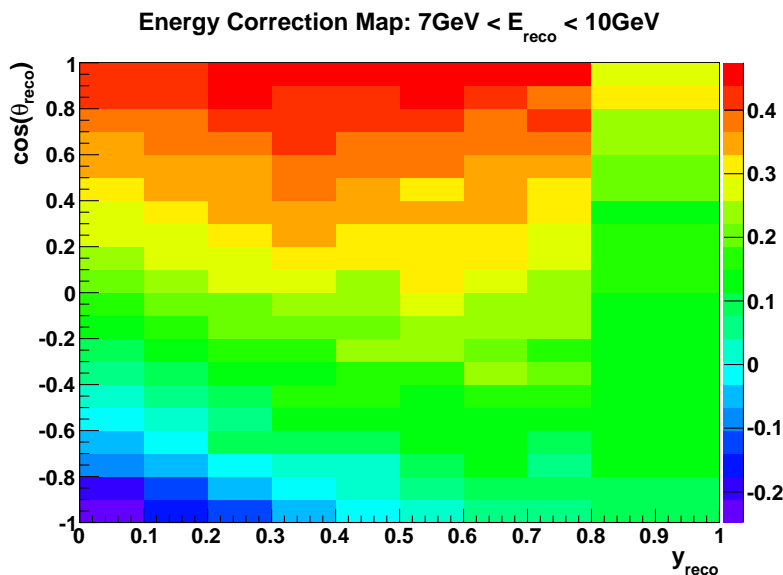


Figure D.1: Energy correction factors a used in Eq. D.1 as a function of y_{reco} and $\cos(\theta_{\text{reco}})$ for the E_{reco} -bin with $7 \text{ GeV} < E_{\text{reco}} < 10 \text{ GeV}$.

D.2 Additional plots

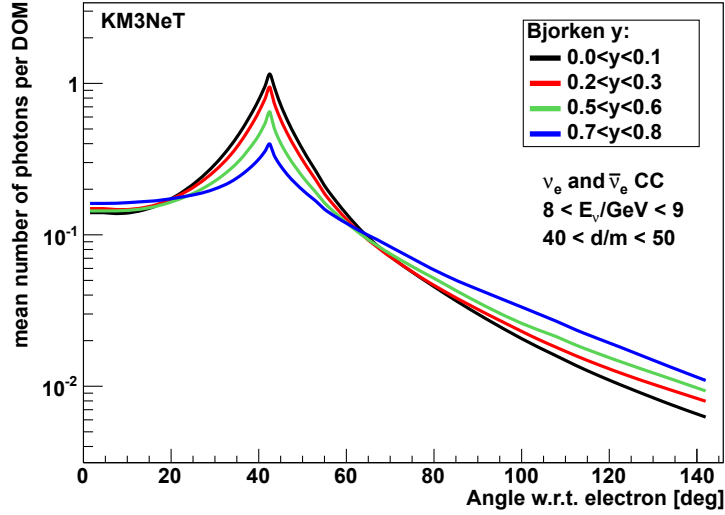


Figure D.2: Smoothed counterpart of Fig. 12.4 (left).

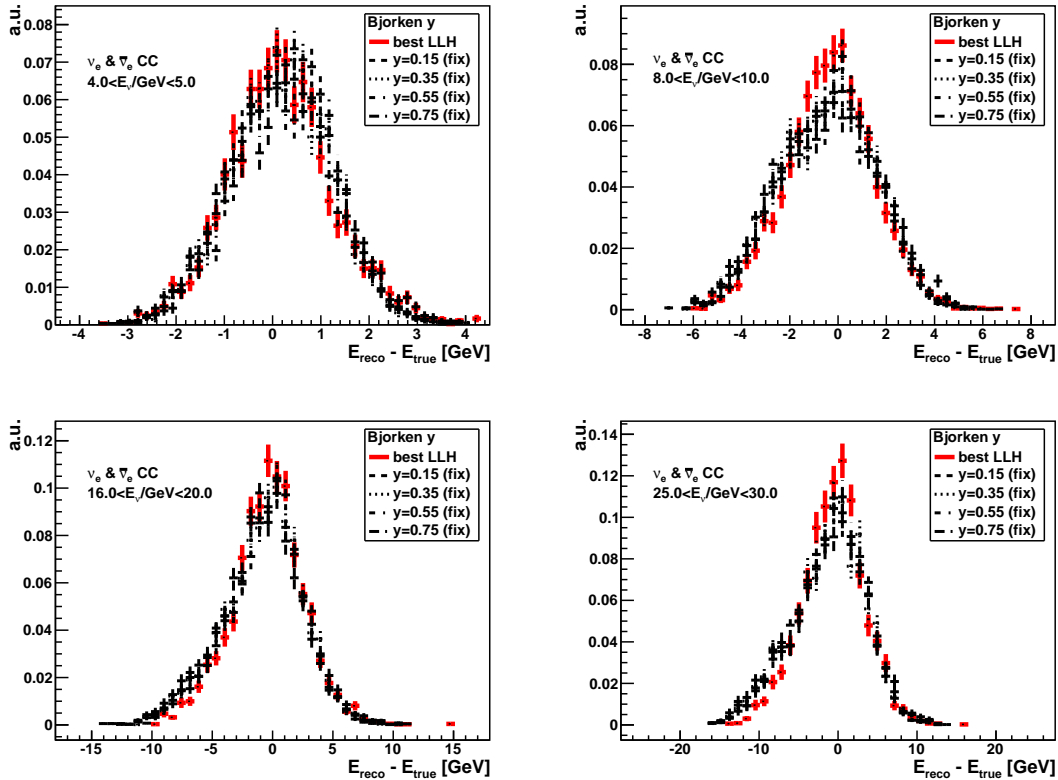


Figure D.3: Difference between reconstructed energy E_{reco} and true neutrino energy E_{true} in four different neutrino energy bins for $\bar{\nu}_e$ CC events weighted according to the Bartol flux model. Reconstruction results for the normal reconstruction procedure (red) and four different fixed inelasticity y assumptions (black) are shown separately. The benchmark detector with 6 m vertical spacing between DOMs is assumed. Distributions are normalised to unity.

Bibliography

- [1] nobelprize.org, *The Nobel Prize in Physics 2015*, Website
http://www.nobelprize.org/nobel_prizes/physics/laureates/2015.
- [2] E. K. Akhmedov, S. Razzaque and A. Yu. Smirnov, *Mass hierarchy, 2-3 mixing and CP-phase with Huge Atmospheric Neutrino Detectors*. JHEP **02**, 082 (2013), [arXiv:1205.7071 [hep-ph]]. [Erratum: JHEP07,026(2013)].
- [3] S. Adrián-Martínez et al., *Letter of intent for KM3NeT 2.0*. J. Phys. **G43**, 084001 (2016), [arXiv:1601.07459 [astro-ph.IM]].
- [4] C. Spiering, *Towards high-energy neutrino astronomy. A historical review*. Eur. Phys. J. **H37**, 515 (2012), [arXiv:1207.4952 [astro-ph.IM]].
- [5] W. Pauli. Letter to Tübingen conference participants, 1930. English translation in: L. M. Brown. *The idea of the neutrino*. Physics Today 31 (1978).
- [6] C. L. Cowan et al., *Detection of the free neutrino: A Confirmation*. Science **124**, 103 (1956).
- [7] G. Danby et al., *Observation of High-Energy Neutrino Reactions and the Existence of Two Kinds of Neutrinos*. Phys. Rev. Lett. **9**, 36 (1962).
- [8] K. Kodama et al., *Observation of tau neutrino interactions*. Phys. Lett. **B504**, 218 (2001), [arXiv:hep-ex/0012035].
- [9] F. Halzen and A. D. Martin, *Quarks and Leptons: An Introductory Course in Modern Particle Physics*. Wiley-VCH, 1984.
- [10] D. Griffiths, *Introduction to Elementary Particles*, 2nd edn. Wiley-VCH, 2008.
- [11] K. A. Olive et al., *Review of Particle Physics*. Chin. Phys. **C38**, 090001 (2014).
- [12] Fukuda, Y. and others, *Evidence for oscillation of atmospheric neutrinos*. Phys. Rev. Lett. **81**, 1562 (1998), [hep-ex/9807003].
- [13] J. A. Formaggio and G. P. Zeller, *From eV to EeV: Neutrino Cross Sections Across Energy Scales*. Rev. Mod. Phys. **84**, 1307 (2012), [arXiv:1305.7513 [hep-ex]].
- [14] K. S. McFarland, *Neutrino Interactions*. In *Proceedings, 61st Scottish Universities Summer School in Physics (SUSSP61)*. 2008. Also in preprint arXiv:0804.3899 [hep-ex].
- [15] J. P. Yáñez Garza, *Measurement of neutrino oscillations in atmospheric neutrinos with the IceCube DeepCore detector*. Ph.D. Thesis, Humboldt University of Berlin, 2014.
- [16] D. I. Scully, *Neutrino Induced Coherent Pion Production*. Ph.D. Thesis, University of Warwick, 2013.
- [17] C. S. Wu et al., *Experimental Test of Parity Conservation in Beta Decay*. Phys. Rev. **105**, 1413 (1957).
- [18] M. Goldhaber, L. Grodzins and A. W. Sunyar, *Helicity of Neutrinos*. Phys. Rev. **109**, 1015 (1958).
- [19] J. M. Conrad, M. H. Shaevitz and T. Bolton, *Precision measurements with high-energy neutrino beams*. Rev. Mod. Phys. **70**, 1341 (1998), [arXiv:hep-ex/9707015].
- [20] G. Stermann et al., *Handbook of perturbative QCD*. Rev. Mod. Phys. **67**, 157 (1995).
- [21] C. H. Llewellyn Smith, *On the Determination of $\sin^2\theta_w$ in Semileptonic Neutrino Interactions*. Nucl. Phys. **B228**, 205 (1983).
- [22] J. G. H. de Groot et al., *Inclusive Interactions of High-Energy Neutrinos and anti-neutrinos in Iron*. Z. Phys. **C1**, 143 (1979).
- [23] S. L. Glashow, *Resonant Scattering of Antineutrinos*. Phys. Rev. **118**, 316 (1960).

- [24] C. H. Llewellyn Smith, *Neutrino Reactions at Accelerator Energies*. Phys. Rept. **3**, 261 (1972).
- [25] S. Kretzer and M. H. Reno, *Tau neutrino deep inelastic charged current interactions*. Phys. Rev. **D66**, 113007 (2002), [arXiv:hep-ph/0208187].
- [26] D. Casper, *The Nuance neutrino physics simulation, and the future*. Nucl. Phys. Proc. Suppl. **112**, 161 (2002), [arXiv:hep-ph/0208030].
- [27] R. A. Smith and E. J. Moniz, *Neutrino reactions on nuclear targets*. Nucl. Phys. **B43**, 605 (1972).
- [28] O. Benhar et al., *Spectral function of finite nuclei and scattering of GeV electrons*. Nucl. Phys. **A579**, 493 (1994).
- [29] T. Leitner and U. Mosel, *Neutrino-nucleus scattering reexamined: Quasielastic scattering and pion production entanglement and implications for neutrino energy reconstruction*. Phys. Rev. **C81**, 064614 (2010), [arXiv:1004.4433 [nucl-th]].
- [30] L. Aliaga et al., *Design, Calibration, and Performance of the MINERvA Detector*. Nucl. Instrum. Meth. **A743**, 130 (2014), [arXiv:1305.5199 [physics.ins-det]].
- [31] C. Andreopoulos et al., *The GENIE Neutrino Monte Carlo Generator*. Nucl. Instrum. Meth. **A614**, 87 (2010), [arXiv:0905.2517 [hep-ph]].
- [32] E. K. Akhmedov and A. Yu. Smirnov, *Paradoxes of neutrino oscillations*. Phys. Atom. Nucl. **72**, 1363 (2009), [arXiv:0905.1903 [hep-ph]].
- [33] K. Zuber, *Neutrino Physics*. CRC Press, 2003.
- [34] C. Giunti and C. W. Kim, *Fundamentals of Neutrino Physics and Astrophysics*. Oxford University Press, 2007.
- [35] L. Schulte, *Determining the Neutrino Mass Hierarchy with the Precision IceCube Next Generation Upgrade (PINGU)*. Ph.D. Thesis, University of Bonn, 2015.
- [36] S. Schael et al., *Precision electroweak measurements on the Z resonance*. Phys. Rept. **427**, 257 (2006), [arXiv:hep-ex/0509008].
- [37] B. Pontecorvo, *Neutrino Experiments and the Problem of Conservation of Leptonic Charge*. Sov. Phys. JETP **26**, 984 (1968). [Zh. Eksp. Teor. Fiz.53,1717(1967)].
- [38] Z. Maki, M. Nakagawa and S. Sakata, *Remarks on the unified model of elementary particles*. Prog. Theor. Phys. **28**, 870 (1962).
- [39] G. C. Branco, R. Gonzalez Felipe and F. R. Joaquim, *Leptonic CP Violation*. Rev. Mod. Phys. **84**, 515 (2012), [arXiv:1111.5332 [hep-ph]].
- [40] B. Kayser et al., *On a theory of neutrino oscillations with entanglement*. Phys. Rev. **D82**, 093003 (2010), [arXiv:1006.2372 [hep-ph]].
- [41] C. Giunti, *Neutrino wave packets in quantum field theory*. JHEP **11**, 017 (2002), [arXiv:hep-ph/0205014].
- [42] R. Slansky et al., *The oscillating neutrino: An introduction to neutrino masses and mixings*. Los Alamos Sci. **25**, 28 (1997).
- [43] L. Wolfenstein, *Neutrino oscillations in matter*. Phys. Rev. **D17**, 2369 (1978).
- [44] M. C. Gonzalez-Garcia and M. Maltoni, *Phenomenology with Massive Neutrinos*. Phys. Rept. **460**, 1 (2008), [arXiv:0704.1800 [hep-ph]].
- [45] T. Ohlsson and H. Snellman, *Three flavor neutrino oscillations in matter*. J. Math. Phys. **41**, 2768 (2000), [arXiv:hep-ph/9910546]. [Erratum: J. Math. Phys.42,2345(2001)].
- [46] S. P. Mikheev and A. Yu. Smirnov, *Resonance Amplification of Oscillations in Matter and Spectroscopy of Solar Neutrinos*. Sov. J. Nucl. Phys. **42**, 913 (1985). [Yad. Fiz.42,1441(1985)].

- [47] S. P. Mikheev and A. Yu. Smirnov, *Resonant amplification of neutrino oscillations in matter and solar neutrino spectroscopy*. *Nuovo Cim.* **C9**, 17 (1986).
- [48] Q. R. Ahmad et al., *Direct evidence for neutrino flavor transformation from neutral current interactions in the Sudbury Neutrino Observatory*. *Phys. Rev. Lett.* **89**, 011301 (2002), [arXiv:nucl-ex/0204008].
- [49] R. Davis, *Nobel Lecture: A half-century with solar neutrinos*. *Rev. Mod. Phys.* **75**, 985 (2003).
- [50] G. Bellini et al., *Final results of Borexino Phase-I on low energy solar neutrino spectroscopy*. *Phys. Rev.* **D89**, 112007 (2014), [arXiv:1308.0443 [hep-ex]].
- [51] J. Bernabeu et al., *The Earth Mantle-Core Effect in Matter-Induced Asymmetries for Atmospheric Neutrino Oscillations*. *Phys. Lett.* **B531**, 90 (2002), [arXiv:hep-ph/0110071].
- [52] E. K. Akhmedov et al., *Atmospheric neutrinos at Super-Kamiokande and parametric resonance in neutrino oscillations*. *Nucl. Phys.* **B542**, 3 (1999), [arXiv:hep-ph/9808270].
- [53] E. K. Akhmedov, *Parametric resonance in neutrino oscillations in matter*. *Pramana* **54**, 47 (2000), [arXiv:hep-ph/9907435].
- [54] M. Freund and T. Ohlsson, *Matter enhanced neutrino oscillations with a realistic earth density profile*. *Mod. Phys. Lett.* **A15**, 867 (2000), [arXiv:hep-ph/9909501].
- [55] E. K. Akhmedov, *Parametric resonance of neutrino oscillations and passage of solar and atmospheric neutrinos through the earth*. *Nucl. Phys.* **B538**, 25 (1999), [arXiv:hep-ph/9805272].
- [56] F. Capozzi et al., *Status of three-neutrino oscillation parameters, circa 2013*. *Phys. Rev.* **D89**, 093018 (2014), [arXiv:1312.2878 [hep-ph]].
- [57] M. C. Gonzalez-Garcia, M. Maltoni and T. Schwetz, *Global Analyses of Neutrino Oscillation Experiments*. *Nucl. Phys.* **B908**, 199 (2016), [1512.06856].
- [58] J. Bergstrom et al., *Bayesian global analysis of neutrino oscillation data*. *JHEP* **09**, 200 (2015), [arXiv:1507.04366 [hep-ph]].
- [59] D. V. Forero, M. Tortola and J. W. F. Valle, *Neutrino oscillations refitted*. *Phys. Rev.* **D90**, 093006 (2014), [arXiv:1405.7540 [hep-ph]].
- [60] F. Capozzi et al., *Neutrino masses and mixings: Status of known and unknown 3ν parameters*. *Nucl. Phys.* **B908**, 218 (2016), [arXiv:1601.07777 [hep-ph]].
- [61] S. Adrián-Martínez et al., *Measurement of Atmospheric Neutrino Oscillations with the ANTARES Neutrino Telescope*. *Phys. Lett.* **B714**, 224 (2012), [arXiv:1206.0645 [hep-ex]].
- [62] M. G. Aartsen et al., *Determining neutrino oscillation parameters from atmospheric muon neutrino disappearance with three years of IceCube DeepCore data*. *Phys. Rev.* **D91**, 072004 (2015), [arXiv:1410.7227 [hep-ex]].
- [63] J. P. Yáñez and A. Kouchner, *Measurement of atmospheric neutrino oscillations with very large volume neutrino telescopes*. *Adv. High Energy Phys.* **2015**, 271968 (2015), [arXiv:1509.08404 [hep-ex]].
- [64] A. de Gouvea et al., *Working Group Report: Neutrinos*. In *Community Summer Study 2013: Snowmass on the Mississippi (CSS2013)*. 2013. Also in preprint arXiv:1310.4340 [hep-ex].
- [65] K. N. Abazajian et al., *Light Sterile Neutrinos: A White Paper* (2012), [arXiv:1204.5379 [hep-ph]].
- [66] M. B. Gavela et al., *Large gauge invariant non-standard neutrino interactions*. *Phys. Rev.* **D79**, 013007 (2009), [arXiv:0809.3451 [hep-ph]].
- [67] C. Biggio, M. Blennow and E. Fernandez-Martinez, *General bounds on non-standard neutrino interactions*. *JHEP* **08**, 090 (2009), [arXiv:0907.0097 [hep-ph]].

- [68] C. Kraus et al., *Final results from phase II of the Mainz neutrino mass search in tritium beta decay*. Eur. Phys. J. **C40**, 447 (2005), [arXiv:hep-ex/0412056].
- [69] V. N. Aseev et al., *An upper limit on electron antineutrino mass from Troitsk experiment*. Phys. Rev. **D84**, 112003 (2011), [arXiv:1108.5034 [hep-ex]].
- [70] G. Drexlin et al., *Current direct neutrino mass experiments*. Adv. High Energy Phys. **2013**, 293986 (2013), [arXiv:1307.0101 [physics.ins-det]].
- [71] G. Pagliaroli, F. Rossi-Torres and F. Vissani, *Neutrino mass bound in the standard scenario for supernova electronic antineutrino emission*. Astropart. Phys. **33**, 287 (2010), [arXiv:1002.3349 [hep-ph]].
- [72] J. Lesgourgues and S. Pastor, *Neutrino mass from Cosmology*. Adv. High Energy Phys. **2012**, 608515 (2012), [arXiv:1212.6154 [hep-ph]].
- [73] K. N. Abazajian et al., *Cosmological and Astrophysical Neutrino Mass Measurements*. Astropart. Phys. **35**, 177 (2011), [arXiv:1103.5083 [astro-ph.CO]].
- [74] X. Zhang, *Impacts of dark energy on weighing neutrinos after Planck 2015*. Phys. Rev. **D93**, 083011 (2016), [1511.02651].
- [75] A. J. Cuesta, V. Niro and L. Verde, *Neutrino mass limits: robust information from the power spectrum of galaxy surveys*. Phys. Dark Univ. **13**, 77 (2016), [1511.05983].
- [76] S. Dell’Oro et al., *The contribution of light Majorana neutrinos to neutrinoless double beta decay and cosmology*. JCAP **1512**, 023 (2015), [arXiv:1505.02722 [hep-ph]].
- [77] M. G. Aartsen et al., *Letter of Intent: The Precision IceCube Next Generation Upgrade (PINGU)* (2014), [arXiv:1401.2046 [physics.ins-det]].
- [78] M. G. Aartsen et al., *PINGU: A Vision for Neutrino and Particle Physics at the South Pole* (2016), [arXiv:1607.02671 [hep-ex]].
- [79] C. H. Albright and M.-C. Chen, *Model Predictions for Neutrino Oscillation Parameters*. Phys. Rev. **D74**, 113006 (2006), [arXiv:hep-ph/0608137].
- [80] K. N. Abazajian et al., *Neutrino Physics from the Cosmic Microwave Background and Large Scale Structure*. Astropart. Phys. **63**, 66 (2015), [arXiv:1309.5383 [astro-ph.CO]].
- [81] W. Winter, *Neutrino mass hierarchy: Theory and phenomenology*. AIP Conf. Proc. **1666**, 120001 (2015).
- [82] M. Honda et al., *Atmospheric neutrino flux calculation using the NRLMSISE-00 atmospheric model*. Phys. Rev. **D92**, 023004 (2015), [arXiv:1502.03916 [astro-ph.HE]].
- [83] G. Battistoni et al., *The FLUKA atmospheric neutrino flux calculation*. Astropart. Phys. **19**, 269 (2003), [arXiv:hep-ph/0207035]. [Erratum: Astropart. Phys.19,291(2003)].
- [84] G. D. Barr et al., *A Three - dimensional calculation of atmospheric neutrinos*. Phys. Rev. **D70**, 023006 (2004), [arXiv:astro-ph/0403630].
- [85] S. Choubey and P. Roy, *Probing the deviation from maximal mixing of atmospheric neutrinos*. Phys. Rev. **D73**, 013006 (2006), [arXiv:hep-ph/0509197].
- [86] M. Blennow et al., *Quantifying the sensitivity of oscillation experiments to the neutrino mass ordering*. JHEP **03**, 028 (2014), [arXiv:1311.1822 [hep-ph]].
- [87] X. Qian et al., *Statistical Evaluation of Experimental Determinations of Neutrino Mass Hierarchy*. Phys. Rev. **D86**, 113011 (2012), [arXiv:1210.3651 [hep-ph]].
- [88] M. Blennow, *On the Bayesian approach to neutrino mass ordering*. JHEP **01**, 139 (2014), [arXiv:1311.3183 [hep-ph]].
- [89] G. Aad et al., *The ATLAS Experiment at the CERN Large Hadron Collider*. JINST **3**, S08003 (2008).

- [90] S. Chatrchyan et al., *The CMS experiment at the CERN LHC*. JINST **3**, S08004 (2008).
- [91] S. Ahmed et al., *Physics Potential of the ICAL detector at the India-based Neutrino Observatory (INO)* (2015), [arXiv:1505.07380 [physics.ins-det]].
- [92] A. G. Tsirigotis, Private communication, 2013.
- [93] T. J. Irvine, *Development of Neutron-Tagging Techniques and Application to Atmospheric Neutrino Oscillation Analysis in Super-Kamiokande*. Ph.D. Thesis, University of Tokyo, 2014.
- [94] M. Ribordy and A. Yu. Smirnov, *Improving the neutrino mass hierarchy identification with inelasticity measurement in PINGU and ORCA*. Phys. Rev. **D87**, 113007 (2013), [arXiv:1303.0758 [hep-ph]].
- [95] P. Adamson et al., *Combined analysis of ν_μ disappearance and $\nu_\mu \rightarrow \nu_e$ appearance in MINOS using accelerator and atmospheric neutrinos*. Phys. Rev. Lett. **112**, 191801 (2014), [arXiv:1403.0867 [hep-ex]].
- [96] K. Abe et al., *Measurements of neutrino oscillation in appearance and disappearance channels by the T2K experiment with 6.6×10^{20} protons on target*. Phys. Rev. **D91**, 072010 (2015), [arXiv:1502.01550 [hep-ex]].
- [97] S. M. Lein, *Muon Neutrino Contained Disappearance in NOvA*. Ph.D. Thesis, University of Minnesota, 2015.
- [98] M. Apollonio et al., *Search for neutrino oscillations on a long baseline at the CHOOZ nuclear power station*. Eur. Phys. J. **C27**, 331 (2003), [arXiv:hep-ex/0301017].
- [99] H. Duan, G. M. Fuller and Y.-Z. Qian, *Collective Neutrino Oscillations*. Ann. Rev. Nucl. Part. Sci. **60**, 569 (2010), [arXiv:1001.2799 [hep-ph]].
- [100] K. Abe et al., *Physics potential of a long-baseline neutrino oscillation experiment using a J-PARC neutrino beam and Hyper-Kamiokande*. Prog. Theor. Exp. Phys. **2015**, 053C02 (2015), [arXiv:1502.05199 [hep-ex]].
- [101] R. Acciarri et al., *Long-Baseline Neutrino Facility (LBNF) and Deep Underground Neutrino Experiment (DUNE) Conceptual Design Report Volume 2: The Physics Program for DUNE at LBNF* (2015), [arXiv:1512.06148 [physics.ins-det]].
- [102] D. S. Ayres et al., *NOvA: Proposal to build a 30 kiloton off-axis detector to study $\nu(\mu) \rightarrow \nu(e)$ oscillations in the NuMI beamline* (2004), [arXiv:hep-ex/0503053].
- [103] F. An et al., *Neutrino Physics with JUNO*. J. Phys. **G43**, 030401 (2016), [arXiv:1507.05613 [physics.ins-det]].
- [104] S.-B. Kim, *New results from RENO and prospects with RENO-50*. Nucl. Part. Phys. Proc. **265-266**, 93 (2015), [arXiv:1412.2199 [hep-ex]].
- [105] M. Bass et al., *Baseline optimization for the measurement of CP violation, mass hierarchy, and θ_{23} octant in a long-baseline neutrino oscillation experiment*. Phys. Rev. **D91**, 052015 (2015), [arXiv:1311.0212 [hep-ex]].
- [106] X. Qian and P. Vogel, *Neutrino Mass Hierarchy*. Prog. Part. Nucl. Phys. **83**, 1 (2015), [arXiv:1505.01891 [hep-ex]].
- [107] W. Winter, *Neutrino mass hierarchy determination with IceCube-PINGU*. Phys. Rev. **D88**, 013013 (2013), [arXiv:1305.5539 [hep-ph]].
- [108] M. Blennow and T. Schwetz, *Determination of the neutrino mass ordering by combining PINGU and Daya Bay II*. JHEP **09**, 089 (2013), [arXiv:1306.3988 [hep-ph]].
- [109] V. Aynutdinov et al., *The BAIKAL neutrino experiment: Physics results and perspectives*. Nucl. Instrum. Meth. **A602**, 14 (2009), [arXiv:0811.1109 [astro-ph]].
- [110] M. Ageron et al., *ANTARES: the first undersea neutrino telescope*. Nucl. Instrum. Meth. **A656**, 11 (2011), [arXiv:1104.1607 [astro-ph.IM]].

- [111] A. Achterberg et al., *First Year Performance of The IceCube Neutrino Telescope*. *Astropart. Phys.* **26**, 155 (2006), [arXiv:astro-ph/0604450].
- [112] C. Kopper, *Performance Studies for the KM3NeT Neutrino Telescope*. Ph.D. Thesis, University of Erlangen-Nürnberg, 2010.
- [113] S. Kuch, *Design studies for the KM3NeT neutrino telescope*. Ph.D. Thesis, University of Erlangen-Nürnberg, 2007.
- [114] P. A. Čerenkov, *Visible Radiation Produced by Electrons Moving in a Medium with Velocities Exceeding that of Light*. *Phys. Rev.* **52**, 378 (1937).
- [115] J. D. Jackson, *Klassische Elektrodynamik*, 3rd edn. De Gruyter, 2002.
- [116] *NIST Digital Library of Mathematical Functions*, Website <http://dlmf.nist.gov>.
- [117] E. Longo and I. Sestili, *Monte Carlo Calculation of Photon Initiated Electromagnetic Showers in Lead Glass*. *Nucl. Instrum. Meth.* **128**, 283 (1975). [Erratum: *Nucl. Instrum. Meth.* 135,587(1976)].
- [118] C. H. V. Wiebusch, *The Detection of faint light in deep underwater neutrino telescopes*. Ph.D. Thesis, RWTH Aachen University, 1995.
- [119] J. Brunner, *Cherenkov light from HE electromagnetic and hadronic showers*. ANTARES internal note (ANTARES-SOFT-2012-015).
- [120] V. Niess, *Détection acoustique sous-marine de neutrinos de ultra haute énergie dans le cadre de l'expérience ANTARES*. Ph.D. Thesis, University of Marseille, 2005.
- [121] M. P. Kowalski, *Search for neutrino induced cascades with the AMANDA-II detector*. Ph.D. Thesis, Humboldt University of Berlin, 2004.
- [122] T. A. Gabriel et al., *Energy dependence of hadronic activity*. *Nucl. Instrum. Meth.* **A338**, 336 (1994).
- [123] R. C. Smith and K. S. Baker, *Optical properties of the clearest natural waters (200–800 nm)*. *Appl. Opt.* **20**, 177 (1981).
- [124] J. A. Aguilar et al., *Transmission of light in deep sea water at the site of the ANTARES Neutrino Telescope*. *Astropart. Phys.* **23**, 131 (2005), [arXiv:astro-ph/0412126].
- [125] G. Riccobene and A. Capone, *Deep seawater inherent optical properties in the Southern Ionian Sea*. *Astropart. Phys.* **27**, 1 (2007), [arXiv:astro-ph/0603701].
- [126] M. Smoluchowski, *Molekular-kinetische Theorie der Opaleszenz von Gasen im kritischen Zustande, sowie einiger verwandter Erscheinungen*. *Ann. Phys.* **330**, 205 (1908).
- [127] A. Einstein, *Theorie der Opaleszenz von homogenen Flüssigkeiten und Flüssigkeitsgemischen in der Nähe des kritischen Zustandes*. *Ann. Phys.* **338**, 1275 (1910).
- [128] C. W. James and J. Hofestädt, *Ice and water optical properties*. KM3NeT internal note (KM3NeT_SIM.2015_001).
- [129] S. H. D. Haddock, M. A. Moline and J. F. Case, *Bioluminescence in the Sea*. *Annu. Rev. Mar. Sci.* **2**, 443 (2010).
- [130] G. Aggouras et al., *Operation and performance of the NESTOR test detector*. *Nucl. Instrum. Meth.* **A552**, 420 (2005).
- [131] P. A. Rapidis, *The NESTOR underwater neutrino telescope project*. *Nucl. Instrum. Meth.* **A602**, 54 (2009).
- [132] E. Migneco et al., *Recent achievements of the NEMO project*. *Nucl. Instrum. Meth.* **A588**, 111 (2008).
- [133] A. Capone et al., *Recent results and perspectives of the NEMO project*. *Nucl. Instrum. Meth.* **A602**, 47 (2009).

- [134] P. Bagley et al., *KM3NeT: Technical Design Report for a Deep-Sea Research Infrastructure in the Mediterranean Sea Incorporating a Very Large Volume Neutrino Telescope*. ISBN 978-90-6488-033-9, 2010.
- [135] S. Adrián-Martínez et al., *Expansion cone for the 3-inch PMTs of the KM3NeT optical modules*. JINST **8**, T03006 (2013).
- [136] S. Adrián-Martínez et al., *The Positioning System of the ANTARES Neutrino Telescope*. JINST **7**, T08002 (2012), [arXiv:1202.3894 [astro-ph.IM]].
- [137] P. Kooijman, *The mechanical structure and deployment procedure of the KM3NeT detection unit*. In *Proceedings, 34th International Cosmic Ray Conference, PoS(ICRC2015) 1173*. 2015.
- [138] J. A. Aguilar et al., *The data acquisition system for the ANTARES Neutrino Telescope*. Nucl. Instrum. Meth. **A570**, 107 (2007), [arXiv:astro-ph/0610029].
- [139] S. Adrián-Martínez et al., *Deep sea tests of a prototype of the KM3NeT digital optical module*. Eur. Phys. J. **C74**, 3056 (2014), [arXiv:1405.0839 [astro-ph.IM]].
- [140] S. Adrián-Martínez et al., *The prototype detection unit of the KM3NeT detector*. Eur. Phys. J. **C76**, 54 (2016), [arXiv:1510.01561 [astro-ph.IM]].
- [141] P. Migliozi and F. Terranova, *Learning from tau appearance*. New J. Phys. **13**, 083016 (2011), [arXiv:1107.3018 [hep-ex]].
- [142] T. Ohlsson, H. Zhang and S. Zhou, *Effects of nonstandard neutrino interactions at PINGU*. Phys. Rev. **D88**, 013001 (2013), [arXiv:1303.6130 [hep-ph]].
- [143] W. Winter, *Atmospheric Neutrino Oscillations for Earth Tomography*. Nucl. Phys. **B908**, 250 (2016), [arXiv:1511.05154 [hep-ph]].
- [144] J. Becker Tjus, *Neutrinos from Colliding Wind Binaries: Future Prospects for PINGU and ORCA* (2014), [arXiv:1405.0471 [astro-ph.HE]].
- [145] Distefano, Carla, *gSeaGen: a GENIE-based code for neutrino telescopes*. EPJ Web Conf. **116**, 08001 (2016), [arXiv:1602.00501 [astro-ph.IM]].
- [146] C. Andreopoulos et al., *The GENIE Neutrino Monte Carlo Generator: Physics and User Manual* (2015), [arXiv:1510.05494 [hep-ph]].
- [147] Y. Becherini et al., *A Parameterisation of single and multiple muons in the deep water or ice*. Astropart. Phys. **25**, 1 (2006), [arXiv:hep-ph/0507228].
- [148] G. Carminati, A. Margiotta and M. Spurio, *Atmospheric MUons from PARAMetric formulas: A Fast GENERator for neutrino telescopes (MUPAGE)*. Comput. Phys. Commun. **179**, 915 (2008), [arXiv:0802.0562 [physics.ins-det]].
- [149] C. Forti et al., *Simulation of atmospheric cascades and deep underground muons*. Phys. Rev. **D42**, 3668 (1990).
- [150] A. G. Tsirigotis, A. Leisos and S. E. Tzamarias, *HOU reconstruction & simulation (HOURS): A complete simulation and reconstruction package for very large volume underwater neutrino telescopes*. Nucl. Instrum. Meth. **A626**, 185 (2011).
- [151] S. Agostinelli et al., *GEANT4: A Simulation toolkit*. Nucl. Instrum. Meth. **A506**, 250 (2003).
- [152] D. Bailey, *Monte Carlo tools and analysis methods for understanding the ANTARES experiment and predicting its sensitivity to dark matter*. Ph.D. Thesis, University of Oxford, 2002.
- [153] R. Brun et al., *GEANT3*. CERN Report DD/EE/84-1, 1987.
- [154] J. Hofestädt, *Differences between KM3/GEASIM and KM3Sim* (unpublished). Presentation at ORCA telephone conference, 17.12.2013.

- [155] A. Ferrari and P.R. Sala, *GEANT Hadronic Event Generators: a comparison at the single interaction level*. ATLAS internal note (PHYS-No-086).
- [156] A. G. Tsirigotis, *Detector simulations for KM3NeT V3.3*. KM3NeT internal note (KM3NeT_SIM.2014.001).
- [157] C. W. James, Private communication, 2015.
- [158] S. Adrián-Martínez et al., *Intrinsic limits on resolutions in muon- and electron-neutrino charged-current events in the KM3NeT/ORCA detector* (2016), [arXiv:1612.05621 [physics.ins-det]].
- [159] C. W. James and J. Hofestädt, *Ice and water optical properties*. KM3NeT internal note (KM3NeT_SIM.2015.001).
- [160] M. Ackermann et al., *Optical properties of deep glacial ice at the South Pole*. J. Geophys. Res. **111**, D13203 (2006).
- [161] M. G. Aartsen et al., *Measurement of South Pole ice transparency with the IceCube LED calibration system*. Nucl. Instrum. Meth. **A711**, 73 (2013), [arXiv:1301.5361 [astro-ph.IM]].
- [162] C. W. James, *km3 release v4r4*. ANTARES internal note (ANTARES-SOFT-2012-007).
- [163] M.-O. Pleinert, *Investigation of 'kinked' muon tracks*. KM3NeT internal note (KM3NeT_THES.2016.003).
- [164] T. Rauch, *Variation of photon direction of non-muonic interaction products*. KM3NeT internal note (KM3NeT_THES.2016.002).
- [165] J. Hofestädt and C. W. James, *Studies of intrinsic resolution to low energy electron and muon neutrino events with neutrino telescopes*. In *Proceedings, 34th International Cosmic Ray Conference, PoS(ICRC2015) 1084*. 2015.
- [166] S.-F. Ge and K. Hagiwara, *Physics Reach of Atmospheric Neutrino Measurements at PINGU*. JHEP **09**, 024 (2014), [arXiv:1312.0457 [hep-ph]].
- [167] M. R. Bowlby and J. F. Case, *Flash kinetics and spatial patterns of bioluminescence in the copepod *Gaussia princeps**. Mar. Biol. **110**, 329 (1991).
- [168] I. G. Priede et al., *The potential influence of bioluminescence from marine animals on a deep-sea underwater neutrino telescope array in the Mediterranean Sea*. Deep Sea Res. **55**, 1474 (2008).
- [169] P. J. Herring, *The Spectral Characteristics of Luminous Marine Organisms*. Proc. R. Soc. Lond. (Ser. B) **220**, 183 (1983).
- [170] Website http://antares.in2p3.fr/Gallery/CNRS/LineConstruction/116_Antares_Vincenttriplet.jpg.
- [171] S. Escoffier and A. S. Cussatlegras, *Correlations between bioluminescence and environmental parameters with ANTARES data in 2003 (PSL) and 2005 (MILOM)*. ANTARES internal note (ANTARES-PHYS-2006-007).
- [172] C. Tamburini et al., *Deep-Sea Bioluminescence Blooms after Dense Water Formation at the Ocean Surface*. PLoS ONE **8**, 1 (2013).
- [173] V. Kulikovskiy, *Neutrino astrophysics with the ANTARES telescope*. Ph.D. Thesis, University of Genova, 2014.
- [174] S. Escoffier, *Bioluminescence studies with the ANTARES Prototype Sector Line* (2005). ANTARES internal note (ANTARES-SITE-2005-001).
- [175] I. Salvadori, *K40 Calibration: Updates* (unpublished). Presentation at ANTARES/KM3NeT Collaboration meeting in Noto, Italy, 16.06.2016.
- [176] R. J. Barlow, *A Guide to the Use of Statistical Methods in the Physical Sciences*. Wiley-VCH, 1989.

- [177] S. Razzaque and A. Yu. Smirnov, *Super-PINGU for measurement of the leptonic CP-phase with atmospheric neutrinos*. JHEP **05**, 139 (2015), [arXiv:1406.1407 [hep-ph]].
- [178] M. de Jong, *The ANTARES Trigger Software*. ANTARES internal note (ANTARES-SOFT-2005-005).
- [179] B. Bakker, *Trigger studies for the ANTARES and KM3NeT neutrino telescopes*. M.Sc. Thesis, University of Amsterdam, 2011.
- [180] J. Hofestädt, *Trigger Studies for ORCA* (unpublished). Presentation at ANTARES/KM3NeT Collaboration meeting in Ischia, 22.05.2015.
- [181] J. Hofestädt, *Shower reconstruction with the KM3NeT/ORCA detector*. In *Proceedings, 34th International Cosmic Ray Conference*, PoS(ICRC2015) 1083. 2015.
- [182] C. Kopper, *A software framework for KM3NeT*. Nucl. Instrum. Meth. **A602**, 107 (2009).
- [183] F. Folger, *Search for a diffuse cosmic neutrino flux using shower events in the ANTARES neutrino telescope*. Ph.D. Thesis, University of Erlangen-Nürnberg, 2014.
- [184] D. Boersma, *Gulliver*, Website (protected)
<https://wiki.icecube.wisc.edu/index.php/Gulliver>.
- [185] J. Hofestädt, *Shower Reconstruction for ORCA* (unpublished). Presentation at ANTARES/KM3NeT Collaboration meeting in Leiden, Netherlands, 22.05.2014.
- [186] CNRS/CC-IN2P3, *Centre de Calcul IN2P3/CNRS*, Website <http://cc.in2p3.fr>.
- [187] V. Van Elewyck, P. Keller and M. Lindsey Clark, *The Calibration Units of the KM3NeT neutrino telescope*. In *Proceedings, 34th International Cosmic Ray Conference*, PoS(ICRC2015) 1160. 2015.
- [188] F. Capozzi, E. Lisi and A. Marrone, *PINGU and the neutrino mass hierarchy: Statistical and systematic aspects*. Phys. Rev. **D91**, 073011 (2015), [arXiv:1503.01999 [hep-ph]].